

THESIS

QUANTIFYING THE LIMITS OF CONVECTIVE PARAMETERIZATIONS:
A STATISTICAL CHARACTERIZATION OF SIMULATED CUMULUS
CONVECTION

Submitted by

Todd R. Jones

Department of Atmospheric Science

In partial fulfillment of the requirements

For the Degree of Master of Science

Colorado State University

Fort Collins, Colorado

Spring 2010

COLORADO STATE UNIVERSITY

March 10, 2010

WE HEREBY RECOMMEND THAT THE THESIS PREPARED UNDER OUR SUPERVISION BY TODD R. JONES ENTITLED QUANTIFYING THE LIMITS OF CONVECTIVE PARAMETERIZATIONS: A STATISTICAL CHARACTERIZATION OF SIMULATED CUMULUS CONVECTION BE ACCEPTED AS FULFILLING IN PART REQUIREMENTS FOR THE DEGREE OF MASTER OF SCIENCE.

Committee on Graduate Work

David Thompson

Sanjay Rajopadhye

Advisor: David A. Randall

Department Head: Richard H. Johnson

ABSTRACT OF THESIS

QUANTIFYING THE LIMITS OF CONVECTIVE PARAMETERIZATIONS: A STATISTICAL CHARACTERIZATION OF SIMULATED CUMULUS CONVECTION

This study reviews and characterizes such departures from convective quasi-equilibrium, that is, fluctuations about the equilibrium state that are found to be present in convective simulations of a cloud-resolving model (CRM) that lead to effects of non-equilibrium and non-deterministic behavior. Information about such behavior is hypothesized to be important to the development of stochastic convective parameterizations that are employed to introduce temporal variability into general circulation models (GCMs) in an informed manner to improve the statistics of various fields. Following a process similar to the methods used by Xu *et al.* (1992) the response of the statistical characteristics of a variety of convection-related parameters to an imposed periodic large-scale forcing is determined in terms of a variety of convective variables. More specifically, a number of CRM simulations are employed to address various issues, among which are how the response varies with changes in the length of the forcing period, how the response varies with computational domains of varying sizes, and how different points in the response to a cyclical forcing compare to the response to a comparable time-averaged constant forcing. Additionally, this thesis includes the results of the CRM's participation in the TWP-ICE intercomparison study that was used to validate the model.

As a control, the model is subjected to a series of constant forcing simulations for a variety of large-scale forcing magnitudes, which provides a cloud-resolving model representation of statistical equilibrium. It is shown that the coefficient of variation is not independent of forcing magnitude as may be expected, particularly for forcing magnitudes that are very small or very large. Seemingly minor variations are expected to bias aspects of GCM simulations in ways that can alter the representation of statistical (periodic) features.

With the application of a periodic forcing at varying period lengths and consideration of the simulation results on a series of subdomain sizes, it is shown that there is a considerable range of responses to a given large-scale forcing that are dependent upon the rate of change in the forcing and in the size of the averaging domain. Specifically, the analyses show that the more slowly a forcing varies, the more it is well approximated by an equilibrium assumption. The point at which the transition between being an acceptable approximation of equilibrium or not occurs is approximately located where the timescale of the variation of the large-scale forcing is greater than 30 hours. Convective activity is also found to be dependent upon whether the large-scale forcing was increasing or decreasing and also the rate at which it was doing so.

Further, nondeterministic variability for a given situation is much greater at smaller domain sizes; this is the problem of insufficient sample size, which is one that grows in importance as grid spacing in GCMs approaches the lower tens of kilometers. This relationship is best described by a logarithmic function of the domain area. Based on the statistics for the weather regime presented in this thesis, the best recommendation is that the line between determinism and non-determinism should be drawn such that the

considered area (grid box area) is no smaller than about half the domain size used in this thesis. This is equivalent to about 33,000 km² or grid spacing slightly larger than 180 km.

Cumulatively, the results of the performed experiment highlight both the complexity underlying the development of, and the need for, stochastic convective parameterization. Classical assumptions about quasi-equilibrium are never exact and break down altogether when the time scale for changes in the resolved-scale weather is near or less than the convective adjustment time. This is a problem that is made more severe in newer high-resolution models (*e.g.* Arribas 2004; Bechtold *et al.* 2008) just because shorter time scales are inherent in convective systems with smaller spatial scales. The basics of a statistical approach for the development of a stochastic parameterization are outlined.

Todd R. Jones
Department of Atmospheric Science
Colorado State University
Fort Collins, CO 80523
Spring 2010

Table of Contents

Title Page	i
Signature Page	ii
Abstract of Thesis.....	iii
List of Figures	viii
List of Tables	xiv
Chapter 1 - Introduction.....	1
1.1 Overview	1
1.2 Thesis Outline	4
Chapter 2 - Background.....	6
2.1 The Arakawa-Schubert cumulus parameterization	6
2.2 Qualitative and quantitative characteristics of QE fluctuations	10
2.3 Stochastic parameterizations	17
Chapter 3 - Numerical Simulations	29
3.1 Introduction	29
3.2 Model.....	29
3.3 Experimental Design	32
Chapter 4 – Model Validation.....	36
4.1 TWP-ICE CRM Intercomparison Study	36
4.1.1 <i>Background</i>	36
4.1.2 <i>Experiment Design</i>	40
4.2 Intercomparison Results	44
Chapter 5 - Simulation Results	54
5.1 Constant Forcing Simulations	54
5.2 Periodic Forcing Simulations.....	62
5.2.1 <i>Snapshot Views</i>	63
5.2.2 <i>Sounding Features</i>	73
5.2.3 <i>Composite Analysis – Full Domain</i>	85
5.2.4 <i>Composite Analysis – Partial Domains</i>	120
5.2.5 <i>Extended Composite Analysis</i>	132
5.2.6 <i>Correlation Analysis</i>	152
5.2.7 <i>Probability Density Function Variations</i>	162
5.3 More Periodic and Constant Forcing Comparisons.....	172
Chapter 6 – Discussion and Conclusions	180

Appendix 1 – TWP-ICE Simulation Data List	187
Reference List	191

List of Figures

Figure 2.1. Vertical profiles of temperature and relative humidity for various typhoon observations from Lord and Arakawa (1980) pointing out that when cumulus convection exists, a relatively dry atmosphere has a larger lapse rate than a more moist atmosphere.....	10
Figure 2.2. Time series of hourly surface precipitation for weak shear (F01, F15), strong shear (F12, F05), moderate shear (F13, V13), no shear (Q03), and a shear case for a 512-km and 1024-km domains from X92.....	13
Figure 2.3. The ensemble mean and standard deviation of (a) the total and (b) the mesoscale horizontal kinetic energies from X92 demonstrating the phase delay in response to large-scale forcing that is due to mesoscale organization.	14
Figure 2.4. Particle moving in a bi-modal potential well with two stable equilibria, corresponding to baroclinic waves of wavenumbers 1 and 2 (Williams 2005).	20
Figure 2.5. Particle moving in a potential well with a single mode shown with two perturbation amplitudes and differing locations of equilibrium.	21
Figure 3.1. The sheared, prescribed u-wind profile with which each simulation is initialized (a and the maximum value profiles of the prescribed large-scale advective cooling and moistening (b).....	34
Figure 4.1. The TWP-ICE experimental domain and observing platforms.....	37
Figure 4.2. Cumulative rainfall at three locations in the Northern Territory during the 2005-2006 monsoon season. Figure courtesy of Lori Chappel, Australian Bureau of Meteorology. (Reproduced from Fridlind <i>et al.</i> 2010).	42
Figure 4.3. Surface precipitation rate for the noted models. The acronyms are described in Section 4.1.1. The reference data is based on radar observations.	45
Figure 4.4. As in Figure 4.3, but for the precipitation rate at the 2.5-km level.	46
Figure 4.5. As in Figure 4.3, but for the cloud fraction.	47
Figure 4.6. As in Figure 4.3, but for the cloud top heights.....	48
Figure 4.7. As in Figure 4.3, but for the cloud base heights.....	48
Figure 4.8. Profile time series of cloud fraction for (a) CSUVVM, (b) DHARMA, and (c) EULAG and (d) the observed cloud frequency at the Darwin ARM site (Xie <i>et al.</i> 2009).....	49

Figure 4.9. Profile time series of tracers for (left) CSUVVM (center) EULAG, and (right) MESONH. The panels show tracers at the (a, b, c) boundary layer, (d, e, f) lower troposphere, (g, h, i) middle troposphere, and (j, k, l) upper troposphere levels.	51
Figure 5.1.1. Time evolution of the domain-averaged surface precipitation rate (black) for each of the constant forcing simulations (plot titles). The time series mean (red) and standard deviation bounds (blue) are overlaid.	55
Figure 5.1.3. As in Figure 5.1.1, but for non-precipitating condensate.	57
Figure 5.2.1. a.) the time-mean surface precipitation rate; b.) the time-relative standard deviation of the surface precipitation rate; and c.) the mean-scaled standard deviation of the surface precipitation rate for constant forcing simulations CF1 through CFX.	58
Figure 5.2.2. As in Figure 5.2.1, but for cloud fraction.	60
Figure 5.2.3. As in Figure 5.2.1, but for non-precipitating condensate.	61
Figure 5.3. Description is found in the text. (a) Snapshots from F02 and (b) F06.	65
Figure 5.4. Vertical cross section of the sum of cloud water and ice mass per unit horizontal area showing the zy-plane at various values of x, moving west to east from (a) to (f). This figure corresponds to Figure 5.3a.	66
Figure 5.5. As in Figure 5.3. (a) Snapshots from F10 and (b) F12.	67
Figure 5.6. As in Figure 5.3. (a) Snapshots from F14 and (b) F24.	69
Figure 5.7. As in Figure 5.3. (a) Snapshots from F14 and (b) F24.	72
Figure 5.8. As in Figure 5.3. Snapshot from F120.	72
Figure 5.9. Domain-averaged soundings of the noted quantities for each realization of F02. The colors indicate the order of the realizations, with blue being first and red being last. The black solid line indicates the composite average, and the black dashed line represents an estimate of the average height of the convective towers.	75
Figure 5.10. As in Figure 5.9, but for F60.	76
Figure 5.11. Domain-averaged difference of soundings (increasing –decreasing) for the noted quantities from F02. Coloring as in Figure 5.9.	77
Figure 5.12. As in Figure 5.11, but for F10.	77
Figure 5.13. As in Figure 5.11, but for F60.	78
Figure 5.14. Pseudoadiabatic CAPE time series for all simulations. See text for description.	79
Figure 5.15. Pseudoadiabatic CAPE when the large-scale forcing is increasing and decreasing.	80

Figure 5.16. Power spectra for pseudoadiabatic CAPE for the noted simulations. The red curve is indicative of theoretical red noise, and the dashed blue curve shows the 95% significance level.....	81
Figure 5.17. Time series of surface precipitation rate ,(top) pseudoadiabatic CAPE (middle), their lag correlations (bottom left), and a scatterplot and correlation of the normalized CAPE tendency and precipitation (bottom right) for the F08 simulation.....	82
Figure 5.18. As in Figure 5.17 but for the F30 simulation.	83
Figure 5.19. Correlation coefficients versus forcing period for domain averaged precipitation and pseudo adiabatic CAPE tendency.	84
Figure 5.20. The maximum correlation lag between domain averaged precipitation and pseudo adiabatic CAPE tendency plotted versus the forcing period.	85
Figure 5.21. Whole domain average statistical composite of surface precipitation rate for the noted simulations. The black curve is the composite mean. The blue hash-filled region bounded by the dot-dash line is the standard deviation across the cycles. The red curve represents the timing and relative magnitude (0-100%) of the large-scale forcing and is only for reference; no specific values are implied.....	89
Figure 5.22. As in Figure 5.21 but for cloud fraction.....	93
Figure 5.23. As in Figure 5.21 but for non-precipitating condensate.	96
Figure 5.24. As in Figure 5.21 but for precipitable water.	97
Figure 5.25. As in Figure 5.21 but for cloud mass flux through the ~2.5-km level. ...	99
Figure 5.26. As in Figure 5.21 but for upward cloud mass flux through the ~2.5-km level.....	101
Figure 5.27. As in Figure 5.21 but for downdraft cloud mass flux magnitude through the ~2.5-km level.	102
Figure 5.28. As in Figure 5.21 but for integrated buoyancy flux.....	104
Figure 5.29. Composite cloud fraction profiles for the noted simulations. The white line denotes the placement of the normalized large-scale forcing.	105
Figure 5.30. As in Figure 5.29 but for non-precipitating condensate.	106
Figure 5.31. Whole domain composite of surface precipitation rate skewness for (a.) F02, (b.) F08, (c.) F20, (d.) F30, (e.) F60, and (f.) F120. The black curve is the composite mean of the field skewness. The red curve represents the timing and relative magnitude (0-100%) of the large-scale forcing and is only for reference; no specific values are implied.	109

Figure 5.32. As in Figure 5.21 but for the negative of the skewness of the surface precipitation rate over the full domain.	111
Figure 5.33. As in Figure 5.21 but for the domain mean vertical eddy kinetic energy.	113
Figure 5.34. Characteristics of the weighting and impulse response functions of the Ormsby (1961) filter as used in one (top) and two (middle, bottom) dimensions. See text for additional description.	115
Figure 5.35. Raw (left) and filtered (right) vertical (top) and horizontal (middle) eddy kinetic energy fields, and raw and filtered power for a select F12 vertical EKE field (bottom).	118
Figure 5.36. As in Figure 5.21 but for the filtered domain mean vertical eddy kinetic energy.	119
Figure 5.37. As in Figure 5.21 but for noted subdomains of the F30 simulation.	122
Figure 5.38. As in Figure 5.21 but for noted subdomains of the F08 simulation.	125
Figure 5.39. As in Figure 5.21 but for noted subdomains of the F120 simulation. ..	126
Figure 5.40. As in Figure 5.21 but for cloud fraction within the noted subdomains of the F30 simulation.	128
Figure 5.41. As in Figure 5.21 but for non-precipitating condensate within the noted subdomains of the F30 simulation.	129
Figure 5.42. As in Figure 5.21 but for the cloud mass flux through the 2.5-km level within the noted subdomains of the F30 simulation.	130
Figure 5.43. The surface precipitation rate standard deviation for the whole domain case for all periodic forcing simulations.	134
Figure 5.44. As in Figure 5.43 but for the coefficient of variation.	134
Figure 5.45. As in Figure 5.43 but for the quarter domain.	134
Figure 5.46. As in Figure 5.44 but for the quarter domain.	135
Figure 5.47. As in Figure 5.43 but for the 256 th domain.	136
Figure 5.48. As in Figure 5.44 but for the 256 th domain.	137
Figure 5.49. As in Figure 5.44 but for the cloud mass flux and the 16 th domain.	138
Figure 5.50. Maximum standard deviation versus forcing period length at all subdomains for (a.) surface precipitation rate, (b.) cloud fraction, (c.) cloud mass flux, and (d.) non-precipitating condensate.	140
Figure 5.51. As in Figure 5.50 but for the coefficient of variation at the maximum standard deviation.	143
Figure 5.52. As in Figure 5.43 but for F08 for all subdomains.	144

Figure 5.53. As in Figure 5.52 but the coefficient of variation.....	144
Figure 5.54. As in Figure 5.52 but for F120.	145
Figure 5.55. As in Figure 5.53 but for F120.	145
Figure 5.56. Maximum standard deviation versus normalized domain area for all periodic forcing simulations for (a.) surface precipitation rate, (b.) cloud fraction, (c.) cloud mass flux, and (d.) non-precipitating condensate. The green line is the mean of the black curves.....	149
Figure 5.57. As in Figure 5.56, but for the coefficient of variation. Additionally, the red lines denotes the trend lines fit to the green curves.....	151
Figure 5.58. Scatterplots for the full 15 cycles of the F04 (a), F10 (b), F20 (c), F30 (d), F60 (e), and F120 (f) simulations of the domain average values of cloud fraction (upper left), surface precipitation rate (upper right), non-precipitating condensate (lower left), and cloud mass flux (lower right) versus the normalized forcing.	155
Figure 5.59. Scatterplots for the full 15 cycles of the F06 simulation of the full domain (upper left), half domain (upper center), quarter domain (upper right), 16 th domain (lower left), 64 th domain (lower center), and 256 th domain (lower right) average values of cloud mass flux versus the normalized forcing.....	158
Figure 5.60. As in Figure 5.59 but for the F20 simulation.....	160
Figure 5.61. As in Figure 5.59 but for the F60 simulation.....	161
Figure 5.62. Probability density function for the surface precipitation rate calculated over the whole domain and averaged over the entire length of the F14 simulation.	163
Figure 5.63. As in Figure 5.62 but for non-precipitating condensate in the F120 simulation.	163
Figure 5.64. As in Figure 5.62 but for column liquid water in the F30 simulation...	164
Figure 5.65. PDFs of full domain surface precipitation rate averaged over 15 realizations for noted instances in the F12 cycle.	166
Figure 5.66. As in Table 5.3.	170
Figure 5.67. As in Table 5.4.	171
Figure 5.68. Average vertical temperature profiles [K] versus normalized large-scale forcing for (a) constant forcing simulations, (b) F02, (c) F10, and (d) F20.	173
Figure 5.69. As in Figure 5.68 but for relative humidity [fraction]. Additionally, (d) is for F24 rather than F20. The white areas denote regions of supersaturation	174

Figure 5.70. The domain averaged precipitation rate (a) and the cloud fraction (b) versus the normalized forcing for all constant and periodic forcing simulations..... 175

Figure 5.71. Cloud fraction vertical profiles for the CF1 (a) and CFX (b) simulations..... 178

List of Tables

Table 3.1. List of all saved model variables for each model run. The time length of the various model runs ranges from 1.25 to 75 simulated days. All instantaneous variables are 3D, while the time-averaged variables are 2D.....	31
Table 5.1. List of parameters b and c corresponding to the best fit curve (of the form given by equation 5.10) for the green curves of Figure 5.56 and the correlation coefficient for each best fit curve.....	152
Table 5.2. List of parameters b and c corresponding to the best fit curve (of the form given by equation 5.10) for the green curves of Figure 5.57 and the correlation coefficient for each best fit curve.....	152
Table 5.3. Maximum composite values of domain mean surface precipitation rate [mm hr^{-1}] as dependant upon period length and subdomain size for use in calculating a gamma distribution.	170
Table 5.4. As in Table 5.3 but for the standard deviation [mm hr^{-1}] of the means associated with the composite maximum.....	170
Table 5.5. As in Table 5.3 but for the skewness of the means associated with the composite maximum.	171

Chapter 1 - Introduction

1.1 Overview

Generically, the aim of a parameterization is to mathematically describe the statistics of physical phenomena that occur quickly or on small spatial scales in terms of physical phenomena that occur more slowly or on large spatial scales. The goal of cumulus parameterization is to determine changes in the simulated large-scale environment, such as the transports of momentum, energy, and moisture, due to the collective influence of multiple cumulus clouds, which are examples of fast atmospheric phenomena that occur on the small-scale. Parameterization allows modelers to gain computational efficiency by being able to run atmospheric models at larger than cloud-resolving scale resolution as well as an increased level of comprehension of the physical processes represented by a given parameterization. One of the main problems with this approach, as with all simplifications and approximations, is that some process is always left unaccounted for in the system, and in the wake of the application of an approximation, what remains to be determined is the relative importance of that which has been neglected.

As noted by Lin and Neelin (2002), most general circulation and numerical weather prediction models use convective parameterizations that aim only to simulate the mean effects of convection, as represented by a set of expected values based on a local equilibrium hypothesis. This typically involves a deterministic parameterization that includes an assumed balance between large-scale (resolved) forcings, such as upper-level radiative cooling and low-level moistening of the boundary layer, which act to destabilize

the troposphere, and the small-scale (unresolved, convective-cloud) effects, such as upper-level warming and boundary layer drying by cumulus convection, which act to destroy the instability. Put another way, there is an assumed equilibrium between convection, radiation, and large-scale dynamics, whereby increases in convective available potential energy (CAPE) brought about by radiative cooling, evaporation at the surface, and large-scale dynamical motions would be balanced by CAPE-reducing warming and drying associated with cumulus convection.

The equilibrium assumption can only be exactly true, however, in the limit of averaging over an infinite number of convective clouds, and its validity relies, in part, on the existence of a scale separation between the large-scale environment and the clouds themselves. Historically, such a separation of scales has been hoped for in the mesoscale (on the order of five to several hundred kilometers) with energetic peaks on smaller and larger scales (*e.g.* van der Hoven 1957). However, more recent work, which considered more high-resolution, long-term observations from the Rain in Shallow Cumulus (RICO) field campaign (Roy 2009), has shown what has generally been accepted but not critically assessed. That is, the spectral gap is at the very least not a universal property for the vast majority of atmospheric fields.¹

Additionally, there is a contribution to the variability of convection that arises inherently from small-scale motions and which deviates from the expected response of the atmosphere to given large-scale temperature, momentum, and moisture fields. Knowledge of these motions has prompted recognition of the fact that while such a balance is certain in a time-averaged sense, it is actually only statistical (Randall *et al.* 1994). Fur-

¹ In one investigative subset by Roy (2009), vertical velocity was shown to have a relative spectral power gap in the mesoscale.

ther, nonlinear interactions between these small-scale fluctuations have been shown (*e.g.*, Randall *et al.* 1994) to produce spontaneous large-scale temporal variability that occurs on both short and long timescales. Hence, the assumed equilibrium as presented above is more correctly referred to as statistical convective equilibrium.

Since the number of large convective clouds within a typical $(100 \text{ km})^2$ global circulation model (GCM) grid cell does not usually exceed a count on the order of ten to 100, numbers that one might refer to as “not significantly approaching infinity” (even when looking an ensemble of convective clouds over a period of time on the order of tens to hundreds of minutes), it is expected that, for a given grid cell, there should be some variability through time that departs from the ensemble mean. Small-scale variations of this type not only allow for solutions that deviate from the expected (QE) response to the large-scale forcing, but they also have to the ability to alter the variability of the large-scale motions themselves, especially in the presence of mesoscale organization (Xu *et al.* 1992). Furthermore, the desire to create stochastic convective parameterizations (SCPs) has developed from the realization that QE-based convective parameterizations employed in GCMs fail to reproduce the full spectrum of convective variability that is found in CRM ensembles and observational data. It has been suggested (Neelin *et al.* 2008) that correct representation of convective variability is critical for deducing statistically-based weather features, such as the Madden-Julian Oscillation (MJO), from GCMs. Additionally, implementation of an SCP in a climate model that, without it, would yield weak MJO-like intraseasonal variability, could enhance that variability to improve comparison to observations. Such an improvement would be advantageous for both weather prediction and climate studies.

Implementation of SCPs as a method to introduce, significantly, the effects of subgrid-scale (SGS) convective variability into a GCM can be as simple as introducing a random multiplier to variables in a given parameterization (in a temporal sense) to increase overall ensemble spread and improve probabilistic precipitation forecasts. However, such an approach is not a true physical parameterization, directly linked to resolved processes. A more complex, yet physically based, method requires an understanding of the nature of the deviation from QE to be able to direct convective variability in a more informed manner. Specifically, this means that data must be obtained relating the deviation to both its non-deterministic and non-equilibrium components.

1.2 Thesis Outline

This study reviews and characterizes such departures from convective quasi-equilibrium, that is, fluctuations about the equilibrium state that are found to be present in convective simulations of a cloud-resolving model (CRM). It is the aim of this research to determine the response of the statistical characteristics of a variety of convection-related parameters to an imposed periodic large-scale forcing. This will be done in a manner similar to the methods used by Xu *et al.* (1992, hereafter, X92) who used a two-dimensional CRM. More specifically, a number of CRM simulations are employed to address various issues, among which are whether the response in a three-dimensional simulation is similar to that from the two-dimensional study, how the response varies with changes in the length of the forcing period, how the response varies with computational domains of varying sizes, and how different points in the response to a cyclical forcing compare to the response to a comparable time-averaged constant forcing.

Chapter 2 provides an expanded background view of both early and more current contributions to the science relevant to this thesis. It consists of a brief review and analysis of a well-known example of a QE-based cumulus parameterization developed by Arakawa and Schubert (1974, hereafter AS74), a discussion of the aforementioned QE fluctuations in a qualitative and quantitative sense, and examples of how analyses of the fluctuations have encouraged development of stochastic parameterizations that aim to add the effects of the fluctuations to large-scale models. Chapter 3 is a description of the cloud resolving model used to characterize convective statistics and includes introductory discussion of the design of the numerical simulations. Chapter 4 is devoted to one instance of model validation. In this case, it deals with the performance of the CRM in an inter-comparison study that was done, in part, as a joint element of this thesis. In Chapter 5, I present the CRM results that highlight variations within the QE departures that are dependent upon simulation domain size, the period of the large-scale forcing, and whether the large-scale forcing is increasing or decreasing. Finally, in Chapter 6, a discussion and conclusions are presented.

Chapter 2 - Background

2.1 The Arakawa-Schubert cumulus parameterization

AS74 presents a “closed theory of the mutual interaction of a cumulus cloud ensemble with the large scale environment.” In this parameterization, cumulus clouds are shown to modify the large-scale environment by compensating subsidence between the clouds and by the detrainment of liquid droplet-containing cloud air. Instead of calculating the general cloud effect on the large-scale environment based on a single set of “representative” convective characteristics that might be used to define a certain type of cloud, the parameterization involves a discretization into subensembles or “cloud types.” The definition of a cloud type may be based on any one of a number of cloud parameters, such as entrainment rate, vertical extent, etc. All subensembles are assumed to originate near the planetary boundary layer (PBL) top and to share a common large-scale environment defined by a selection of non-convective processes. Each non-negative fractional entrainment rate that defines a cloud type is allowed to coexist with any number of other active cloud types. Determination of the cloud subensemble thermodynamic properties in AS74, such as the in-cloud moist static energy and water vapor mixing ratio, is accomplished by three main concepts. These are normalization of the subensemble mass flux at cloud base, assumption of nonbuoyancy of cloud air at cloud top, which is assumed to be the only location of detrainment, and specification of moist static energy and the water vapor mixing ratio at cloud base. Once the distribution of the cloud base mass flux over

all subensembles is determined, the cumulus convection parameterization is closed (Lord and Arakawa 1980; Randall *et al.* 1997a).

To close the parameterization, a balance between the stabilizing and destabilizing processes of the system is assumed in terms of the cumulus subensemble kinetic energy budget, such that

$$\frac{d}{dt}K(\lambda)d\lambda = [A(\lambda) - D(\lambda)]M_B(\lambda) \quad (2.1)$$

where $K(\lambda)d\lambda$ is the cloud-scale kinetic energy for a subensemble, $D(\lambda)$ is the cloud-scale kinetic energy dissipation per unit $M_B(\lambda)d\lambda$ (the cloud base mass flux), and $A(\lambda)$ is the subensemble generation of kinetic energy due to the buoyancy force, or the “cloud-work function,” which is defined as the vertical integral of the buoyancy of the cloud air with respect to the large-scale environment. Additionally, the quantity $D(\lambda)M_B(\lambda)$ is equal to the kinetic energy divided by the timescale for kinetic energy dissipation, which is on the order of that of a cloud lifetime as noted below. It can be shown that when the timescale over which (2.1) is applied (timescale of a large-scale process, $\sim 10^5$ s) is much greater than the time for a cloud type λ to decay (a cloud lifetime, $\sim 10^2$ - 10^3 s),

$$A(\lambda) \approx D(\lambda) \quad \text{for } M_B(\lambda) > 0 \quad (2.2)$$

which is a statement of the kinetic energy QE for each cumulus ensemble or that kinetic energy generation tends to balance dissipation. Therefore, when a cloud lifetime is much shorter than the lifetime of a large-scale disturbance, the kinetic energy QE is a good approximation. By extension, if a large scale forcing changes too rapidly, there can be no equilibrium, statistical or otherwise.

Mathematically, the cloud work function is given in AS74 as

$$A(\lambda) = \int_{z_B}^{z_D(\lambda)} \frac{g}{c_p T(z)} \eta(z, \lambda) [s_{vc}(z, \lambda) - \overline{s_v}(z)] dz \quad (2.3)$$

where z_D is the height of the detrainment level; z_B is the cloud base at the PBL; η is the normalized cloud mass flux, satisfying $M_c = \eta M_B$; M_B is the cloud-base mass flux; s_v is the virtual static energy; and the subscript c denotes the in-cloud sounding. Note that for a given λ , $A(\lambda)$ depends only on the large-scale thermodynamic vertical structure, and for $\lambda = 0$, that is, when there is no entrainment, $A(\lambda)$ is equivalent to the CAPE. From this, the closure assumption can be understood in a different way. By taking the time derivative of (2.3) and using the conservation equations for thermodynamic energy and moisture, one obtains

$$\frac{dA(\lambda)}{dt} = JM_B(\lambda) + F(\lambda) \quad (2.4)$$

Following Randall *et al.* (1997b), (2.4) is written in simplified form such that J represents the kernel of the resulting integral, and JM_B represents the integral over all cloud types, thus representing all terms involving convective processes, and is usually negative as the process of convection tends to reduce the vertical integral of buoyancy. The F term represents the large-scale (non-convective) forcing as defined by AS74, and it tends to be positive, increasing buoyancy and the tendency for convection.

By setting (2.4) approximately equal to zero (certainly the cloud work function will vary from day to day and possibly significantly hour to hour), and assuming that some forcing is being applied, we can see the assertion of QE once again, such that any convective instability created by the forcing term is consumed by the effects of cumulus convection almost instantaneously. Randall *et al.* (1997b) note that while in a steady-

state situation, such an equilibrium is trivially satisfied, the assertion of the relation is that the equilibrium holds approximately even when the forcing varies in time in a sufficiently slow manner. This argument is easily maintained given the above discussion of the separation of timescales for large-scale processes and convection, but the question that remains is one of how well separated these timescales must be and how rapidly the forcing may be permitted to fluctuate for this relationship to hold.

Lord and Arakawa (1980) hypothesized that the dissipation per unit cloud base mass flux $D(\lambda)$ is an intrinsic property that is quasi-constant for each cumulus subensemble, to a first approximation, because dissipation in clouds should depend primarily on momentum entrainment through cloud boundaries and downward drag due to precipitation falling within the cumulus updrafts rather than properties of the large-scale state. In relation to (2.2), the values of the cloud-work function should also be quasi-constant whenever a particular type of cloud exists. Since the cloud-work function is easily calculated, Lord and Arakawa (1980) examined its value as determined by large-scale moisture and temperature data for 17 possible cloud types (based on vertical extent) for each of seven observational datasets. They found that for a wide range of large-scale stability and relative humidity distributions, there was a remarkable similarity in the cloud-work function statistics for each cloud type. This was determined to be due to the fact that there is a strong coupling between stability and relative humidity values, which essentially align (come to an equilibrium) resulting in approximately the same cloud-work function for various combinations of the variables. To be more exact, they noted “when cumulus convection exists, a relatively dry atmosphere has a larger lapse rate than a more moist atmosphere (Figure 2.1, Figures 6 & 7 from Lord and Arakawa, 1980). The study

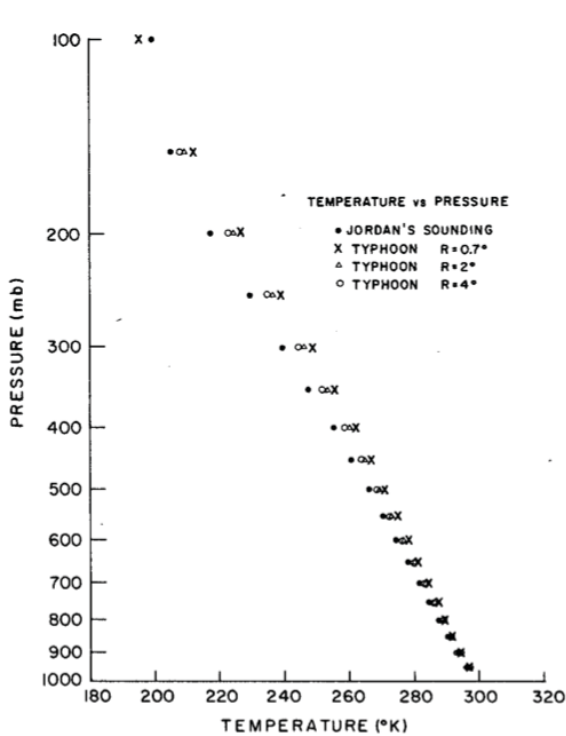


FIG. 6. Temperature (K) versus height (mb) for Jordan's (1958) mean West Indies sounding and the composited typhoon data.

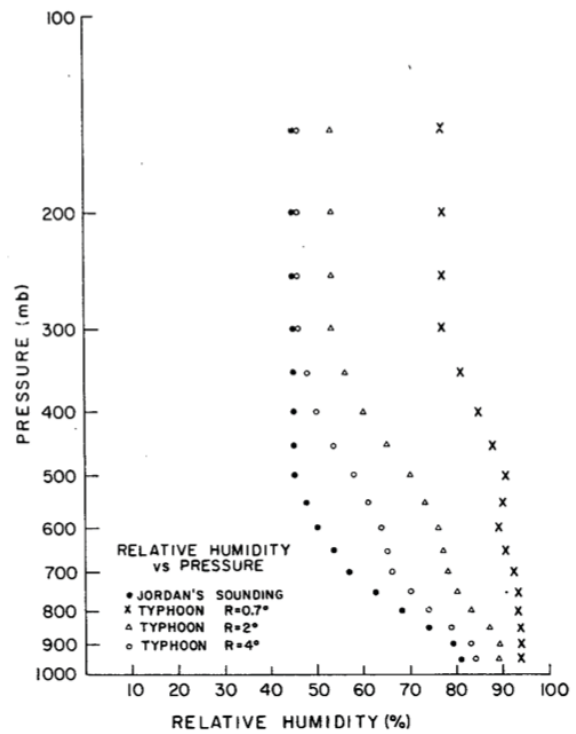


FIG. 7. Relative humidity (%) versus height (mb) for Jordan's (1958) mean West Indies sounding and the composited typhoon data.

Figure 2.1. Vertical profiles of temperature and relative humidity for various typhoon observations from Lord and Arakawa (1980) pointing out that when cumulus convection exists, a relatively dry atmosphere has a larger lapse rate than a more moist atmosphere.

of Lord and Arakawa (1980) lends support to the utility of the AS74 cumulus parameterization.

2.2 Qualitative and quantitative characteristics of QE fluctuations

More than a decade after the Lord and Arakawa study, the AS74 parameterization was evaluated further by performing semiprognostic tests against data from a two-dimensional cumulus ensemble model (CEM), and the results pointed out some limitations of the scheme (Xu and Arakawa 1992). Xu and Arakawa (1992) note that the AS74

parameterization is both deterministic and diagnostic, introducing no prognostic equations for the cumulus clouds themselves, and therefore, the parameterized cumulus clouds have no history of their own. Clearly, this is to be expected for the case of statistical equilibrium with large-scale processes without any free fluctuations, but nondeterministic and nondiagnostic effects are likely to be more important in the presence of mesoscale organization. To assess the significance of these effects the semiprognostic test or single-time step prediction of cumulus activity was implemented to simulate the effect of mesoscale developmental organization. The tests were performed for a sinusoidal large-scale forcing with a period of 27 hours, and validation data was created from multiple realizations of the repeating periodic forcing from the CEM averaged with respect to the phase of the large-scale forcing and in space (to represent a large grid cell).

While it was found that the AS74 parameterization is essentially valid and cumulus activity is rather strongly modulated by the large-scale processes, the AS74 parameterization failed to capture some of the nonmodulated, high-frequency fluctuations and the systematic phase delays in modulation that occur in the presence of wind shear that typically leads to more organized convection. It was additionally noted that nondeterministic errors are greater for smaller averaging distances in the CEM, as would be expected, and that there is a remaining deviation from the expected cloud-work function QE found in the “true” CEM data that is more significant for deep and middle clouds than for shallow clouds when mesoscale effects are neglected. Xu and Arakawa (1992) conclude that errors due to the nondiagnostic aspect of AS74 are more significant for coarse-resolution models that do not resolve mesoscale features. This means that the physical memory (lagged response) effect of the mesoscale is unlikely to be present in GCMs that

assume QE. Further, errors due to the nondeterministic aspect of AS74 increase with finer resolution. An additional test in which convective downdrafts were added to the semiprognostic version of AS74 also improved the results.

In further analysis involving the two-dimensional CEM of Xu and Arakawa (1992), X92 attempted to determine the extent to which cumulus convection can be parameterized deterministically and diagnostically and whether the imposed separation of scales that is required by AS74 and other convective parameterizations is significantly affected by mesoscale cloud organization, thereby limiting the parameterizability of cumulus clouds. Using the CEM with 2-km horizontal grid spacing over a 512-km domain, simulations with a periodic time-varying large-scale forcing were run to examine the systematic and nonsystematic fluctuations of cumulus activity for various cases of mesoscale organization (shear) and surface types. It was shown that the magnitude of the fluctuations seems to depend on the magnitude of the large-scale forcing and the basic wind shear, as well as the domain size. Most importantly, as shown in their Figures 3 & 4 (Figure 2.2) the response to the cyclic forcing is not identical at a given phase of the large-scale forcing, indicating that the modulation is not completely deterministic.

They also find that the modulation exhibits some phase delays when the basic wind shear is strong as a consequence of mesoscale organization and that the modulation of the mesoscale processes by the large-scale forcings is weaker than that of the convective-scale processes, pointing to a need for a nondiagnostic parameterization (Figure 2.3, their Figure 9). The same figures also show variability in the response as proportional in magnitude to the mean response, and that such scatter in fields representative of convection, such as vertical motion or surface precipitation, can have a standard deviation on the

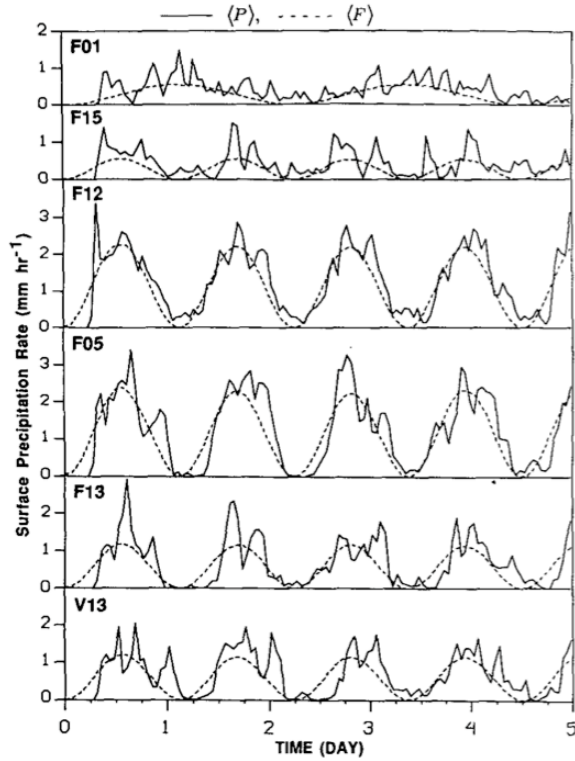


FIG. 3. Time sequences of the hourly rate of entire domain-averaged surface precipitation rates (solid) for F01, F15, F12, F05, F13, and V13. As a reference, time sequence of the imposed large-scale advective effect is shown with an arbitrarily chosen amplitude by the dashed line.

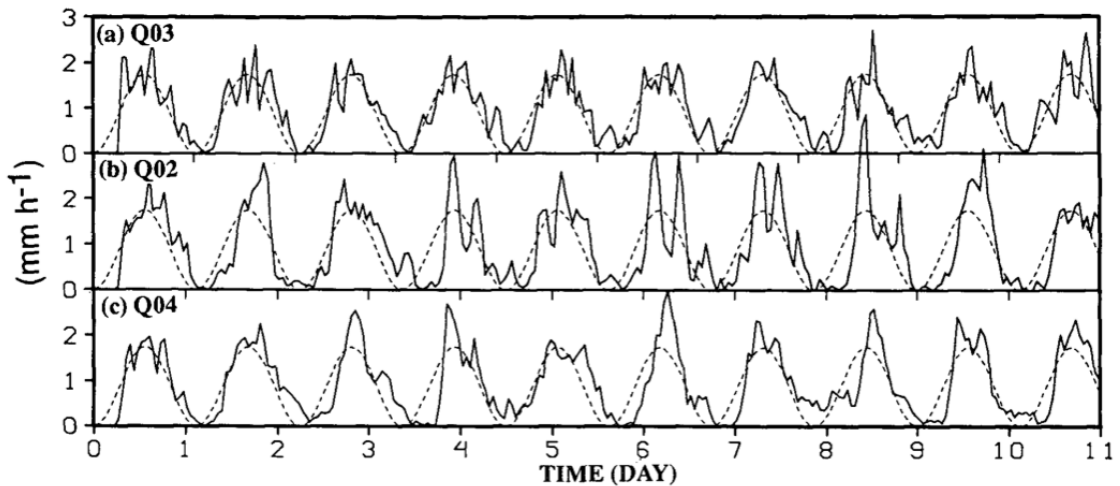


FIG. 4. Same as Fig. 3 except for Q02, Q03, and Q04.

Figure 2.2. Time series of hourly surface precipitation for weak shear (F01, F15), strong shear (F12, F05), moderate shear (F13, V13), no shear (Q03), and a shear case for a 512-km and 1024-km domains from X92.

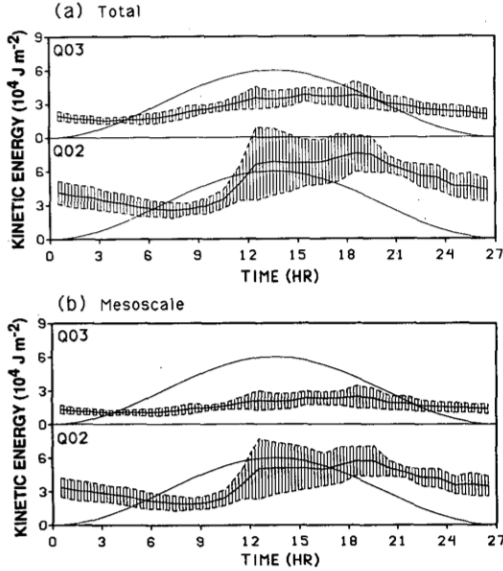


FIG. 9. Same as Fig. 5 except for (a) the total and (b) mesoscale eddy horizontal kinetic energies of Q03 and Q02.

Figure 2.3. The ensemble mean and standard deviation of (a) the total and (b) the mesoscale horizontal kinetic energies from X92 demonstrating the phase delay in response to large-scale forcing that is due to mesoscale organization.

order of the mean values, a finding that was also discovered by Katzfey and Ryan (2000). As will be discussed later, I have obtained very similar results, with some slight differences from a three-dimensional CRM study, and these results will be discussed in Section 5.

Xu (1994) notes that to ensure that a closure assumption is quasi-universally valid, it should be sensitive neither to convective cloud regimes nor to the horizontal resolution of the large-scale models. However, two-dimensional CEM analysis testing various supplementary closure constraints in modified versions of AS74 found weak to moderate dependencies on horizontal resolution. In particular, constraints placed directly on the intensity of a cumulus ensemble, such as a coupling of vertical cloud mass flux and large-scale vertical mass flux, were found to vary in strength with varying averaging distances.

Again using the two-dimensional CEM, Xu and Randall (1998) determined the length of the adjustment timescale that is associated with the aforementioned phase delays due to mesoscale convection under different large-scale advective processes. They found that the lag ranged from 1-5 hours in various simulations without dependence on large-scale advective forcing. This time has been interpreted as the adjustment timescale from “disequilibrium” to QE states in the presence of large-scale forcing. While there was no large-scale forcing dependence, the adjustment timescale decreased with decreasing averaging distances, suggesting that the cloud-work function-based QE becomes more accurate as horizontal averaging distance decreases. At least, this would be true for small averaging distances in which the mean vertical velocity was large. However, small lags for smaller subdomain sizes may also be related to the fact that large-scale and convective scale processes become less separable for smaller subdomains. They also determined that the largest source of deviation from QE (toward instability) is the accumulation of generalized CAPE (GCAPE) due to the imposition of large-scale advective cooling rather than from large-scale advective moistening of the boundary layer.

Today there are questions of the continued feasibility of the AS74 approach as the trend is toward the use of grids with finer and finer resolution. One of the basic assumptions of AS74 was that the parameterization focused on the consideration of a large horizontal area that could contain large numbers of cumulus clouds, while at the same time was small enough to represent a fraction of the conditions that constitute the large scale. With the move toward smaller grid columns, the ability to generate sound statistics describing the field for a given situation will decline, though the ability to resolve whatever is defined as large-scale (synoptic features in the case of grid spacings on the order of

those in typical GCMs, mesoscale features in the case of grid spacings on the order of tens of kilometers) will be retained or even enhanced without regard to whether they are correct.

A further major assumption of AS74 is that the time scale for changes of the large-scale forcing is much longer than the time that it takes for the convection to adjust to the forcing (convective adjustment time); this is the assumption that leads to the idea of cloud/large-scale balance in QE. The typical adjustment time for deep cumulus clouds is on the order of a few hours, and that for smaller clouds is somewhat less. It can be argued that the diurnal cycle does not qualify for the required separation of time scales, and even the applicability to synoptic weather events can be questioned. To make matters worse, as resolution continues to increase, the time scales associated with changes in grid-averaged weather can become relatively short. This is true for mesoscale features, such as a squall line that can occupy the bulk of a grid cell and pass through it very quickly.

The effect of less reliable statistics, brought on by the small sample sizes inherent to fine resolution, is the appearance of non-deterministic or stochastic fluctuations in the convection that are only partially predictable. Such stochastic convection will later lead to uncertainty in the larger scales. Further, finite convective adjustment time scales can cause the convective response to a forcing to significantly lag changes in the forcing if the forcing is changing rapidly enough. This was shown in the case of X92's 27-hour (nearly diurnal) forcing period, and here it is shown to become a more severe problem with decreasing grid spacing. Despite these known issues of inadequate sample size and separation of time scales that clearly show how QE-derived cumulus convection will not

be able to produce the detailed interactions between large-scale atmospheric motions and convection, equilibrium thinking has pervaded the development of cumulus parameterizations for over four decades. The meteorological community, with hopes of creating innovative models with grid spacings in the mesoscale range, is now realizing that these issues can no longer be ignored.

2.3 Stochastic parameterizations

The realization that QE-based convective parameterizations fail to reproduce the full spectrum of convective variability found in CRM ensembles and observations has prompted the development of new approaches to cumulus parameterization. Further, the lack of high-frequency, small-scale variability in the GCM-generated precipitation fields and convective heating rates may be damaging to the ability of GCMs to simulate the large-scale, low-frequency aspects of climate variability (Ricciardulli and Garcia 2000; Horinouchi *et al.* 2003). In a review article on the convective parameterization problem, Arakawa (2004) discusses the more recent trend away from deterministic and diagnostic closures and even ensemble averaging methods toward prognostic and nondeterministic closures of varying types, including stochastic parameterizations, relaxation methods, triggered adjustments to equilibrium, and the more advanced superparameterization (SP), which seems particularly promising.² While the paper nobly stresses the need for the very interesting “unified cloud parameterization,” that is, one which encompasses both

² Interestingly, the effect of superparameterization is similar, from the perspective of stochastic input into a large-scale model. The embedded CRM provides the effect of the small-scale variability. The equivalency of the two methods is unclear, but if the effect is comparable, the less computationally costly method is likely to be preferred.

cumuliform and stratiform clouds, it is, like superparameterization, well beyond the scope of this thesis. This thesis will instead devote a portion of space to the discussion of the development of stochastic parameterizations as a preferred method to ameliorate convective variability issues in GCMs. Stochastic parameterizations attempt to supply a simulation with the temporal convective variability that would otherwise be lost due to assumptions, such as scale separation, which are not justified and issues, such as sampling error, which can lead to inappropriate representations of variability.

To frame the problem in a different way, we can examine the issue of non-predicted variability in terms of many of the other issues that cause discrepancies between the modeled atmosphere and the real atmosphere, rather than focusing directly on deviations from QE. Formally, the thermodynamic and dynamic equations for weather and climate are written as deterministic equations, which upon inspection appear to imply that weather forecasts can be determined for any future date based solely on a set of initial conditions. Of course, the discovery of the chaotic nature of weather (Lorenz 1963) put to rest any such notions. Fortunately, as Palmer and Williams (2008) observe, some initial flow states (*e.g.* those that appear smooth or stable) do allow for useful degrees of predictability, even if the system is chaotic by nature. The degree to which a forecast has uncertainty, then, can be determined by methods, such as ensemble forecasting, which essentially look at the spread among forecast variables (larger meaning a less predictable state) from multiple realizations of a model run, each with slightly differing values in the initial conditions of the flow field.

The world might be a happier place if this sensitive dependence on initial conditions was the only source of forecast uncertainty; by gauging the uncertainty in measure-

ments that initialize the model, we could have a good feeling for the amount of uncertainty in the subsequent forecasts. It might be even happier if the impact of the unresolved scales could be made arbitrarily small by simply increasing the resolution, which Lorenz (1963) shows cannot be done.³ Other sources of uncertainty arise from the numerical models themselves, as the deterministic equations of motion are discretized in some way, such as onto a gridded, spectral, or other representation. Information on motions below the grid scale is lost, adding to uncertainty.⁴ The effect of those motions is replaced by parameterizations that take the place of directly calculating the effects of clouds, gravity waves, flow over topography, turbulence, microphysics, or radiation, which add further degrees of uncertainty because they rely on bulk methods, which, like AS74, tend to break down as grid spacing decreases due to poor statistical sampling. Williams (2005) notes, “Despite the unquestioned partial success of this technique [parameterizing], it cannot be rigorously justified or derived from first principles.” Sardeshmukh *et al.* (2001) further show that conventional parameterizations lead to systematic drift of climate models compared to reality, a problem that is endemic in climate modeling and shows itself, for example, in the inability of some models to reproduce anticyclonic blocking patterns (Palmer and Williams 2008).

One approach to account for the uncertainty and variability found in CRMs and observations is to use stochastic (random, nondeterministic) parameterizations. The aim of a stochastic scheme is to introduce variability in time into the numerical representation

³ In fact, it has been shown by Nicolis (2004) that the mean square error derived from the neglect of the SGS features grows initially at the same rate independent of the model resolution.

⁴ As a side note, the same ideas can be applied to the modeling of the oceans, where the most important SGS features are eddies on the order of 1-100 km.

of the system (Ball and Plant 2008), and the idea was suggested over four decades ago as adding random noise to climate models in an attempt to mimic the properties and impacts of the processes occurring on the SGS (Hasselmann 1976). Often, the application of a stochastic parameterization is described in terms of a double potential well (Williams 2005, Palmer and Williams 2008, Wilks 2008). Figure 2.4 shows a depiction of such a possible potential well as used in Williams (2005). In this case, for a system at equilibrium with wavenumber 2 with the absence of noise or with very low amplitude noise, it would be very unlikely for the system to ever shift into the wavenumber 1 equilibrium. By extension, the addition of random perturbations of significant magnitude will increase the likelihood that the system will shift into a new regime, thereby extending the whole range of variability of the system. This is known as a noise-induced transition, a concept that has been applied to the explanation of transitions between glacials and interglacials, El Niño and La Niña states, different El Niño regimes, and multiple oceanic thermohaline circulation regimes.

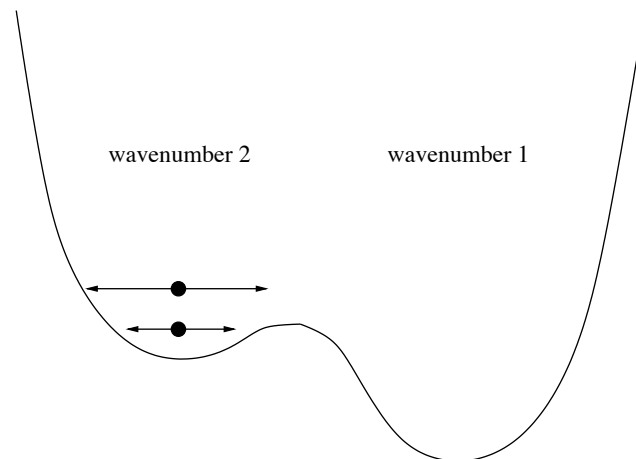


Figure 2.4. Particle moving in a bi-modal potential well with two stable equilibria, corresponding to baroclinic waves of wavenumbers 1 and 2 (Williams 2005).

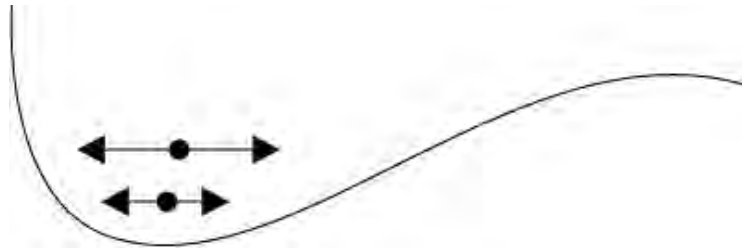


Figure 2.5. Particle moving in a potential well with a single mode shown with two perturbation amplitudes and differing locations of equilibrium.

Similarly, a shift in equilibrium can be caused by changing the amplitude of random perturbations in a system described by a single potential well. If the characteristics of the well are not symmetric (*e.g.* Figure 2.5), greater perturbations will change the average location of the equilibrium toward the side of the well that has the less steep slope. When perturbations are increased for physical processes that can be described by the depicted shape, biases become more clearly visible. This relationship may allow for tuning of well-described biases. In this situation, the “transition” is not likely to be as abrupt and dramatic as the case for the bi-modal well; rather the transition, or shift, will be more gradual and proportional to the amplitude of the perturbations (Palmer *et al* 2005). Pamer *et al.* (2005) note:

“This picture already has relevance to the real atmosphere. As shown, for example, in Corti *et al.* (1999), atmospheric low-frequency variability of the northern winter flow appears to have clear (non-Gaussian) regime behavior, and in recent decades, the dominant regime corresponds to anomalously westerly flow across midlatitudes. By contrast, blocking-type flow patterns correspond to subdominant regimes. As discussed by Molteni & Tibaldi (1990), models with insufficient transient activity would tend to overpopulate the dominant regimes and underpopulate the secondary regimes. In a recent study Jung (2005) sug-

gests that this picture describes the systematic error of the most recent versions of the ECMWF model.”

The process of implementation can be as simple as introducing a random multiplier to variables in a given parameterization to increase overall ensemble spread and improve probabilistic precipitation forecasts as was done in one of the earliest attempts by Buizza *et al.* (1999). The Buizza scheme has led to considerable improvement in weather forecasts. Similarly, one could implement a parameterization as described by Wilks (2008) as

$$\frac{dX}{dt} = R(X) + U(X), \quad (2.5)$$

where R represents the resolved processes, and U represents the unresolved processes. In a conventional deterministic parameterization, U is determined as a mean response to some forcing, and equation (2.5) contains no randomness. Hasselmann (1976), for reasons discussed in Wilks (2008), determined that the effects of the unresolved scales on the resolved scales could be represented by Gaussian white noise, such that (2.5) could be modified as

$$\frac{dX}{dt} = R(X) + U(X) + \sigma z(t). \quad (2.6)$$

Here, σ is the square root of the Gaussian variance characterizing the uncertainty of the parameterized effects, and $z(t)$ is Gaussian white noise of unit variance. When a parameterization of this form is integrated numerically, the effect is that random noise centered on $U(X)$ is added to the system. This type of parameterization, predictably, allows for the exhibition of more variability than its deterministic counterpart. However, such an approach is not a true physical parameterization, directly linked to a physical resolved proc-

ess.

Subsequently, Lin and Neelin (2002) have proposed that knowledge of the statistical distribution of variability demonstrated in CRMs and observations can be used to relate the distribution of parameterization constraints to subgrid variability. They presented two approaches; in one, stochastic processes are introduced to the convective parameterization itself with included physical considerations but without prior knowledge of the distribution of convective properties, and in another, the statistics of the convective properties are estimated empirically and used to directly control high order moments of the convective heating statistics. Both approaches are applied to a GCM in Lin and Neelin (2002). In the end, it is determined that stochastically parameterizing the unresolved physics (approach 1) has merit in light of modifications to intraseasonal variability, as opposed to the climatology, and that parameterizing the statistics of convective heating (approach 2) is not as fruitful. The heating strongly interacts with the large-scale in unexpected ways in approach 2, such that the resulting output is fundamentally different from the input statistics.

Song *et al.* (2007) and Bright and Mullen (2002) have applied approach 1 from Lin and Neelin (2002) to mesoscale models, as well, introducing stochastic variability through a convective trigger function, a method in which the convective parameterization is enacted only conditionally. The approach used by Song *et al.* (2007) was to give the trigger function in the Kain-Fritsch convective parameterization scheme (Kain and Fritsch 1993) within the Penn State-NCAR Mesoscale Model (MM5) stochastic ability by allowing random selection of parameters from a range of values determined by a training set of diverse observed radar reflectivities using a Bayesian learning technique. The

approach, as applied to cases from the International H₂O Project (IHOP), showed a strong potential to improve forecasts of convective precipitation in mesoscale models. They noted that the randomness tended to break the spatial and temporal continuity (related to a vertical velocity conditional trigger) that was inherent in the original formulation of the convective parameterization scheme. While the tests showed promise, successful application to multiple types of convection (*e.g.*, tropical) would be more conclusive. Further, Williams (2005) notes that the use of a trigger function in deterministic convective cloud parameterizations may have the effect of naturally introducing fluctuations about the long-term mean. However, they are unlikely to reproduce probability distributions like those calculated by Shutts and Palmer (2004) who used an ‘ultra-high-resolution’ CRM (1 km by 40 km) to obtain statistics on fields such as the temperature tendency.

A number of other studies have also reported the successful addition of statistical spread to large-scale numerical models following implementation of stochastic processes. Teixeira and Reynolds (2008) devised a modification to the Navy Operational Global Atmospheric Prediction System (NOGAPS), an ensemble prediction system, in which parameterizations are used in a stochastic manner based on probability distribution functions (PDFs) obtained from the parameterizations of an ensemble of models with varying initial conditions. Instead of viewing a parameterization as a deterministic indicator of a mean value, they consider parameterization results as a *probable* value of some variable. PDFs of these values are then used to constrain random determination of the future states of a variable. Results of this method showed an increase in ensemble spread in multiple variables.

In an attempt to determine the extent to which deterministic convective param-

eterizations fail to capture statistical fluctuations in deep-convective forcing and to provide PDFs that may be used in stochastic parameterization schemes, Shutts and Palmer (2007) used a coarse-graining technique on CRM fields and found much broader PDFs at the cloud-scale, as one would expect. They also found that standard deviations of temperature tendency fluctuations were linearly dependent on the mean temperature tendency, which lends support to the stochastic methods of Buizza *et al.* (1999), mentioned above, that is used operationally at the European Centre for Medium-Range Weather Forecasts (ECMWF). This lies in contrast to the square-root dependency determined by Craig and Cohen (2006). On a related note, further studies by Cohen and Craig (2006) found that the distribution of mass flux of individual clouds is exponential for various imposed radiative cooling rates and vertical wind shear profiles and that larger CRM domains have mass flux statistics nearer theoretical predictions, indicating that the mass flux variance is affected by the size of the domain.

Plant and Craig (2008) have developed a stochastic parameterization scheme based on a modification of the Kain-Fritsch parameterization scheme mentioned above. The parameterization involves convective plumes being drawn at random from a PDF that defines the chance of finding a plume of a certain cloud-base mass flux that is determined by a CAPE closure method. In this study, it is found that the new scheme produces the desired distributions of convective variability without altering the mean state. They point out that one might hope to find relatively little variability in the convective response after averaging over CRM areas on the order of numerical weather prediction (NWP) or climate models, however their results show considerable spread for an area of $(16 \text{ km})^2$. This raises concerns for the continued use of QE convective parameterizations

at ever-finer horizontal grid resolutions, such as those on the order of 20-50 km that have already used in some global weather prediction models (Arribas 2004; Bechtold *et al.* 2008).

Recently, Shutts *et al.* (2008) have introduced an interesting new approach to the field of stochastic parameterizations. The idea, which is reminiscent of superparameterization or multi-scale modeling, is a dual-grid approach that has its basis in techniques adopted from the field of computer graphics and flow visualization. Any atmospheric scientist who has ever played with a high-quality video game or flight simulator might be impressed at how well represented clouds appear on the screen. How are they able to simulate cloud motions and interactions with cloud motions in real time (~40 frames per second) and have it look so realistic? The basis of the models used in games is the same as ours, that being the same thermodynamic and dynamic equations, however their goal is simply the visual representation of the cloud and algorithmic stability rather than accurate representation of their microphysics. This allows game developers to make drastic simplifications to their models and makes the simulation computationally cheap.

In their tests, both a fine and a coarse grid are used. The fine grid is used to do a computationally cheap simulation of SGS processes, and then the results are coarse-grained and applied to the coarse grid. Conversely, the effects of the processes that are represented on the coarse grid also have the ability to influence the fine grid. The cheap computation done on the fine grid in this case is a two-dimensional cellular automaton (CA) (this is referred to as an emulator), though in theory, it could be just as complicated as an embedded CRM. The use of CAs, which have no basis in physics, to add variability to a system was originally suggested by Palmer (1997). To be put into use in the con-

text of ensemble prediction, each forecast member would see a different evolving pattern of stochastic forcing from the underlying CA. Results of their testing showed the use of CA in a dual grid to be quite feasible for operational use. The authors believe that it would produce improvements in operational models as has been the case for the majority of stochastic methods, especially those that rely upon CA to provide stochastic kinetic energy backscatter. This refers to the idea that kinetic energy moving upscale from the unresolved flow is available to the resolved flow as a kinetic energy source. The introduction of kinetic energy backscatter gives models the ability to reduce large-scale systematic error (e.g., Berner *et al.* 2008).

A number of others have also seen success in stochastic modeling, such as in modeling ENSO events (Zavala-Garay *et al.* 2003), in the study of the atmospheric quasi-biennial oscillation (Piani *et al.* 2004), in enhancing ocean sea-surface temperature predictability (Scott 2003), and in modeling the impacts of ocean eddies (Berloff 2005). There is also a wide variety (as reported by Ball and Plant 2008) of plausible stochastic methods that have been proposed and that are being actively investigated. Those mentioned include perturbing the inputs to a parameterization (e.g. Tompkins & Berner 2008), perturbing the parameters used within it (e.g. Byun & Hong 2007), perturbing its outputs (e.g. Teixeira & Reynolds 2008) and even constructing new parameterizations designed explicitly to be stochastic from the outset (e.g. Plant & Craig 2008). The growing acceptance that the use of stochastic elements in GCMs may be desirable for both theoretical and practical reasons led Ball and Plant (2008) to assert that the question may soon change from “*why a stochastic method to which stochastic method.*” [Emphasis in original.] Their paper goes on to note that there are many unknowns yet to be worked

through, such as what might happen if two different stochastic parameterizations are used simultaneously in different parts of a model. They cite the dangers of double counting the variability, but one also may worry about the simple hazards of appending additional, possibly unphysical, features capable of error-increasing multiplicative noise.

The aim of the Ball and Plant (2008) study is to test five stochastic parameterizations, including that developed by Plant and Craig (2008) as discussed above, within a single column model (SCM). The test seems to limit the applicability of their results to any operational use of the schemes because inherent deterministic parameterization errors that affect model dynamics may not be apparent in the SCM, and previous discussion of the use of stochastic parameterizations (*e.g.*, Palmer 2001) has suggested that an ideal stochastic method would be non-local. Additionally, the variability feedback with the large-scale dynamics is likely to be a critical part of the entire concept. Among the interesting results, we find that the spread of the models has a clear dependence on the large-scale forcing, which is a relevant finding for this paper. Additionally, Ball and Plant (2008) show that stochastic physics schemes designed to represent model uncertainty or QE departures can actually change the mean state of the model (like shifting equilibria in the bi-modal potential well as explained previously in discussion of Figure 2.4). Finally, they show that the stochastic scheme that was most promising was a simple scheme in which the parameters of the deterministic parameterization are selected randomly from within a given range of acceptable bounds. Determining correct values for such bounds based on a statistical inquiry into data from CRMs or observations may be critical to the success of stochastic parameterizations, regardless of the particular stochastic scheme employed, and ascertaining what the bounds might be is a key goal of this study.

Chapter 3 - Numerical Simulations

3.1 Introduction

The studies by Plant and Craig (2008) and Cohen and Craig (2006), mentioned above, included the derivation of exponential PDFs of cloud-base mass fluxes from a three-dimensional CRM with 2-km horizontal resolution that was run to statistical equilibrium. Additionally, the previously mentioned studies by X92 used two-dimensional CRM runs with periodic large-scale forcings to quantify the variability of the convection. Motivated by these and other studies, comparison runs have been performed using the three-dimensional anelastic model based on the vorticity equation or vector vorticity model (VVM, a.k.a CSUVVM) developed by Jung and Arakawa (2008). This study constitutes one of only a handful of experiments so far performed with this model. Its first evaluation as part of a CRM intercomparison study is currently underway. A description of the model and the numerical simulations performed follows.

3.2 Model

While most three-dimensional cloud models base the formulation of convective dynamics on the momentum equations, the model employed in this study bases convective dynamics on the vorticity equation. Thus, the prognostic variables of the model dynamics include the horizontal components of vorticity at all heights and the vertical component of vorticity and the horizontally uniform part of the horizontal velocity at one selected height. The motivation for the use of the vorticity core has its roots in physical

atmospheric processes, including strongly rotational quasi-geostrophic motion, which dominate flow at the large scales, and induction of convection by way of the generation of horizontal vorticity by buoyancy, which is ubiquitous at the small scales (Randall and Konor 2008). By basing the model on three-dimensional vorticity, meteorologically important processes can be represented much more directly and explicitly. That is, there is a guarantee of the conservation of potential vorticity, which is not ensured in conventional models. Further, the solution for the pressure perturbation in an anelastic model based on the momentum equations, which is calculated using a diagnostic elliptic equation that is often complicated to solve, has been replaced with the solution for vertical velocity, given the predicted horizontal components of vorticity using an elliptic equation (Jung and Arakawa, 2008).

The simulations were performed on a doubly periodic grid of $(256 \text{ km})^2$ with 2-km horizontal grid spacing. In the vertical, a stretched grid (Krueger 1988) is employed to enhance vertical resolution near the surface. The depth of the domain is approximately 19 km with 35 layers having a grid interval of approximately 100 m near the surface stretching to 1 km near the top of the model. This grid set-up is nearly identical to that used by X92 whose two-dimensional model spanned 512 km and used two fewer vertical layers. The model is stepped forward in 10-second intervals, and time differencing is second-order Adams-Bashforth except, of course, for the first time step where the first-order backward scheme is used for buoyancy and turbulence variables and the first-order forward scheme is used for the physics variables.

Similarly to the model used by Xu *et al.*, (1992), the VVM includes three-phase microphysics (Krueger *et al.* 1995; Lin *et al.* 1983; Lord *et al.* 1984), a surface flux pa-

parameterization using the flux-profile relationships given by Deardorff (1972), a first order turbulence closure (Shutts and Gray 1994), and a radiative transfer parameterization (Fu *et al.* 1995) option that has not been used due to its computational expense. In its place is the model's default Newtonian cooling operating at full strength with a relaxation timescale of one day above 15 km, linearly decreasing to zero at and below 10 km elevation. The VVM also includes a Rayleigh-type friction in the top five layers to absorb upward-propagating gravity waves.

In all simulations, the surface is ocean with a prescribed sea surface temperature of 299.88 K and surface roughness of 0.2 mm. The Coriolis parameter for 15°N is used

Table 3.1. List of all saved model variables for each model run. The time length of the various model runs ranges from 1.25 to 75 simulated days. All instantaneous variables are 3D, while the time-averaged variables are 2D.

<i>INSTANTANEOUS</i>	<i>MODEL DATA</i>	<i>POST-PROCESSED DATA</i>
<i>10 min</i>	<i>Potential Temperature</i>	<i>Temperature</i>
	<i>z-Vorticity</i>	<i>Relative Humidity</i>
	<i>x-Vorticity</i>	<i>Cloud Field</i>
	<i>y-Vorticity</i>	<i>Dry Static Energy</i>
	<i>z-Wind Velocity</i>	<i>Moist Static Energy</i>
	<i>x-Wind Velocity</i>	<i>Saturated Moist Static Energy</i>
	<i>y-Wind Velocity</i>	<i>Buoyancy</i>
	<i>Water Vapor Mixing Ratio</i>	
	<i>Cloud Water Mixing Ratio</i>	
	<i>Rain Water Mixing Ratio</i>	
	<i>Cloud Ice Mixing Ratio</i>	
	<i>Snow Mixing Ratio</i>	
	<i>Graupel Mixing Ratio</i>	
	<i>TIME-AVERAGED</i>	<i>MODEL DATA</i>
<i>10 min avg</i>	$u'w'_{sfc}$	
	$v'w'_{sfc}$	
	$\theta'w'_{sfc}$	
	$q_v'w'_{sfc}$	
	<i>Surface Precipitation Rate</i>	

in all simulations. The x-component of the geostrophic wind is held constant at its original profile throughout each simulation, while the y-component is initially zero and free to vary. Each simulation is initialized with thermodynamic conditions that are horizontally uniform, and then clouds are initiated by the introduction of small (± 0.25 K), random perturbations to the potential temperature in the lowest 100 m of the model for 30 minutes of integration time. This portion of the simulation was not included in any of the analyses; in all cases, only times after the first 300 hours of integration were considered. A list of model output saved for future use is given in Table 3.1.

3.3 Experimental Design

One of the main goals of the study is to determine the effect on the convective response due to forcings on varying time scales. Therefore, the first step was to select the time scales upon which the large-scale forcings would vary. It was also a requirement to structure the experiment following X92. The model is designed to simulate a field of cumulus clouds under a given set large-scale conditions as if the domain represents a single column of a GCM. As such, information about the large-scale rates of destabilization and moistening are imposed on the model domain in a horizontally uniform manner. In this case, large-scale advective cooling and moistening rates, $-Q_1$ and $-Q_2$ as defined by Yanai *et al.* (1972), are prescribed in this way.

In order to vary the forcing in time, we again followed the methods of X92 and applied a periodic scaling factor to the forcing which took the form,

$$f(t) = \frac{1 - \cos\left(\frac{2\pi t}{T}\right)}{2}, \quad (3.1)$$

where T is the period of the time variation and t is the current time. The intent was to view the effects from time-varying forcings that had periods that were both significantly less than and greater than the length of a day, although simulations with periodic forcings on the order of a day were also conducted to obtain the full spectrum of effects. 13 periodic forcing simulations were run to a length of 15 cycles, beyond the initial 300 hours of simulation that were needed to bring the model system into QE, with periods ranging from 2-120 hours. Specifically, simulations were run with 2, 4, 6, 8, 10, 12, 14, 16, 20, 24, 30, 60, and 120-hour period forcings. After this point, a simulation will be identified by the length of the period of the forcing preceded by an ‘F.’ For example, the six-hour period run is F06. This will hold true in all subsequent text and figures, except for the case of the 120-hour period simulation for which the text will refer to it as F120, but figures will simply be denoted as ‘120’. Each of the 15 cycles simulated in each run can be viewed as 15 individual realizations of the same event with differing initial conditions. As such, the cycles can be composited to generalize the convective response for each period length.

All of the model runs begin with the same initial conditions, which were created from observational profiles obtained during GATE (Global Atmospheric Research Program’s (GARP) Atlantic Tropical Experiment) Phase-III (Sui and Yanai 1986). These initial conditions included moderate vertical wind shear (Figure 3.1a) and a modified (greatly increased in magnitude) profile of the GATE-III values for advective cooling and moistening (Figure 3.1b). The vertically integrated magnitudes of these maximum

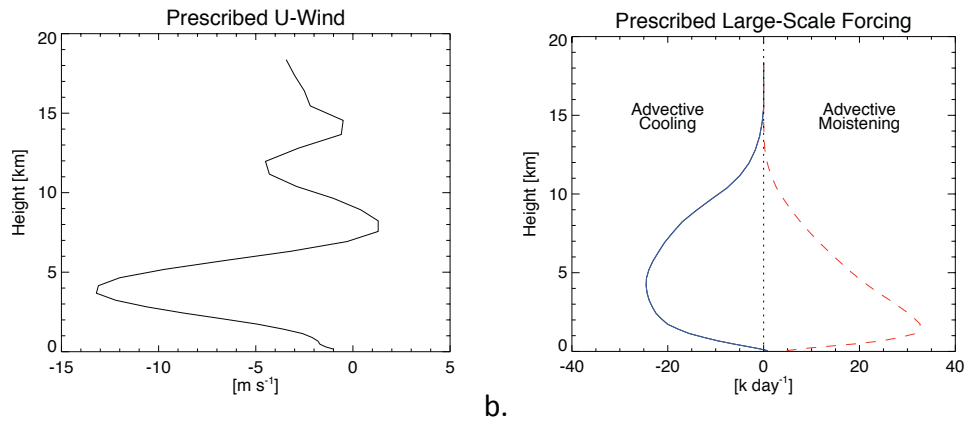


Figure 3.1. The sheared, prescribed u-wind profile with which each simulation is initialized (a) and the maximum value profiles of the prescribed large-scale advective cooling and moistening (b).

forcings are 1668.77 W m^{-2} and 60.8 mm day^{-1} , respectively. These latter two profiles provide the maximum bounds for the time-varying forcings.

Since the effect of the domain size on the convective response is also a major concern of this study, most of the analyses performed on the data have been structured to show this effect. To obtain statistics and other response properties as functions of domain size, the simulation results are subdivided into smaller portions prior to analysis. For example, to look at the effects on a domain one quarter the size of the full domain, the data is grouped into four equally sized squares, the analysis is performed, and then those results are averaged to give the statistics of the convective response on the smaller domain. Subdomains included in this study have the dimensions of (256, 128, 64, 32, and 16 km)². These will be referred to as the whole, quarter, eighth, 16th, 64th, and 256th domains in all text and figures, respectively. Additionally, the full domain is also subdivided in half, with dimensions 256 by 128 km. In this special, non-square-subdomain case, the two halves are grouped in both E-W and N-S orientation separately before the

four distinct halves are then analyzed. This will, unsurprisingly, be referred to as the half domain in all text and figures.

In order to determine how the convective response to a cyclical forcing compares to the convective response to a constant forcing, an additional 10 6.25-day simulations were run with a constant forcing in increments of 10% of the maximum large-scale forcing from the periodic simulations. They are initialized in the same fashion as the variable forcing simulations, including a 300-hour spin-up period. These simulations will be referenced in the text and in figures by ‘CF’ followed by a single digit representing the interval of the maximum forcing. For example, CF8 refers to a constant forcing that is equal to 80% of the maximum large-scale forcing values. The exception to this is the simulation run at 100% of the maximum; it is referred to as CFX, with ‘X’ being the Roman numeral ten for some degree of stylistic consistency. The importance of this subset of simulations is the investigation of the nature of QE departures from a system that should be very close to QE since it is not being forced away from QE in any direct manner. The results from these constantly forced simulations should assist in the validation of assumptions that are currently in place in large-scale numerical models, specifically that variability around the mean convective response scales with the magnitude of the mean convective response.

Chapter 4 – Model Validation

4.1 TWP-ICE CRM Intercomparison Study

4.1.1 *Background*

In order to provide a solid basis for using the VVM, it was decided that the model should undergo some form of formal testing, as prior to this thesis, no such evaluation had been performed. A cursory search for a suitable evaluation mechanism happened upon a well-structured CRM intercomparison. In the most general sense, the ultimate results of an intercomparison provide comparisons of the performance of multiple models against observational data for a given atmospheric situation in order to define model deficiencies and strengths in both a relative and quasi-absolute sense. The intercomparison that was selected is based on the Tropical Warm Pool-International Cloud Experiment (TWP-ICE) that took place near Darwin, Australia from January 20 through February 13, 2006. TWP-ICE was a reasonably detailed observing experiment, which sought to describe the evolution of tropical convection, specifically large-scale heat, moisture, and momentum budgets at 3-hourly time resolution, while making detailed observations of cloud properties and the impact of clouds on the environment at the same time (May *et al.* 2008). In fact, some features of the observations are not explicitly calculated in the VVM model. A much more detailed description of TWP-ICE and the subsequent CRM intercomparison has been documented by Fridlind *et al.* (2010).

Figure 4.1 shows the observational domain and the locations of several observing platforms. The experimental domain was located on a highly-instrumented site operated by the US Department of Energy’s Atmospheric Radiation Measurement (ARM) Program. Additionally, a polarimetric weather radar operated by the Australian Bureau of Meteorology (BOM) was located near the center of the domain, surrounded by a 3-hourly radiosonde sounding array and surface energy budget sites (flux sites in Figure 4.1). Further, TWP-ICE was coordinated with the Aerosol and Chemical Transport in tropical conVEction (ACTIVE) Program, which gathered in situ measurements of environmental aerosol properties (Vaughan *et al.*, 2008). The data that was gathered through both TWP-

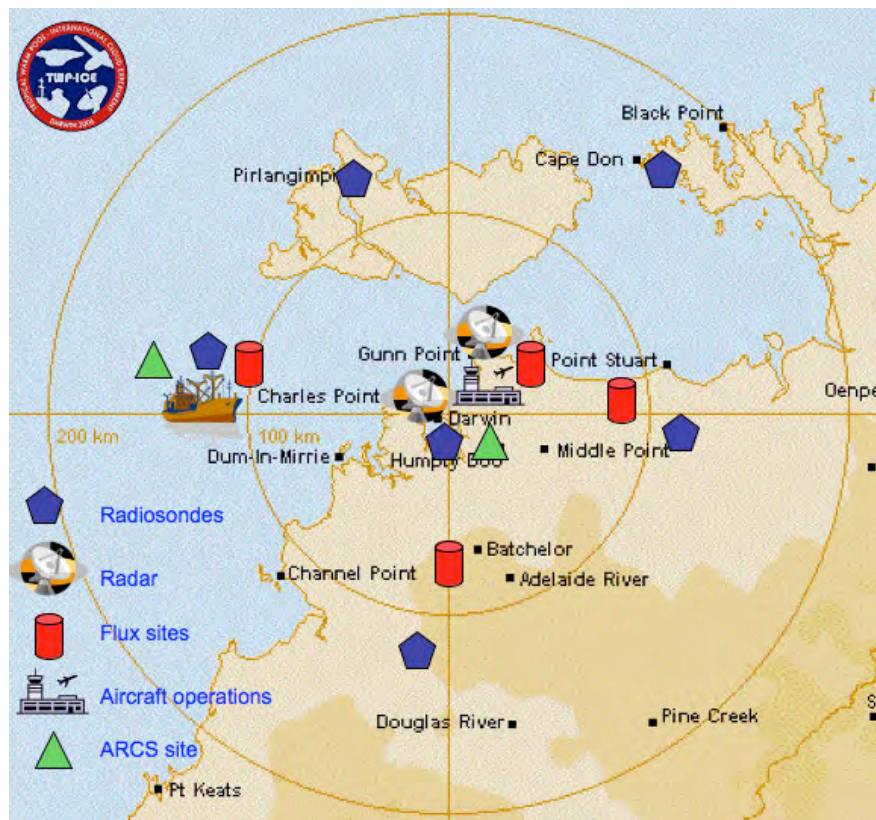


Figure 4.1. The TWP-ICE experimental domain and observing platforms. (Source: <http://acrf-campaign.arm.gov/twpice/>)

ICE and ACTIVE are archived and accessible online; see Fridlind *et al.* (2010) for more information.

One of the main issues that TWP-ICE aimed to address was to provide the observations required to better understand and model tropical convection generally and cirrus outflow in particular in order to further develop GCM climate forecasting skill. Fridlind *et al.* (2010) cite Randall *et al.* (2007), a contribution to the IPCC AR4, as demonstrating the need for improvements in the representation of clouds. An appropriate test bed for the representation of clouds, via testing of parameterizations, is a CRM, because cloud properties vary on short time and space scales. Additionally, the intercomparison shall allow progress toward understanding the influence of tropical deep convection on water vapor concentrations and convective transport through the tropical tropopause through the use of high-resolution cloud modeling.

Prior to the TWP-ICE intercomparison, the GEWEX Cloud Systems Study (GCSS) program has coordinated such CRM studies internationally, often based on major field experiments. Using the path paved by those studies, the specifications for a GCSS CRM intercomparison case study based on the analysis of data gathered during the TWP-ICE and ACTIVE programs has been developed. The CRM intercomparison has been, as the observational experiment was, performed as a joint exercise of the Atmospheric Radiation Measurement (ARM) Cloud Modeling Working Group (CMWG) and the GCSS Precipitating Cloud Systems (PCS) working group, as well as the Stratospheric Processes And their Role in Climate (SPARC) program. While ARM and GCSS have previously coordinated, this has been the first joint ARM/GCSS/SPARC intercomparison.

The TWP-ICE CRM intercomparison has outlined three specific objectives. The first objective is to evaluate model performance and methodology. To accomplish this task, the intercomparison sets out to answer four questions:

- Where do simulations and data disagree most widely?
- Are data sources sufficient to evaluate model performance?
- What additional data gathering efforts should be pursued?
- Is the methodology used sufficient to answer these questions?

It is this set of questions, and particularly the first, that is most relevant to this thesis. It is in this way that we shall determine, to some extent, the validity of the VVM. To answer these questions, greater than 50 observation and modeling datasets from a wide variety of sources representing greater than 20 variables have been collected in preparation for the validation of 8 CRMs from various institutions. Please refer to Fridlind *et al.* (2010) for the specific variables and data sources. The availability of the specified observed variables set guidelines for the required output of the CRMs. Many of the diagnostics were not included in previous studies.

The CRMs included in the TWP-ICE intercomparison are the VVM, operated by myself with the assistance of Thomas Cram and Celal Konor; the Distributed High-Resolution Aerosol-Radiation-Microphysics Application (DHARMA) model, operated by Ann Fridlind and Andrew Ackerman at NASA Goddard Institute for Space Studies (GISS); the two-dimensional version of the semi-Lagrangian Eulerian model (EULAG), operated by Hugh Morrison and Wojtek Grabowski at the National Center for Atmospheric Research (NCAR); the Iowa State University (ISU) two-dimensional Cloud-Resolving Model, operated by Sunwook Park and Xiaoqing Wu at ISU; the non-

hydrostatic mesoscale atmospheric model of the French research community (Més0-NH), operated by Jean-Pierre Chaboreau at the University of Toulouse, France; the Nonhydrostatic Anelastic Model under Segmentally-Constant Approximation (NAM-SCA) operated by Jun-Ichi Yano at the Centre National de Recherches Météorologiques (CNRM) at Météo-France; the System for Atmospheric Modeling (SAM), operated by Jiwen Fan at the Pacific Northwest National Laboratory (PNNL); and the UK Meteorological Office Large Eddy Model (UKMO-LEM), operated by Adrian Hill, Jon Petch, and Paul Field at the UK Meteorological Office.

The second and third objectives of the intercomparison are more technical in nature. The first is to quantify predicted convective transport to and from the tropopause, with particular attention paid to the temporal and spatial characteristics of the vertical mass transport (specifically of water vapor but also with regard to tracers), the role of ice sublimation as a water vapor source, and the role of dehydration as a water vapor sink during overshooting convection. To assist in meeting this objective, four tropospheric tracers are to be tracked, and budget profiles of water vapor and hydrometeors are requested. The final objective is to study the evolution of anvil cirrus clouds through the entirety of their life cycle. There has been a hypothesized influence of tropical anvil cloud cover and precipitation efficiency on the expected response of tropical deep convection to sea surface temperatures that have increased due to greenhouse warming. As such, monsoon events that occurred during the observational period are used as a focus to determine relationships between convective activity and anvil ice water path and precipitation efficiency.

4.1.2 Experiment Design

The time period of focus for the intercomparison is from 0Z on January 18, 2006 through 0Z on February 3, 2006, a total of 16 days. This corresponds to ordinal days 18–34 of 2006. During these 16 days, both active and suppressed monsoon conditions were observed as shown in Figure 4.2. Fridlind *et al.* (2010) describe the time period in the following way:

- active monsoon conditions (19.5–25.5), comprising the first 6 days following a minimal 36 hours for model spin-up
- suppressed monsoon conditions (28–34), comprising the last 6 days of the simulated time period (avoiding the few days following 25 January when large quantities of aging anvil cirrus were advected into the domain from a mesoscale convective system located approximately 24 hours upwind)
- three 24-hour periods bounding the primary build-up and decay of consecutive monsoon events of varying strength (19.5–20.5, 22.125–23.125, and 23.5–24.5), which we refer to hereafter as events A, B, and C
- the 24-hour period of outflow cirrus evolution after event C (24.5–25.5)

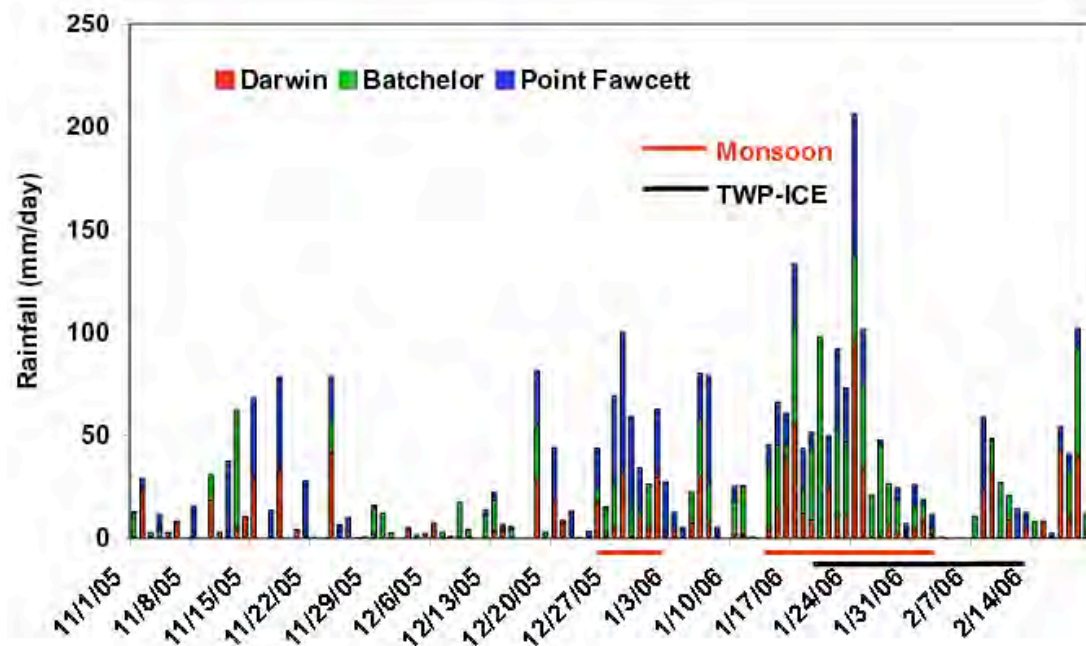


Figure 4.2. Cumulative rainfall at three locations in the Northern Territory during the 2005–2006 monsoon season. Figure courtesy of Lori Chappel, Australian Bureau of Meteorology. (Reproduced from Fridlind *et al.* 2010).

The model framework was specified for the simulations. All models were asked to meet the following guidelines (Fridlind *et al.* 2010):

- model domain footprint representative of the TWP-ICE domain size of approximately 31,000 km² (e.g., about 176 km east-west by 176 km north-south, or a 2-dimensional model domain representing a similar area)
- model domain height of at least 24 km
- fully-periodic horizontal boundary conditions
- uniform initial conditions at 0Z 18 January derived from mean observed profiles
- random initial perturbations of -0.25 to 0.25 K in grid cells located below 500 m
- run time of 16 days, ending at 0Z 3 February
- sea surface temperature fixed at 29°C and interactive surface fluxes
- surface albedo fixed at 0.07 in all shortwave bands
- ozone profile fixed based on sonde and OMI measurements
- interactive diurnal radiation with domain centered on the Darwin ARM site (12.425°S, 130.891°E)
- horizontally uniform nudging of horizontal winds above 500 m to the mean observed profiles with a 2-hour time scale
- application of large-scale forcings derived from observations, adopted at full strength below 15 km, linearly decreasing to zero strength at 16 km
- horizontally uniform nudging of mean water vapor and mean potential temperature to mean observed profiles with a 6-hour time scale, adopted at full strength above 16 km, linearly decreasing to zero strength at 15 km
- sponge layer nudging of horizontal winds and potential temperature toward their horizontal means using a nudging coefficient that increases with a \sin^2 vertical dependence from zero at 20 km to $(100 \text{ s})^{-1}$ at 24 km and above

Additional requirements regarding the consistency of the large-scale forcings

were also specified but will not be reproduced here. The tracers, mentioned previously, were added to the VVM and initialized with a mixing ratio of 1.0 within four source layers (surface boundary layer, 0-250 m; lower troposphere, 2-4 km; mid-troposphere, 4-6 km; and upper troposphere, 14-17 km). They were reset to 1.0 at the end of each time step. The tracers were subjected to advection, mixing, and large-scale vertical motion, and each tracer experienced a uniform decay proportional to the local tracer mixing ratio with a 6-hour e-folding time. Further, the intercomparison set guidelines for various aerosol concentrations to be used in the simulation. However, the VVM is currently unable to handle aerosol information.

Excepting the following items and those specified by the intercomparison, the VVM details for the TWP-ICE simulation were identical to those described in Section 3.2. Most importantly, the large-scale forcing of the model was derived from a 3-hourly dataset in the form of the large-scale vertical motion (applied to condensate and tracers), Q_1 , and Q_2 , which were linearly interpolated in time to be applied at each time step. The time step used was 5 seconds, and the domain was square with horizontal dimensions of 176 km and doubly periodic boundary conditions. The vertical grid was stretched with a top at approximately 25 km. The grid spacing was 1 km. The simulation was run with the GCM version of the rapid radiative transfer model (RRTMG. See <http://rtweb.aer.com/> for more information.) radiation package, implemented once every five minutes of simulated time. Listed in Appendix 1 are the approximately 170 variables that were predicted or diagnosed from the VVM TWP-ICE simulation. Additional variables were requested but were not able to be produced due to model limitations. These included optical thickness measures, hydrometeor diameters, projected areas, and

number concentrations, simulated radar reflectivity, and Doppler velocities.

4.2 Intercomparison Results

As not all of the results from the TWP-ICE CRM intercomparison are currently available, a selection of the results will be shown here. Many of the following figures were created automatically by a program written and operated by Renata McCoy of the Lawrence Livermore National Laboratory.

First, there is the time series of the surface precipitation rate (Figure 4.3), because problems in getting this field correct are likely to be indicative of much larger issues. In this case, the CSUVVM has performed quite well in comparison to both the reference data as well as the other models. That is, it does not greatly deviate from either. There are a couple of notable deviations from the reference data. These are seen in the cases of the EULAG and the NAMSCA models, which appear to overestimate the precipitation, especially near maxima. Additionally, many of the models overestimate the precipitation slightly, but by a factor of two, when the precipitation rate is very small. This positive bias at low precipitation rates has a cumulative effect of an overall positive bias from radar observations. Radar observations for the intercomparison period have a mean of 0.56 mm hr⁻¹. All models have a greater mean. Two of the models, DHARMA and MESONH, achieved almost the exact observed value. The most strongly deviating model was the VVM, with a mean of 0.78 mm hr⁻¹, which is a nearly 40% overestimate. This is approximately solely due to overestimates of precipitation rates during the suppressed monsoon conditions present during the second half of the simulation period.⁵

⁵ The numerical data reported here has been obtained from Fridlind *et al*, (2009).

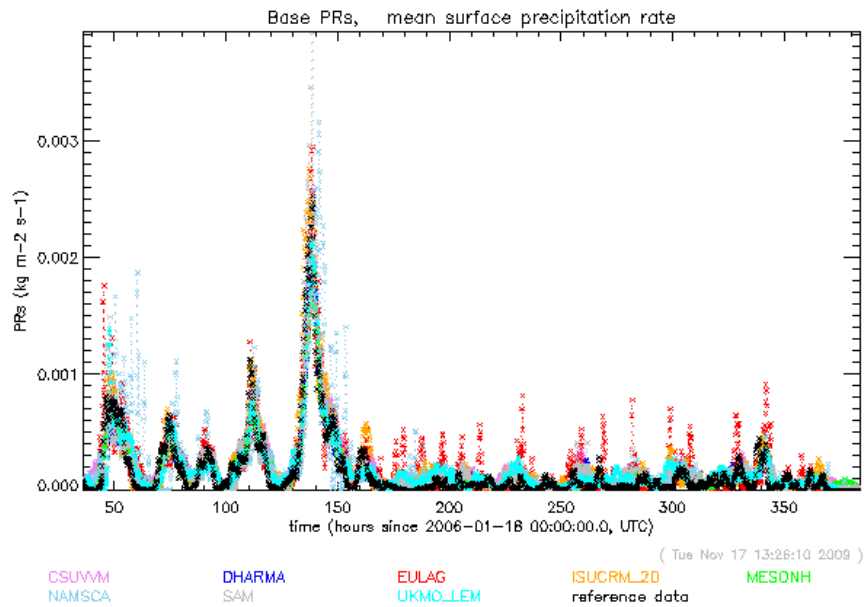


Figure 4.3. Surface precipitation rate for the noted models. The acronyms are described in Section 4.1.1. The reference data is based on radar observations.

Moving up vertically through the data, we can compare domain mean precipitation rates at 2.5 km elevation, as well. This is shown in Figure 4.4. For this variable, fewer models have submitted results. Once again, the CSUVVM has done quite well in identifying the temporal location of precipitation events, though the agreement with the reference data is not as good as in the previous case. While its performance appears to be comparable to the DHARMA model, the CSUVVM really only does a better job of prediction of this variable than the MESONH models. The issue of overestimates for light precipitation events remains, as the simulation period mean for the VVM is nearly double the value derived from radar. The mean for the MESONH is higher still, while the DHARMA and EULAG models simulate the mean precipitation rate at the 2.5-km level with in two hundredths of a millimeter per hour of the observational value. When this variable is resampled at 2.5-km resolution, the deviations grow stronger for each model (not shown).

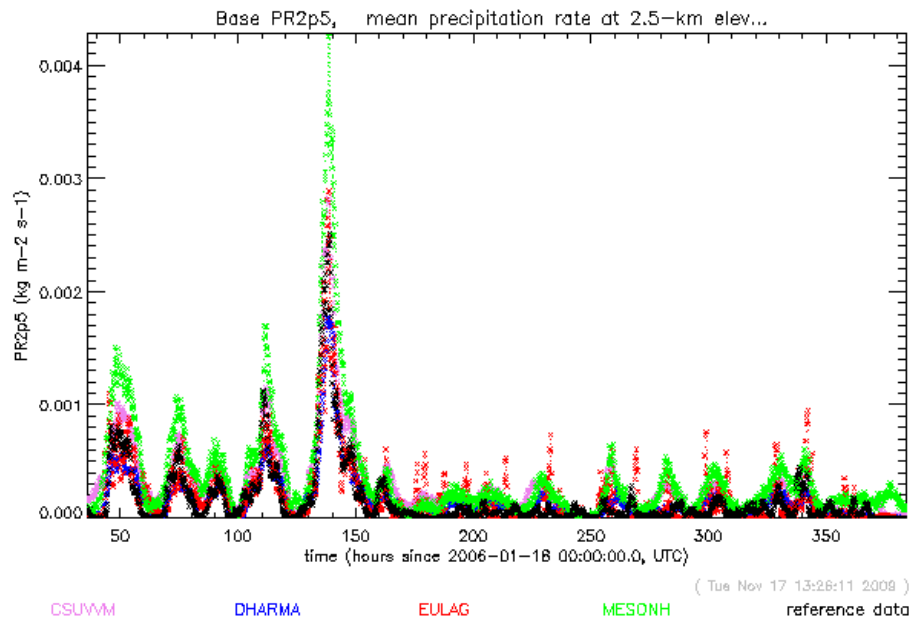


Figure 4.4. As in Figure 4.3, but for the precipitation rate at the 2.5-km level.

Included in the interesting scalar variables are some cloud fields. The first we will look at is the cloud fraction (Figure 4.5). This field is particularly interesting because there is very little agreement between the models. A few of the models, such as SAM and DHARMA show periods where the cloud fraction becomes quite small in comparison to the other models. Such results seem quite realistic when compared to those from the CSUVVM, which stay very near one for the majority of the simulation. The intercomparison definition of a cloud, though, is a total cloud water and ice mixing ratio minimum threshold of 10^{-6} , which is very near most of the maximum values reported in the CSUVVM. Cloud fraction variation can be seen with a slight modification to the threshold. However, there is some cause for concern given that there is variation in each of the other reporting models at the original threshold.

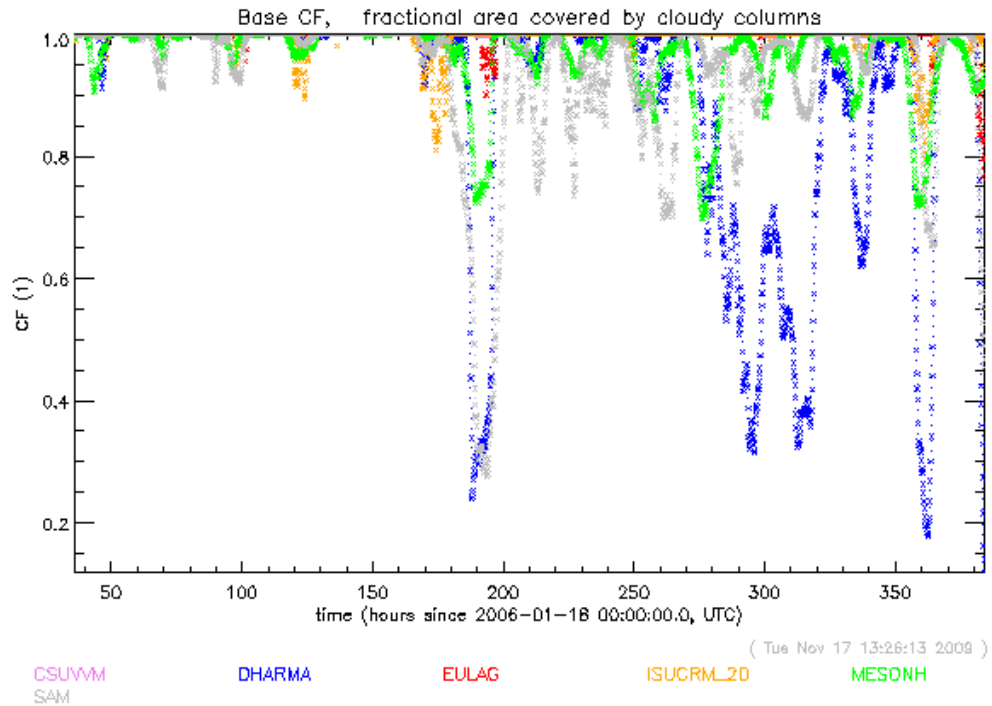


Figure 4.5. As in Figure 4.3, but for the cloud fraction.

There are also a number of interesting differences in the cloud top and base fields. The cloud top heights are shown in Figure 4.6. Here, the CSUVVM falls near the middle of the pack, lying away from extremes of both magnitude and variability. Of course, with cloud fraction values that are very near one for the vast majority of the simulation, large swings in the cloud top heights are not to be expected. The main outlier for this variable is the EULAG, which consistently has cloud top heights greater than those of the other models. More realistic models include SAM, DHARMA, and MESONH.

The cloud base height data is shown in Figure 4.7. Here, the CSUVVM tends to hug the fringe of the model range, with bases toward the lower end of that range. The concern, once more, is the lack of variability in this variable in comparison to the other models. A lack of readily available observational data for validation makes this analysis

difficult, but such smoothness does not appear physical. Granted, the model is not the worst of the bunch, taking their average to be the standard.

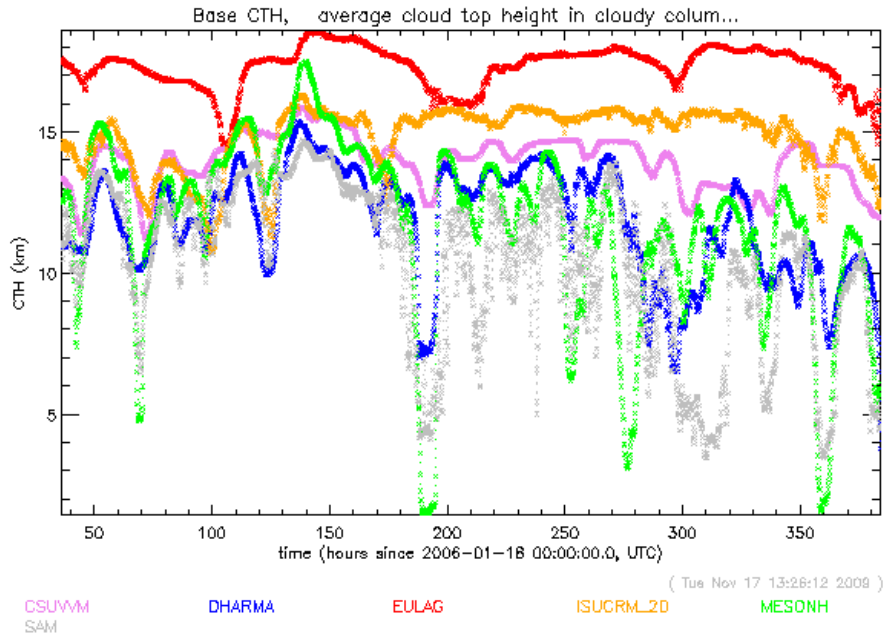


Figure 4.6. As in Figure 4.3, but for the cloud top heights.

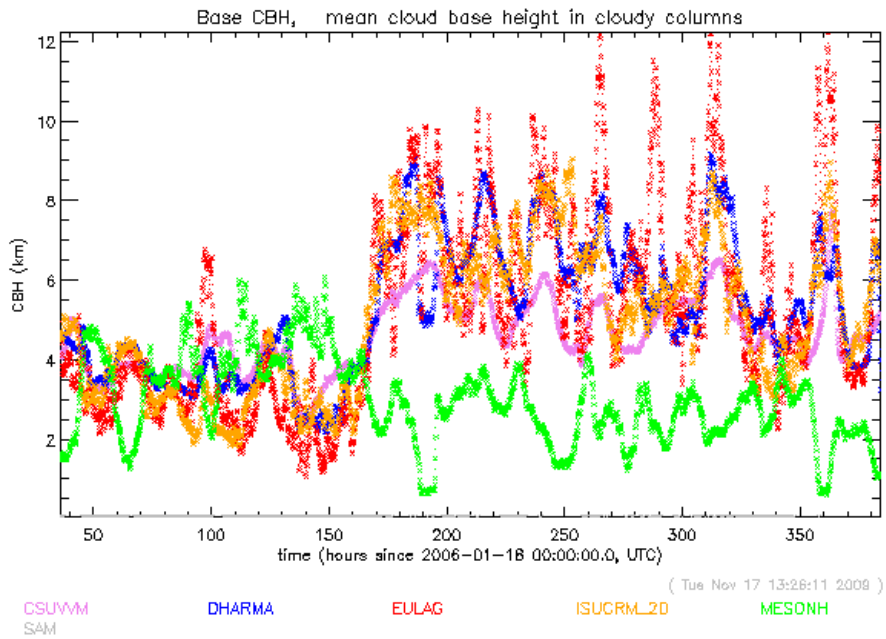


Figure 4.7. As in Figure 4.3, but for the cloud base heights.

Further simulations and observations of cloudiness are shown in Figure 4.8, which shown the profile time series of cloud fraction. Initially, the model (of those presented) that most closely estimates observations is EULAG, though the depth, intensity, and temporal extent of the cloud amount at its highest are each overestimated. Additionally, as was seen in Figure 4.6 and with a conversion between pressure and height (not shown), the maximum cloud height is too high in EULAG. However, the overall structure is well approximated. The VVM has similar structure, but small-scale variations

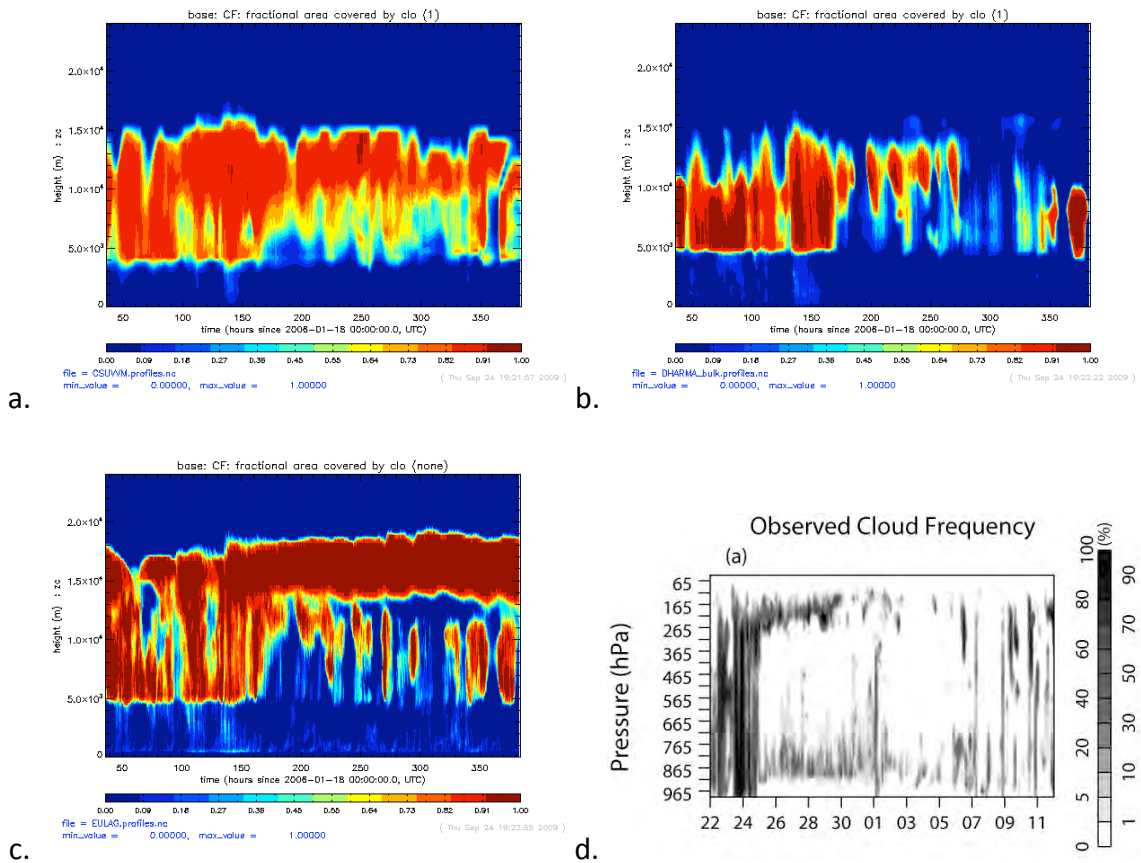


Figure 4.8. Profile time series of cloud fraction for (a) CSUVVM, (b) DHARMA, and (c) EULAG and (d) the observed cloud frequency at the Darwin ARM site (Xie *et al.* 2009). The abscissa in panel (d) denotes time ranging from 00Z on 22 January through 00Z on 12 February 2006. The initial date in the observational data corresponds to 96 hours in the model data. The ends time in the model data corresponds to approximately 03 February in the observational data.

seem to be lacking. This may be attributed to the point-type measurements of the observations. The gap in the midlevel clouds following the first event is absent, though this may be a byproduct of the measurements, as well, as low-level clouds and this midlevel gap is absent from all model simulations.

Other microphysical properties of note are the mean liquid and ice water paths. Neither of these variables, not their variations, are shown here because available plots either lack observational data or show erroneous data. Readers are referred to Fridlind *et al.* (2010) that will have correct figures when published. At all sampling resolutions and variations (maximum values, only considering points where precipitation is beyond a certain threshold, etc. See appendix.), the models show similar evolution and a general consistency, but the simulation mean values are often orders of magnitude greater than observational data. Further, there is some cause for concern in this thesis, in that the VVM is often one of the most deviate from the observations and, occasionally, some of the other models. There appears to be some correlation to the microphysical parameterizations used, but this needs to be examined more closely.

To aid in the objective to quantify convective transport, four tracer variables were requested. To date, the results of these tracer transports have only been made available for the CSUVVM, EULAG, MESONH, NAMSCA, and UKMO-LEM models. Shown in Figure 4.9 are the results from the first three models. The tracers in the NAMSCA model seem to have been implemented incorrectly and simply diffuse. The results of the UKMO-LEM have been omitted in order to save space and because their results are qualitatively similar to CSUVVM and EULAG results. For this variable, no comparable observation is available, so consensus will be the useful metric. The clear outlier of the

group is the MESONH, which exhibits much stronger convective effects throughout the simulation and especially for the lower three tracers. This is consistent with the very high precipitation rate values that were reported during strong events in the MESONH. The vertical tracer transport in the CSUVVM is slightly greater than that in EULAG. The

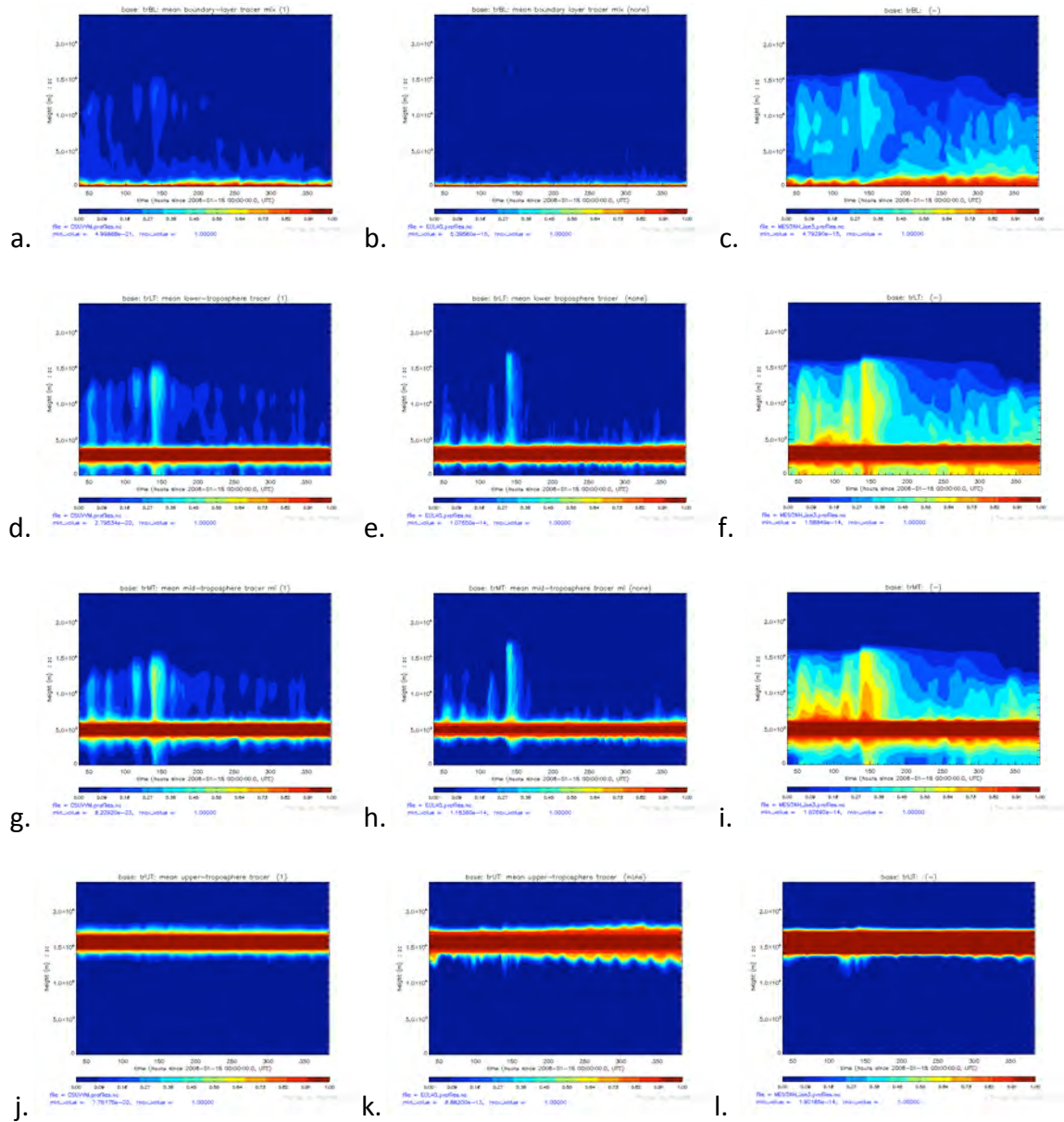


Figure 4.9. Profile time series of tracers for (left) CSUVVM (center) EULAG, and (right) MESONH. The panels show tracers at the (a, b, c) boundary layer, (d, e, f) lower troposphere, (g, h, i) middle troposphere, and (j, k, l) upper troposphere levels.

EULAG results are most similar to the results that are seen in the UKMO-LEM (not shown). Overall, the lower and middle troposphere tracers show the greatest amount of transport in each model. This is to be expected as these lie within the region of strongest vertical velocity. Transport at the upper troposphere layer seems to vary the strongest from model to model. The CSUVVM shows very little motion, while the MESONH and the UKMO-LEM show activity coincident with the strongest convective events. There is some correlation to convective events in the case of the EULAG model simulation, but in its latter half, there arises a sort of oscillatory behavior that is not seen in the other models and appears to be related to the diurnal cycle. Given these results, there is good agreement relative to vertical transport that bodes well for the use of the VVM in this thesis.

With the results that have been presented, some generalizing conclusions can be drawn. There is a positive bias in a few models, including the VVM, in the precipitation data due mainly to an inability to correctly simulate light precipitation. This property is slightly reduced at the surface compared to the 2.5-km level for most models. Cloudiness parameters, including cloud top and base heights, are highly variable among the model simulations, indicating significant uncertainty. The related liquid and ice water paths also show considerable variability from model to model. The mean liquid water path seems to be totally unconstrained by measurements, and model and observed domain mean and maximum values of ice water path have very little in common. In both cases, the models report values much higher than observations.

This all seems to lend some concern to the use of the VVM for this statistical study. It was often one of the furthest outliers of the group of models for certain micro-physical variables. Its performance in the case of the tracer variable was somewhat

promising, indicating some element of dynamical strength, or at least agreement with other models. Perhaps one of the more detrimental features of this model is that in comparison to the others, it shows noticeably less temporal variability in many of the variables presented, especially compared to observations. This lack of variability, or smoothness, is particularly apparent in the cases of the cloud variables. There is also some evidence for this in the tracer data. This feature is particularly troubling because the aim of the thesis is to characterize simulated convective variability and to do so with an assumption about how well the model represents reality. It seems that in this case, the temporal variability seen in the observations is not well represented by the VVM. However, the following analysis will not specifically be on temporal variability but rather the nondiagnostic and nondeterministic variability that arises when very similar large-scale forcings are applied. This variability does, though, ultimately feed into temporal variability through chaotic interactions. The connection is rather complex and not easily described. At any rate, this observation suggests that the results of the following analysis should be compared to the results of the same tests upon other models, specifically those exhibiting more temporal variability. One particular model of interest is SAM, which as seen in Figure 4.6 does, indeed, show significantly more temporal variability.

Chapter 5 - Simulation Results

5.1 Constant Forcing Simulations

In order to provide a set of ‘control’ simulations for later comparison to the variable forcing simulations, 10 constant forcing simulations were performed as described in Section 3.3. We will briefly look at the results of those simulations focusing on the convective response to the applied large-scale forcing. One obvious and broad indicator of the intensity of convection is the resultant precipitation. The time evolution of the domain-averaged surface precipitation rate is shown for each of the constant forcing simulations (Figure 5.1.1). Here, and throughout the paper, the surface precipitation rate has been calculated as the rainwater fall rate in the lowest layer of the model.

One feature that is immediately visible in Figure 5.1.1 is the gradual increase in the magnitude of the precipitation rate, represented by the black lines, as the forcing is increased. This feature is especially apparent when viewing the red lines, representing the time mean. In fact, the increase in the mean precipitation is almost exactly linear with respect to the normalized forcing (Figure 5.2a). Quantitatively, there is an increase of approximately a quarter of a millimeter per hour for each ten percent increase in large-scale forcing. Based on the prescribed forcing profiles (Figure 3.1), this corresponds to approximately -2.5 K day^{-1} of peak advective cooling and 3.5 K day^{-1} equivalent of peak advective moistening.

The other very important feature of Figure 5.1.1 is that though the simulation is

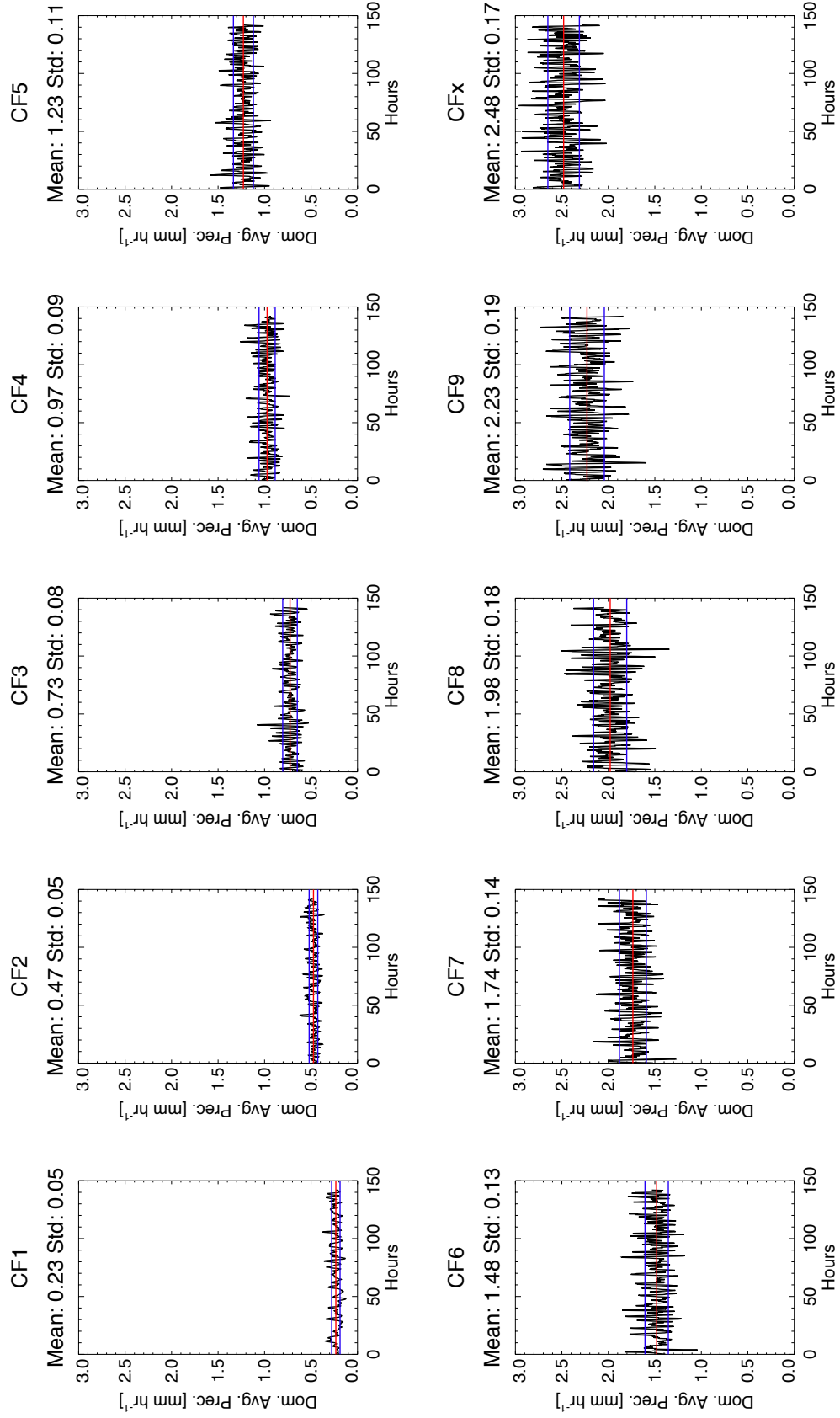


Figure 5.1.1. Time evolution of the domain-averaged surface precipitation rate (black) for each of the constant forcing simulations (plot titles). The time series mean (red) and standard deviation bounds (blue) are overlaid; values are printed above each panel.

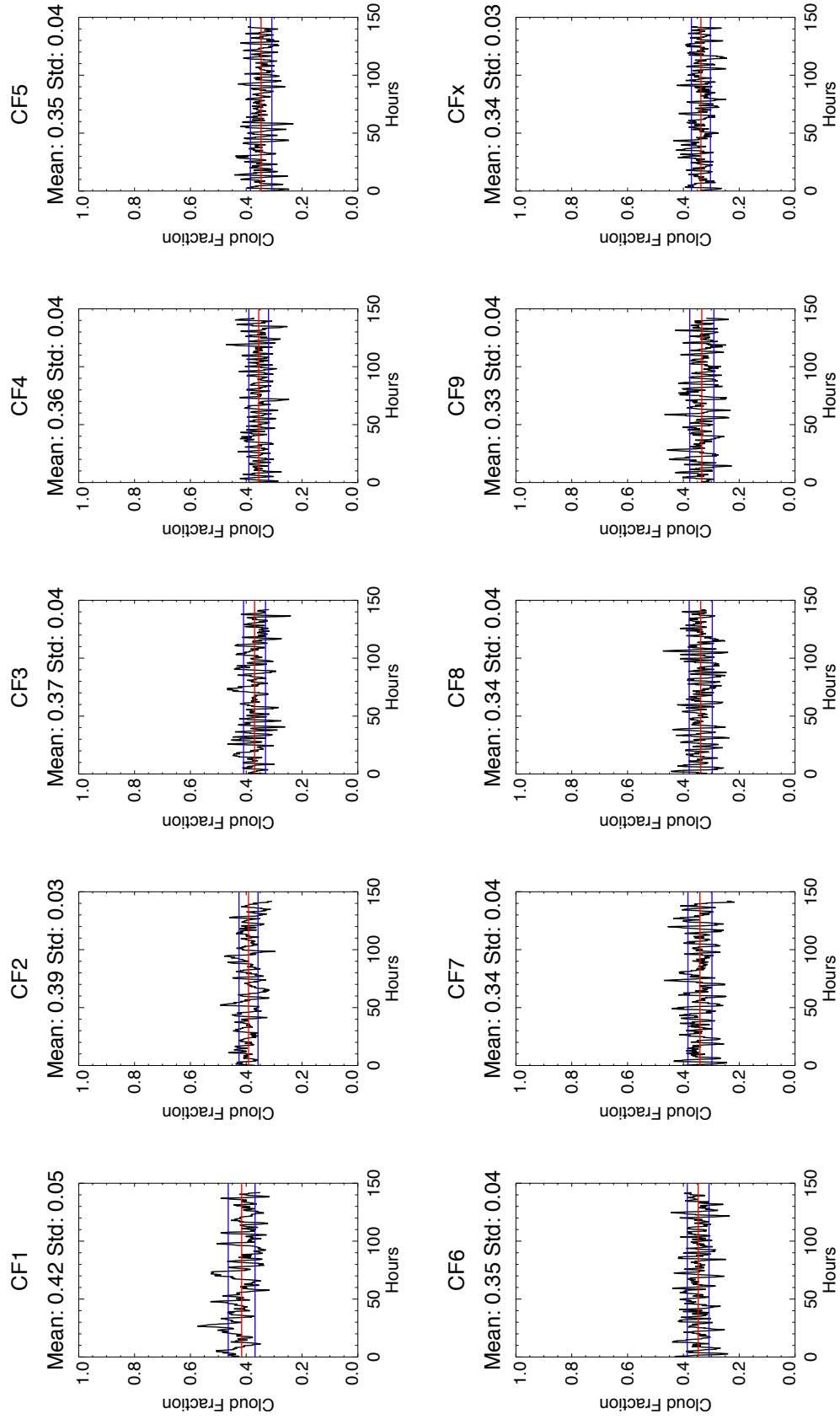


Figure 5.1.2. As in Figure 5.1.1, but for cloud fraction.

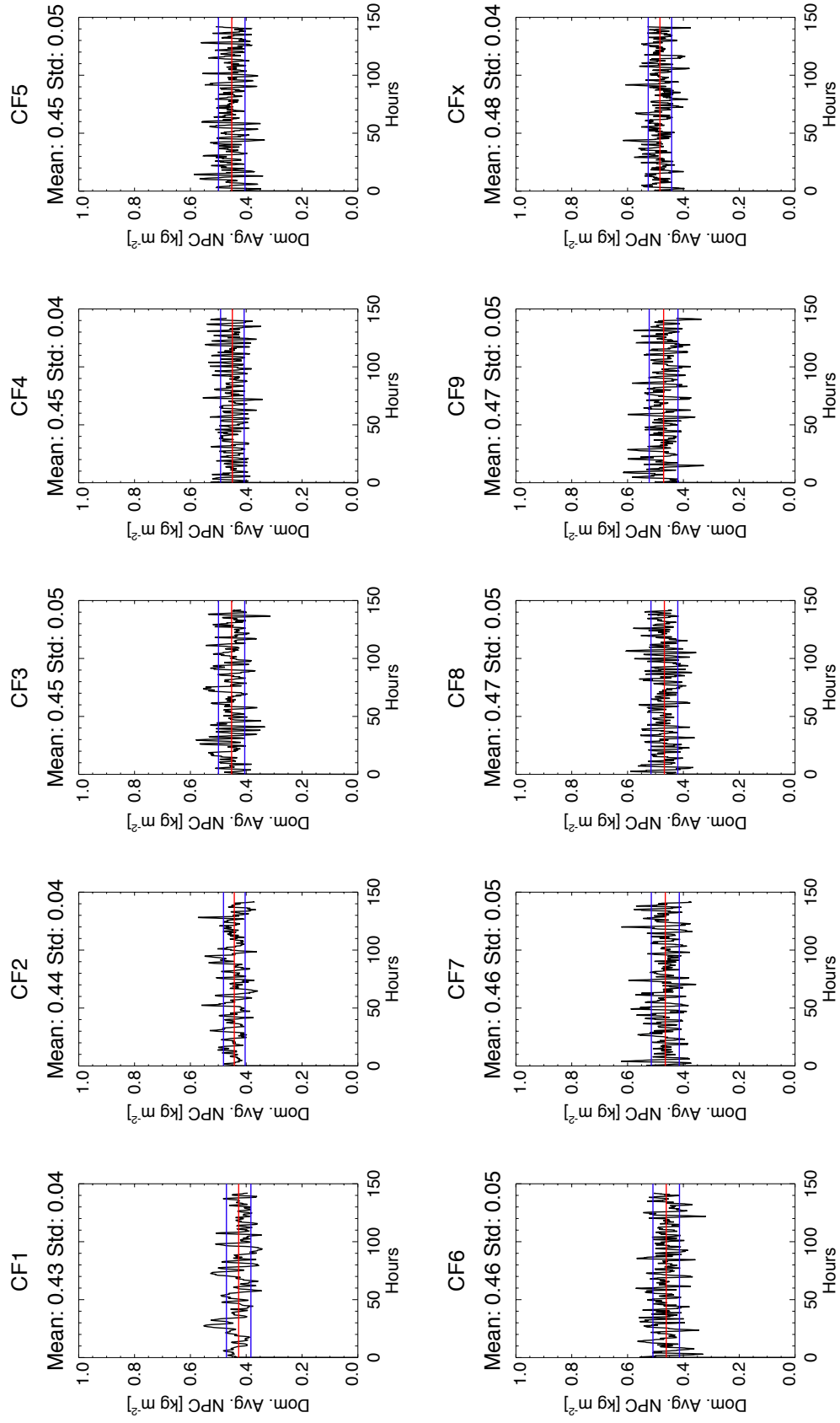


Figure 5.1.3. As in Figure 5.1.1, but for non-precipitating condensate.

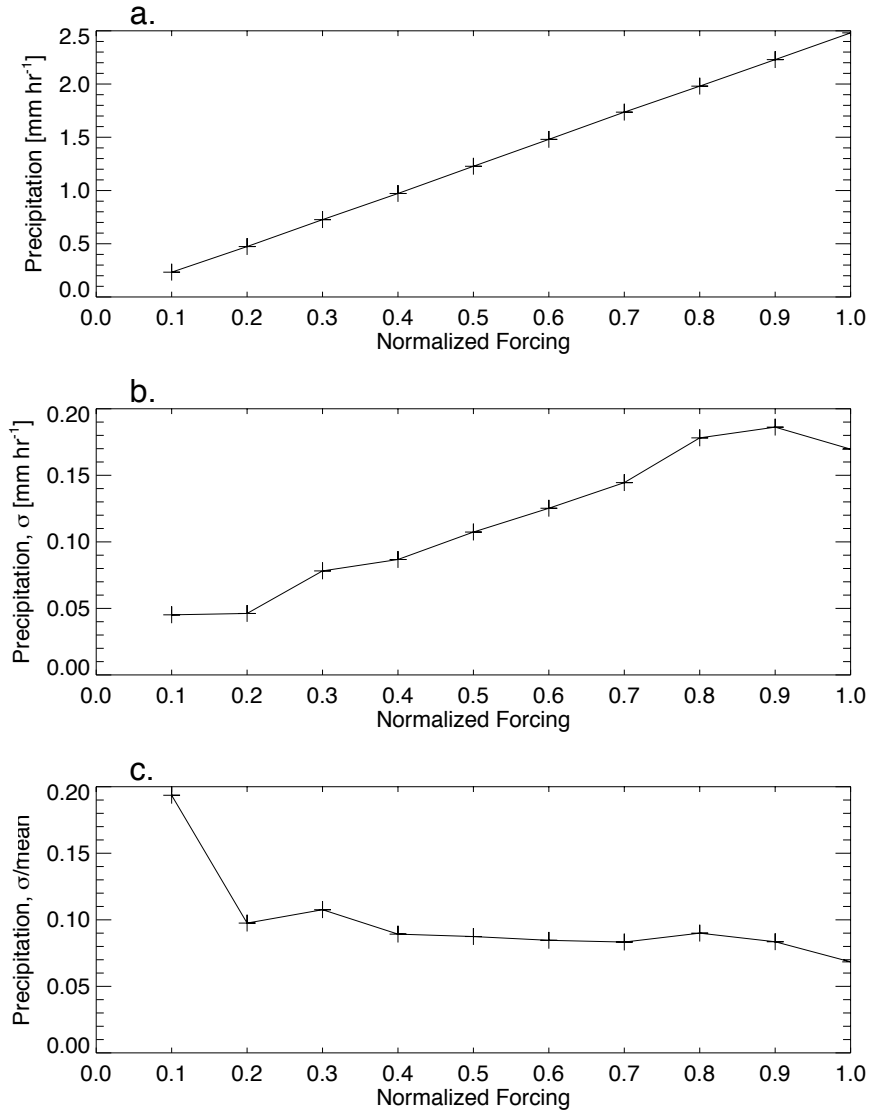


Figure 5.2.1. a.) the time-mean surface precipitation rate; b.) the time-relative standard deviation of the surface precipitation rate; and c.) the mean-scaled standard deviation of the surface precipitation rate for constant forcing simulations CF1 through CFX.

forced with constant large-scale values, the response as seen in the domain average precipitation rate is clearly not constant. Rather is it demonstrating characteristics of the statistical equilibrium mentioned in Section 1.1, where the variance about the mean is small with respect to the mean. A measure of this variance as pertaining to the time series in Figure 5.1.1, is the standard deviation of the precipitation rate, denoted by the blue lines.

It is shown in Figure 5.2b that the standard deviation has a near linear increase with increasing forcing, similar to that of the increase of the mean but with differences at the extremes of the forcing values that were applied. Specifically, the trend is mostly linearly increasing between twenty and ninety percent of the maximum forcing (CF2–CF9).

Dividing the time-respective standard deviation by the time mean of the precipitation rates for each constant forcing simulation, we obtain the results shown in Figure 5.2c. For the majority of the normalized forcing values, this normalized standard deviation value is nearly constant. This is a result that many modelers would expect to discover: the standard deviation (variability) scales with the mean. In fact, this is an assumption on which some convective parameterizations rely in order to represent the variability correctly (*e.g.* ECMWF models). However, the results here indicate that there is the possibility of a non-constant scaling of the variability about the mean response.

The clearest exceptions to this ‘rule’ are seen where the forcing values are either very small or very large. When the large-scale forcing is 10 percent of the maximum (CF1, weak forcing), the standard deviation about the mean is greater than twice the mean-relative magnitude that was simulated in the other constant forcing runs. At the other end of the spectrum, when the forcing is at its maximum (CFX), the mean-scaled standard deviation is approximately 80 percent of that of the constant forcing runs CF2–CF9. Further, over these simulations where the scaling appears to be most constant, there is actually a slight decrease in the mean-scaled variability as the large scale forcing is increased. Depending on where the line is drawn, there is an 8-23 percent decline in the mean-scaled variability over the range that appears nearly constant.

In addition to the precipitation rate, the same analysis has been performed for the

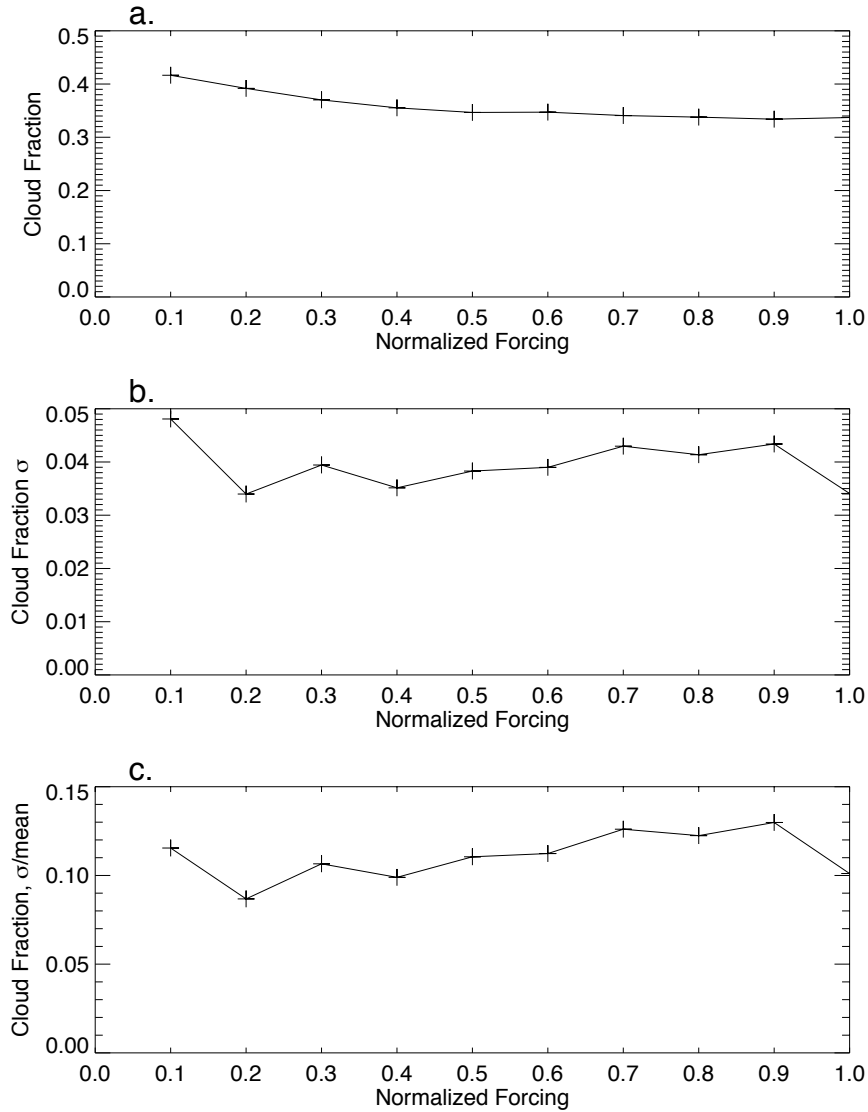


Figure 5.2.2. As in Figure 5.2.1, but for cloud fraction.

comparable variables of cloud fraction and non-precipitating condensate, a variable whose definition shall be expanded upon in Section 5.2. Figures 5.1.2, 5.1.3, 5.2.2, and 5.2.3 have been supplied to demonstrate the statistical behavior of these other convection-related variables. There are a few interesting features in these figures. First, we see that cloud fraction tends to asymptotically decrease with increasing forcing strength. That result seems counterintuitive in that one might expect the forcing to directly increase the

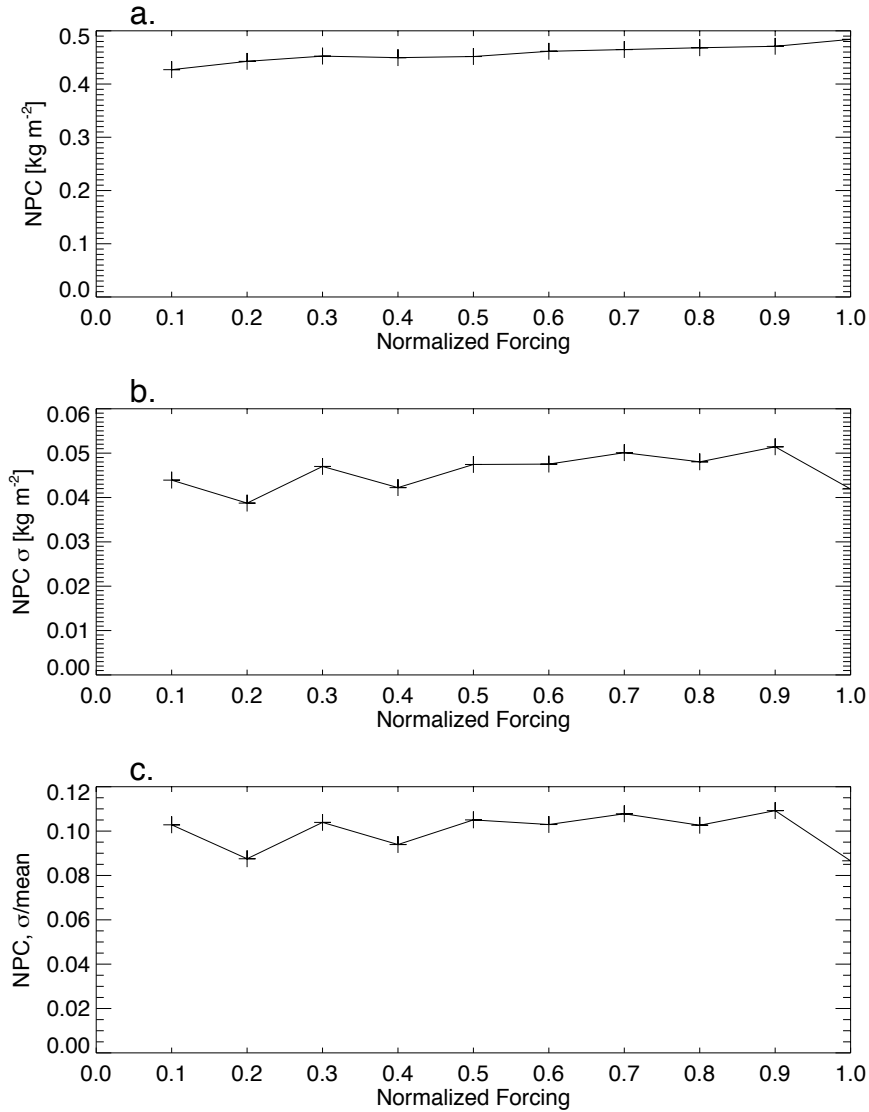


Figure 5.2.3. As in Figure 5.2.1, but for non-precipitating condensate.

amount of cloud in a given domain. This cognitive issue is relieved slightly by the result from the non-precipitating condensate, which increases to some extent with increases in the large-scale forcing. This means that the clouds become more dense.

At this point, it is only speculation, but there may be a significant impact from using an assumed constant mean-scaled variability in a convective parameterization. Assuming that these results are truly representative, convective parameterizations assuming

constant scaling would report far too little variability in situations where the large-scale forcing is small and possibly somewhat too much variability (and progressively more so) as stronger forcings are encountered. With the nonlinearity inherent in atmospheric processes, such sustained misrepresentations could easily have vast impact on many aspects of a given simulation. In order to validate the findings of these constant forcing model runs, it would be advantageous to perform longer simulations at finer forcing intervals within the VVM and other cloud-resolving models to obtain both greater confidence in the statistics and a more detailed representation of how the mean-scaled variability responds to various magnitudes of large-scale forcings. From that information, one could be able to create or modify a convective parameterization (especially a stochastic version) that would be constrained to meet the requirements of the statistics. It would be interesting to see how much this factor alone would improve or degrade GCMs or NWP models.

5.2 Periodic Forcing Simulations

In this section, the focus is on the results of the periodic forcing simulations that were run, in essence, as a sensitivity study to characterize the model response to a set of varying large-scale forcings. The section begins with an overview of the nature of what the simulations produced via images of the simulation precipitation and cloud fields. Following that, composite results of various convectively important fields will be discussed with particular attention being paid to convective variability and some interesting features of the mean convection.

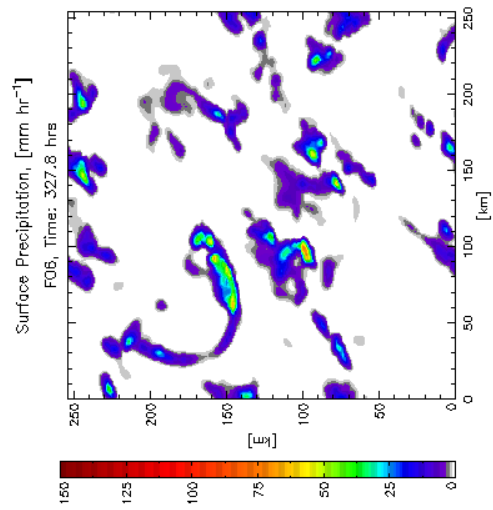
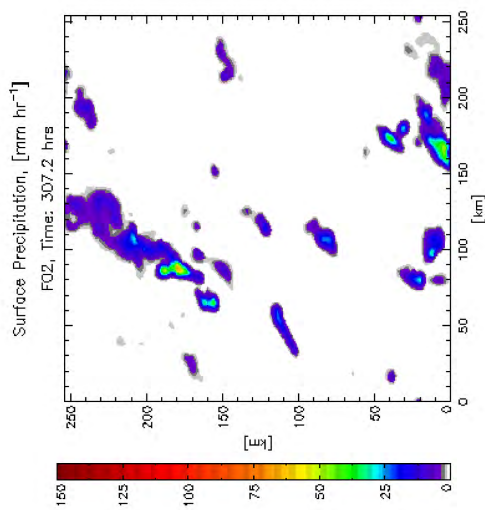
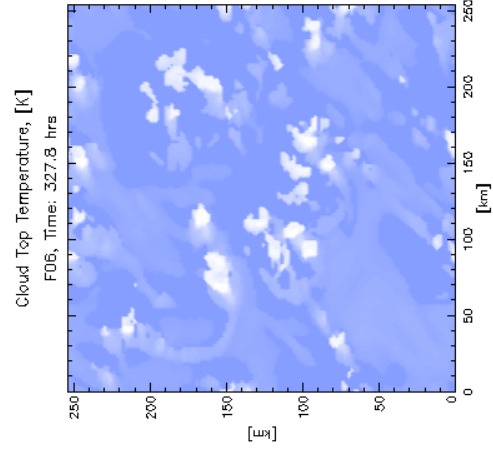
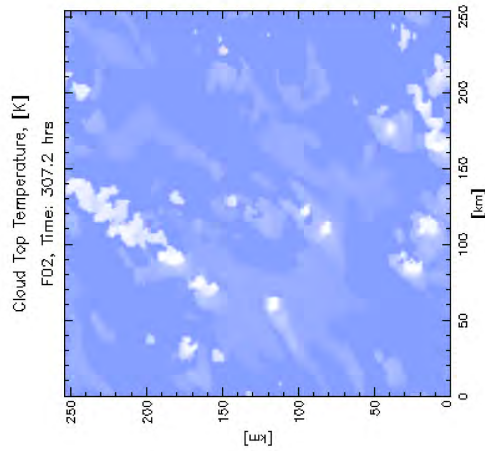
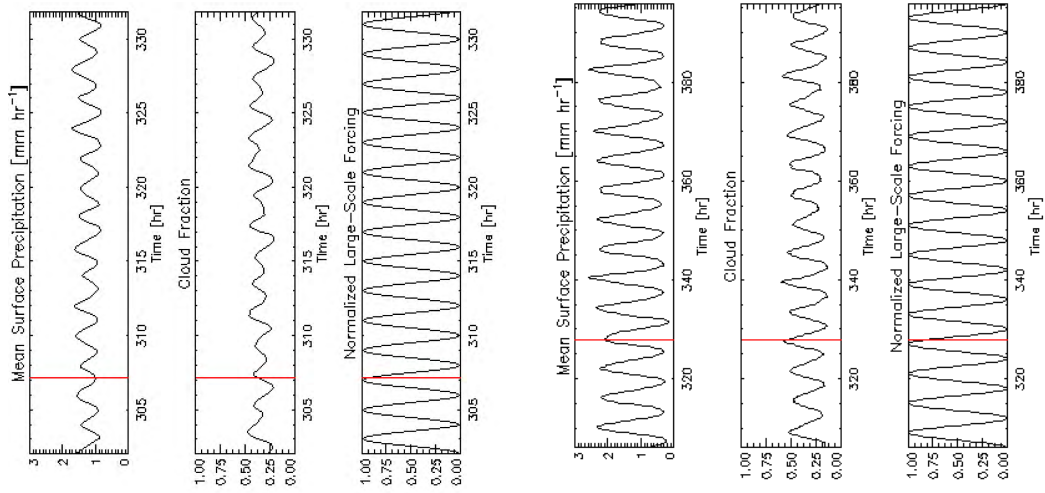
5.2.1 *Snapshot Views*

To begin, we will look at some selected model output snapshots from the various periodic forcing simulations. Figure 5.3a depicts the simulated surface precipitation rate (left panel) and the cloud top temperatures (center panel) 7.2 hours past the ~ 300 hour model spin-up period of the F02 (2-hour period) simulation. The three panels on the right of the same figure show the time series values of the mean surface precipitation rate (top), the domain cloud fraction (middle), and the corresponding 2-hour normalized large-scale forcing (bottom). The top of a cloud is defined as the height where the sum of the cloud liquid and ice water is greater than 0.1 kg m^{-2} when integrating downward from the model top. The vertical red lines on the rightmost three panels denote the point in the simulation that is rendered in the left and center panels of the figure. For reference, the uppermost portion of the domain in these figures shall be referred to as the north of the domain.

At this point in the F02 simulation where the forcing is oscillating relatively rapidly, the large-scale forcing has just begun to decline from its maximum, the cloud fraction ($\sim 35\%$) is approaching a local maximum, and the mean surface precipitation is at a local minimum ($\sim 1 \text{ mm hr}^{-1}$). The apparent counterintuitive nature of this alignment of variables shall be discussed later in this paper. At this point, we will focus on the nature of the convective fields. Here, we see that for the domain as a whole, the convection (most clearly represented by cold cloud tops and greater intensity surface precipitation) appears mainly scattered and unorganized. In the northern portion of the domain, there appears to be a quasi-linear feature. Set in motion, a series of these figures would show what appears to be a strong convective cell moving to the southwest at approximately 6

m s^{-1} leaving a trail of (anvil) clouds and precipitation in its wake. In fact, this is shown in Figure 5.4. Following along from panel (a) to panel (f) (west to east), we can see the most intense clouds at low and middle levels between 150 and 200 km north. Trailing this region (Figure 5.4e-f), the cloud is high and thin east of $x = 100$ km and appears to spread out horizontally somewhat. Going further north and east this same feature continues (not shown). From just this snapshot, we can clearly see that the model has the ability to produce realistic convective cells.

A snapshot from the F06 simulation is shown in Figure 5.3b. At this point in the simulation, the mean surface precipitation, cloud fraction, and large-scale forcing values are each near a local maximum. Comparing the time series from Figure 5.3b to those of Figure 5.3a, we notice that the amplitudes of the convective variables have increased greatly. The main reason for this is that the longer period allows for longer sustained periods of large and small large-scale forcing application. The precipitation and cloud fraction appear to better correlate with the large-scale forcing, as well. In the left and center panels for the F06 simulation snapshot, an interesting feature stands out. A bowed structure is visible in the northwest portion of the domain. Watching the field progress at 10-minute intervals (not shown), the bow echo-like feature develops from an intensifying squall line moving to the southwest. The development is more clearly visible in the cloud field than in the precipitation field. Shortly after this point, this mesoscale structure decays over the next two hours, and the overall structure of the convection is scattered as in the F02 simulation, though the intensity of the convection is greater.



a.

b.

Figure 5.3. Description is found in the text. (a) Snapshots from F02 and (b) F06.

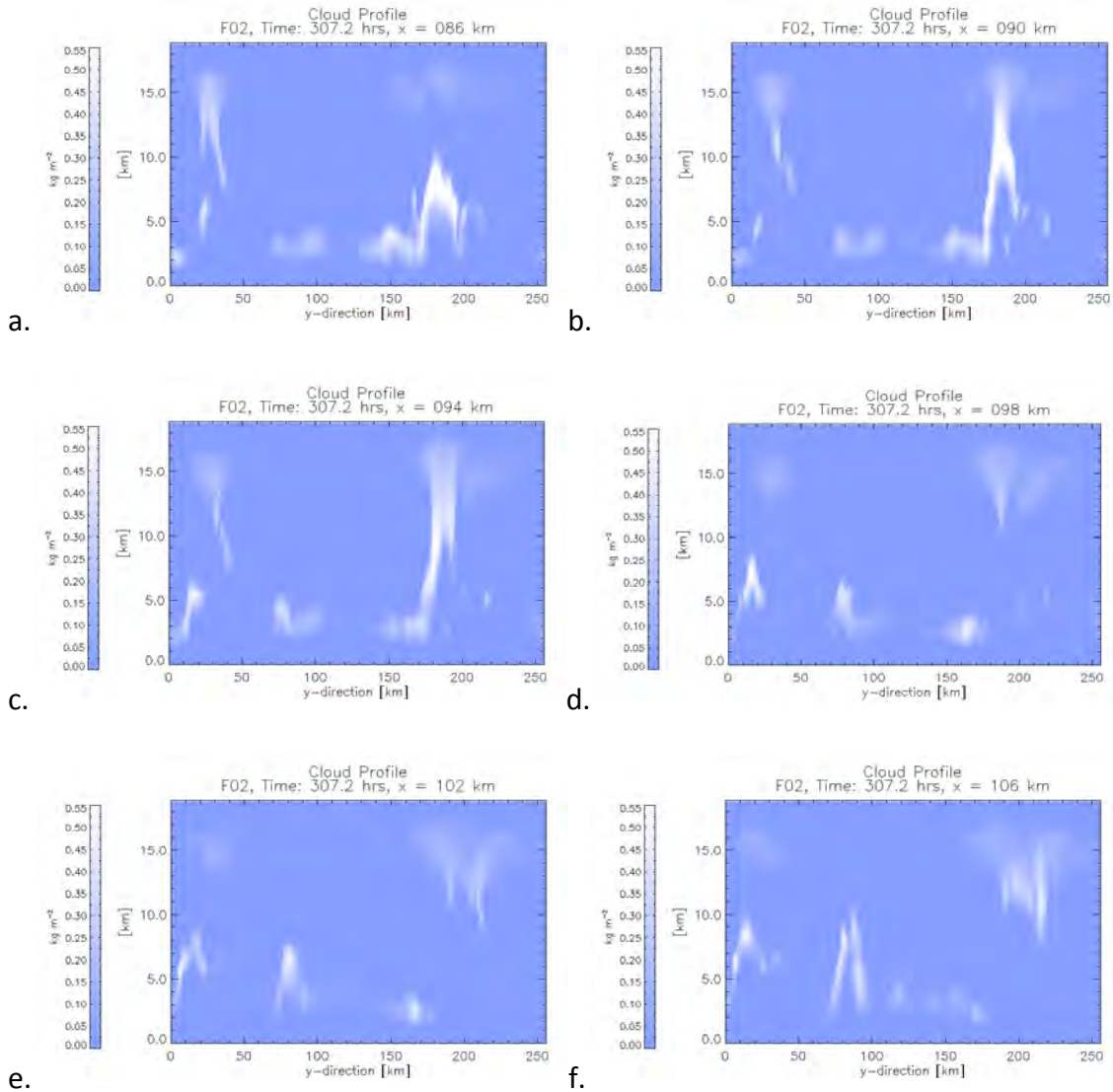
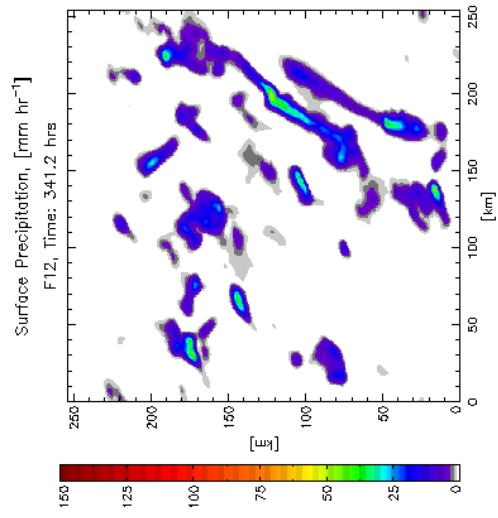
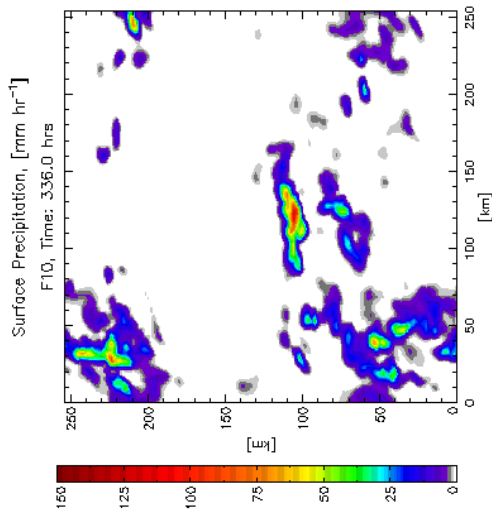
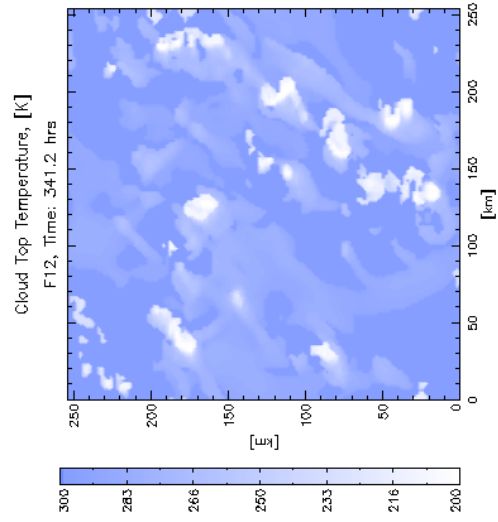
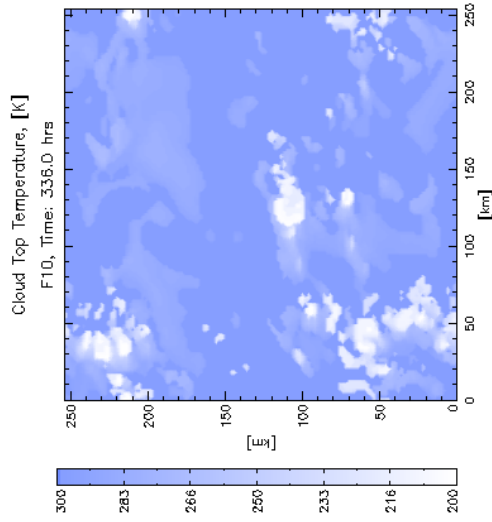
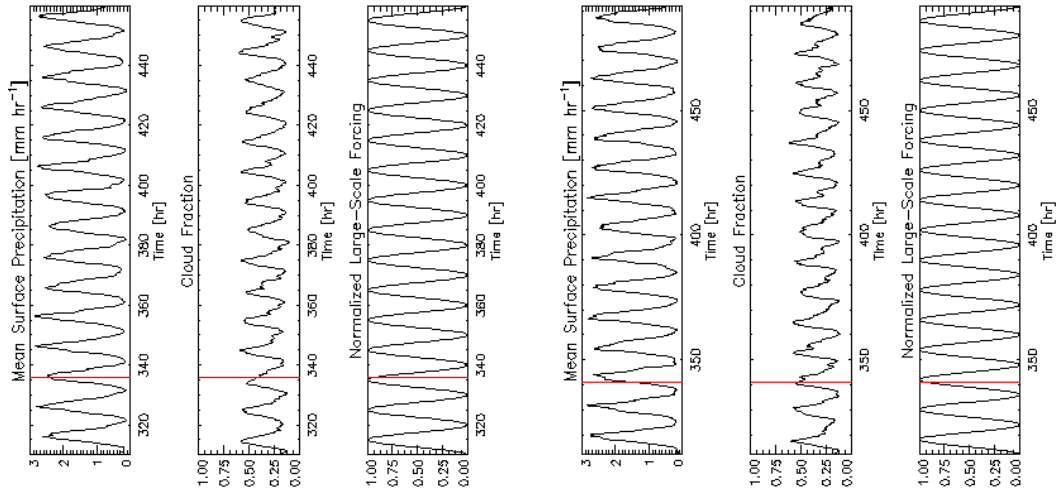


Figure 5.4. Vertical cross section of the sum of cloud water and ice mass per unit horizontal area showing the zy-plane at various values of x, moving west to east from (a) to (f) This figure corresponds to Figure 5.3a..

Snapshots of the F10 and F12 simulations are shown in Figure 5.5. As with the last increase in period, the amplitudes and maximum values of the mean surface precipitation and cloud fraction have increased for the reasons mentioned above. However, one new feature in the time series of these variables is that they are not as smoothly periodic. In fact, these convective variables tend to linger past what one might expect to



a.

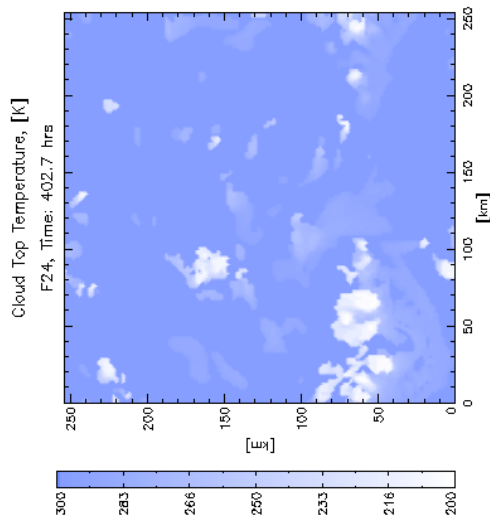
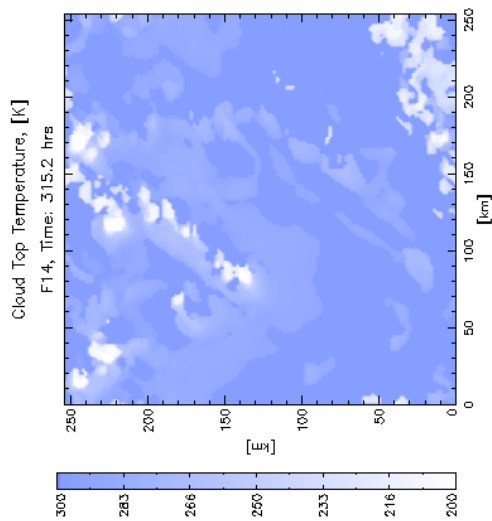
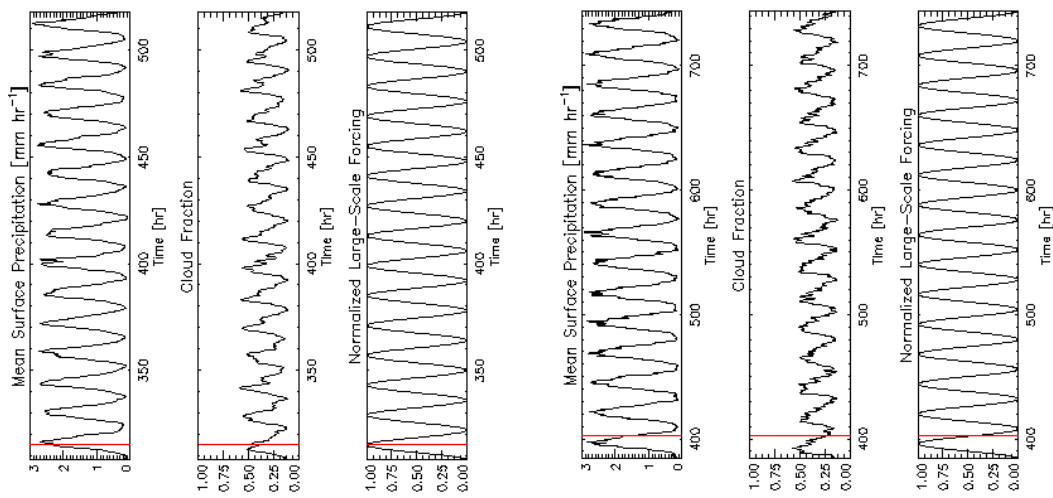
b.

Figure 5.5. As in Figure 5.3. (a) Snapshots from F10 and (b) F12.

be their peak. This phenomenon was termed by X92 as modulation by mesoscale activity. In essence, this refers to the fact that once convection achieves mesoscale organization, it gains the ability to sustain itself beyond the forcing from the large-scale.

F10 and F12 both show degrees of mesoscale organization. In Figure 5.5a showing an image from F10, there are 2 or three distinct areas of organization. There is a convective cluster in the northwest as well as in the southwest; however, these may actually be the same feature due to the periodic boundary conditions. Additionally, there is a strong linear feature spanning ~ 80 km over its widest dimension that, when set in motion, appears to be squall-like. This is more evident in the precipitation field than in the cloud field. Similarly, in Figure 5.5b showing an image from F12, there are two distinct linear features in the southeast of the domain measuring up to 100 km in length. As time progresses, the two features converge and intensify. It is somewhat interesting that a few of the examples shown involve linear mesoscale features. This is likely because a mesoscale structure is, to the first order, a function of the vertical wind shear profile. Since each simulation is given an identical profile, it would be likely to see similar mesoscale organization in each simulation.

A number of other interesting features are present in the simulations, as well. For instance, during F14 and F24 (Figure 5.6), large, organized mesoscale clusters/lines have produced precipitation via outflow, that is, a band of precipitation ahead of the main storm cluster often caused by downdrafts spreading away from the main storm. In both cases, this minor feature lasts less than an hour but is a testament to the model's abilities.



a.

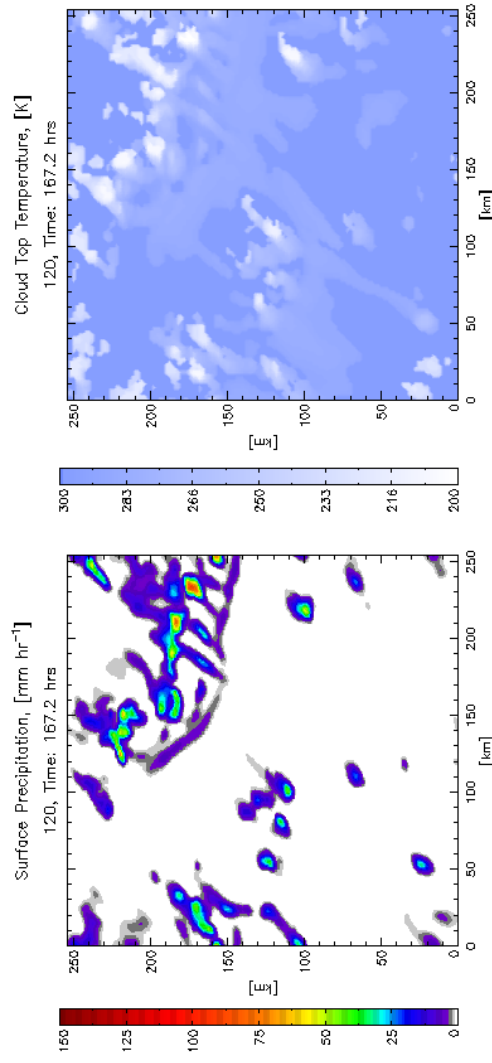
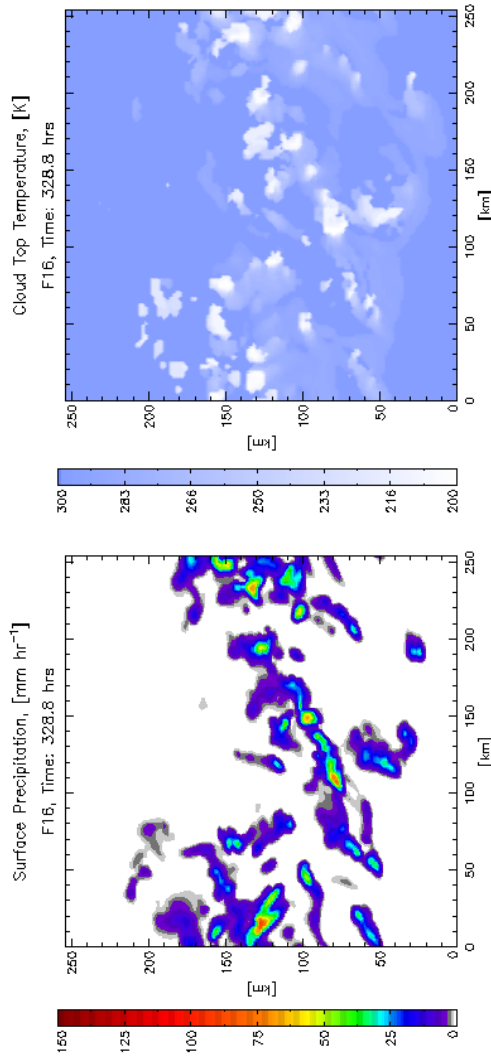
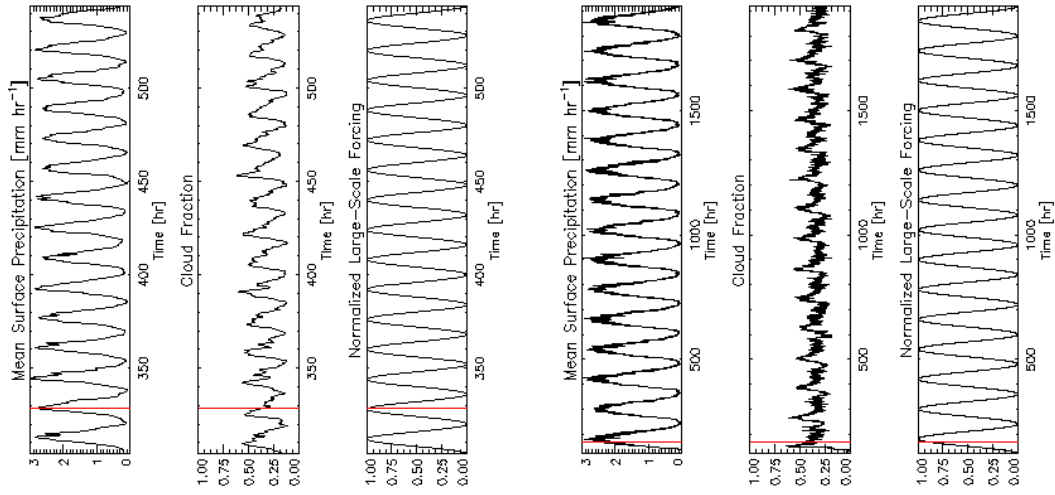
b.

Figure 5.6. As in Figure 5.3. (a) Snapshots from F14 and (b) F24.

Further, there is even larger-scale organization in a few instances. This is shown in Figure 5.7. In the case of F16 (Figure 5.7a) at a point where the mean surface precipitation, cloud fraction, and large-scale forcing are each near their local maximum, there is a band of organized convection that spans the entire width of the domain. In motion, this band moves as a cohesive unit from north to south, though there is not much in the way of visually striking organization in any other sense. It is likely that the presence of this feature is the reason for the slightly broadened precipitation peak that immediately follows this point in the simulation. Additionally, in the F120 simulation snapshot (Figure 5.7b), we see another large band of organized precipitation/convection in the northeast section of the domain. The feature is over 150 km from east to west, and it is accompanied by a preceding outflow boundary as shown in F14 and F24 (Figure 5.6).

The reason for showing Figure 5.8 is twofold. First, it is inherently different from each of the other examples in that it is a snapshot (from F120) coincident with a large-scale forcing local minimum. The surface precipitation field in this figure is representative of all other periodic forcing simulations when a local minimum is encountered in the large-scale forcing.⁶ That is, it is very empty. Second, there is an interesting feature in the cloud top field near the south-central portion of the domain. There appear to be two areas of rotation, denoted by the comma-shaped cloud formations. This complex feature is unique to the longest period forcings. There is little that one can analyze regarding this feature, as it is very short-lived (~30-40 minutes) due to the decline of the large-scale forcing and the subsequent shutdown of convection.

⁶ This is not the case, however, when the convection is 180° out of phase with the periodic large-scale forcing, such as in F02 and to a lesser extent in F04 and F06.



a.

b.

Figure 5.7. As in Figure 5.3. (a) Snapshots from F16 and (b) F120.

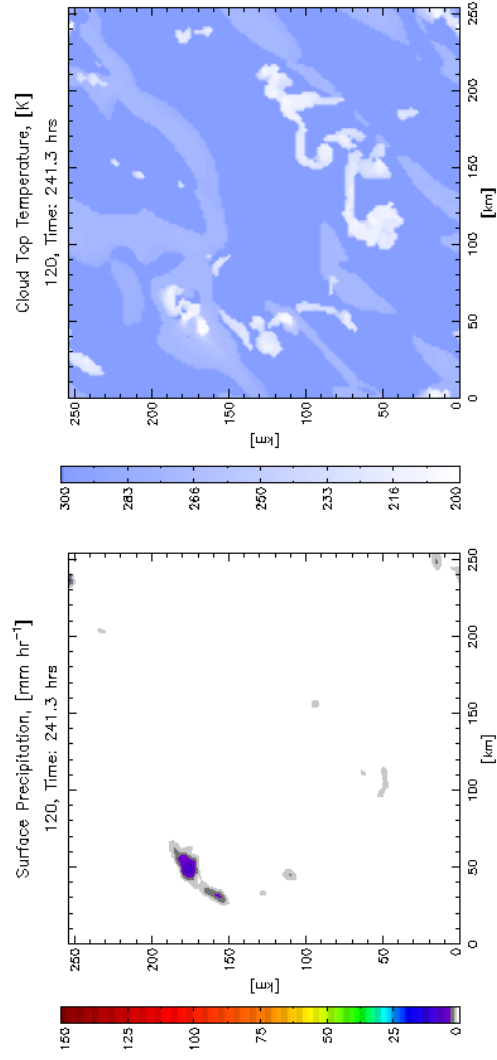
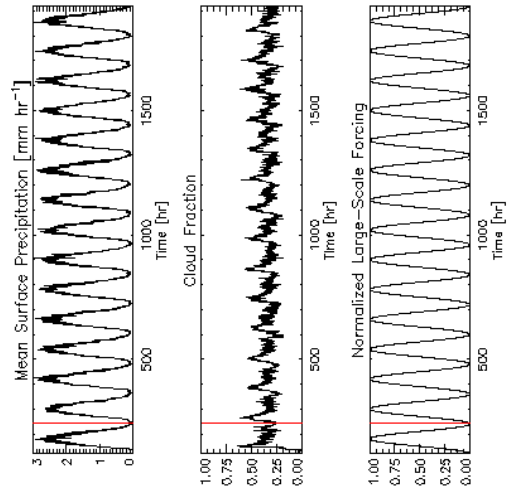


Figure 5.8. As in Figure 5.3. Snapshot from F120.

Again, it is important to note that there is a continued increase in the amplitude and maximum magnitude of the mean surface precipitation and cloud fraction and the forcing period is lengthened. It is also important to keep in mind while comparing these snapshots that there is a significant change in the resolution on the time axes. Some precipitation variations in the F120 simulation are on the order of the amplitude of the F02 simulation, and the time resolution on the image makes that difficult to see. Lastly, it is interesting to note that as the forcing period length increased, the plateau following the maxima in mean surface precipitation rates tended to vanish, while those in the cloud fraction time series became more prominent. The reason for this will be discussed later.

5.2.2 Sounding Features

In this section, the focus shall be on features that can be seen in domain-averaged soundings and related vertical structure features. Most of the items for discussion are not directly going to be useful for the stochastic aspect of convective parameterizations; they are mainly just observations relating to the idealized nature of the periodic forcing simulations.

Figure 5.9 shows (from left to right) the domain averaged temperature, moisture, moist static energy and saturated moist static energy profiles at points 25% (top) and 75% (bottom) of the way through the forcing cycle for F02. The colors indicate the order of the realizations, with blue being first and red being last. Also, the black line indicates the composite average. The temperature profile in both cases is approximately moist adiabatic, and the water vapor mixing ratio seems to be approximately equal in both cases. In the most slowly varying simulations (F60, Figure 5.22), there is a slight trend toward

warming and moistening at the surface with corresponding increases in the moist static energy and saturated moist static energy.

The moist static energy (MSE, h) is defined as usual:

$$MSE = c_p T + gz + L_v r, \quad (5.1)$$

with the saturated moist static energy (SMSE, h^*) being calculated in the same way except that r is replaced by the saturation water vapor mixing ratio. It is typical to have this MSE profile in the tropics with increases upward in the upper levels and decreases upward in the lower levels. The tendency to increase at upper levels is mainly due to MSE becoming equivalent to the dry static energy (DSE) as moisture falls off with altitude. The tendency to decrease at lower levels in the tropics is due to the strong moisture gradient near the surface. In the presence of this strong gradient, the general upward increase in DSE is overwhelmed so that the MSE decreases upward.

On the SMSE plots, the solid purple line is the composite MSE sounding for reference. Note that the two curves are approximately equal in the cold upper atmosphere. From its position at the surface, we can estimate the average height of convective towers, which is denoted by the black dashed line. On average, there are some quite tall clouds over the domain. This holds for both the shown F02 and F60 cases.

Some of the most interesting features are seen in the difference plots between the increasing portion of the forcing and the decreasing portion of the forcing (Figures 5.11-5.13, for F02, F10, and F60, respectively). In the case of the F02 simulation, we see that the surface is initially slightly cooler than when the forcing is decreasing, and the differences from iteration to iteration are highly variable compared to differences in the more slowly varying, equilibrated runs. Being cooler seems counterintuitive, but we must

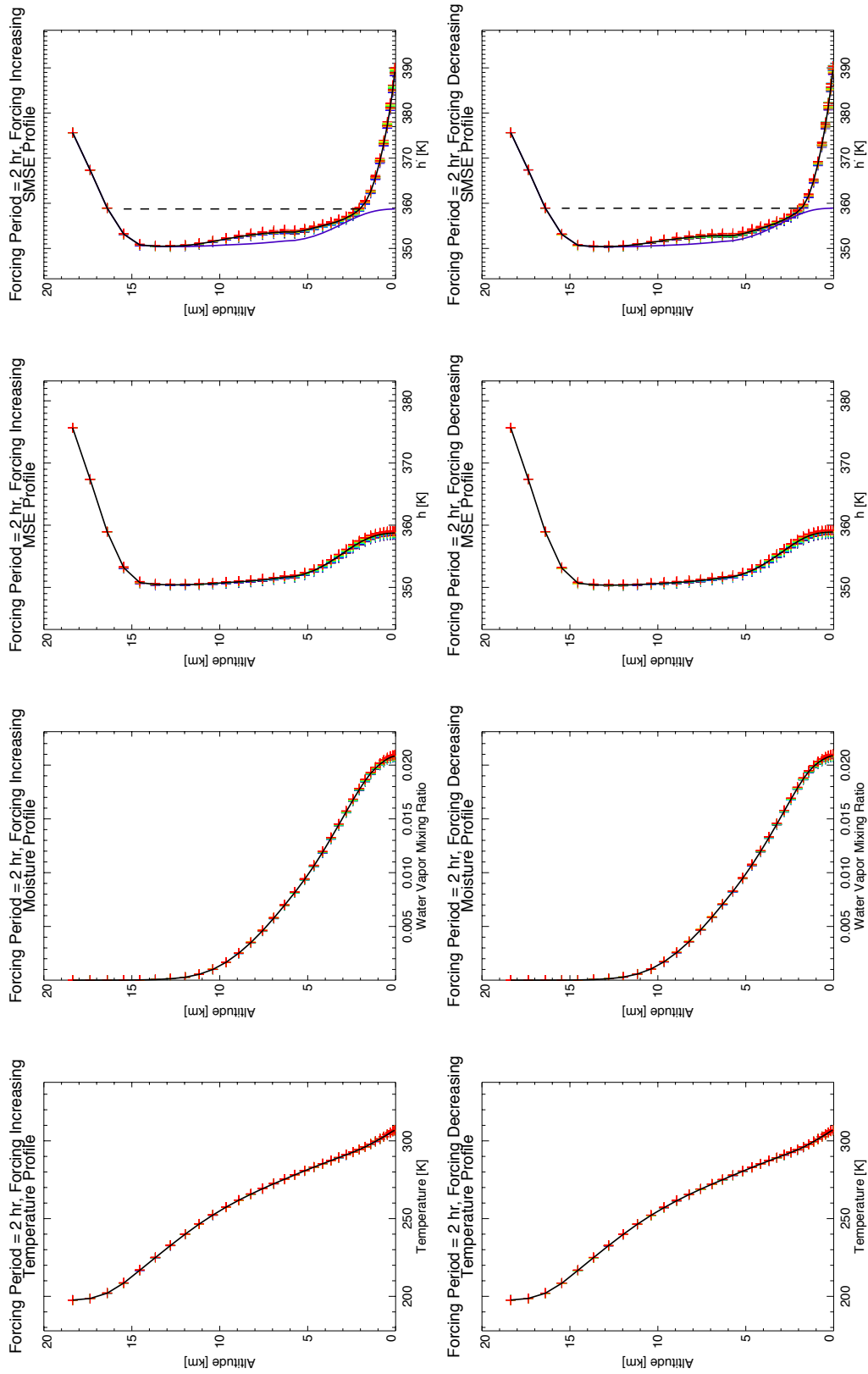


Figure 5.9. Domain-averaged soundings of the noted quantities for each realization of F02. The colors indicate the order of the realizations, with blue being first and red being last. The black solid line indicates the composite average, and the black dashed line represents an estimate of the average height of the convective towers.

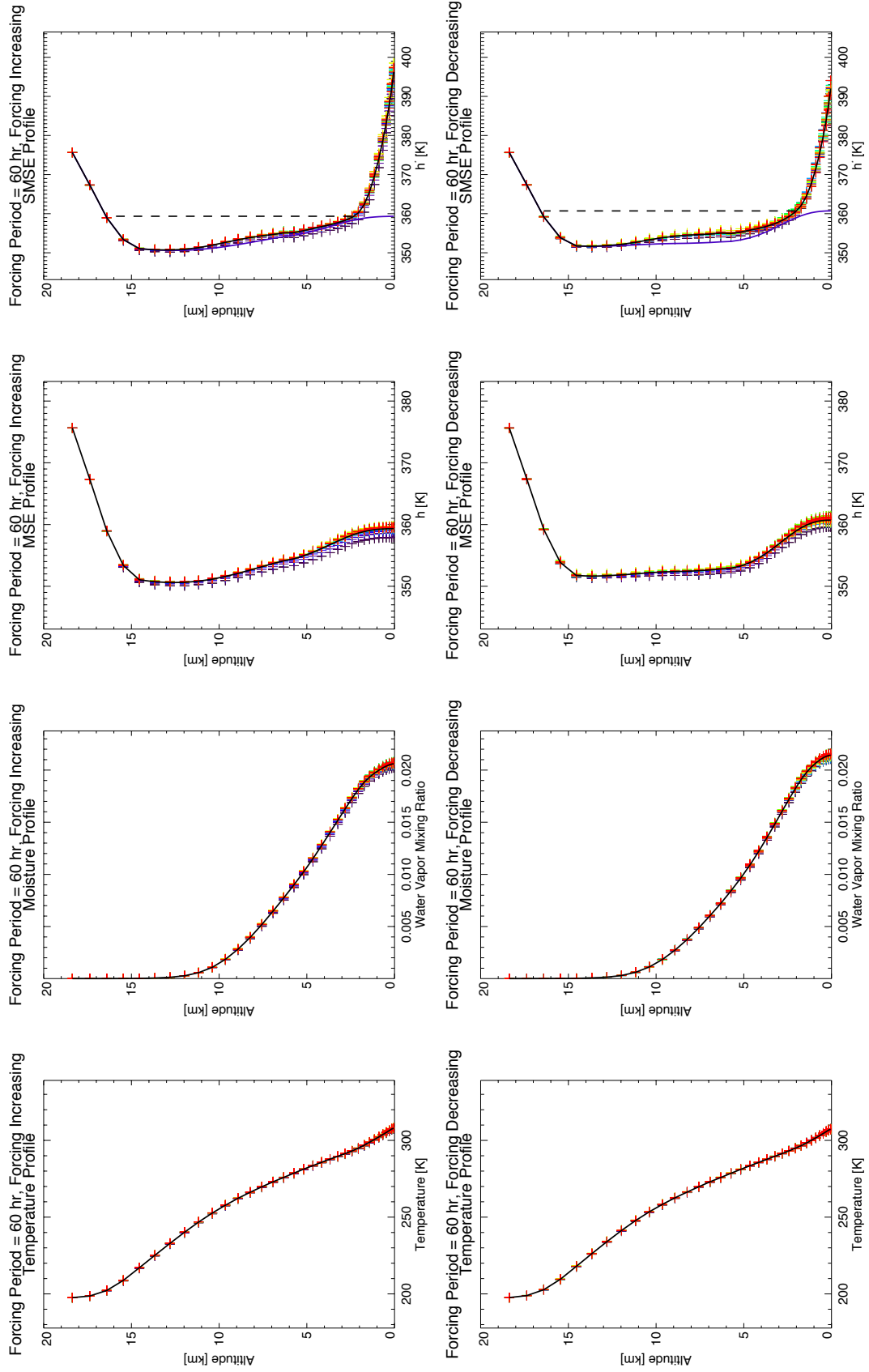


Figure 5.10. As in Figure 5.9, but for F60.

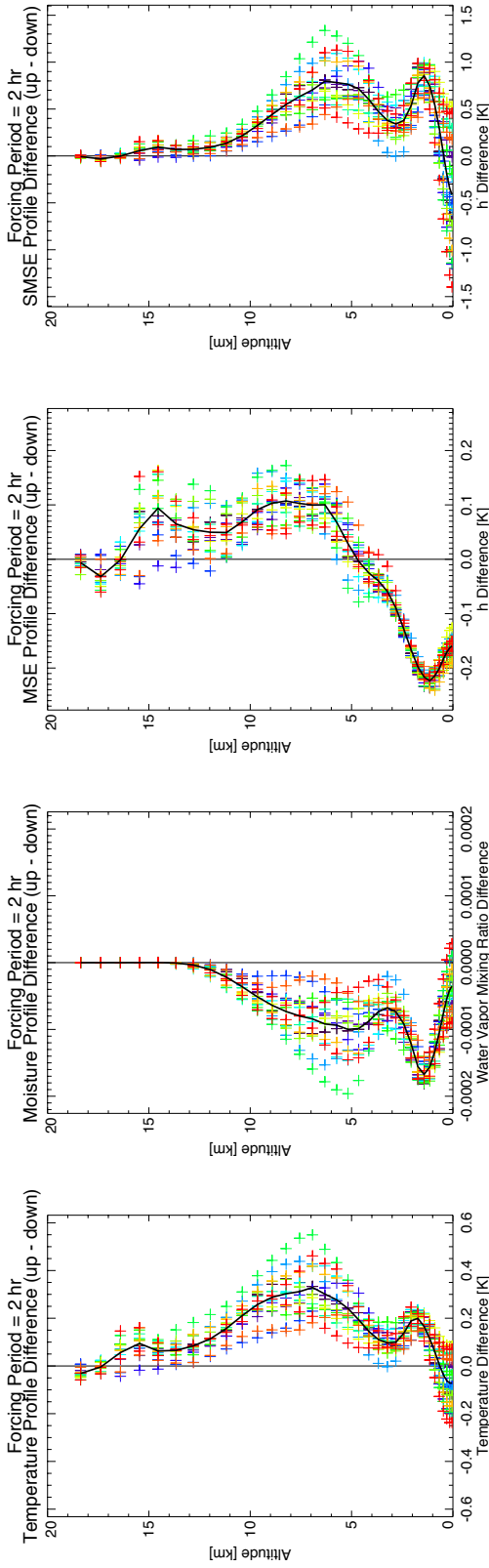


Figure 5.11. Domain-averaged difference of soundings (increasing –decreasing) for the noted quantities from F02. Coloring as in Figure 5.9.

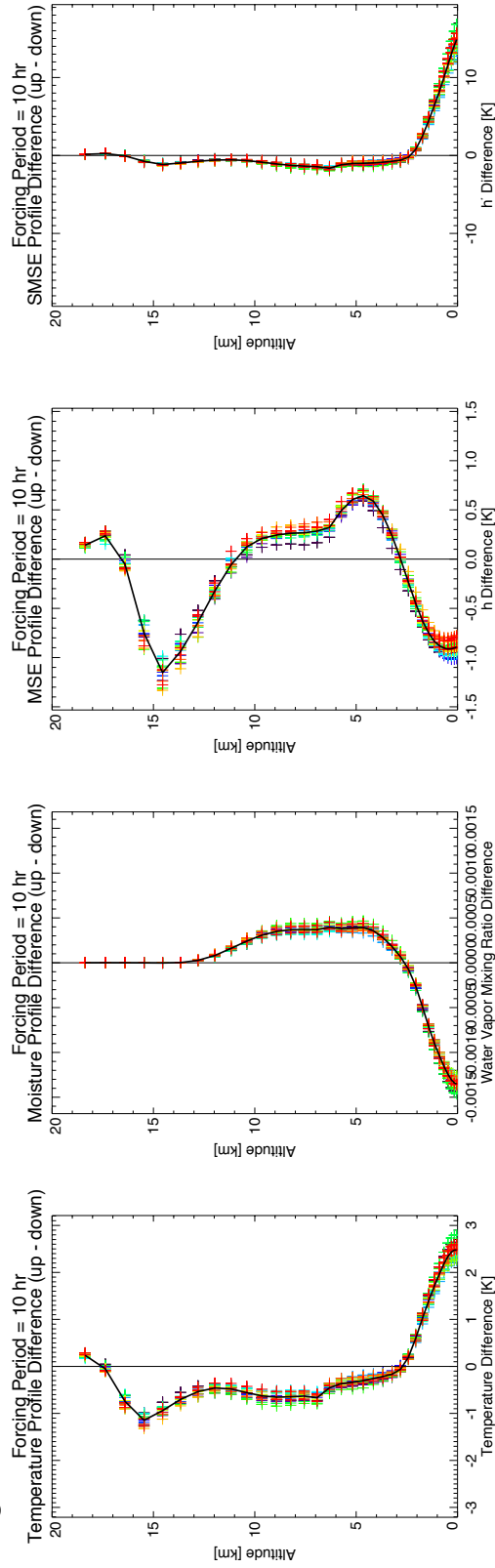


Figure 5.12. As in Figure 5.11, but for F10.

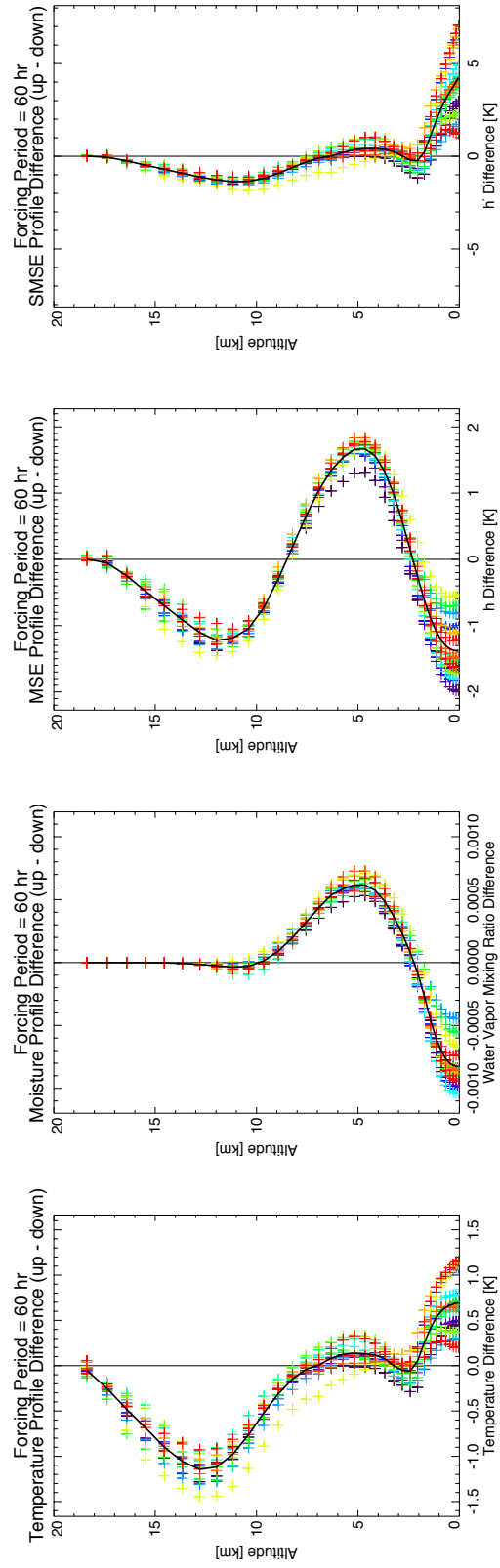


Figure 5.13. As in Figure 5.11, but for F60.

remember that the F02 response is out of phase with the forcing. In the F10 and F60 simulations, the surface starts off warm, dry, and with less moist static energy, before convection acts to cool, moisten, and stabilize the surface atmosphere. Also of note is the fact that the SMSE tends to only change near the surface, where it is most directly affected by the swings in surface temperature and the water vapor mixing ratio. These soundings are more representative of the situation of the other simulations compared to F02.

Further analysis shows trends in the convective available potential energy (CAPE). Figure 5.14 shows the CAPE time series for each of the simulations. The color trend indicates the simulation, with blue meaning faster varying forcing and red meaning more slowly varying forcing. The quickly varying forcings have a much smaller range for CAPE as there is little time for development one way or the other. The opposite is

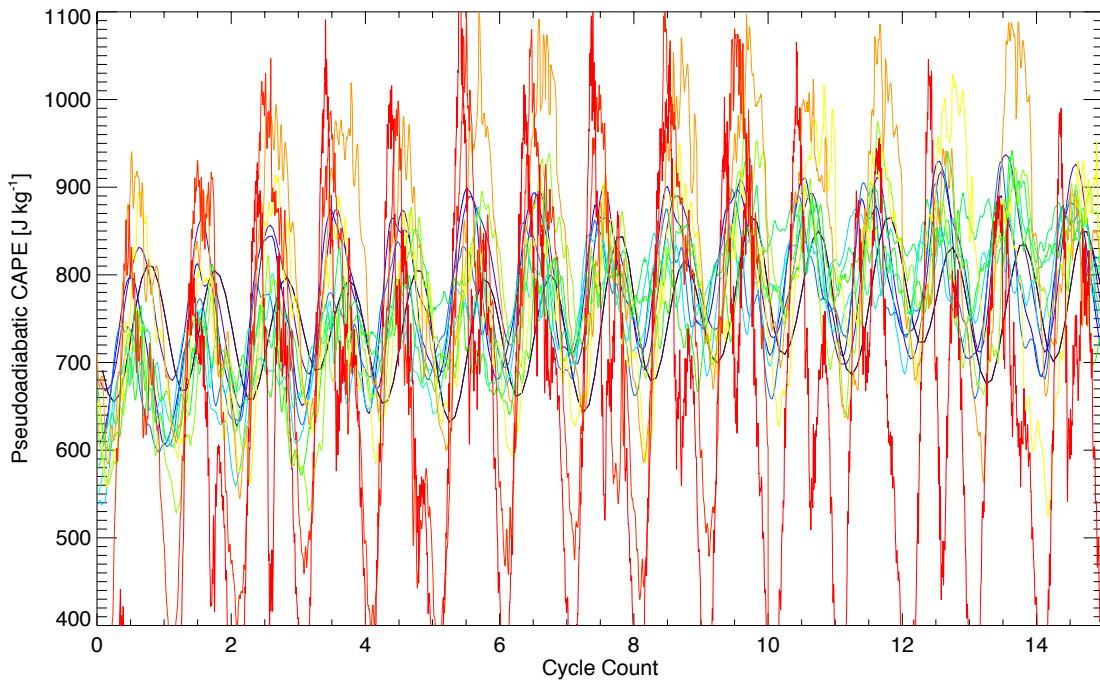


Figure 5.14. Pseudoadiabatic CAPE time series for all simulations. See text for description.

true for the more slowly varying forcings. Interestingly, for simulations in the middle range (e.g. F12 and F14), there is very little evidence of the forcing cycle in the CAPE time series.

Similarly to the previous sounding analysis, Figure 5.15 shows the average value for CAPE coincident with the point at which the forcing is most rapidly increasing and decreasing, depending on the simulation. To generalize, the CAPE is greater when the forcing is decreasing than when it is increasing. This is likely due to the influx of surface moisture at that point in the simulation.

Another feature involving the CAPE was noticed upon inspection of the time series of some simulations with long forcing periods. There seemed to be a significant mode of variability apart from the main forcing period. Spectral analysis confirmed these

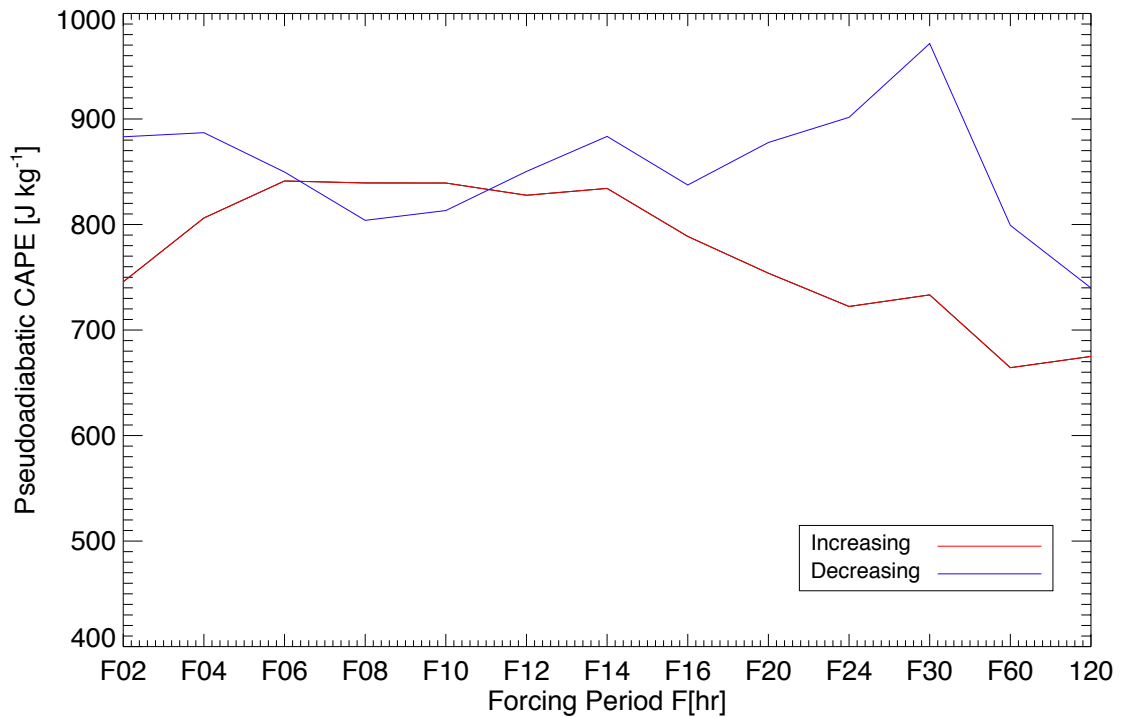


Figure 5.15. Pseudoadiabatic CAPE when the large-scale forcing is increasing and decreasing.

suspicions, and the results are shown in Figure 5.16. The F60 simulation has an additional spectral peak at about 30 hours, and the F120 simulation has an additional, very strong spectral peak at about 60 hours. The reason for the existence of these peaks remains elusive.

Lastly, correlations were performed comparing the CAPE and its tendencies to the surface precipitation rate. Two examples of this are shown in Figures 5.17 and 5.18 for the F08 and F30 simulations. In the F08 simulation, we are beginning to see the diminishing evidence of the forcing period at the mid-range as noted above. In this case,

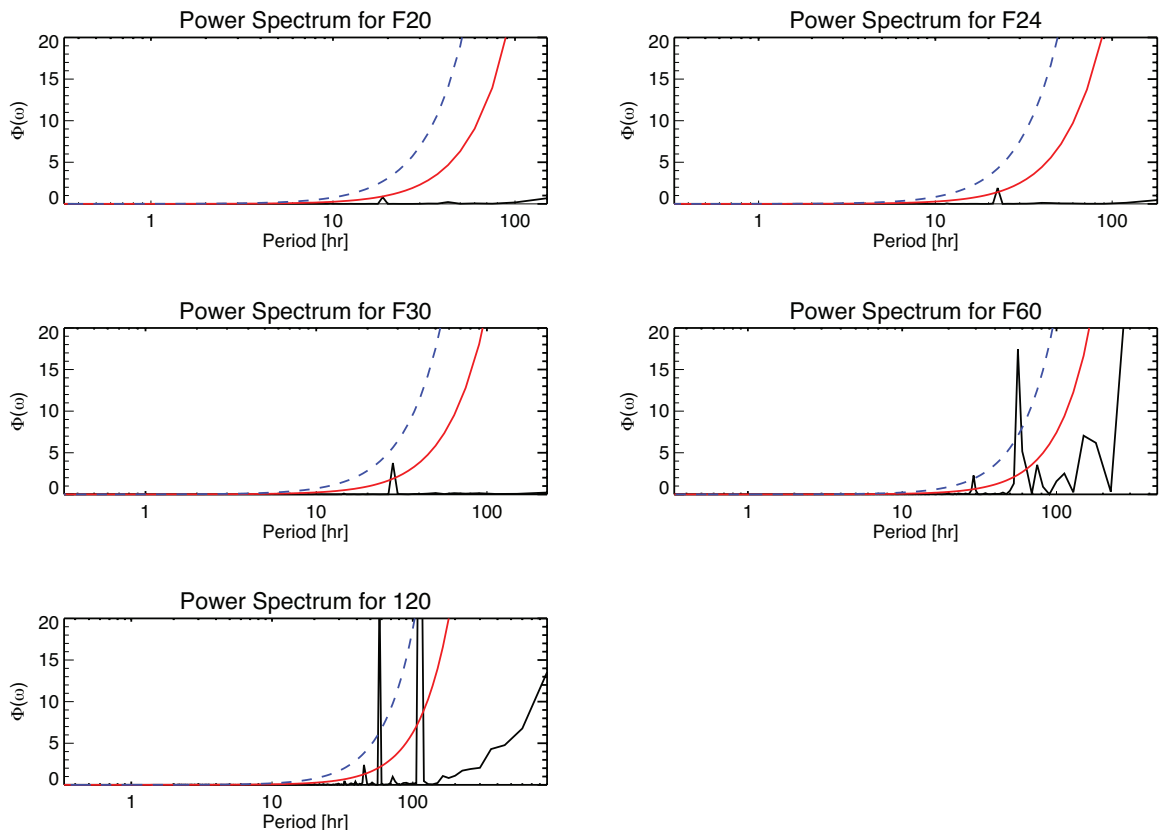


Figure 5.16. Power spectra for pseudoadiabatic CAPE for the noted simulations. The red curve is indicative of theoretical red noise, and the dashed blue curve shows the 95% significance level.

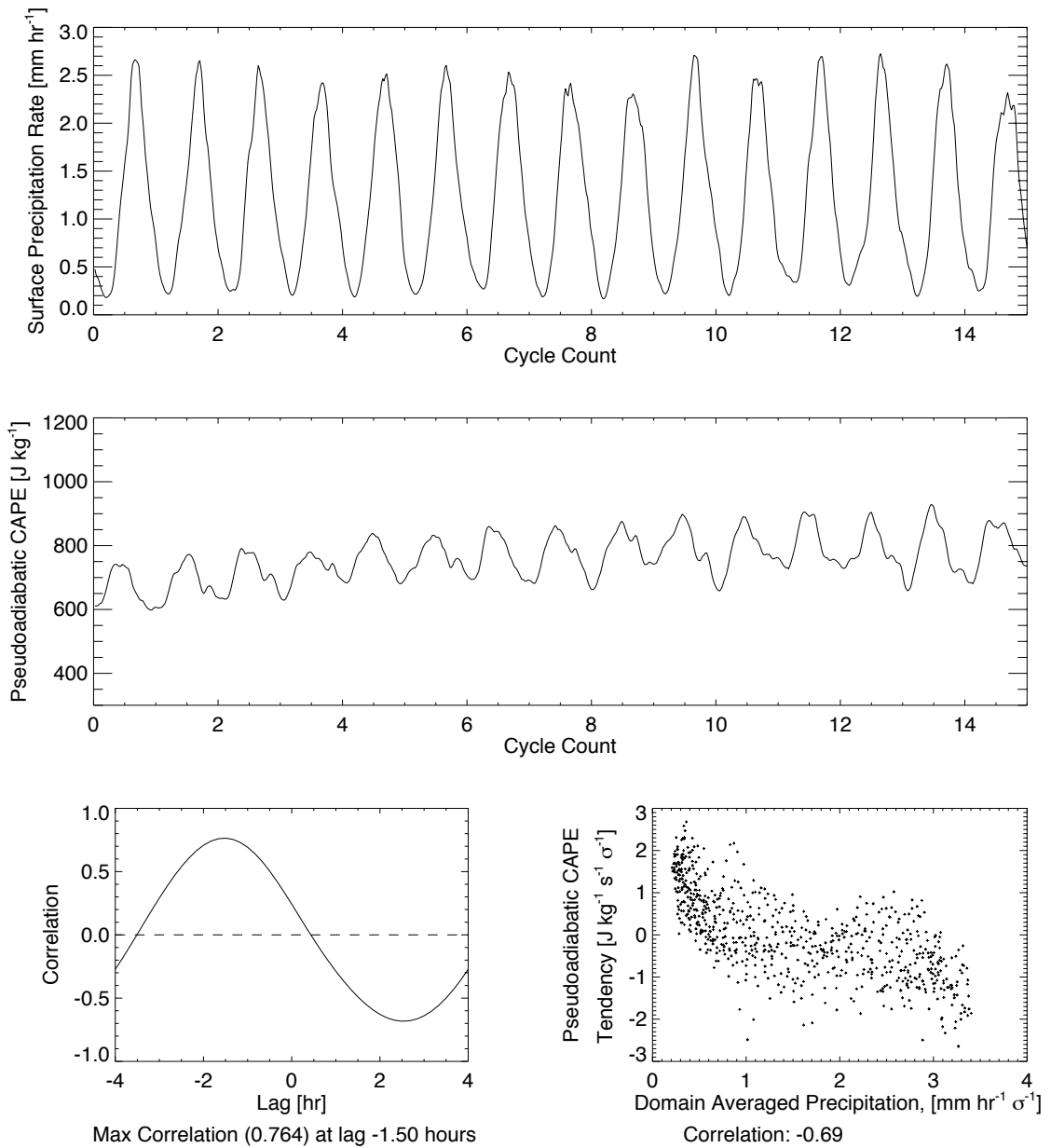


Figure 5.17. Time series of surface precipitation rate ,(top) pseudoadiabatic CAPE (middle), their lag correlations (bottom left), and a scatterplot and correlation of the normalized CAPE tendency and precipitation (bottom right) for the F08 simulation.

the maximum correlation lag is found at -1.5 hours, meaning that the CAPE peaks 1.5 hours before of the precipitation maximum. It is also interesting that in this case, the domain-averaged precipitation is negatively correlated with the CAPE tendency. Perhaps

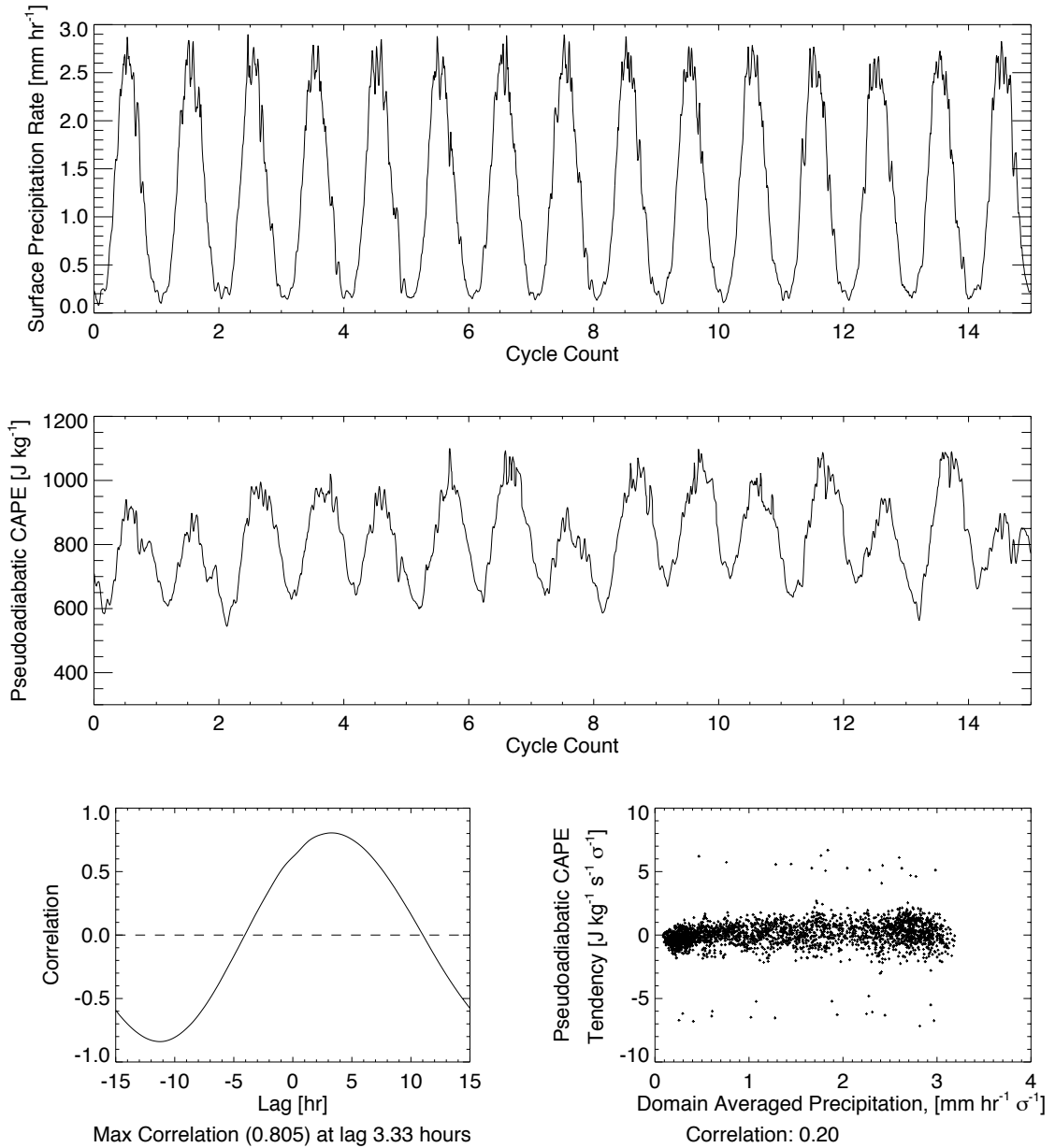


Figure 5.18. As in Figure 5.17 but for the F30 simulation.

this is indicative of expending CAPE to create convection. However, a very different picture emerges from the F30 analysis. In this case, the maximum in precipitation rate precedes the maximum in CAPE by three and one third hours. Additionally, the correlation between the CAPE tendency and the surface precipitation rate is almost non-existent. The correlation coefficient is 0.20. When the CAPE did change significantly in either di-

rection, there was about equal chance of getting light or heavy precipitation. The same is true for very small variations in CAPE. For the F30 simulation, one can see precisely where this data is coming from. Both the CAPE and precipitation transitions are rapid and their more extended maxima and minima tend to coincide with the other's transition. So, when the precipitation is falling off, for instance, the CAPE is temporarily settled into a maximum.

The final two figures summarize this correlation analysis. When each of the periodic forcing simulations are analyzed, their results show a striking pattern. The correlations between domain-averaged precipitation and pseudoadiabatic CAPE tendency, when plotted against the forcing period (on an uneven scale) appear to form a sine wave (Figure 5.19). When the forcing period is short, there is a negative correlation, and when it is longer the correlations becomes slightly positive, though very near zero. A very similar structure emerges when plotting the maximum correlation lags (Figure 5.20). For shorter periods, the CAPE leads the precipitation, and for longer periods, the reverse is true.

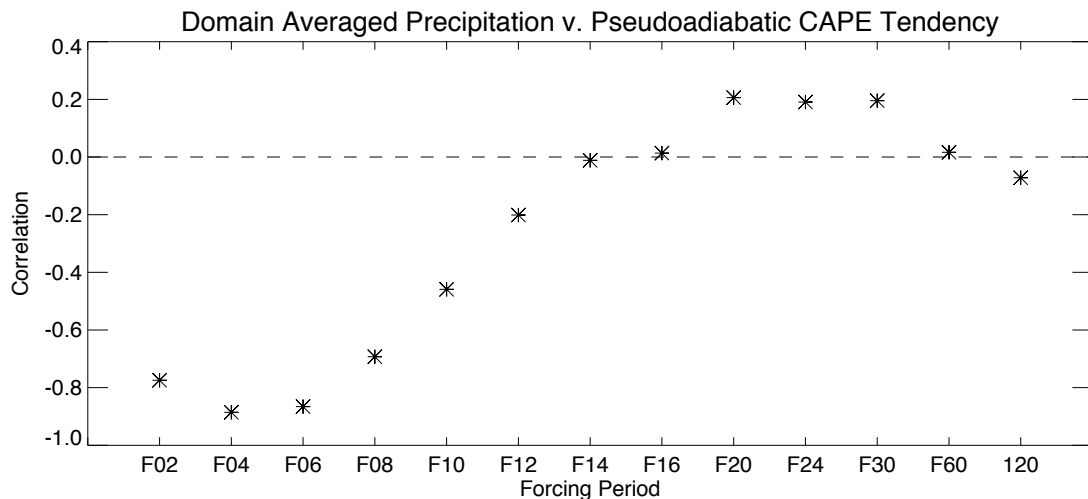


Figure 5.19. Correlation coefficients versus forcing period for domain averaged precipitation and pseudo adiabatic CAPE tendency.

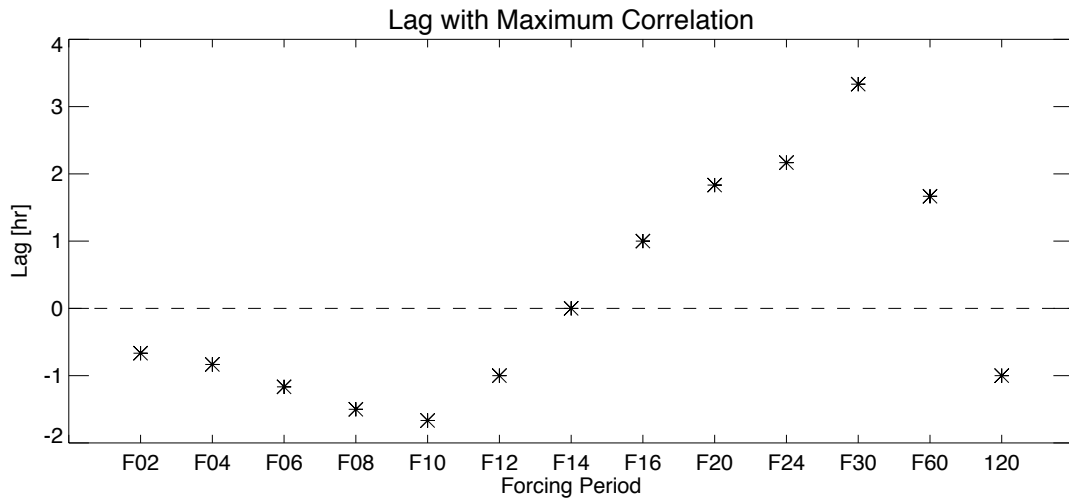


Figure 5.20. The maximum correlation lag between domain averaged precipitation and pseudo adiabatic CAPE tendency plotted versus the forcing period.

These seem to be very peculiar and non-intuitive results. It was expected that the relationship between CAPE and precipitation be more consistent and robust.

5.2.3 Composite Analysis – Full Domain

We will now investigate the way in which a suite of convection-related variables interact with the various periodic forcing lengths, as well as differing averaging areas (subdomains). The ultimate reason for running multiple instances (realizations, cycles) of the same periodic forcing was to composite the results of each of the 15 cycles of the forcing to obtain reasonably robust statistics for each particular case of forcing periodicity. It is assumed that to a reasonable approximation, each cycle in an individual simulation is identical, save for slightly differing initial conditions. In this way, the method is very similar to running an ensemble of simulations. See X92 for an example of the same approach.

To begin, the specific methodology for this task was to separate the 15 cycles in each of the thirteen simulations for each considered variable (usually a domain mean) and to average the results across the fifteen realizations. From this, a valuable and easily obtainable parameter, the standard deviation across the cycles (realizations), has been determined. This can be interpreted as a measure of the nondeterministic behavior of simulated systems, given that each realization is initialized with similar conditions, as is done in ensemble modeling. It should be made clear that this is not the standard deviation of a given spatial atmospheric variable field at a point in time. Such a measure would be a more direct measure of subgrid-scale variability, which is interesting but not exactly helpful under the auspices of creating a stochastic parameterization. Operationally, GCMs only give a single (mean/bulk) value for a grid point. For a stochastic parameterization based on the results of this paper, that value could imaginably fall in, and be randomly selected from, the likely distribution of means bounded with respect to standard deviation of the means of each realization for a specific large-scale forcing, thereby approximating the stochastic effect of nondeterminism.

Immediately, when I think of convection, I think of the ensuing flood of precipitation. Thus, the first convective-response variable we shall explore is the surface precipitation rate, which in the case of the tropics is most frequently all rain.

Returning briefly to the top-right panel of Figure 5.6b, we see the time series of the domain averaged surface precipitation rate for F24. Two features of interest are that the precipitation appears to lag the forcing slightly and that there is considerable scatter deviating from what one might expect from strict equilibrium in response to the large-scale forcing in the bottom-right panel of the same figure. Clearly, the system is not in

strict equilibrium; however, it may well be within the expected range variability about equilibrium (variations expected from statistical equilibrium) based on viewing this result alone. Interestingly, the variability in the time series from this set of simulations appears to be much less than that obtained from the two-dimensional simulations of X92. I suspect that this is at least partially due to their far smaller domain area whose mean, determined by a far smaller sample size, would be much more sensitive to extreme convective events. In fact, they have an example of this in their Figure 5 (panels (b) and (c), referring to simulations Q02 and Q04), which in comparing identically initialized simulations on two differing domains (512-km and 1024 km) shows that the nonsystematic fluctuations (standard deviations) of the mean surface precipitation rates become less pronounced in the case of the larger domain. This is most clear near the peak of the forcing. Complementary results from this 3D study will be addressed later on.

These results allude to the fact that 2D models are likely to be deficient when compared to 3D models in terms of variable statistics beyond order one. Often, some seek to justify 2D simulations because they are computationally affordable on the required domain size, whereas 3D simulations are not. Certainly this was much more acceptable reasoning two (or even one, e.g. Khairoutdinov and Randall (1997)) decades ago, but given the relative ease and simplicity of contemporary computing, it's not much of an excuse anymore.⁷ There will always be fundamental differences when considering the two options. For instance, when convection is random or clustered, the thermodynamic soundings produced by 2D vs. 3D tend to diverge significantly. Spe-

⁷ Of course, the goal of the study will take precedence. Some statistical characteristics will be in agreement, especially when 3D convection is two-dimensionally organized as, for example, in squall lines.

cifically, Petch *et al.* (2008) show that results in 2D simulations differ significantly from 3D simulations in the low level humidity structure and associated fields due differences in entrainment processes, which lead to substantial differences in both cloud amount and moisture transport by the clouds.

Zeng *et al.* (2007) suggested that the sensitivity of buoyancy damping to dimensionality can give rise to fluctuations in precipitation in 2D that are not present in 3D simulations. This may even be part of the reason that the variability in precipitation in X92 was greater than will be seen in this thesis. The greater standard deviation shown by X92 will likely have some contribution from the smaller sample size involved (their 9 to my 15). Note, though, that we are not talking about the standard deviation of a field, but the standard deviation of the mean of a field. The idea that the standard deviation exhibits this behavior is a common misconception. The standard deviation does not decline as the sample size increases, however, the standard error (standard deviation divided by the square root of the sample size) does. One way to think about it is that the standard deviation is a measure of the variability of a single item, while the standard error is a measure of the variability of the average of all the items in the sample. What does happen is that the standard deviation becomes more stable and robust as the sample size increases.

Compositing the realizations for each simulation, we have obtained a series of plots (Figure 5.21) that describe the statistics of the surface precipitation rate as ascertained from the entirety of the domain. Here, only the results for F02, F08, F16, F30, F60, and F120 will be shown for most considered variables in the composite analysis. This selection of simulations should provide a sufficient representation of the differences that appear as the length of the forcing period is increased. Results for the remaining

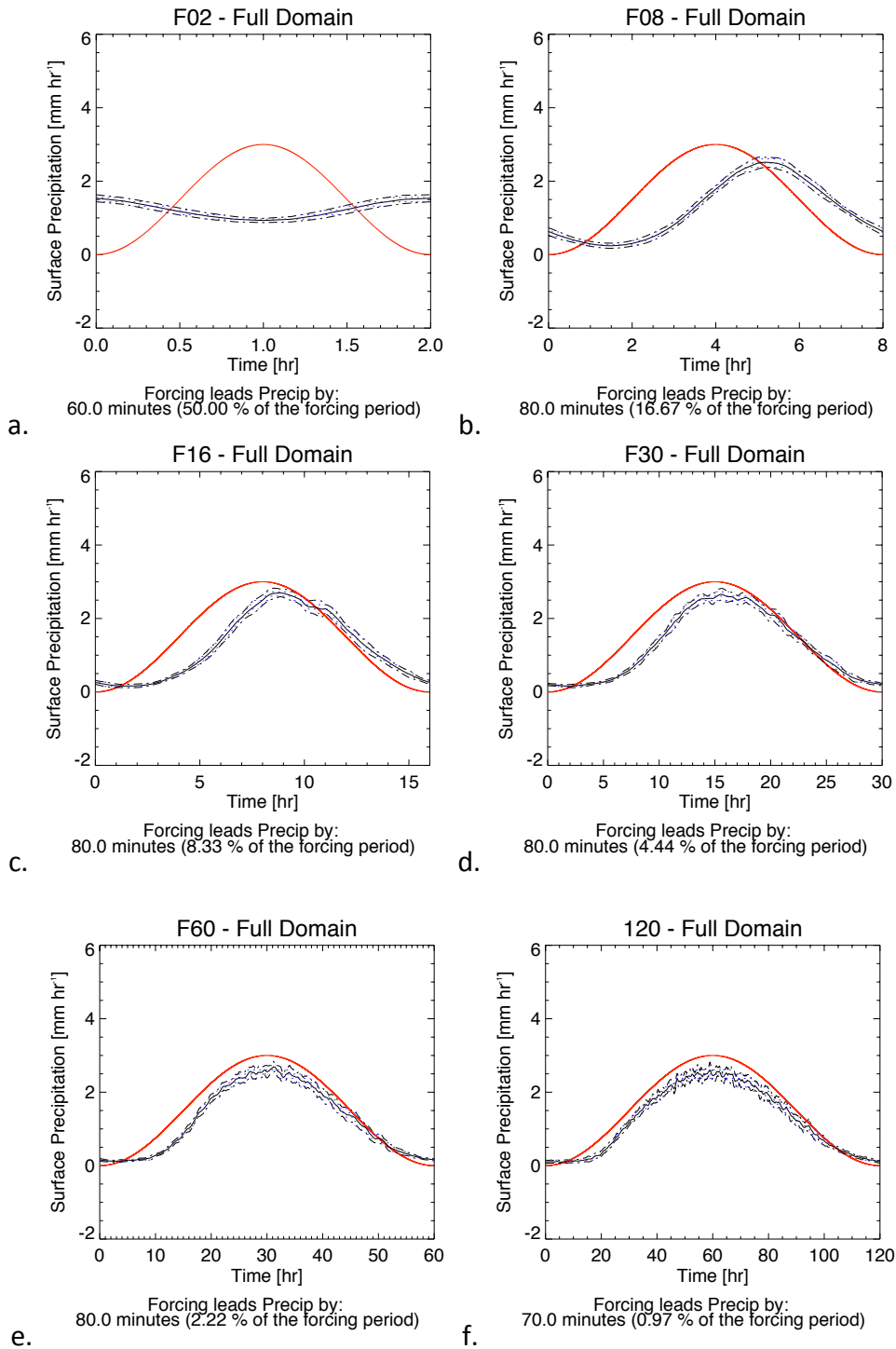


Figure 5.21. Whole domain average statistical composite of surface precipitation rate for the noted simulations. The black curve is the composite mean. The blue hash-filled region bounded by the dot-dash line denotes the ± 1 range of standard deviation across 15 realizations. The red curve represents the timing and relative magnitude (0-100%) of the large-scale forcing and is only for reference; no specific values are implied.

simulations have also been created, but in the interest of space, they have been omitted.

Compared to the raw time series, the data in the composite plots are much more smooth, as the variability around the mean has been averaged out to some degree. This is less applicable to the composites of the long period (F60, F120) simulations that continue to show a lack of smoothness in the means. This is due to the higher magnitude variability that was shown in some of the later snapshot figures in Section 5.2.1 that occurs due to more time being available at high forcing to repeatedly organize mesoscale convection causing sharp swings in the mean. It is expected that this variability in the mean curve would vanish as in the shorter period simulations (F02-F08) with the inclusion of a greater number of realizations. However, the computational and temporal cost (not to mention the storage costs) to reach that number of realizations for a cycle of 120 hours seems excessive to clean up a feature that has already been significantly smoothed. Clearly, the variability about the mean has been significantly reduced through averaging, as shown by the very thin blue region (standard deviation) bounding the mean curve. Note also, that the standard deviation does not change significantly with changes in the forcing period length for this whole domain case.

The second very important feature of this set of composites is both visually apparent and spelled out in the text of each panel of Figure 5.21. This is the aforementioned phase lag between the precipitation and the forcing. It mainly occurs for a combination of two reasons. One is the systematic phase delay shown by X92 (their Figure 9) to be caused by the presence of mesoscale organization. This feature is evidenced by the somewhat kinked nature of the mean precipitation curve, in which the rapid onset of precipitation and more gradual decline is characteristic of the life cycle of mesoscale con-

vective systems (X92, Abdullaev *et al.* 2009). The other reason is that the forcing period and the convective adjustment time for cumulus clouds (~1.5 hours) are near the same order of magnitude. Chiefly, this means that the forcing is changing too rapidly for the convection's latency. Disregarding F02⁸ for which this second influence is dominant (especially since there is no time to generate strong convection, let alone organized convection), we see that in each of the remaining cases, the forcing leads the precipitation by ~80 minutes, very near the suggest convective adjustment time stated above. As the length of the periodic forcing is increased, the relative lag decreases, while the absolute lag remains approximately constant. This measure was determined by finding the maximum lag correlation between the composite mean precipitation and the normalized periodic forcing. More than anything else, this is simply a measure of the separation of the two maxima, while the mesoscale modulation effects are specific to the somewhat kinked nature of the increasing leg of the precipitation field as has been determined by X92.

An additional feature that will continue to be visible in the coming figures is the plateau or minima immediately following the primary maxima in the F16 simulation. This decline, while reminiscent of some composites from X92, seems to be purely a feature of this particular simulation (Figure 5.21c). Looking back to the upper right panel of Figure 5.7a, one can clearly see that this small minimum in the mean is caused by that feature being present in a handful of cycles of the series. Its recurring appearances point to some secondarily fundamental process involving the temporary rapid breakdown of

⁸ The convention used in the figure text that “The forcing leads the precipitation by...50% of the forcing period” is based on the trend that the forcing always leads the response in subsequent simulations. It is entirely valid, statistically, to interpret this figure as showing the peak response leading the peak forcing. In a physical sense, however, such a relationship seems unlikely.

convection following its peak. The fact that it is not present in all cycles, however, leads to the conclusion that it is either an element of non-determinism or possibly the result of a feature with a timescale that interacts prominently the dominant timescale of F16.

Figure 5.22 shows the same analysis but for cloud fraction. Apparently, not all suspected convection-representing variables are created equal. The cloud fraction is not modulated in the same fashion as the precipitation. Here, for F02, the result is similar with the cloud fraction being 90 degrees out of phase with the large-scale forcing. Contrastingly, the two are almost exactly in phase for the F08 simulation, and the cloud fraction actually *leads* the forcing in all longer period simulations. The reason for this seems to be partly due to remnants of non-precipitating (most often cirrus or stratus-type clouds) clouds being left over from the previous convective realization. Referring back to Figure 5.8 where the F120 forcing is at its minimum, there is nearly zero precipitation, but a significant amount of cloud cover remains in the domain. The following peak in cloud cover corresponds to the increasing forcing of the following cycle, and the following rapid cloud cover decline and plateau corresponds to an abrupt organization of convection that has the effect of clustering clouds into more densely packed regions of higher clouds exhibiting more intense convection and precipitation. In this way, areal cloud cover does not immediately correspond to more intense convection. This is painfully obvious when you consider the differences in the horizontal extent of stratus versus cumulus regimes.

Nonetheless, this raises an interesting question. Why would the cloud fraction lead the forcing by greater relative *and* absolute amounts with increasing period lengths

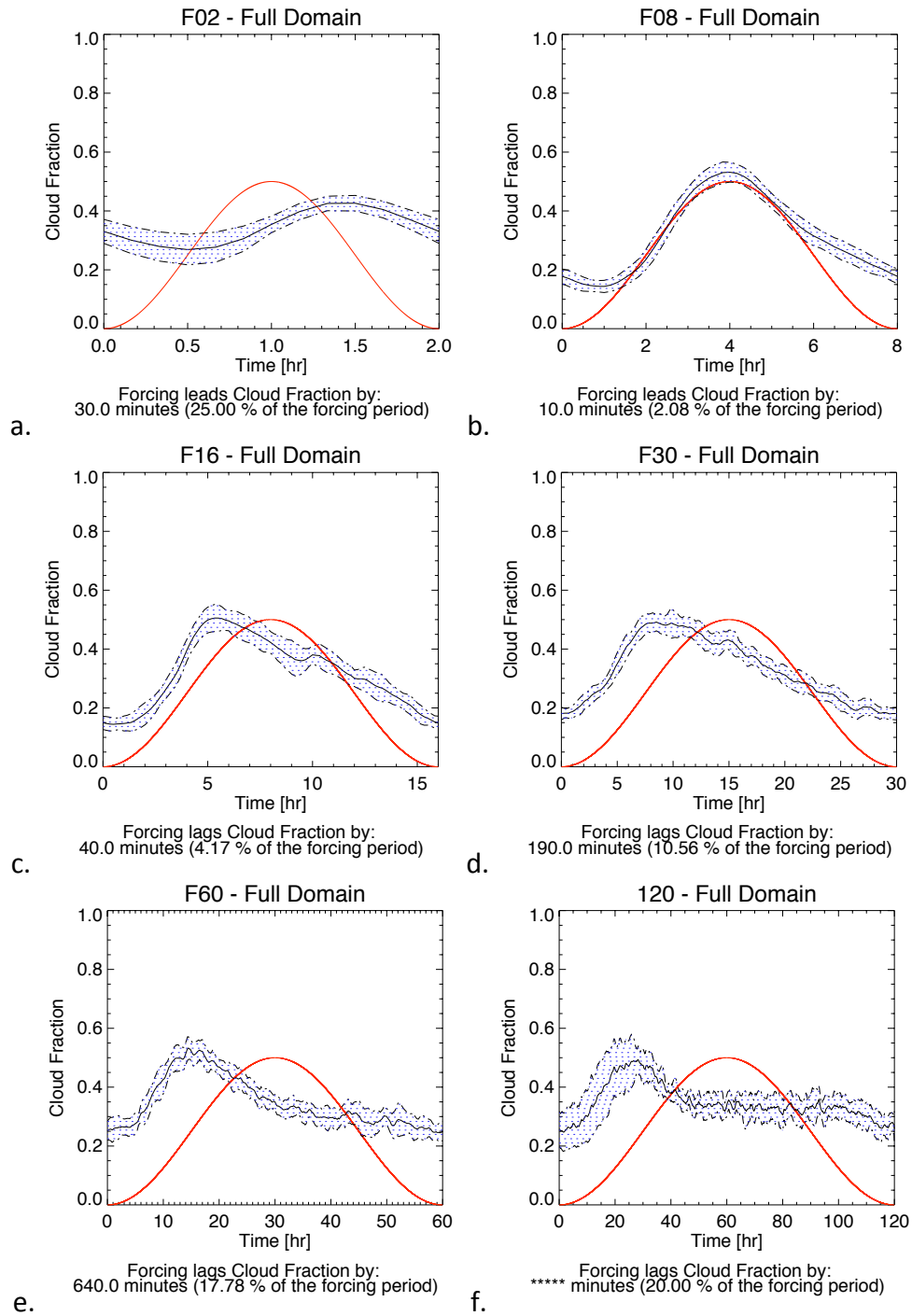


Figure 5.22. As in Figure 5.21 but for cloud fraction. See text for missing values denoted above by asterisks.

for each and every cycle?⁹ (The absolute measure for the F120 case, by the way, is 24 hours.) Looking at the data in Figure 5.22, the relative lag appears to be approaching a limit as the forcing period becomes longer, which leads one to suspect that the relationship is some function of the rate at which the forcing is changing. As the rate slows, the relative lag becomes more consistent relative to the forcing but still earlier in an absolute sense. Comparing panels (c-f) in Figures 5.21 and 5.22, the rapid increase in the precipitation rate always seems to correspond to the sudden decrease in the areal cloud cover indicating, as discussed, the transition to greater mesoscale organization. The lags for the cloud fraction were calculated in the same fashion as for the precipitation; however, the correlation to align the maxima in the curves has a different meaning in this case. Here the lag time seems to indicate what we could perhaps call a “mesoscale adjustment time” as the peaks in cloud fraction immediately precede mesoscale organization.

The conclusion to be gleaned from this is that the more rapid the rate of increase of the large-scale forcing, the more quickly the convection organizes in an absolute sense. This seems to be true with a few caveats. The rate that is important is the actual acceleration of the [K day⁻¹] value rather than the normalized rate of change. This should be verified in the future with a simple scaling of the maximum permitted large-scale forcing. It may be possible to define the process of convection organization by the steepness of the initial ascent of the precipitation rate and the corresponding initial descent of the cloud

⁹ One might even question whether this is the correct interpretation. One could take the view that the cloud fraction maximum preceding the forcing maximum is actually a heavily lagged response to the previous forcing cycle. However, one look at the right, center panel of Figure 5.8, which begins at the first iteration of the simulation, rather than 300 hours into the simulation as in corresponding figures, shows that this cannot be the case. The early maximum feature is present in the first realization, and its position relative to the forcing does not vary significantly.

fraction. If the slopes of these parameters are below some threshold, mesoscale organization is not likely to occur, or at least it will not occur consistently. For panels (a & b) in Figures 5.21 and 5.22, this is likely to be the case. Rapid forcing changes did not allow convection to organize, and there is therefore no steepness in the precipitation or cloud fraction curves. To generalize, for mesoscale organization to occur, the forcing must change rapidly, but not too rapidly (as in these two cases). Since this idea has been formed out of one isolated set of simulations, it would likely be worth the effort to reproduce the general form of these results under different conditions (vertical wind shear, etc.) and on a large enough domain to satisfactorily isolate the mesoscale features numerically before trying to assign a quantitative value to the hypothesis.

Another variable that behaves similarly to cloud fraction is non-precipitating condensate (NPC, Figure 5.23), which is defined here as the vertically integrated sum of cloud water and cloud ice. The standard deviations about the mean remain fairly constant for all period lengths, though they tend to be slightly larger when the mean variable is at its maximum, as was the case for precipitation (though hardly noticeable) and cloud fraction. This follows from the standard deviations scaling with the mean in the equilibrium simulations in Section 5.1. There is even the repeated tendency, as shown in panels (a) of Figures 5.22 and 5.23 (See also panels b & c of Figure 5.2), for the standard deviation to scale greater than the mean when the forcing or response is very low. Though the decline of cloud fraction correlates better with the rapid increase in precipitation that, together, indicate mesoscale development, there is a similar correlation with the peak and initial decline of the non-precipitating condensate variable. This occurs later relative to the forcing, but that seems logical, as cloud fraction (cloud horizontal extent) would tend to

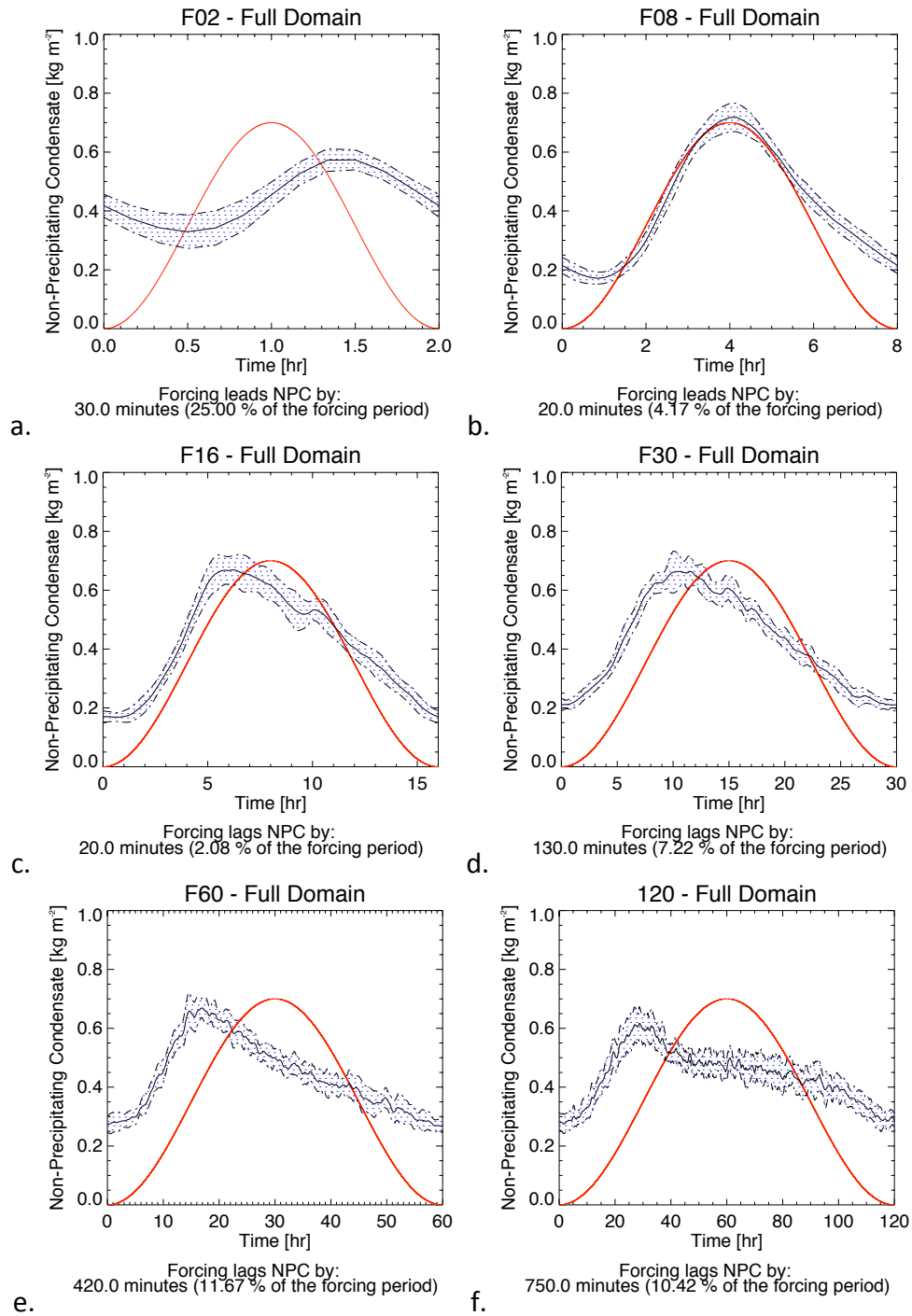


Figure 5.23. As in Figure 5.21 but for non-precipitating condensate.

peak before the non-precipitating condensate value (cloud vertical extent) on the general basis of considering a single domain value.

A further variable that has similar features as those seen in the case of NPC is the

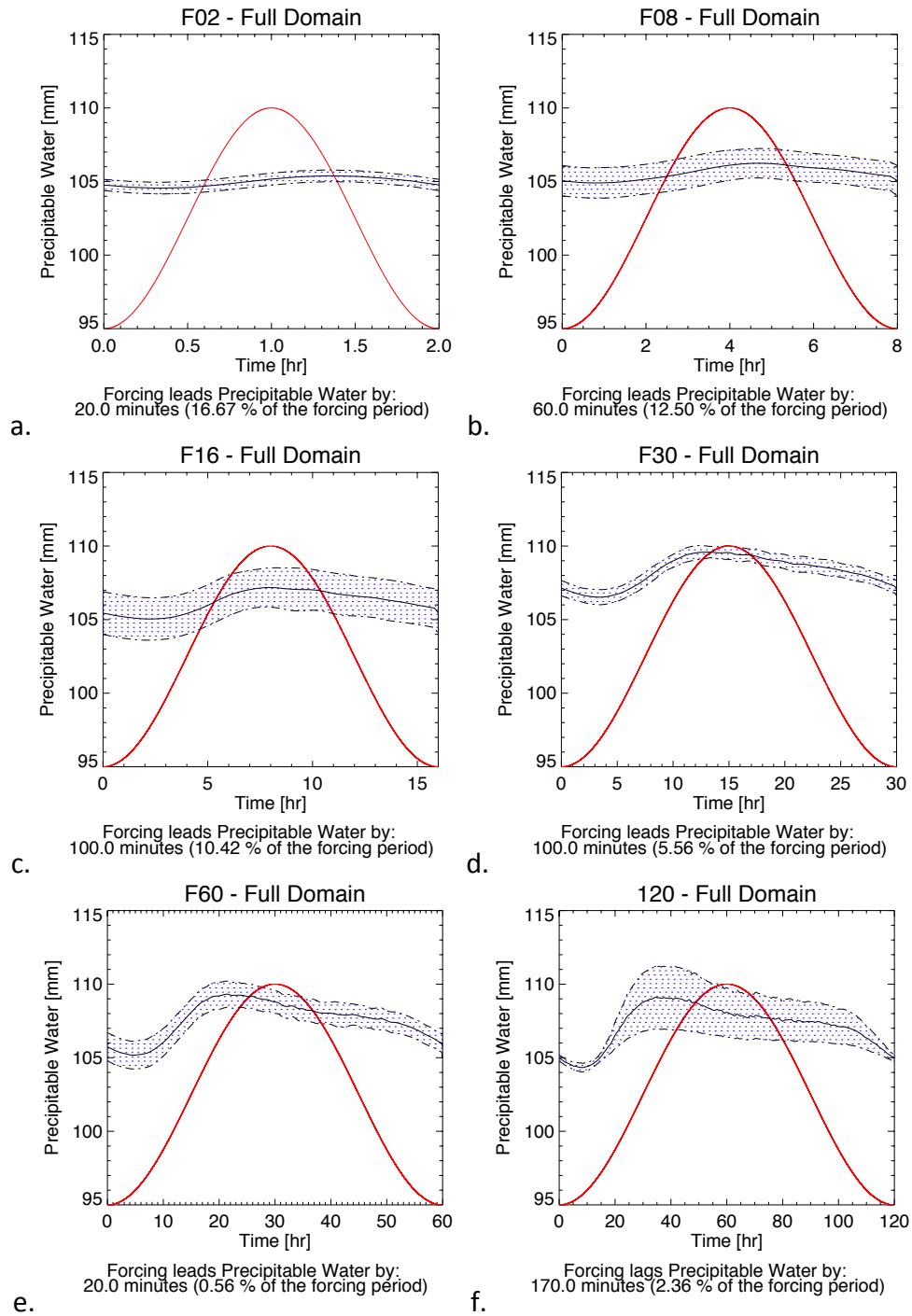


Figure 5.24. As in Figure 5.21 but for precipitable water.

column precipitable water, defined as the total mass of water vapor over a column. While there are some qualitative similarities, there are also some interesting differences. This is shown in Figure 5.24. The first thing that one may notice is that the precipitable

water is a much less variable quantity. The second point of interest is its magnitude, which is very large in comparison to the global average, which is about a quarter of what is seen here. Bear in mind, though that the forcings used in this simulation are extremely strong and are the main reason for this high value. Similarly to NPC, the composite mean curve for precipitable water takes the shape such that an early maximum is seen followed by a sort of extended, plateaued maximum. In this case, however, the initial maximum is not as pronounced or separated from the plateau. Because of this, the lag correlation analysis does not conclude that the precipitable water curve is leading the forcing at any time. Instead, the forcing is reported to be leading the precipitable water in each case, much like it has been reported for the flux variables. Physically, this appears to represent a build-up of precipitable water to a critical level prior to precipitation events that deplete that store. Though conceptually, one would think of precipitable water as a storage variable, the analysis here seems to place the variable in limbo based on its characteristics in comparison to more concrete examples of flux and storage variables. That is, it has characteristics of both.

Another variable of interest is the cloud mass flux. Figure 5.25 shows the results of the composite analysis across the full domain for the cloud mass flux variable approximately located at the 2.5-km level. In this case, the cloud mass flux is a horizontal domain average of the sum of cloud liquid and ice water within a layer multiplied by the vertical velocity at that layer. Negative values are possible, and positive values refer to movement of cloud liquid and ice water upward. The results here are very similar to those for surface precipitation (Figure 5.21). In each example shown, the standard deviation about the mean for each realization is small, indicating the presence of a relatively

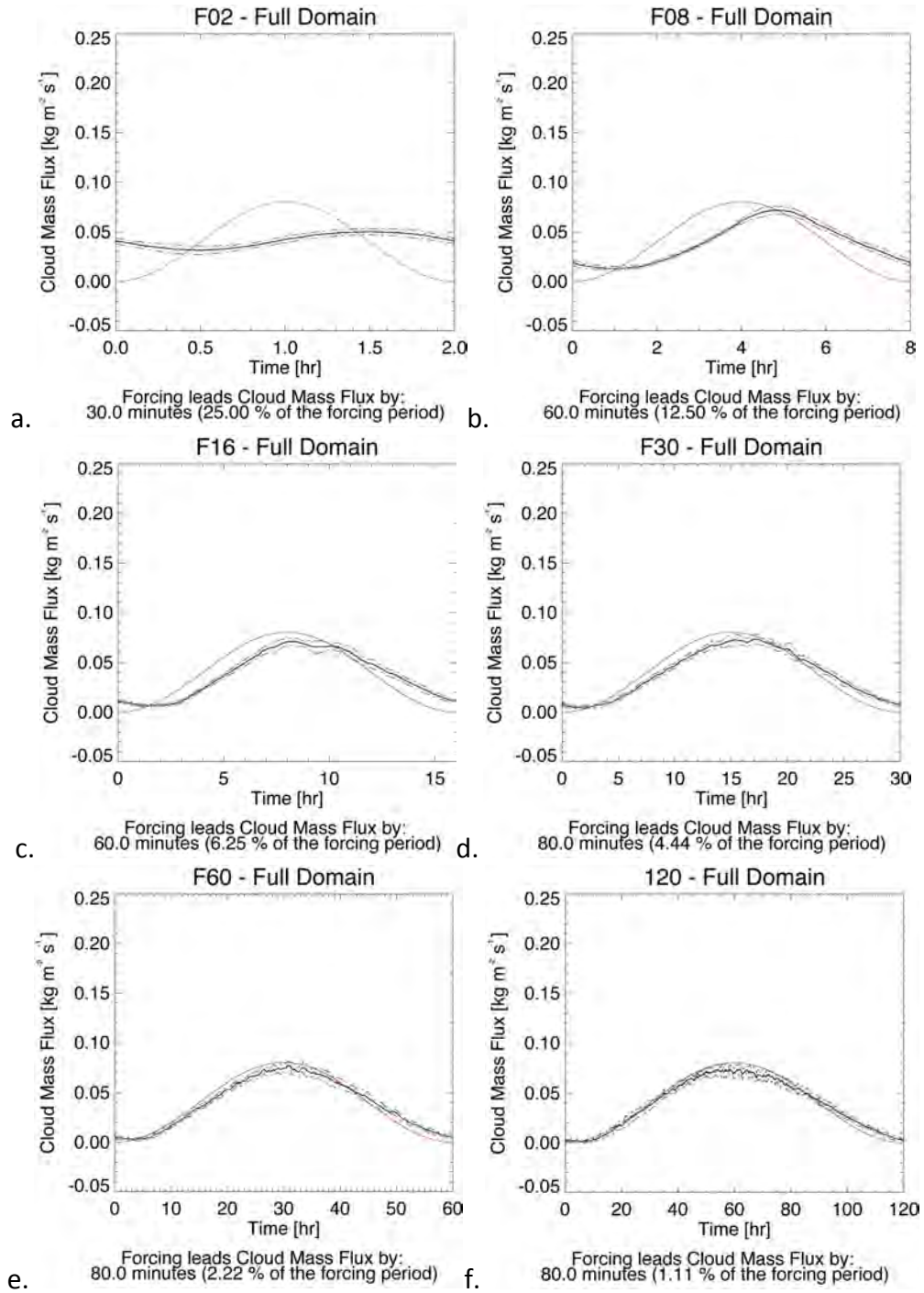


Figure 5.25. As in Figure 5.21 but for cloud mass flux through the ~ 2.5 -km level.

high level of determinism. Further, the response to the forcing as measured by the cloud mass flux moves from being 90° out of phase at very short forcing periods (Figure 5.25a) to being only $\sim 1\%$ out of phase by the point the forcing period has been increased to 120

hours (Figure 5.25f).

As a departure from what was seen in the surface precipitation composites, the absolute lag is slightly more variable between simulations. Specifically, it is about 20 minutes shorter for the F08 and F16 cases and 30 minutes shorter in the F02 case. This may simply be an artifact of the variable, such that cloud formation precedes rain production or that the average upward cloud mass flux is significantly weakened by the coincident maximum of falling precipitation, thereby effectively making the maximum occur earlier. It is also possible that this feature is absent from composites with longer period forcings because there is likely to be greater and extended overall cloud presence as evidenced by Figure 5.22 (d-f). Some of these additional clouds, sustained by long periods at high large-scale forcing, may not be precipitating and therefore not observing the effects of the falling precipitation.

Similar results are seen when separating the cloud mass flux variable into exclusive upward and downward components. To focus in on the more convective elements, only velocity magnitudes greater than 0.1 m s^{-1} have been considered in this case. The composites for the updrafts are shown in Figure 5.26, and the downdraft case is shown in Figure 5.27. Compared to the general mass flux composites, there is greater amplitude in both cases, especially the updraft case. The absolute lags are greater in both cases, as well, being greatest in the downdraft case, which is sequentially later. Relative lags decrease with increasing forcing period length in a similar fashion, as well. Interestingly, the maximum mean updraft mass flux very clearly increases in magnitude going from F02 to F60, though the rate of increase is unsteady. This indicates with more certainty that longer forcing periods are indicative of greater convective activity. The increase in

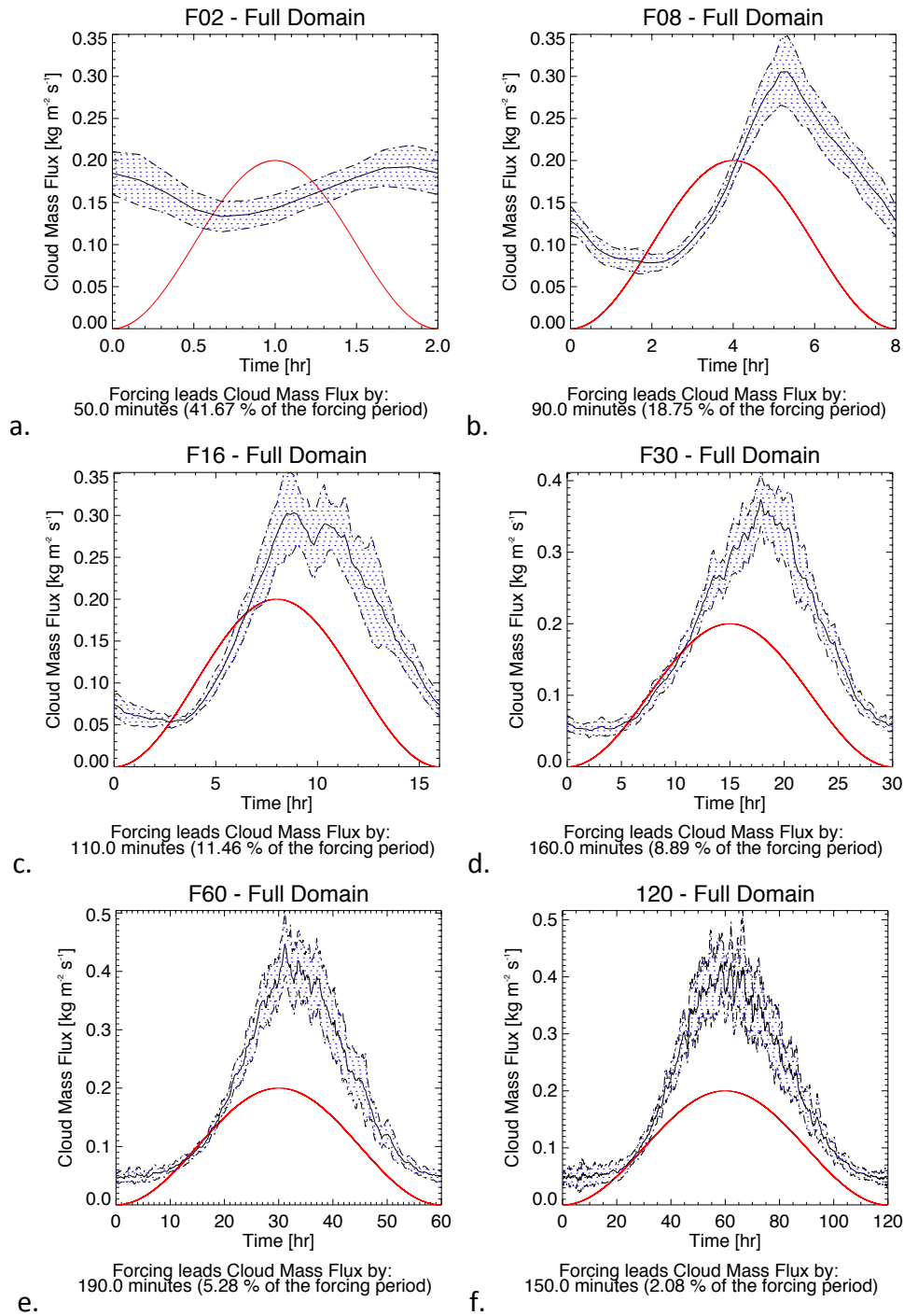


Figure 5.26. As in Figure 5.21 but for upward cloud mass flux through the ~ 2.5 -km level.

intensity is not visible in the downdraft case. It may be possible that the speed threshold was no great enough to remove the influence of the general domain subsidence. Additionally it is noted that the shape of the downdraft mean curve, which is reminiscent of

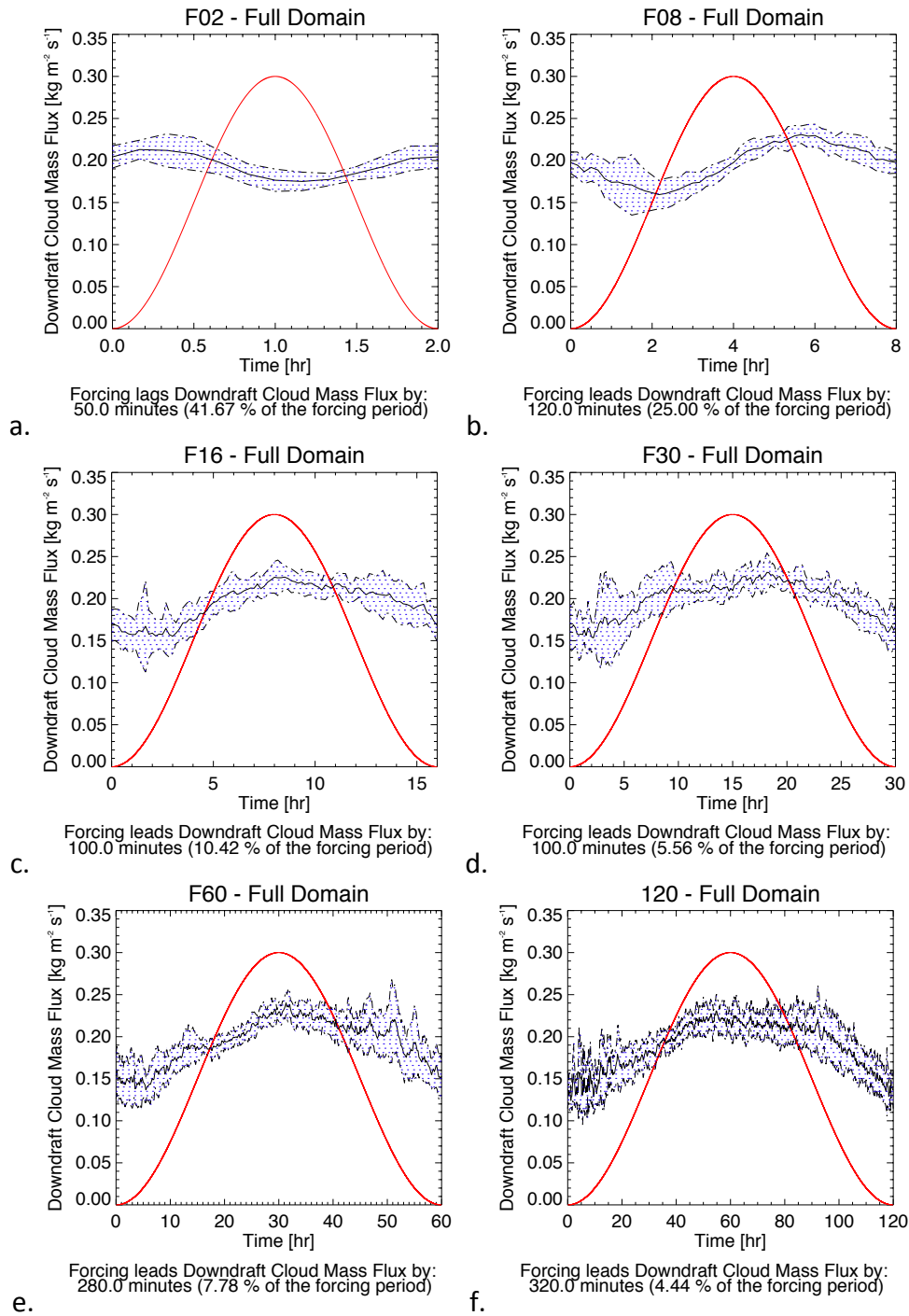


Figure 5.27. As in Figure 5.21 but for downdraft cloud mass flux magnitude through the ~ 2.5 -km level.

the storage variables, is more elongated and includes a plateau level.

One variable that is strongly related to the amount of convection that is occurring

is the integrated buoyancy flux. Here, integrated buoyancy flux, B , has been defined as

$$B = \int_{z_s}^{z_T} \rho c_p \overline{w' T_v'} dz \quad (5.2)$$

T_v is the virtual temperature in this case, and the integral is bounded from the surface to the top of the model. The composite analysis results are shown in Figure 5.28. Many of the features seen in other variables in the composite analyses are present in this case, as well. Variability, as measured by the standard deviation across realizations, is shown to scale in a qualitative sense with the mean. We also see a consistency in the absolute lag between the buoyancy flux and the forcing, though it is more tenuous than in other variables and lacks a coherent trend. The relative lag, on the other hand, shows a more consistent trend of decreasing with increasing forcing period length. Of all of the variables shown thus far, the buoyancy flux is the most in sync with the large-scale forcing, especially for longer periods. The two tend to rise and fall in proportion to one another at all points along the oscillation, without much evidence for plateau-like features.

By comparing vertical profile fields of variables, such as cloud fraction, water mass, and vertical velocity, we are able to obtain a more detailed view of what is occurring in the model. Such an analysis should aid in shedding some light upon the plateau issue that has been discussed above. First, we can see the change in the vertical distribution of cloud fraction (Figure 5.29). This data should be compared to Figure 5.22, which shows the vertical composite of these profiles. The results show that the most appreciable drop in cloud fraction is found near the 5-km level, with a thin amount of cloud just overtop of that level. This thin layer (~ 6.5 km) appears to be representative of anvil outflow, though it is not. This is actually a secondary maximum related to the freezing level.

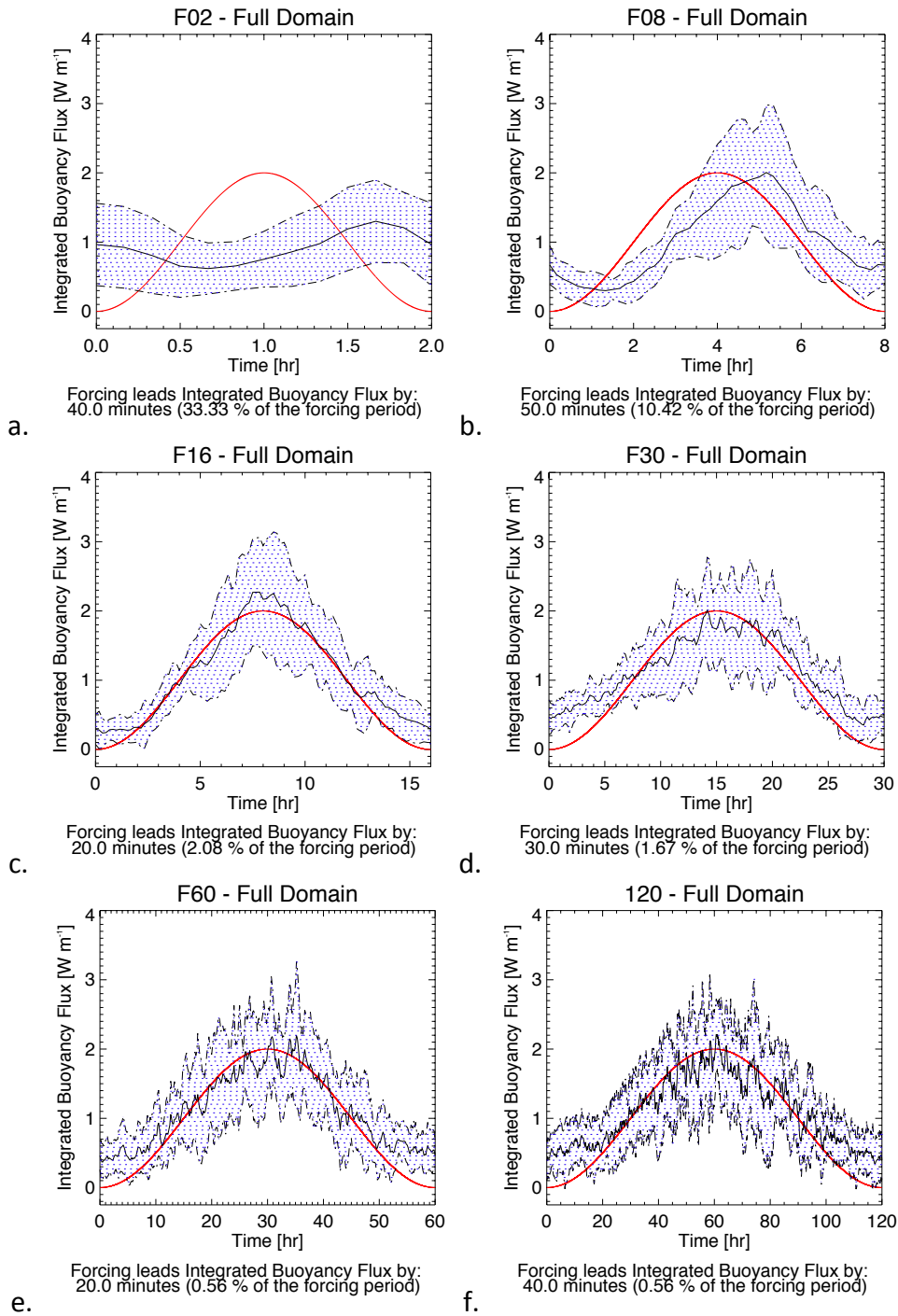


Figure 5.28. As in Figure 5.21 but for integrated buoyancy flux.

Anvil clouds are present at the 10-13 km level.

A few of the same features are more clearly visible on contours of cloud mass (Figure 5.30). The lower maximum in cloud amount is clearly visible near the freezing

level, and the upper anvil top is also prominent. However, there does not appear to be

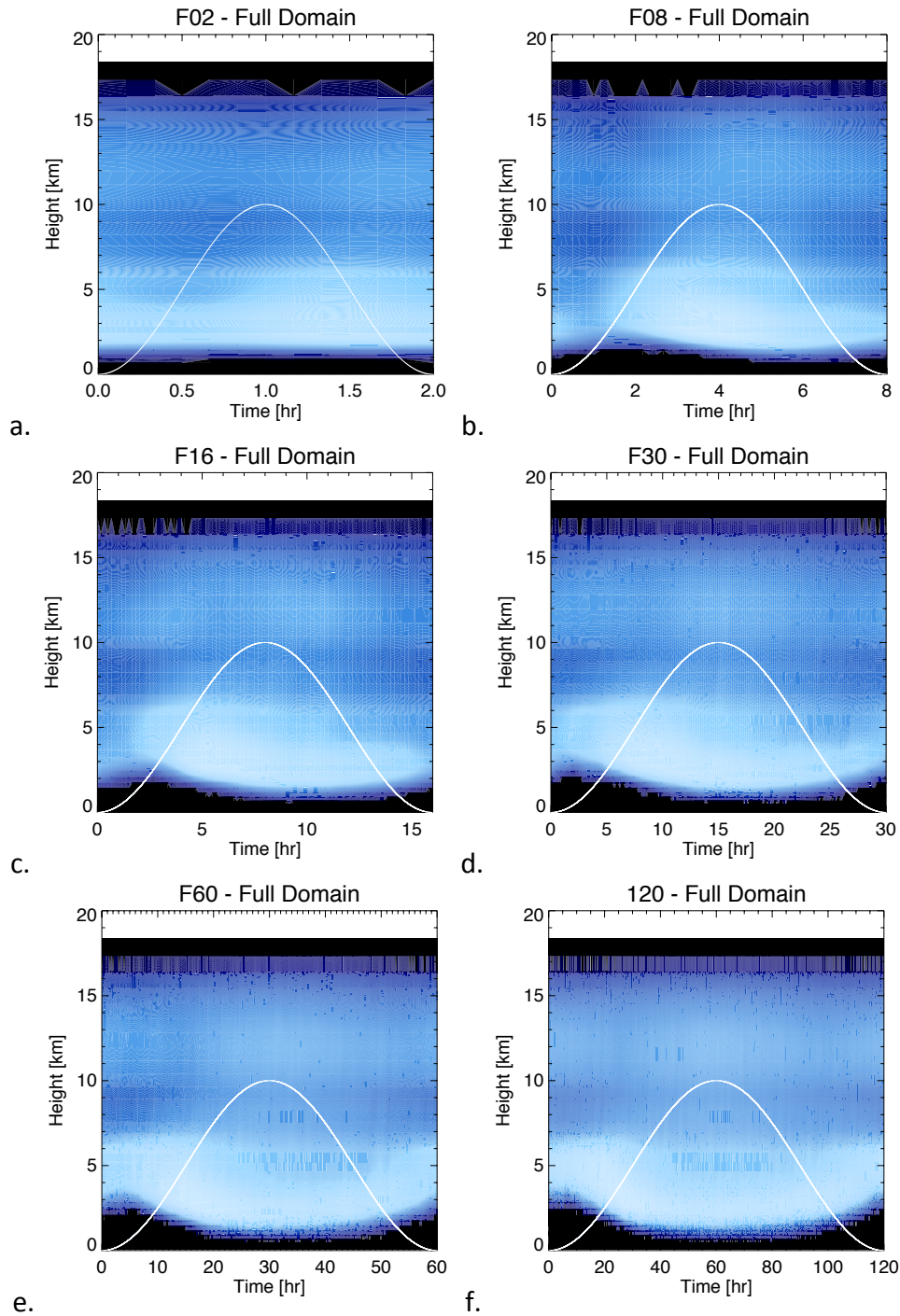


Figure 5.29. Composite cloud fraction profiles for the noted simulations. The white line denotes the placement of the normalized large-scale forcing. White indicates a greater cloud fraction, with blue indicating less. Maximum cloud fraction values at a given height do not exceed 40%.

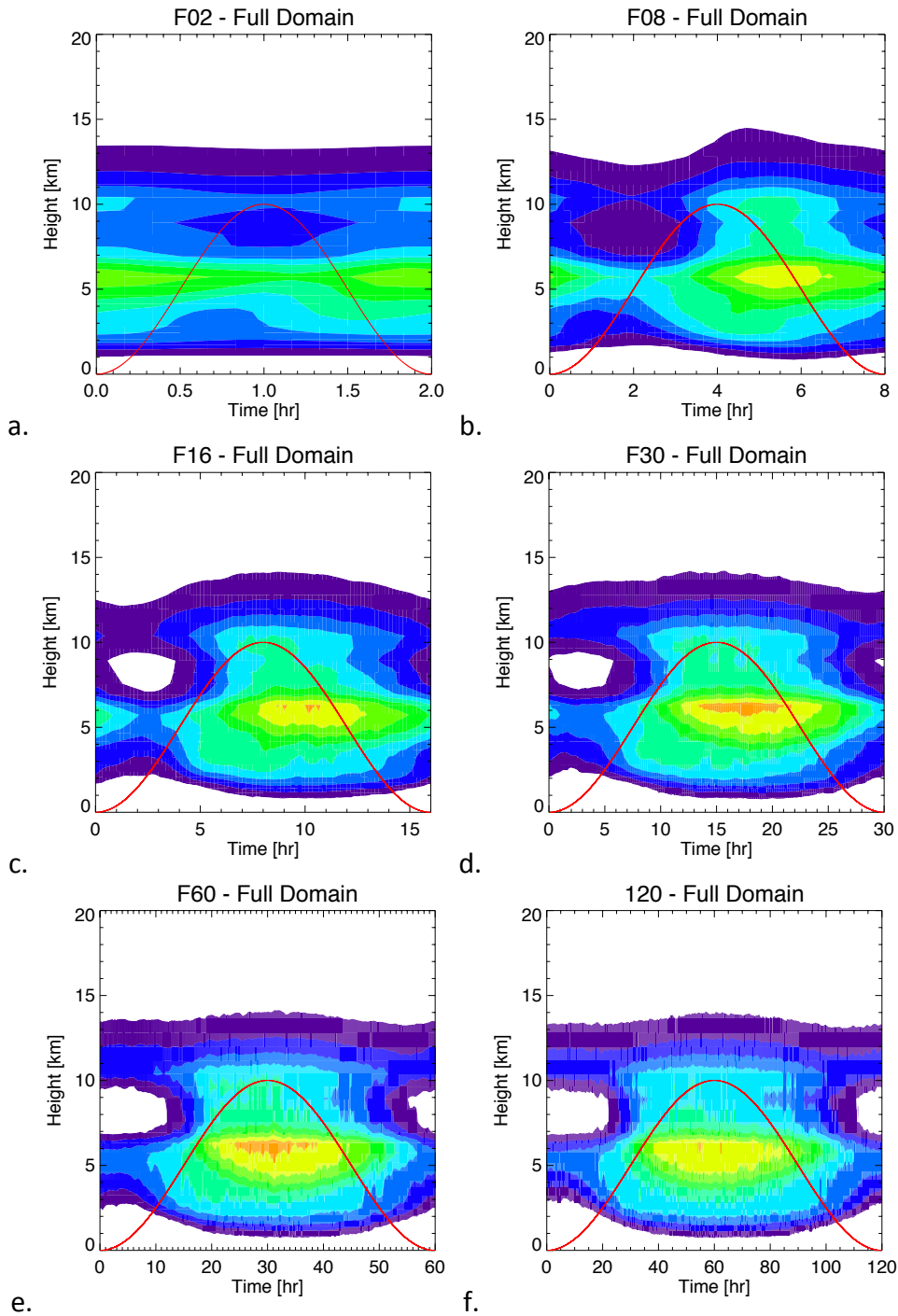


Figure 5.30. As in Figure 5.29 but for non-precipitating condensate. Here, the color scale is linear, with reds indicating large amounts and violets indicating small amounts.

any distinct minimum at 5-km in the NPC profile time series. Further there does not appear to be any visible lag in the column total. As such it is unclear as to what causes the

previously mentioned early cloud field maximum and mid-period decline. Comparison of 5.29 and 5.30, though, leads me to believe that we are seeing evidence for the accumulated effect of multiple cloud regimes within the domain. If there is reduced cloud fraction, but not cloud mass, at a given domain-averaged level, then it would be reasonable to conclude that the domain has moved into a regime of isolated convective towers from a more dominant stratiform situation. Analysis of cloud top heights (not shown) shows that there is a secondary maximum in the heights of clouds that occurs near the freezing level occurring in the early part of the periodic forcing. After that point, most clouds are very shallow. Additionally, analysis of the vertical velocity profile time series shows sequential areas of rising and sinking motion near the freezing level and in the 10-15 km height range, indicative of cloud tops at both levels.

In the course of research, it was suggested that another method of gauging the prominence of convective elements could be derived from statistical analysis of the surface precipitation field. This particular analysis involves the skewness. The skewness (a variation on the third statistical moment) is a measure of the extent to which the probability distribution function of a field is asymmetrical. Numerically, a positive skewness indicates that the distribution is skewed to the positive direction, that is, the longer tail of the distribution is toward positive infinity. The reverse is true for a negative skewness. It was suggested that the skewness of the surface precipitation might act as a proxy for what we shall call “convectiveness.”

The hypothesis was that under periods of intense convection in the domain, there would be a positive skew to the distribution of surface precipitation, since the greatest precipitation values would be greatly increased. Thus, positive skewness of the field

would indicate strong convectiveness, and the skewness could then be analyzed in composite in a similar fashion to the other convection-related variables.

These calculations were performed, and the results are shown in Figure 5.31. Given the hypothetical interpretation given above and the results for the previously discussed variables, the results may be somewhat surprising. In each of the previous cases, the F02 mean was always anticorrelated, with respect to phase lag, to some extent with the forcing signal. In this case, the mean skewness does not lag the forcing at all. Regarding results from longer period forcings, the skewness and the forcing tend to become increasingly out of phase. One additional feature to notice in Figure 5.31 is that the lag times are different from those for the other variables. In the relative sense, they are approximately equal to 50% minus the percentage lag in the previous variables, and the indication of lag or lead should be swapped. This is to say that the skewness signal is out of phase with the means of the previous variables.

Technically, we know for certain that the maxima in the response and the forcing should be relatively coincident, assuming that the period of the forcing is sufficiently long. Therefore, the original hypothesis about the skewness is incorrect, and an alternate interpretation is required. But as Thomas Edison once noted, “Just because something doesn't do what you planned it to do doesn't mean it's useless.” Comparing Figure 5.21 with Figure 5.31, we see that greater skewness values are associated with lower rates of mean surface precipitation and vice versa. So let's take a moment to consider the progression of the skewness during one cycle. Skewness, being a measure of asymmetry, is highly sensitive to outliers. More specifically, the skewness is almost always greater in the case of a longer, narrower tail (think a single, unusually large outlier) than in the case

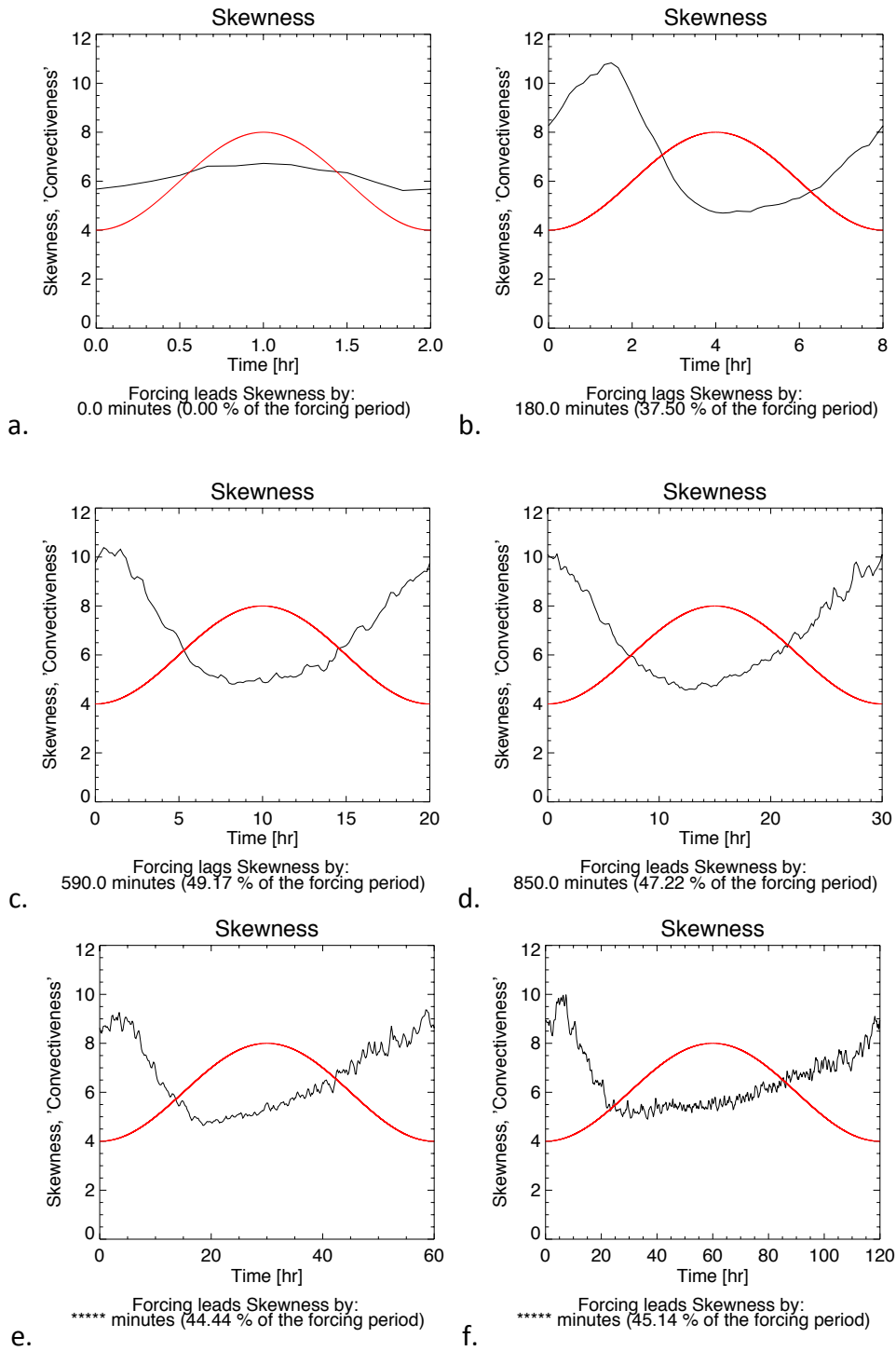


Figure 5.31. Whole domain composite of surface precipitation rate skewness for (a.) F02, (b.) F08, (c.) F20, (d.) F30, (e.) F60, and (f.) F120. The black curve is the composite mean of the field skewness. The red curve represents the timing and relative magnitude (0-100%) of the large-scale forcing and is only for reference; no specific values are implied.

of a longer, thicker tail (think two equal outliers). In the case of precipitation, being a positive definite variable that has its base at zero, outliers are generally restricted to being positive numbers that are greater than the mean.¹⁰ As precipitation increases over the domain and the mean is increased, the distribution center is shifted toward the positive, making the positive skewness less intense. This is true even with accompanying outliers, which are still going to have some upper bound based on precipitable water. In contrast, when mean precipitation is low, the distribution will be centered near zero allowing the skewness to spike for any significant precipitation. To conclude, this all means that the original hypothesis was the opposite of what actually happens; intense convection can be represented by low skewness values.

Additionally, tropical rainfall may appear to be essentially convective in nature, but experiments over tropical maritime locations have shown that almost all convection occurs in association with stratiform rain (Houze 1997). The younger parts of the cumulonimbus clouds are entirely convective. When convection decays, though, clouds become stratiform and co-exist with the embedded convective columns. Stratiform rainfall generally occurs more frequently in the tropics (think spatially), yet convective rainfall accounts for most (~70%) of the cumulative rainfall, because its intensity is so much higher.

In order to create a simple representation of this new interpretation of the skewness, Figure 5.32 was created, showing the composite results analyzed for the negative of the skewness (inverted shape of the curve is important) shown in Figure 5.31. The actual values in this plot are not exactly important, but the shapes of the curves are important.

¹⁰ This is why the skewness of the precipitation field is rarely negative.

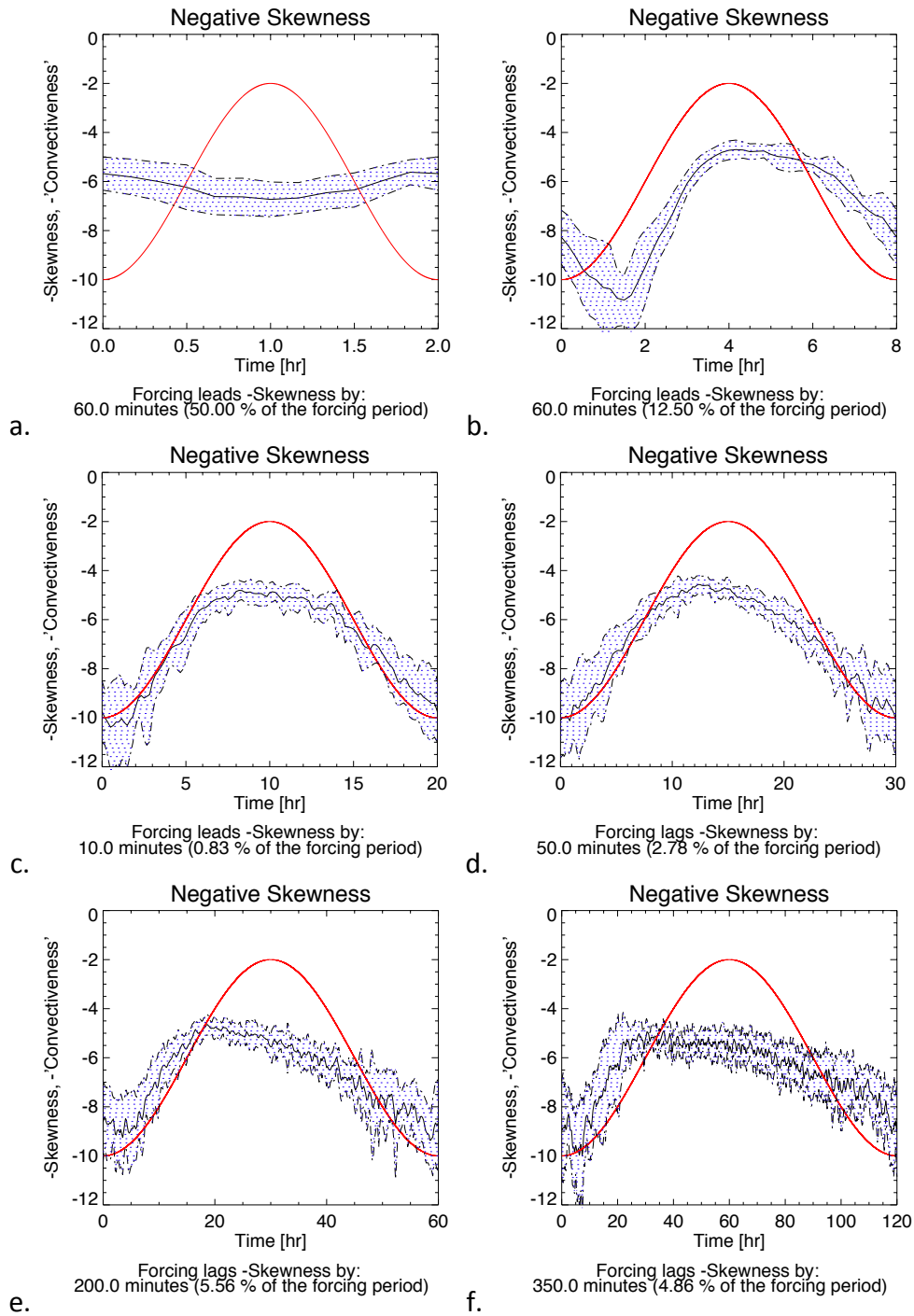


Figure 5.32. As in Figure 5.21 but for the negative of the skewness of the surface precipitation rate over the full domain.

Here we see features that are similar to those of the other variables. The curve for F02 is out of phase with the forcing just as it was for surface precipitation, and the curve moves toward being in phase with the forcing as the forcing length is increased. What may be

surprising is that at longer forcing periods, the forcing begins to lag the maximum of the negative skewness. This is in contrast to the results from the surface precipitation (on which these statistics are based), but it is compatible with the results for cloud area and non-precipitating condensate. However, what we do have is quite good agreement with the expected form of the response as discussed above. Equating the negative of the skewness of precipitation with a measure of convectiveness, the convectiveness builds suddenly and rapidly and then encounters a gradual decline, in general agreement with the applied forcing. Additionally for this measure, we see that the standard deviation does not scale proportionately with the mean; it does the opposite. This temporal distribution of variability is accounted for by the sensitivity of the skewness to low mean surface precipitation rates.

An additional measure that can be used as an indicator of convective activity is the vertical eddy kinetic energy (EKE). This is an effective indicator because it is mainly a measure of updraft and downdraft intensity. In order to obtain this value, the procedure outlined in X92 was followed and will be recounted here. First, it is assumed that a given quantity, A , may be separated into large-scale and eddy-scale components, such that

$$A \equiv [A] + A', \quad (5.3)$$

where $[A]$ is the large-scale component and A' is the eddy-scale component. Here, $[A]$ has been defined as

$$[A] \equiv \frac{1}{\tau} \int_{t-\tau/2}^{t+\tau/2} \frac{dt}{L_x L_y} \int_0^{L_x} \int_0^{L_y} A dx dy \quad (5.4)$$

In (5.4), L_x , L_y , and τ are the horizontal extents and the time interval for defining the large-scale component, respectively. The horizontal extent used in the averaging is 256

km, and the time interval was selected based on the period of the forcing and ranged from forty minutes to just over 4 hours. It should be noted that, when performing this operation to obtain the EKE, the large-scale component was most often several orders of magnitude less than the total.

Using the eddy-scale component, A' , to obtain the eddy-scale velocities, u' , v' , and w' , the vertical and horizontal EKEs can be computed as:

$$K_Z \equiv \int_0^{\infty} w'^2 \rho_0 dz, \quad (5.5)$$

and

$$K_H \equiv \int_0^{\infty} [u'^2 + v'^2] \rho_0 dz. \quad (5.6)$$

Here, ρ_0 is the model reference state density.

Figure 5.33 shows sample results (F14 and F20) from the composite analysis of K_Z . The kinked nature of the early response and slow decline in magnitude also evident in some instances this variable, though these features become less evident with increasing

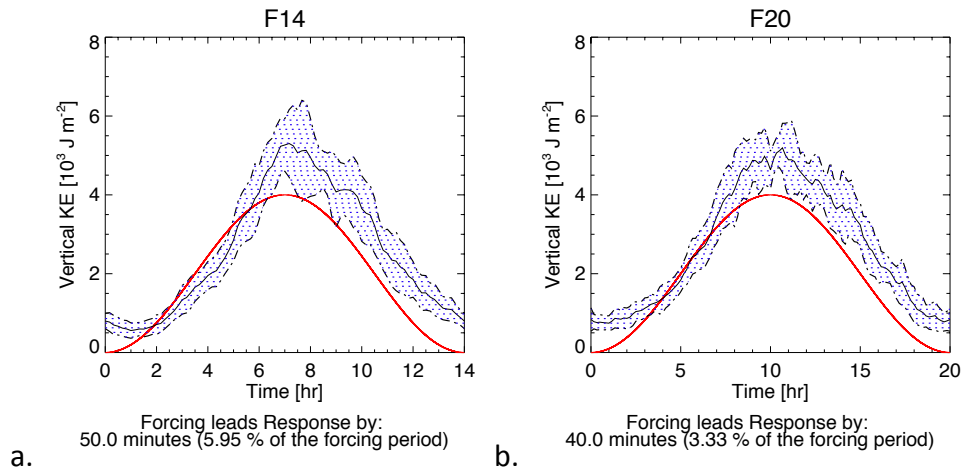


Figure 5.33. As in Figure 5.21 but for the domain mean vertical eddy kinetic energy.

period length. Additionally, the relative lag from the forcing tends to decrease as we have seen in other variables, but the absolute lag declines with increasing period length. The decline may be characterized as falling somewhere in between the precipitation variables and the cloud variables. It is most similar to the cloud mass flux. This indicates a reduction in the level of mesoscale influence at longer forcing periods as modulation by the large-scale forcing becomes more effective. For no simulation does the forcing lag the mean response; however, at the greatest forcing lengths considered (60 and 120 hours) the separation is only 10 minutes. It is unlikely that the maximum in the vertical EKE would ever precede the maximum in the forcing, since this variable has little latency on the large-scale.

Additionally, the eddy kinetic energy data were analyzed to obtain the component that is due only to mesoscale features. Here, as in X92, the mesoscale is numerically defined as features with dimensions larger than approximately 32 to 64 km. To generate the physical pattern that would be representative of the mesoscale, a low-pass filter (Ormsby 1961) is used following the specifics given in X92 and from Kuan-Man Xu (personal communication). The filter is applied in physical space as a two-dimensional array of weights derived from the following formula:

$$W(\tau) = \frac{\cos(2\pi f_C \tau) - \cos(2\pi f_T \tau)}{2\pi^2 (f_T - f_C) \tau^2} \quad (5.7)$$

This filter is designed to allow full retention of features greater than the *cutoff* frequency, f_C , and excludes features smaller than the *roll-off* termination frequency, f_T , with a gradual transition between the two. The two frequencies correspond to wavelengths of 64 km and 32 km, respectively. More details of this filter's characteristics are shown in Figure 5.34. The top row of panels shows (from left to right) the one dimensional weighting

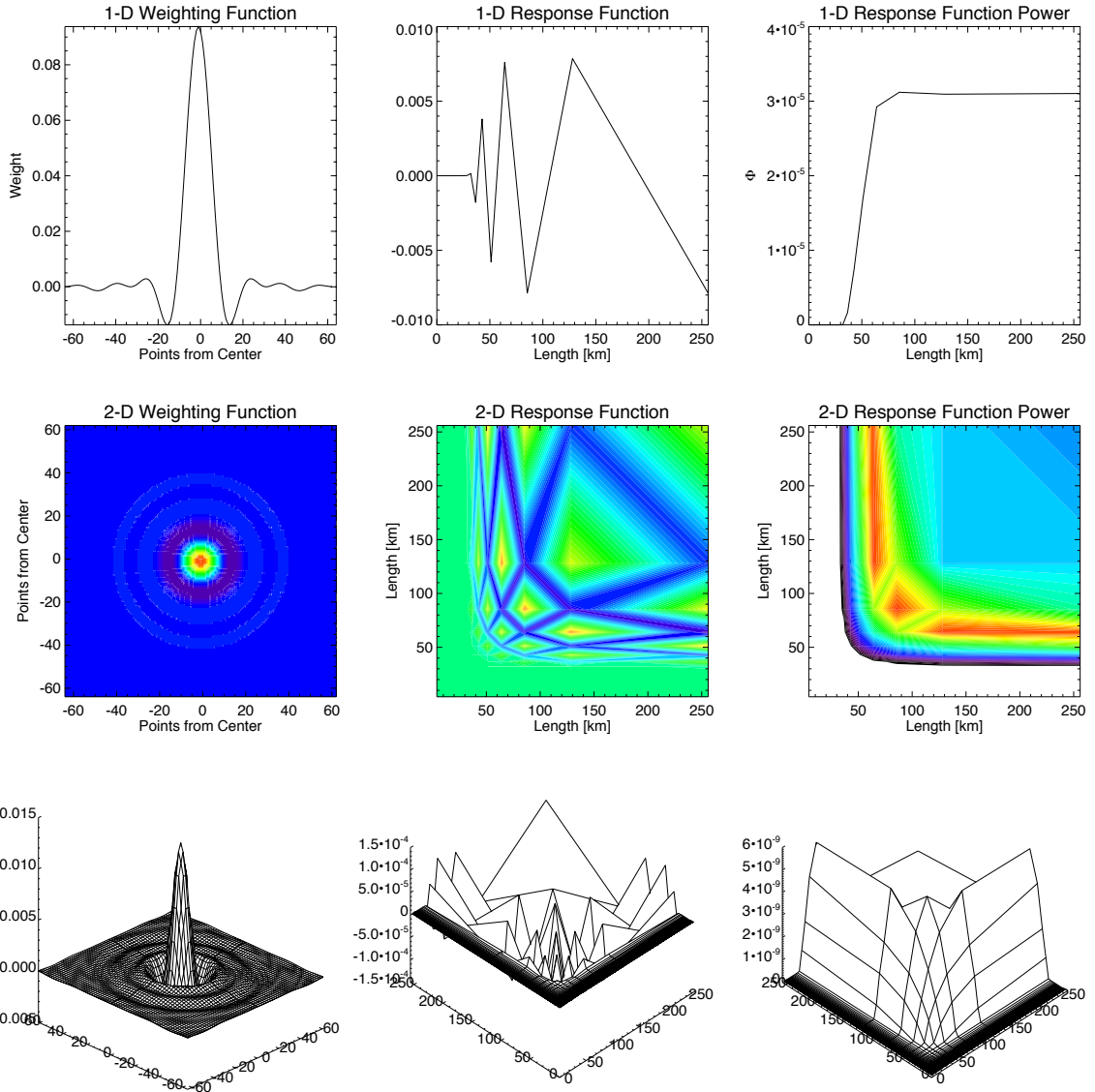


Figure 5.34. Characteristics of the weighting and impulse response functions of the Ormsby (1961) filter as used in one (top) and two (middle, bottom) dimensions. See text for additional description.

function as calculated from (5.7), the response function of the one-dimensional filter, and the overall power that will be retained when using the filter. It is important to note the negative side lobes on the weighting function that cause significant distortions in both physical space and spectral space. This distortion shows up clearly in the in the cen-

tral panel of Figure 5.34. The impulse response function power, power that will be retained after application of the filter, shows that power is evenly retained at wavelengths greater than 64 km and that power has been eliminated at wavelengths shorter than 32 km.

To produce the two-dimensional filter (left panels, middle and bottom rows), the one-dimensional filter weights were set to be radially equidistant from the maximum, covering a space of 128×128 points. The sum of the two-dimensional weights equals one. The colored contours in the middle row of Figure 5.34 are meant only to denote relative differences in values. Red colors indicate a maximum, and violet/black indicates the minimum. The color scale for the two-dimensional weight contours is linear, while that for the response function and power contours are exponential. Specific values may be inferred from corresponding panels in the bottom row of Figure 5.34. The response function in two dimensions is much more complex than that from one dimension, but similar distortions are visible in this case, as well. More importantly, it is confirmed that this two-dimensional filter will retain the most power at wavelengths greater than 64 km and remove all variability at wavelengths shorter than 32 km (the white space on the colored power contour plot is equivalent to zero power).

For clarity, the filter is applied by convolution of the weights, W , with the raw data, R , such that

$$F_{t,u} = \sum_{i=0}^{k-1} \sum_{j=0}^{k-1} R_{t+i-k/2, u+j-k/2} W_{i,j} \quad (5.8)$$

where F is a single point in the filtered field. In this case, the weight array has dimensions k by k , where k is less than t and u . The filter is applied at each point with edge

wrapping of the filter, which is possible because of the cyclic boundary conditions of the model.

Figure 5.35 shows raw (left) and filtered (right) vertical (top) and horizontal (middle) eddy kinetic energy fields, and raw and filtered power for a select vertical EKE field (bottom) from one point in the F12 simulation as an example. The top four panels incorporate the same color scale, with the violet end of the spectrum indicating low energy and the red end indicating high energy. As expected the vertical EKE is generally much lower (near zero) than the horizontal EKE, save for a few isolated regions that are associated with convection. As previously noted, the use of the filter creates spurious values in the resultant field, though the mean is retained. The white regions in the filtered fields represent areas with negative values of EKE. This is a more common phenomenon when the raw values are near zero (compare horizontal versus vertical). Regardless, these plots show the physical shape of the filtered field, and the removal of spatial variations at dimensions less than approximately 64 km are visually apparent in the filtered(smoothed) field.

The lower two panels of Figure 5.35 show the power in the top two fields as a function of wavelength. Here the shared color scale is exponential with white indicating approximately zero power. We see that the low wavelength power has generally been eliminated incorporating the transition between the roll off termination and cutoff wavelengths. The increase in power near the 50-60 km wavelengths seems to indicate some aliasing has taken place. This will not be important to future calculations. Similar results were obtained using a two-dimensional cosine-weighting (Hanning) filter cutting off at 64 km, with the exception that the cosine filter is sign preserving for positive definite

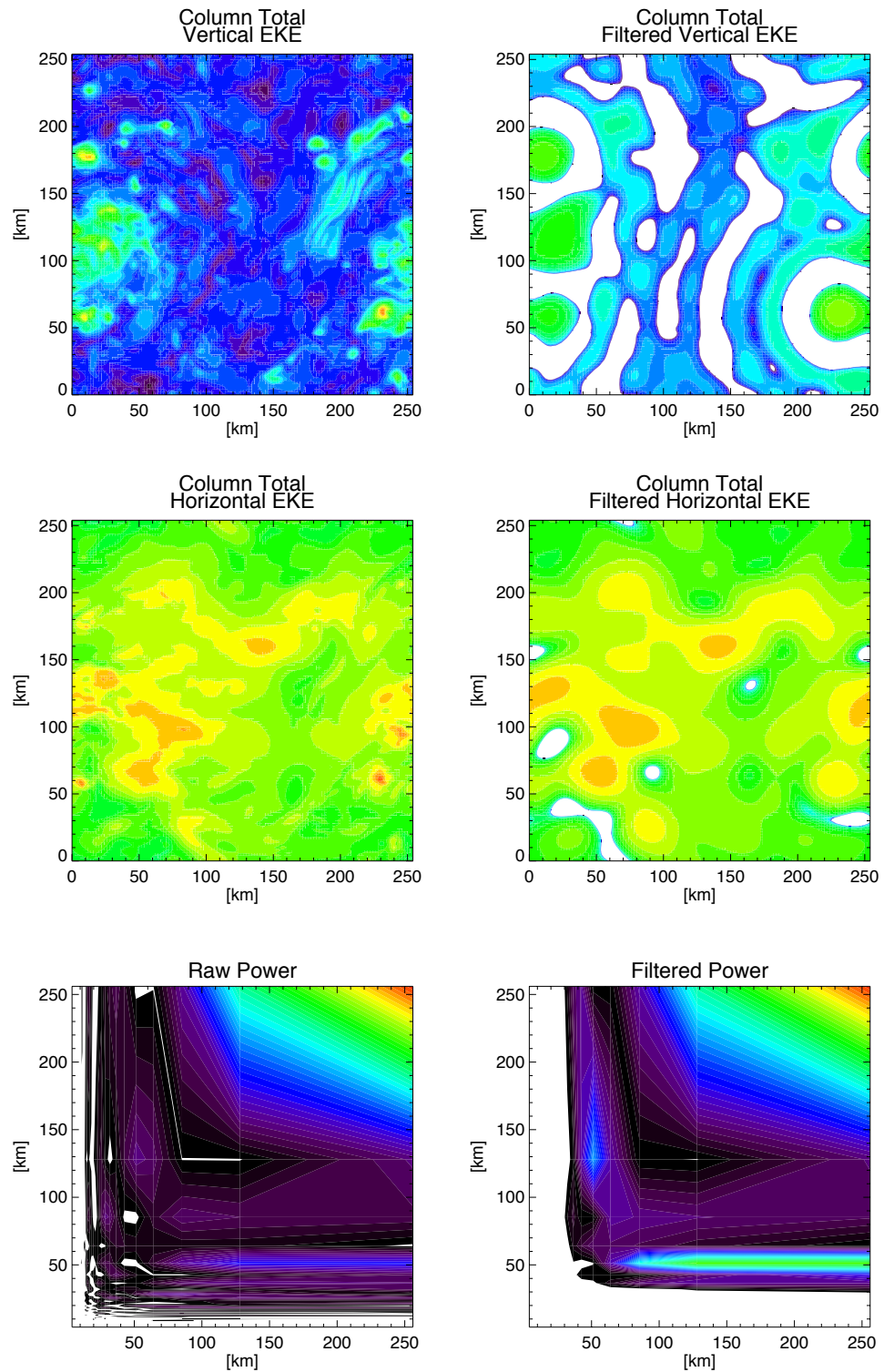


Figure 5.35. Raw (left) and filtered (right) vertical (top) and horizontal (middle) eddy kinetic energy fields, and raw and filtered power for a select F12 vertical EKE field (bottom). See text for description of contours.

variables, and also when selecting various filter bounds for both types of filters (not shown).

In order to estimate the contribution from only the mesoscale, as defined, spectral analysis was performed on each of the EKE fields at all points in time for each simulation. The percentage of power contained in wavenumbers 1-8 (wavelengths greater than 32 km) was used to estimate the fraction of the domain mean EKE that is contributed by the mesoscale. On average, the mesoscale component of the vertical EKE was about 14% of the total and that of the horizontal was about 40%. This differs significantly from the results of X92 in that the percentage is much greater in the vertical and considerably less in the horizontal. Exact numbers on this are difficult to ascertain because the only representations of this statistic are graphical and qualitative (See their Figures 6 and 8.), and the methods that X92 used to obtain the estimate are unclear. On average, for cases presented here, the vertical EKE was usually less than one percent of the average horizontal EKE. However, the two were more comparable in areas of active convection.

Examples, corresponding to Figure 5.33, are shown in Figure 5.36 showing the filtered domain mean vertical EKE for the F14 and F20 simulations. Comparing with the

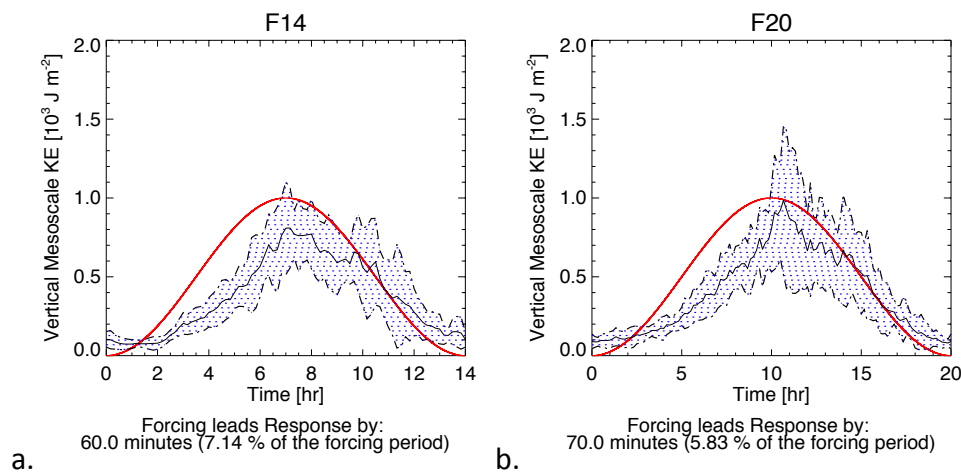


Figure 5.36. As in Figure 5.21 but for the filtered domain mean vertical eddy kinetic energy.

unfiltered version in Figure 5.33, we can see both proposed characteristic features of mesoscale influence. Namely, we see the significant lag in the data maxima and the delayed, slow ramp-up of convection followed by a slower, more shallow decline. Of course, we also note the reduced scale on the ordinate axis. These results are pleasing in that they are very similar to those found by X92 (Figure 2.3); however, having not run a set of simulations in the absence of shear or with differently arranged or powered shear there is nothing that we can say for certain about the way in which convective statistics may vary under different types of mesoscale organization. In fact, without the X92 results for comparison, it would be difficult to make the case for the influence of the mesoscale on the modulation of the convection. Additionally, no more about this measure will be mentioned, because much of the remainder of the work involves other atmospheric features and smaller domains for which the mesoscale is not discernable.

5.2.4 Composite Analysis – Partial Domains

A focus of this study is to determine how convection-related variable statistics vary with changing domain size. Rather than running more simulations with different domain sizes, a subsampling technique has been employed to estimate the effect. The full domain size of $(256 \text{ km})^2$ has been broken down into fractions of one half (rectangular), one quarter, one sixteenth, one 64^{th} , and one 256^{th} . This effectively allows for statistics corresponding to a total of six GCM horizontal grid resolutions of 256, ~181, 128, 64, 32, and 16 km spacing, respectively. Clearly, the goal is to capture the changes in statistics that will be accompanying the ongoing shift of GCM grid spacing from $O(100$

km) to $O(10 \text{ km})$. Specifically, we wish to determine at which resolution the assumptions of QE tend to break down and to characterize how this occurs.

With this set-up, one can still make composites similar to those found in Section 5.2.3. The calculations are slightly more complicated in this case. First, the subdivisions are determined. They are chosen to be regular, square (except for the case of the half domain), and evenly distributed in a grid. Next, the mean of the quantity is calculated for each individual subdomain at each time. The result of this is a set of time series, the number of which depends on the size of the subdomain. In the case of the 256^{th} subdomain size ($16 \text{ km})^2$, there are 256 time series. These are then subdivided into 15 cycles, as was done in the full domain composite analysis, and the standard deviation between the cycles is calculated for each subdivision. It is also at this point that the lag correlations between the periodic forcing and subdomain mean are calculated. Finally, the data is averaged across each of the subdivisions. This ultimately means that the mean that will be shown in each of the plots will remain the same as in the previous section but that the standard deviations will have changed. It is important to remember that we are looking for variations between realizations rather than spatial variations.

Let's look at the surface precipitation rate for the F30 simulation first (Figure 5.37). The most robust result of this comparison is that as the averaging domain is made smaller, the variability in the response as measured by the standard deviation between realizations increases greatly. The surface precipitation rate standard deviation grows from roughly one-tenth of a millimeter per hour in the full domain case to nearly 5 millimeters per hour in the 256^{th} domain case (50 times) near the peak response for the F30 simulation. As the area under consideration is reduced, the likelihood of encountering a wider

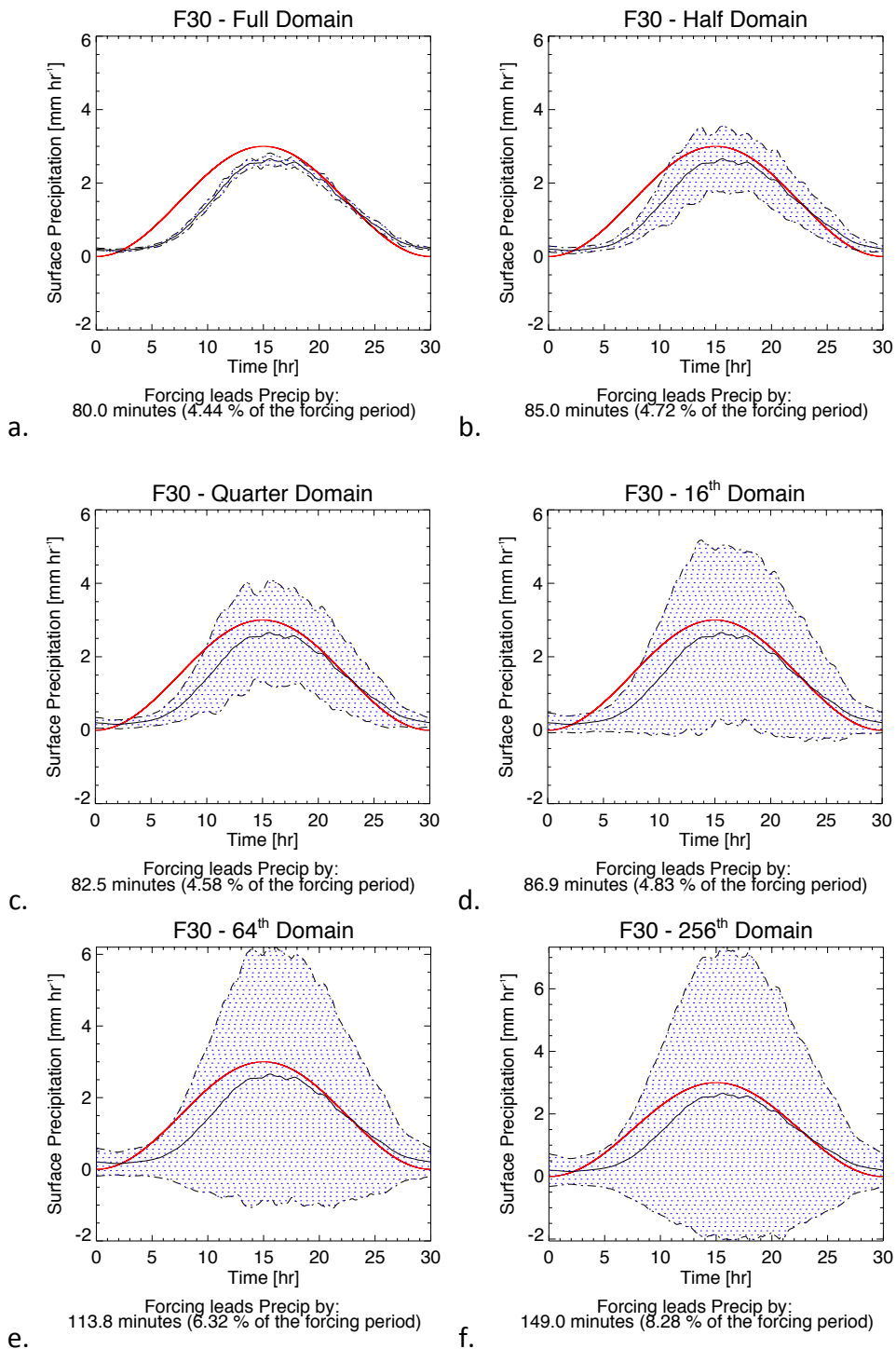


Figure 5.37. As in Figure 5.21 but for noted subdomains of the F30 simulation.

range of values is increased. Note, once again, that this is not an indication of what may be considered subgrid variability. The spatial standard deviation of a given quantity av-

eraged over a number separate domains would certainly decrease as the area of the domain id decreased. It should also be noted that the negative values that appear in the standard deviation curves are simply statistical and do not imply negative precipitation.

Another interesting feature of Figure 5.37 is the series of lag times. Recall that these lags are calculated from subdomain means rather than the final averaged means. Specifically, the lag correlations are calculated for each subdomain, the lag corresponding to the maximum correlation is retained for each subdomain, and finally those lag values are averaged to obtain the values shown in Figure 5.37. This method is not numerically equivalent to averaging the correlations for subdomains and then selecting the lag corresponding to the maximum correlation. The result is that the response lag time has lengthened with the decreasing averaging area. Such increases are due to subdomain areas that experience an increase in convective activity that has been advected from another subdomain and that generally occurs well after the forcing maximum. This is the effect of mesoscale organization that can perpetuate/sustain convective activity independent of the large-scale forcing. The lags in each subdomain do not average to the lag of the full domain because the effect of mesoscale activity is to increase the life time of a given storm from the point of inception caused by a sufficient increase in mesoscale activity. There is not an analogous process to cause convective activity to occur earlier for smaller subdomains. Note also that in the accompanying figures, the mean curve will not show this lag.

Next, this qualitative observation must be given a quantitative characterization. Just fitting a line to the data, it turns out that the relationship between subdomain area and lag time can best be represented by a power relationship of the form,

$$L(a) = 244.85a^{-0.107} \quad (5.9)$$

where $L(a)$ is the lag in minutes and a is the subdomain area in square meters. This indicates that for averaging areas less than those tested, lags would likely increase. Additionally, for reasonably larger averaging areas, the lags may decrease slightly. However, it is likely that this fit, which is based solely on six points, is not accurate at the extremes.

The question that remains is that of where to draw the line that denotes the limit of QE with respect to the grid size. In other words, what is an acceptable amount of variability about the mean? Being as strict as possible, and without using subjective measures, we can arrive at a fairly definitive solution to that question. Going back to Section 5.1 and Figures 5.1.1 and 5.2, we saw that when the model was allowed to run out to a consistent statistical equilibrium, the ratio of standard deviation to the mean was nearly constant at 0.1. We shall assume that this is a good approximation of reality. Given that, any place where this ratio is greater than 0.1, we shall consider QE a poor approximation for use in a model with a corresponding grid spacing. By that measure and a quick look at Figure 5.37, QE is a poor approximation for all grid spacings equal to or smaller than half of the full domain size used; this is equivalent to approximately 181 km. Even loosening the constraint by doubling the acceptable ratio, the same is true. We will return to this measure later.

To broaden the picture of the results obtained by doing the composite analysis on each of the subdomains, Figures 5.38 and 5.39 show the results from the F08 and F120 simulations, respectively. In both cases, the standard deviation increases greatly with decreasing averaging area, and the data do not meet the requirements set for QE above for subdomains equal to or smaller than half of the full domain size. Those similarities to the

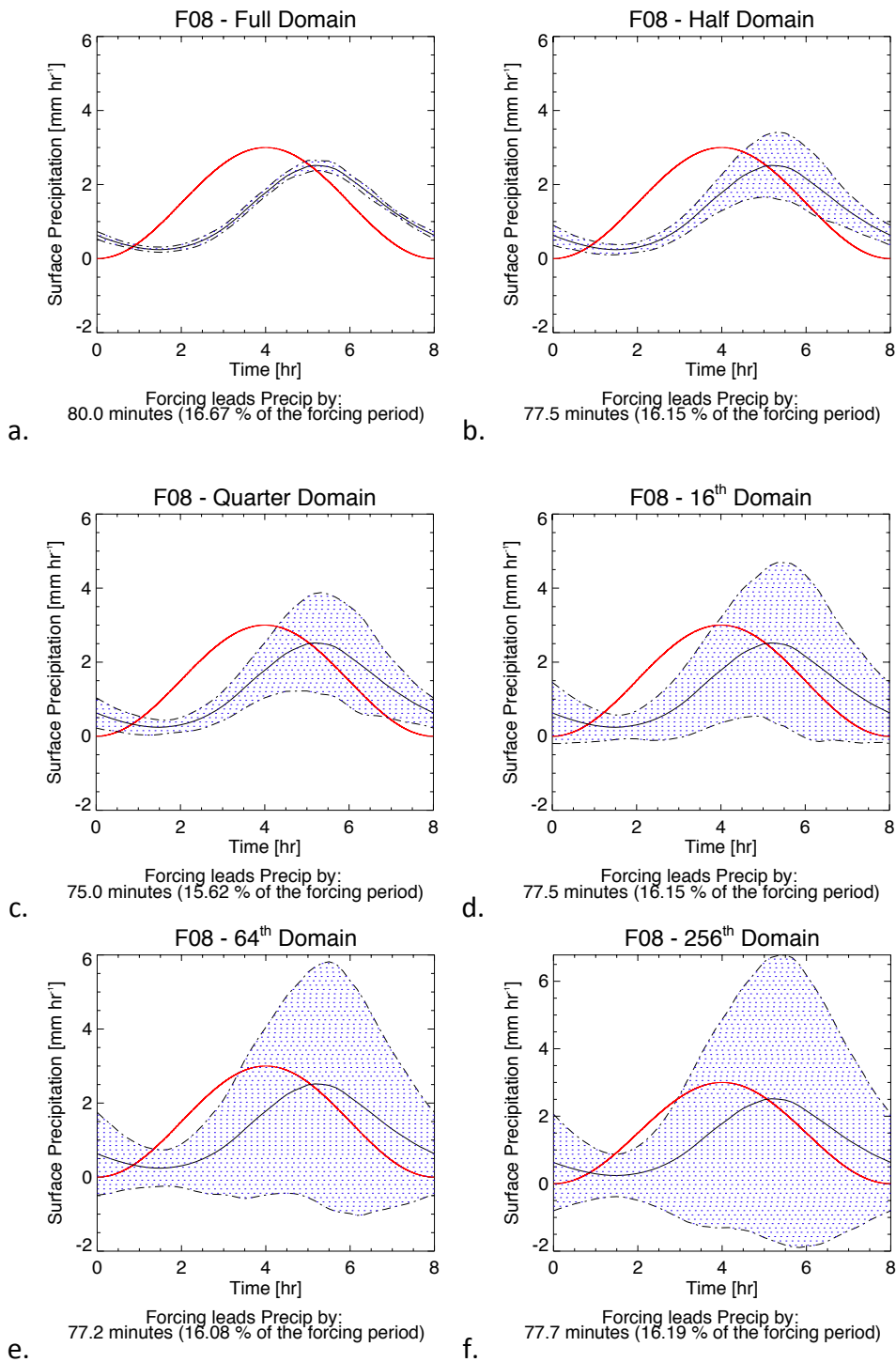


Figure 5.38. As in Figure 5.21 but for noted subdomains of the F08 simulation.

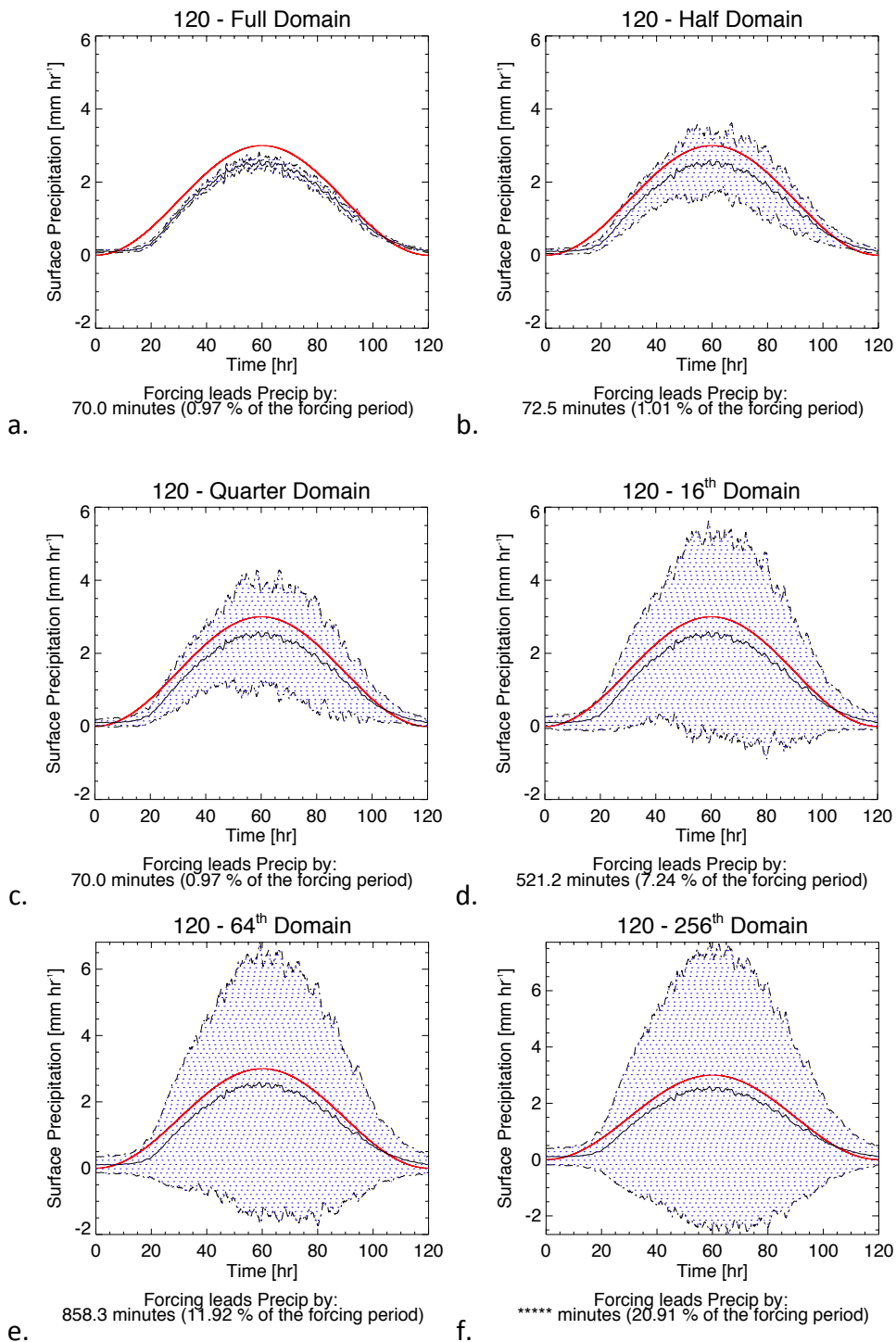


Figure 5.39. As in Figure 5.21 but for noted subdomains of the F120 simulation.

previous example aside, there is an interesting occurrence in the case of the forcing lags.

In the case of the F120 simulation, the relationship between the lag and the subdomain

area can once again be approximated by a power relationship. The constants are different in this case, but the goodness of fit, in terms of an r^2 value, was a slight improvement over that for the F30 simulation (not shown). In contrast, the lags for different averaging areas stay fairly constant in the F08 case, staying between 75 and 80 minutes. Further testing of the relationship between lag and subdomain area shows that for longer periodic forcings, the relationship can very well be determined by a power law, but at shorter forcings, the relationship is much more linear. The reasons for this remain unclear.

Figures 5.40-5.42 compare the F30 composite analysis results at the six domain areal extents for cloud fraction (Figure 5.40), non-precipitating condensate (Figure 5.41), and cloud mass flux through the ~ 2.5 -km level (Figure 5.42). The data in these figures are very similar to those that are presented in Figure 5.37 for the surface precipitation rate. Most specifically, the standard deviation about the mean tends to increase by at least an order of magnitude when reducing the averaging area from the full domain to the 256th domain. This same growth in the variability between realizations is also seen in the other simulations (not shown). The pervasive nature of this feature throughout multiple simulated convection-related variables is indicative of its robust importance.

Interestingly, it is at this point that we begin to see differences amongst the variables that once again fall on either side of the line dividing the precipitation variables from the cloud variables. Aside from the previously noted tendency for the maxima in the cloud variable means to significantly precede the forcing maximum, which remains consistent here, the way in which the lag time periods vary with averaging area is also different between the two variable classes. In the case of the cloud mass flux, the forcing leads the flux by generally increasing amounts as the averaging area decreases. The way

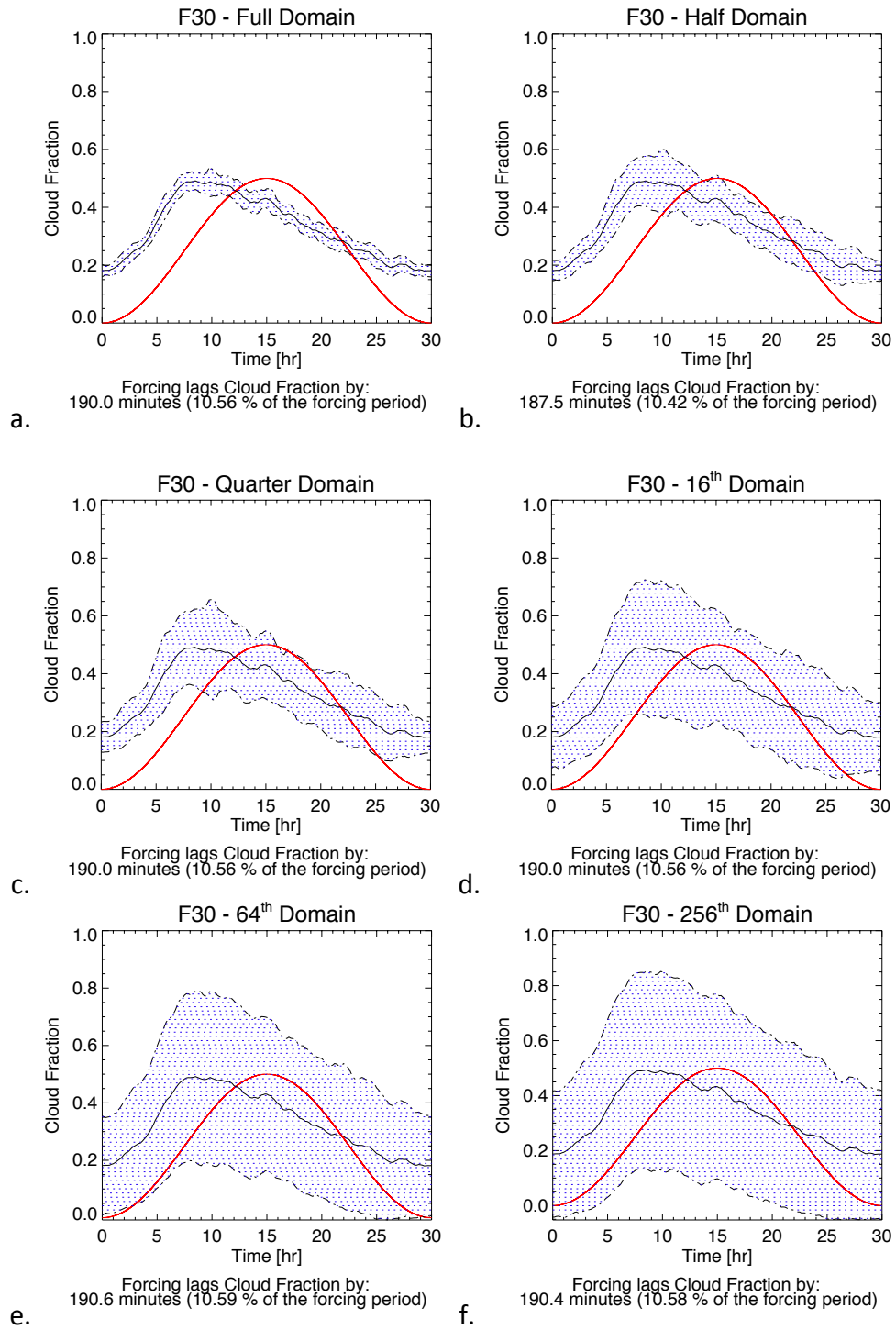


Figure 5.40. As in Figure 5.21 but for cloud fraction within the noted subdomains of the F30 simulation.

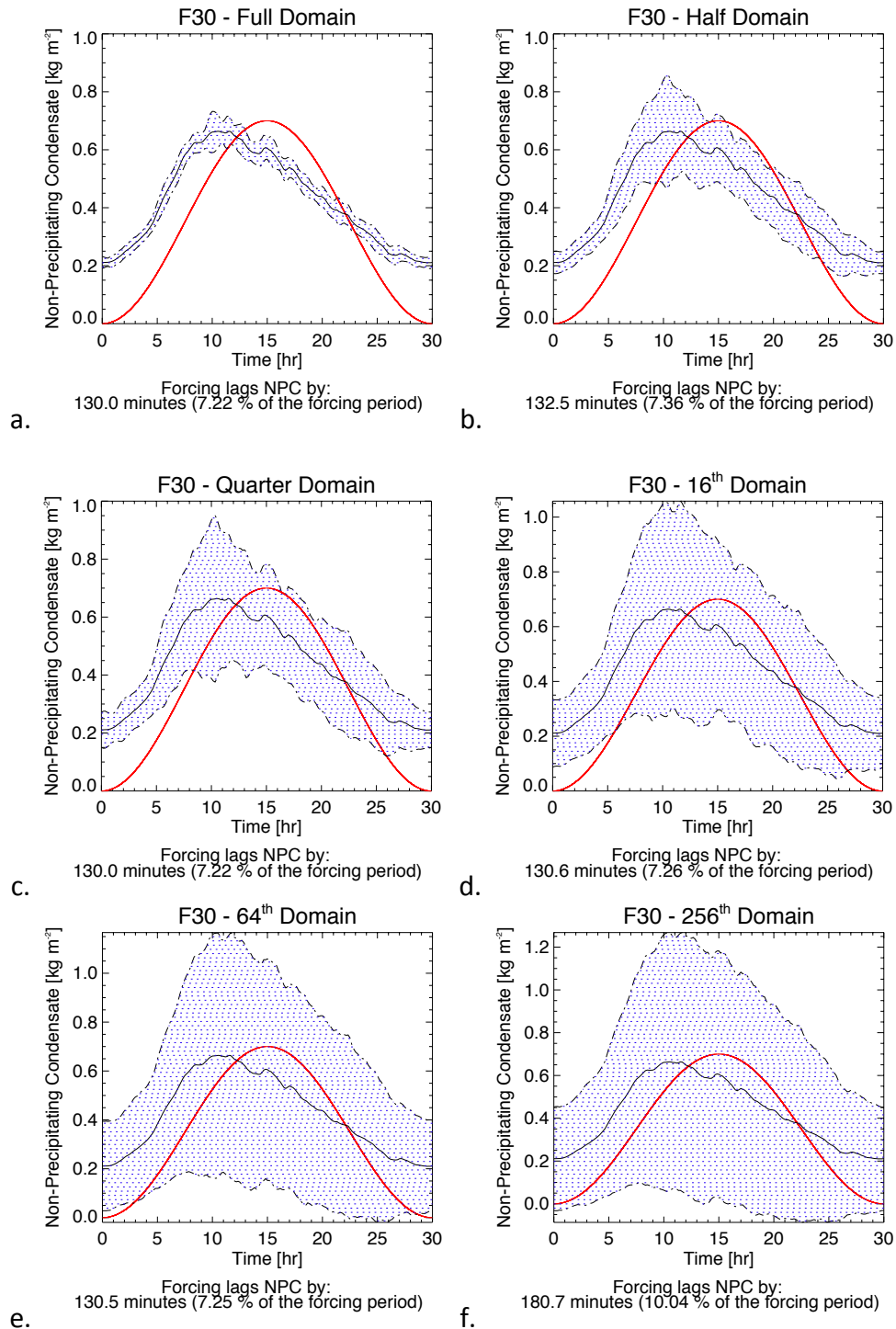


Figure 5.41. As in Figure 5.21 but for non-precipitating condensate within the noted subdomains of the F30 simulation.

in which it does so nearly follows a power law curve; however, the goodness of fit is somewhat less than that from the surface precipitation lag relationship for F30 given in

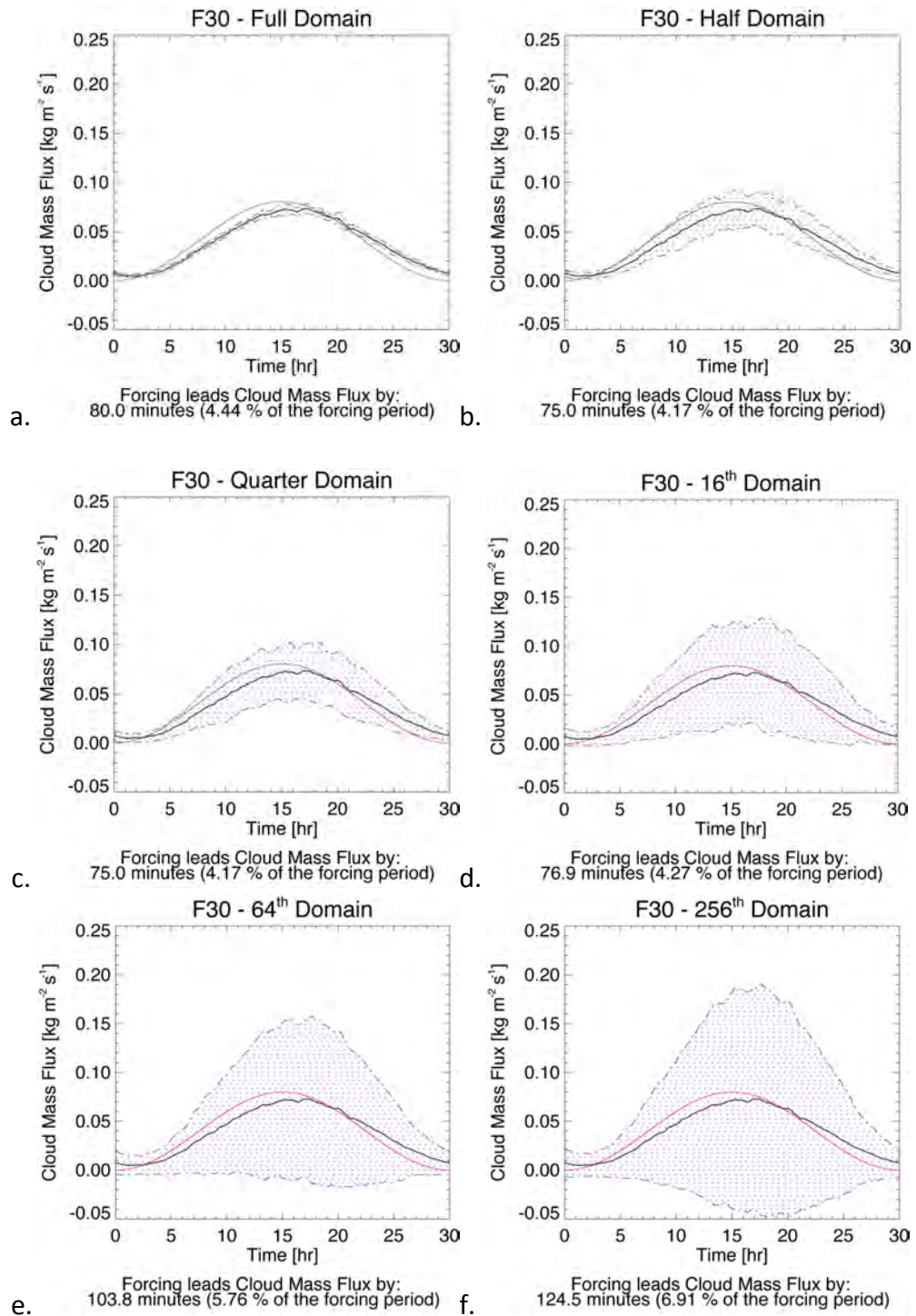


Figure 5.42. As in Figure 5.21 but for the cloud mass flux through the 2.5-km level within the noted subdomains of the F30 simulation.

equation (5.8). Similarly to the lag relationship for surface precipitation in F08 and other short forcing period simulations, the lag relationship for the cloud mass flux stays ap-

proximately (or at least relatively) constant in the same simulations.

In contrast to this, the lag relationships for non-precipitating condensate and cloud fraction remain nearly constant with varying subdomain size and for the full range of simulations in most cases. One critical caveat to accompany this statement is that there are a few wild departures from this behavior that do not have easily classifiable structure. One example of this can be seen clearly in Figure 5.41f, where the lag for the 256th subdomain size for the NPC mean makes a sizeable jump, deviating from the behavior of the larger subdomains. Similar behavior was noted (*e.g.* in F12 and F14) but is not shown. It appears that the most likely explanation for this seemingly erratic behavior is due mainly to the great variability that is present between such small scales. To be more specific, the phenomenon is probably the result of a few strong outliers.

In each of the cases shown, there appears to be a strong tendency for the variability about the mean to greatly increase with decreasing horizontal averaging extent. Using the metric set forth above, none of the variables examined met the criteria to support the use of QE assumptions for grid spacing corresponding to of one half of the full simulation domain area. Additionally, the transition to larger amounts of variability is not the same for each variable in terms of the growth of the standard deviation to mean ratio (coefficient of variation, CV). Because of this, if one were to use another QE-support metric based on this data that, for example, was derived from a rapid shift in the variability, the conclusion would be variable-, and to some extent, forcing periodicity-dependant. But even with such a crude definition of QE acceptability, one would be compelled to draw the line between the full and half or half and quarter domain sizes. This definition would have the effect of excluding GCM or NWP grid spacing smaller than 128 km from the

use of QE assumptions, a point that is somewhat less restrictive than the measure based on the equilibrium simulations.

5.2.5 Extended Composite Analysis

This section contains an extension of the information contained in Sections 5.2.3 and 5.2.4. Presented here is much of the same data but in an amalgamated form that allows for better generalization of the data and their statistics, for example, in terms of assigning trends. We shall begin by getting a better look at the behavior of the full domain realization-averaged standard deviation of the surface precipitation rate across the spectrum of assigned large-scale forcing periodicities (Figure 5.43).

The ordinate axis represents the normalized large-scale forcing for a given cycle with the corresponding point in time increasing upward. The line through the contour plot represents the location in time of the maximum mean value for a given forcing period. This is similar to, but not the same as, the measure of the lag between the large-scale forcing and the mean response variable. Figure 5.43's nearly monochrome appearance seems to tell us very little at first glance, but it presents a full overview of the variability for each full domain simulation in addition to information about the lagged response to the large-scale forcing. We can see that the standard deviation about the mean of the realizations depends very little upon the forcing period. Similarly, Figure 5.44 shows very little dependence of the CV upon the forcing period. Based on the criteria for using QE assumptions, it is clear from Figure 5.44 that the full domain size (256 km in the horizontal) is an acceptable grid spacing at the majority of forcings. It would appear that the use of QE assumptions may be called into question in cases where the large-scale

forcing varies slowly, especially when that forcing is relatively small in magnitude. Bear in mind that there are only two simulations serving as the basis for the right half of these two figures and that subsequently any contours are interpolated and approximate.

Figures 5.45 and 5.46 show the same statistical variables as calculated on a quarter of the full domain. Here, the pattern that occurs in most aspects of the convective variables begins to emerge more clearly. The standard deviation (as shown in Figure 5.45) peaks along with the surface precipitation rate mean (thick black line), which is expected as discussed in Section 5.1 (variability scaling with the mean). Note, though, that this feature does not appear to hold for the smallest forcing periods as the orientation of the mean curve is turned almost 90 degrees due to the forcing being out of phase with the precipitation response. Further, the CV in Figure 5.46 shows that the scaling is not con-

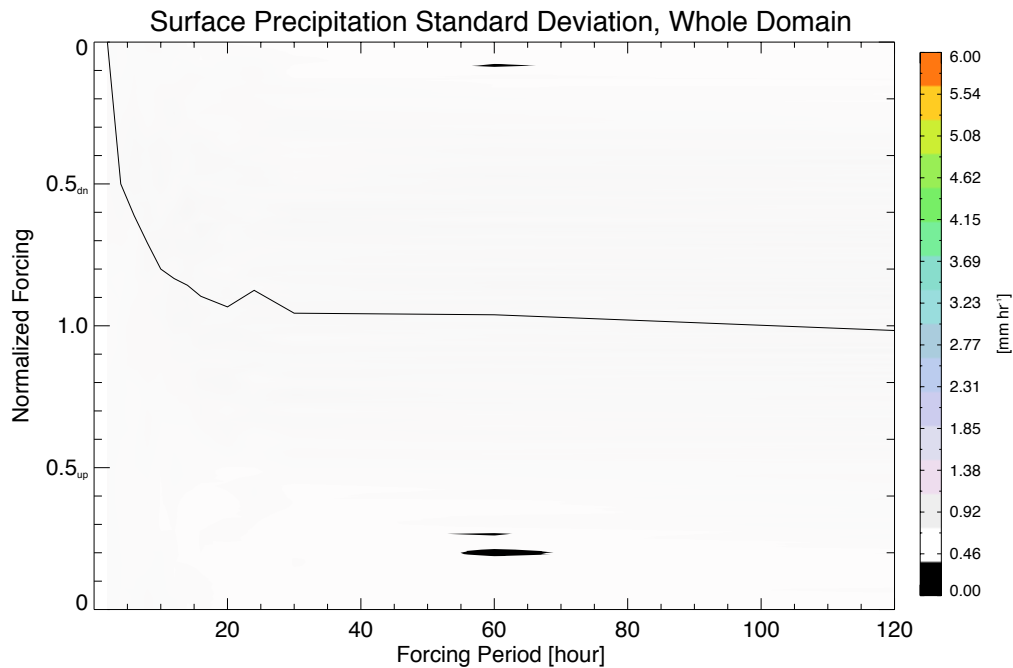


Figure 5.43. The surface precipitation rate standard deviation for the whole domain case for all periodic forcing simulations. Thick line is the location of the maximum mean relative to the normalized forcing. The minimum value on the abscissa is 2 hr.

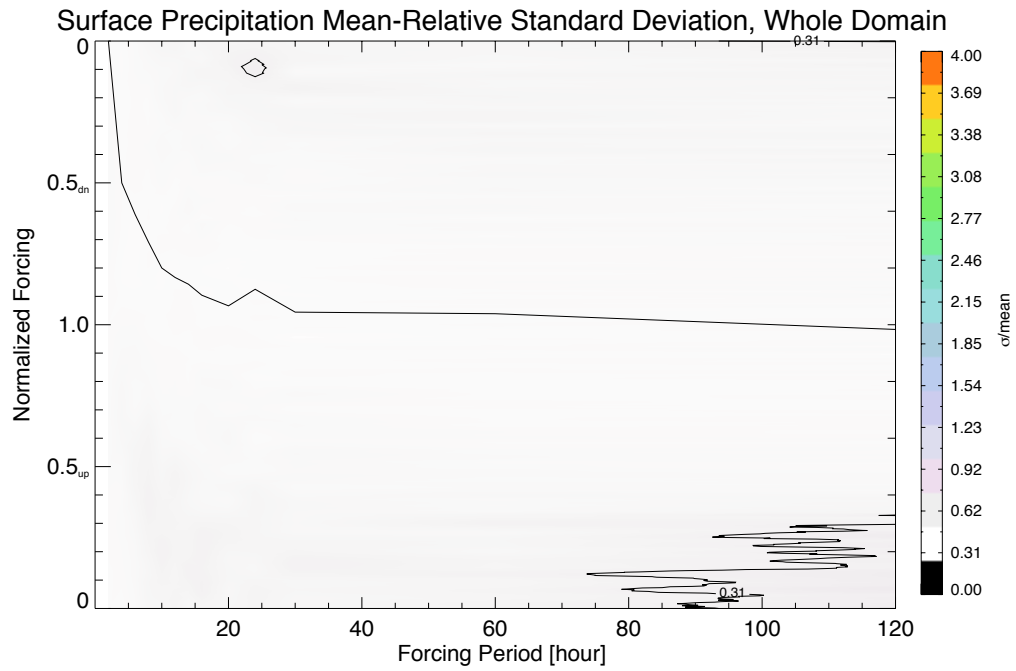


Figure 5.44. As in Figure 5.43 but for the coefficient of variation.

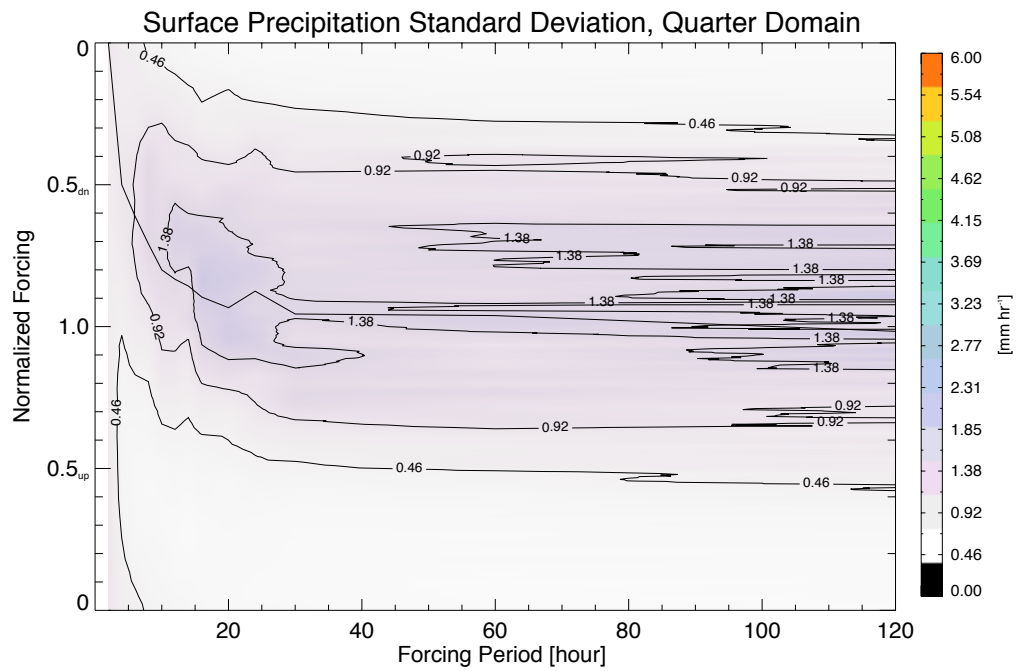


Figure 5.45. As in Figure 5.43 but for the quarter domain.

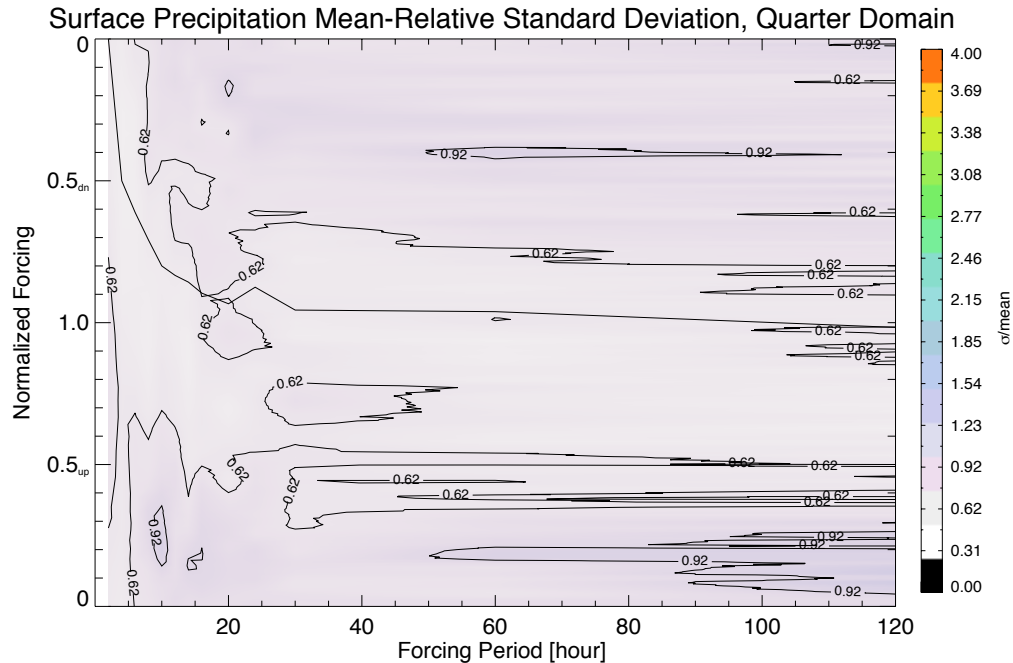


Figure 5.46. As in Figure 5.44 but for the quarter domain.

stant, being especially variable with regard to the magnitude of the normalized forcing. For the range of data on the quarter domain, the CV varies with approximately a factor of two difference between the minimum and maximum values, and we see once more that at this domain size, QE assumptions are becoming more questionable at all forcing periods.

Moving down the spectrum, while leaving out a few figures for brevity, we can look at the same data averaged for the smallest subdomain (256^{th} , $16 \text{ km} \times 16 \text{ km}$). This data is shown in Figures 5.47 and 5.48. The magnitudes of the standard deviations have grown considerably in comparison to larger subdomains (as was shown in the previous section), though the values are very similar when the normalized forcing is less than 0.25. The general pattern in the case of the CV values is also repeated for this subdomain with the values forming a minimum about the line for the maximum mean indicating an inexact scaling with the mean. The magnitude of the CV is much greater than for the larger subdomains approaching the region where the standard deviation is three times the pan-

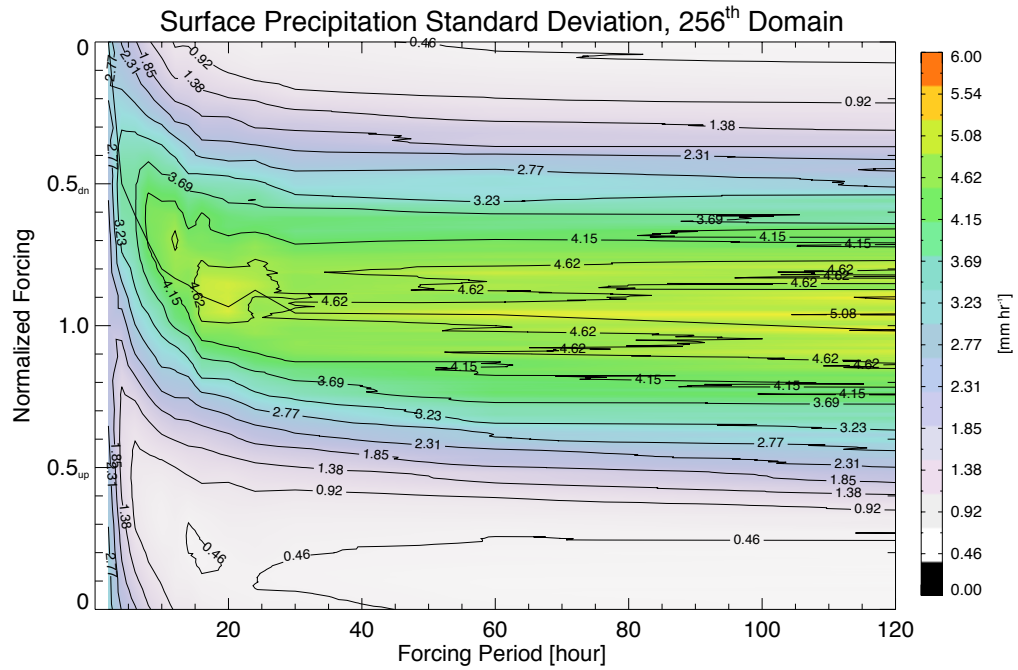
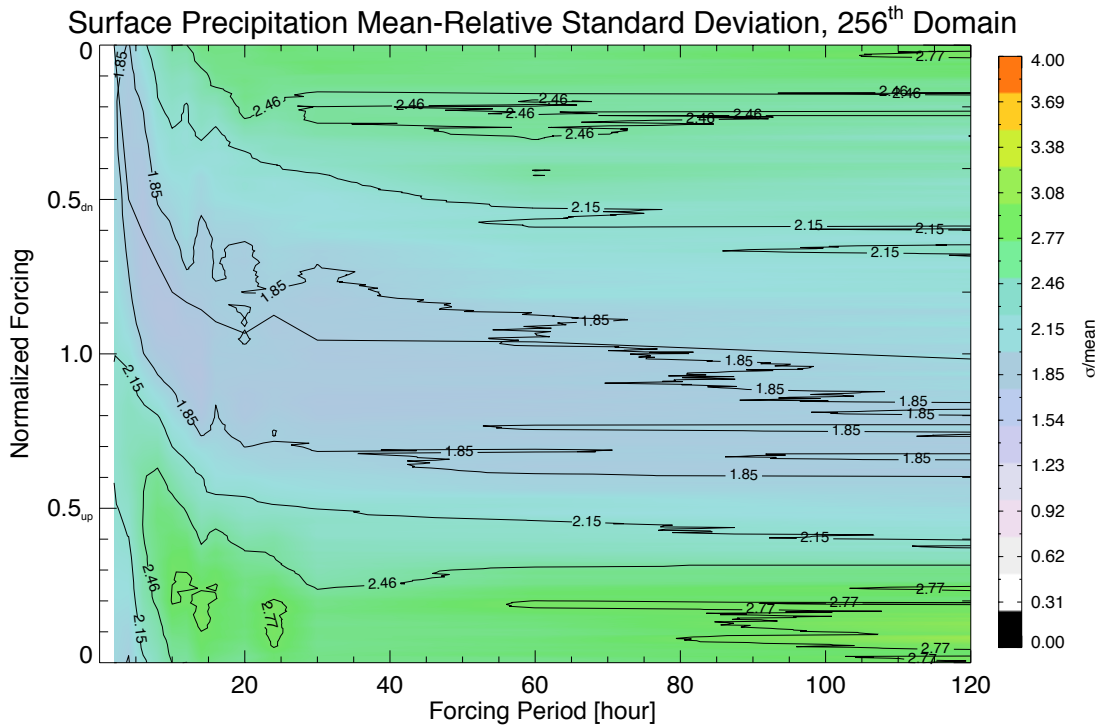


Figure 5.47. As in Figure 5.43 but for the 256th domain.



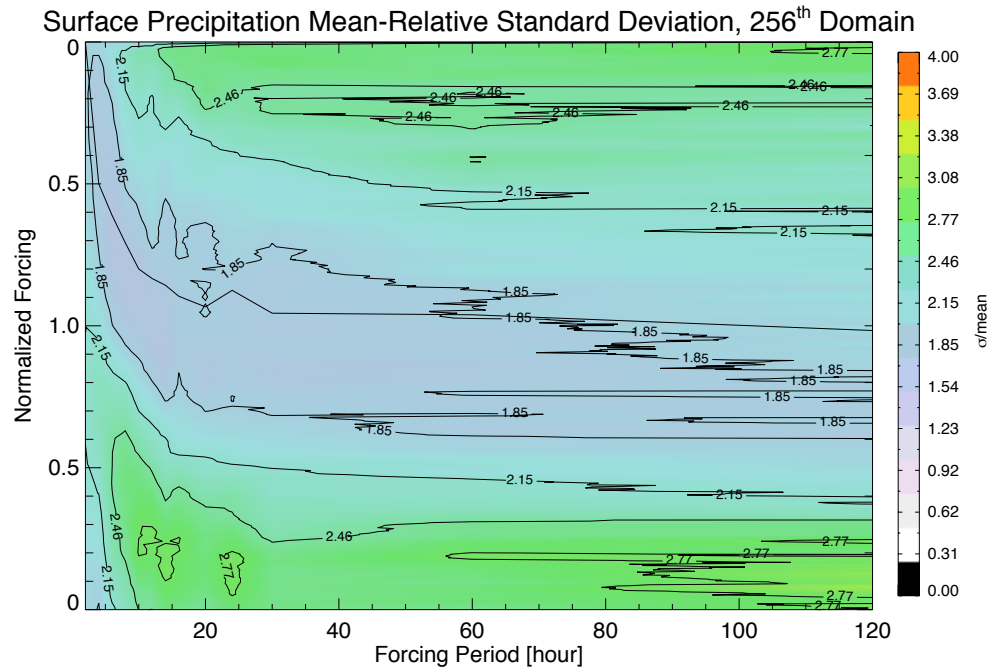


Figure 5.48. As in Figure 5.44 but for the 256th domain.

realization mean. Such a domain is nowhere near the realm of QE applicability. If one planned to parameterize convection at this resolution, the variability features that are shown here are those that need to be approximated by a stochastic parameterization. There is a great deal of variability that would be lacking from a model using a conventional parameterization that surely would have adverse effects in such a simulation.

A very similar pattern is found for the cloud mass flux, the cloud fraction, and the non-precipitating condensate. Figure 5.49 is an example of this similarity in the case of

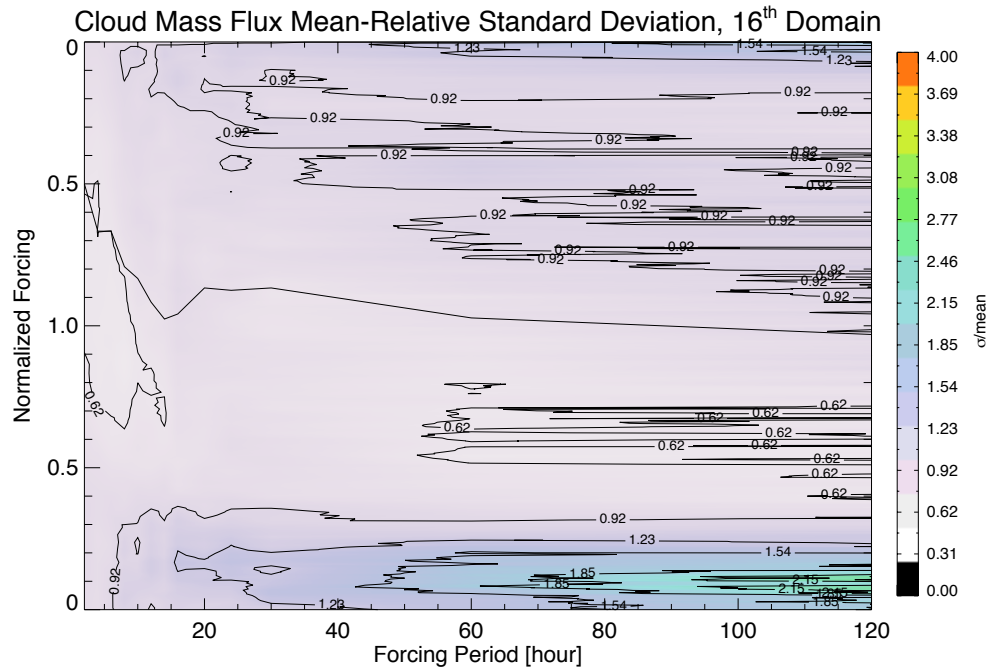
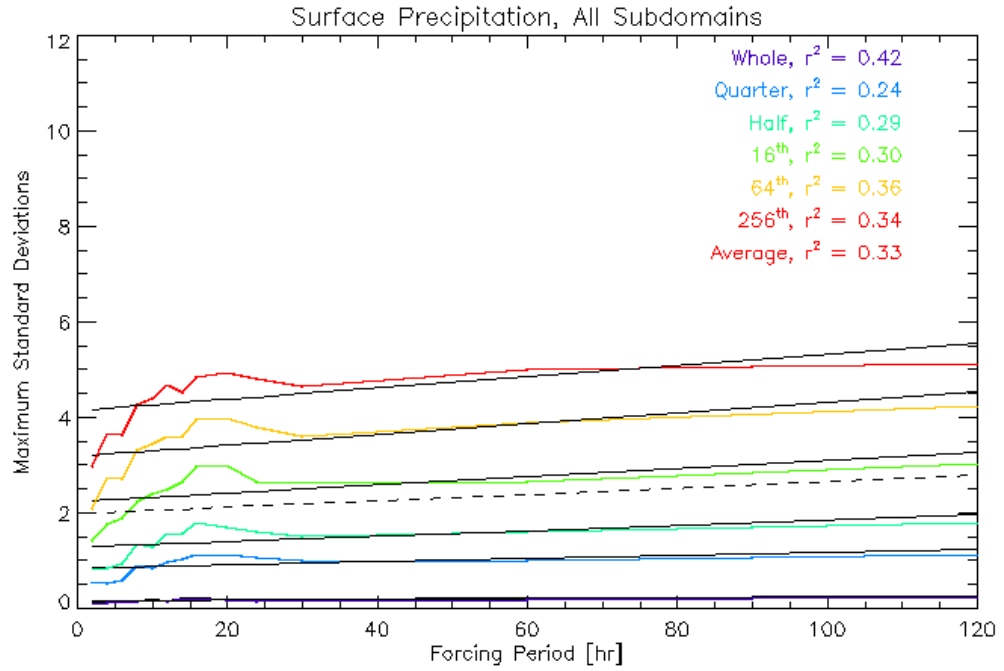


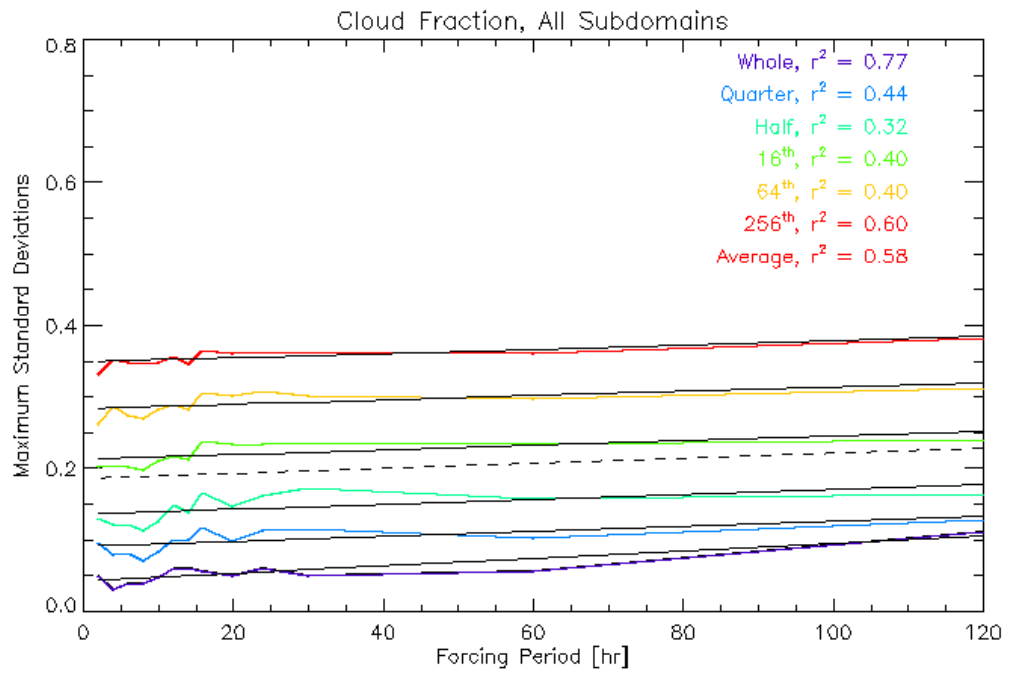
Figure 5.49. As in Figure 5.44 but for the cloud mass flux and the 16th domain.

the cloud mass flux CV at one-sixteenth domain size. Once again, we see that there is an especially large CV cluster corresponding to the response minimum and slowly varying forcing simulations. Figures showing these features for remaining subdomain sizes and variables have been omitted for the sake of preventing redundancy. In their stead, a series of summary figures are provided.

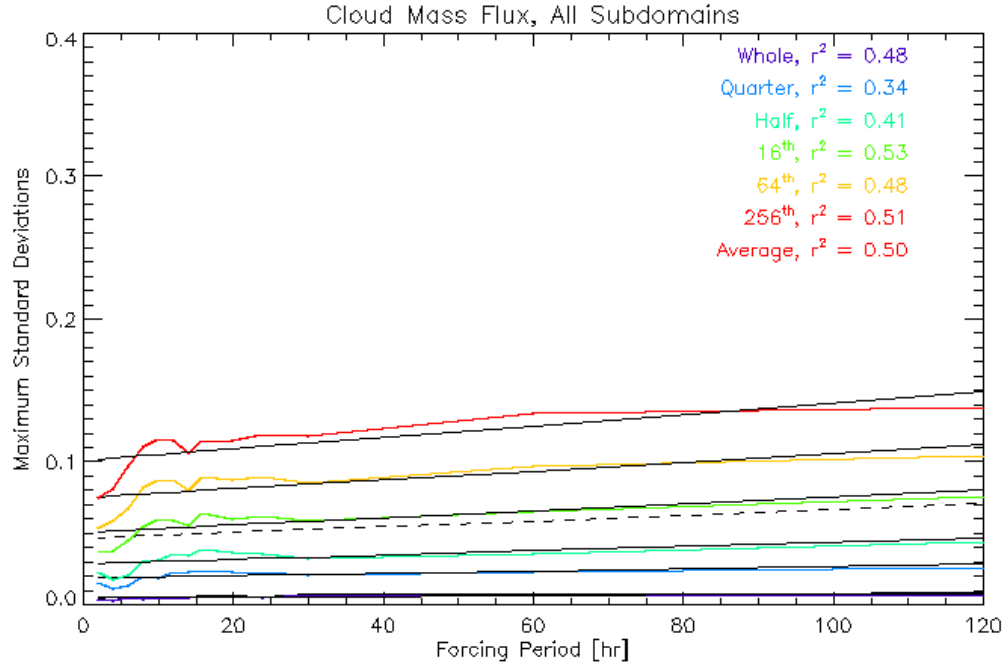
Figure 5.50 shows the dependence of the maximum (for a given composite) standard deviation on period length for each of the four variables at each subdomain. A fea-



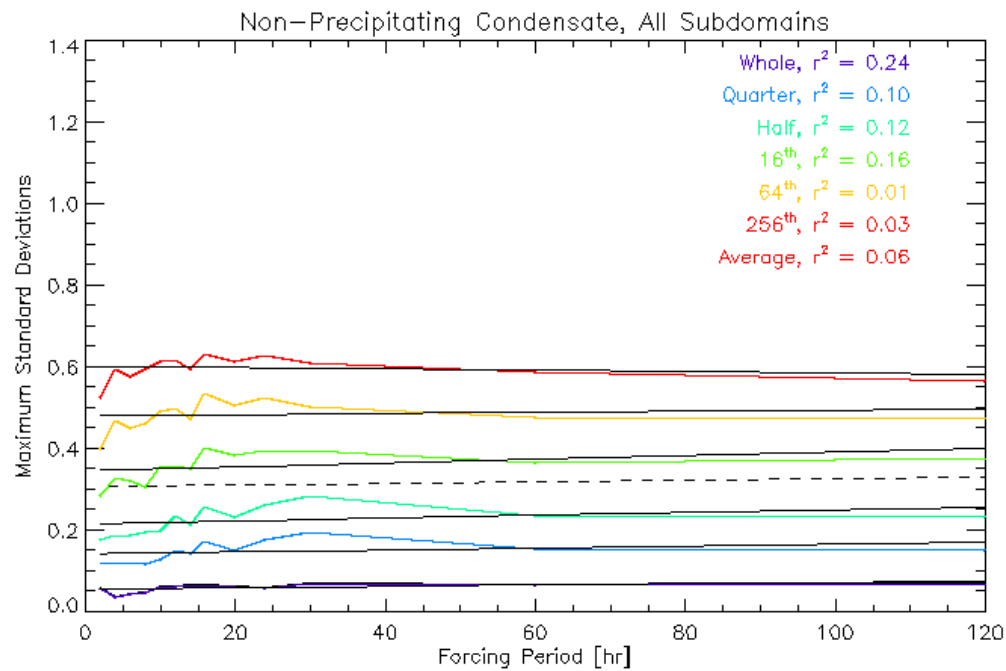
a.



b.



c.



d.

Figure 5.50. Maximum standard deviation versus forcing period length at all subdomains for (a.) surface precipitation rate, (b.) cloud fraction, (c.) cloud mass flux, and (d.) non-precipitating condensate. The black line accompanying each curve is the linear regression, and the dashed line denotes the linear regression for the average of each of the colored curves.

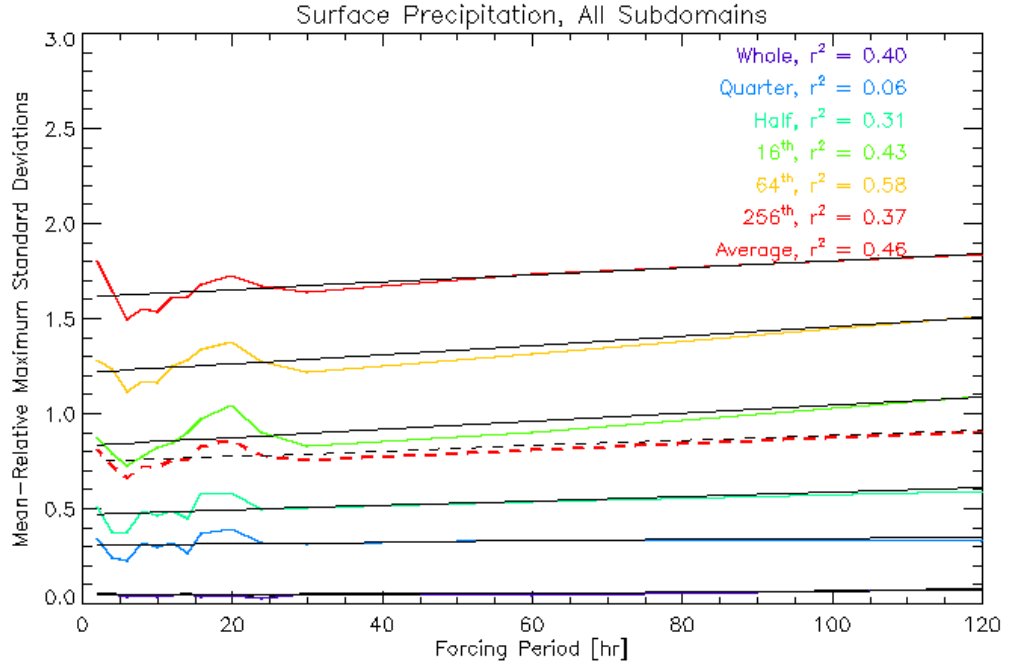
ture that is present in each case is that the maximum standard deviation increases with

decreasing subdomain size, as expected and as noted previously. We also see that there is a slight tendency for the maximum standard deviation to increase with increasing period length. The only exception to this trend is NPC for the 256th subdomain, which shows a trend line that slightly decreases with period. Each of the average trends are positive. The shapes of the curves tend to vary between variables but to a lesser extent within variables, and the curves tend to be more linear for larger subdomains. Most deviations from linearity occur at the shortest periods, and when this occurs, such as for small subdomains in the surface precipitation case, the curve is vaguely logarithmic except for a maximum near the 20-hour forcing period. The case for a linear relationship is weakened somewhat in light of the corresponding correlation coefficients listed in the figures. Correlations are greatest for cloud fraction and cloud mass flux and weakest for NPC. No correlation exceeds 0.77 and most are below 0.45. It is likely that a better relationship could be teased from a larger dataset.

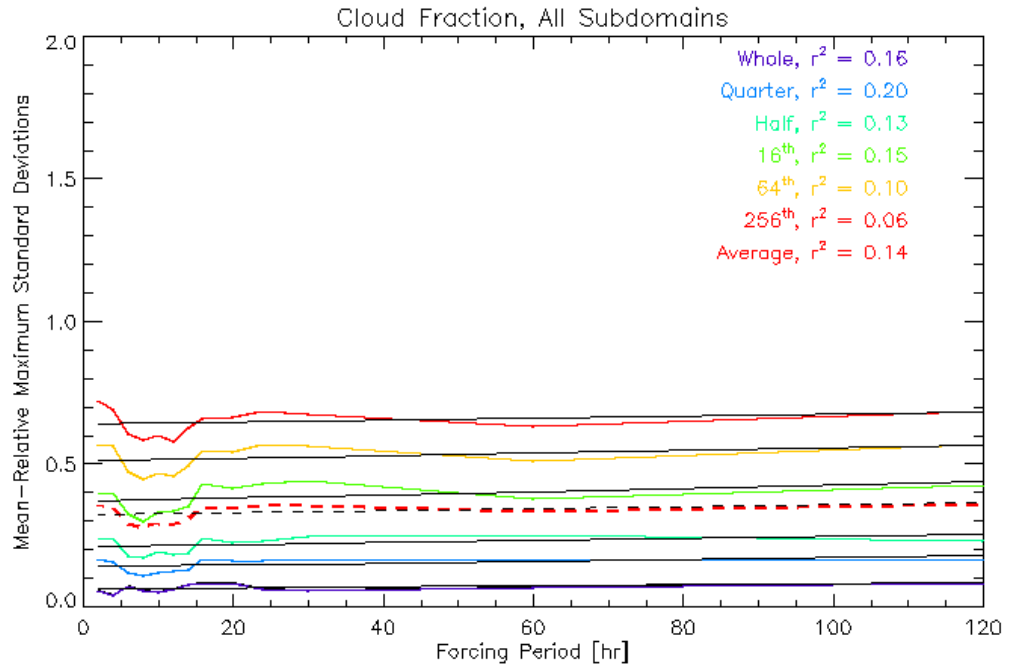
Additionally, Figure 5.51 shows the application of the same technique to the coefficient of variation. As we have seen, the CV increases with decreasing subdomain size. Now we see that it also increases slightly with increasing period length. Similarly to the case of the standard deviation, the trends appear to be nearly linear with deviations from such linearity mainly when the large-scale forcing is changing rapidly. Also once again, the correlations defining the quality of the fit are generally poor and may improve with supplementary data. Overall, there is just a slight (possibly linear) tendency for the variability to increase with period.

While it has been shown that there is very little dependence on the forcing period length (adjusted for the shift in the timing of the response), the extended analysis has also

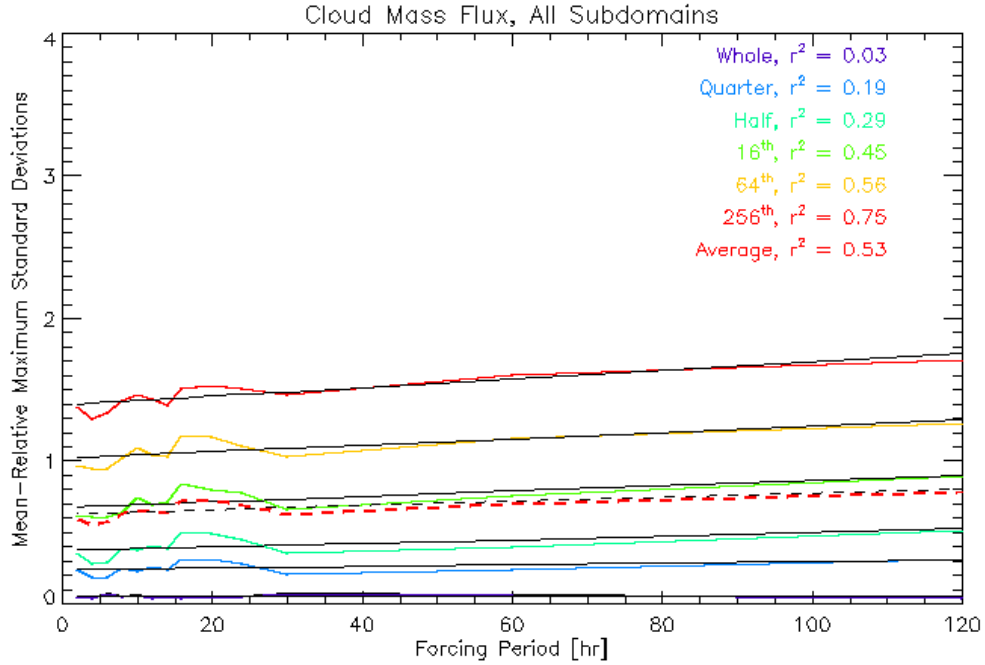
been applied so that the dependence on subdomain size can be better quantified. Figures 5.52 and 5.53 show the results of this analysis of surface precipitation rate for the F08 simulation. When comparing these values to subdomain size, we see that in the case of



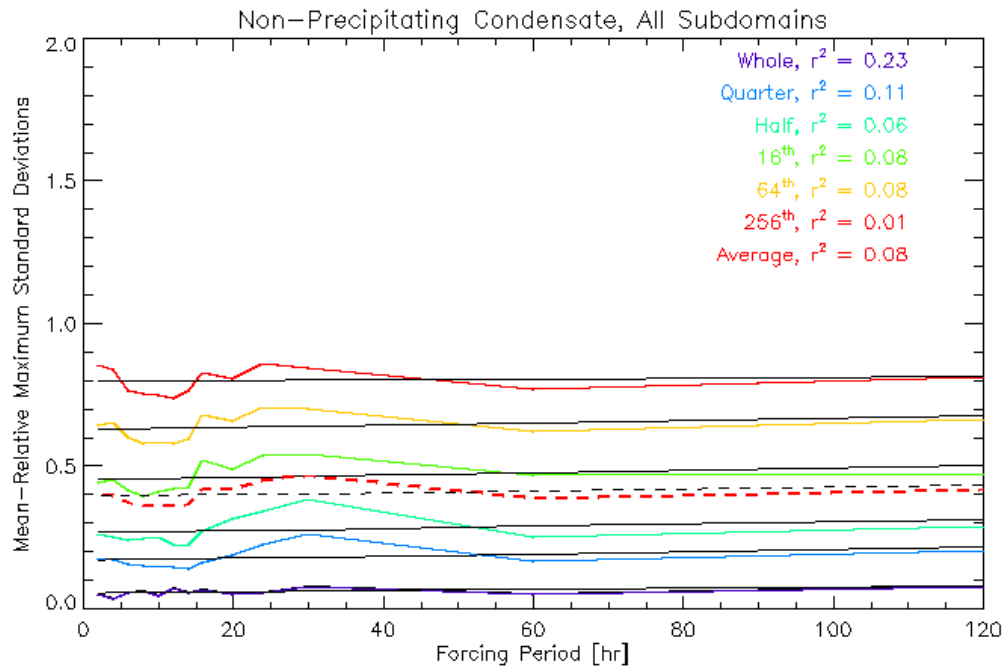
a.



b.



c.



d.

Figure 5.51. As in Figure 5.50 but for the coefficient of variation at the maximum standard deviation. Here, the dashed red line denoted the mean of the colored curves.

Figure 5.52, which shows the surface precipitation rate standard deviation, that there appears to be a strongly nonlinear trend of increasing variability with decreasing area. In Figure 5.53, we see that the CV also appears to increase nonlinearly with decreasing do-

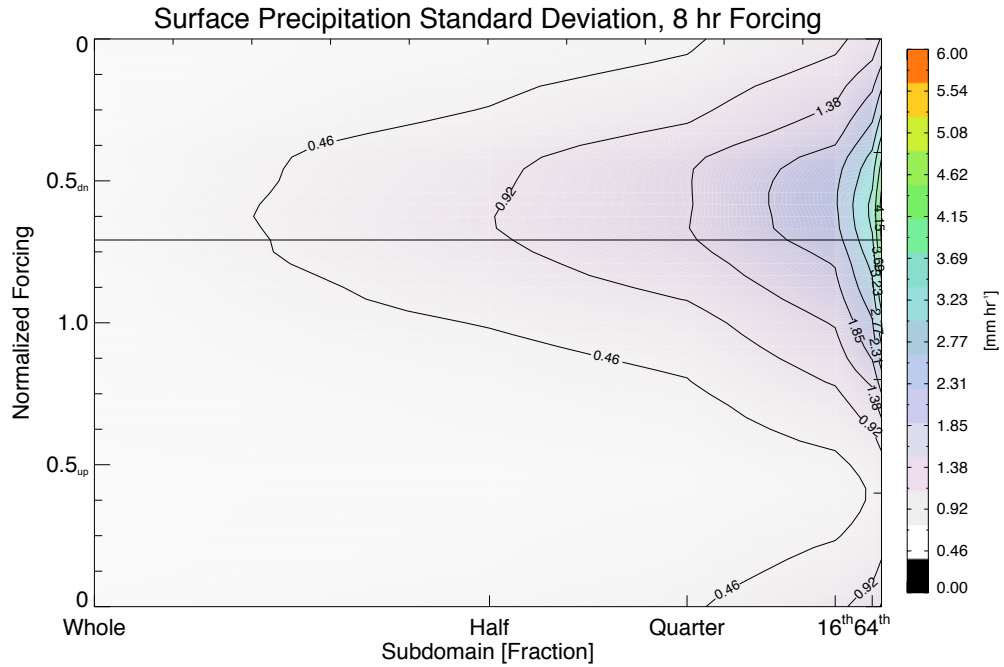


Figure 5.52. As in Figure 5.43 but for F08 for all subdomains. The rightmost point on the abscissa corresponds to a 256th domain.

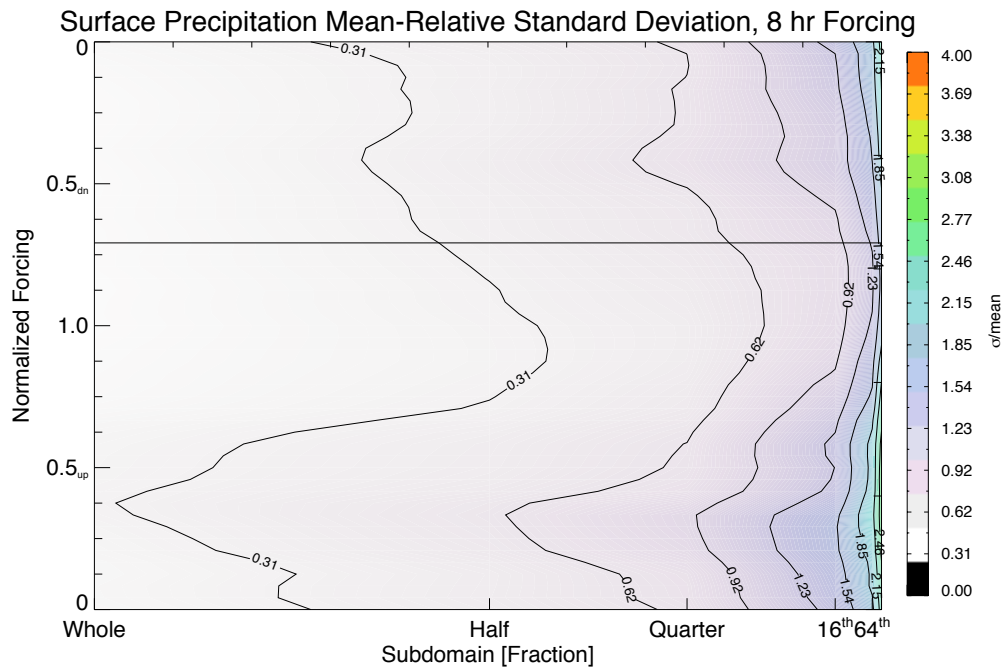


Figure 5.53. As in Figure 5.52 but the coefficient of variation.

main area. Further, as we move to larger forcing periods, such as F120, shown in Figures 5.54 and 5.55, similar nonlinear trends are present, though the position of the data's

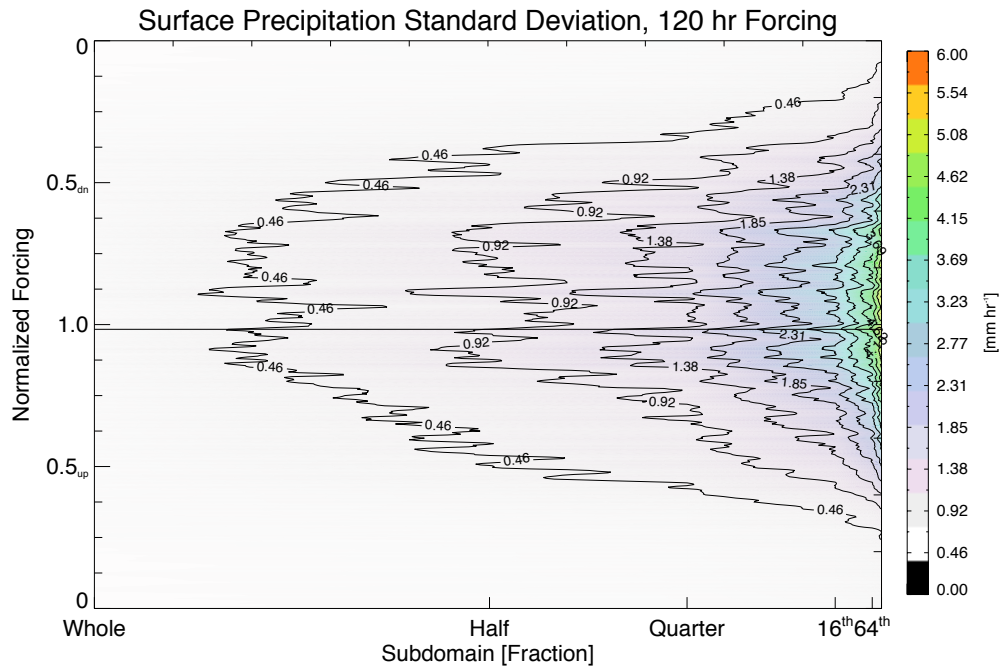


Figure 5.54. As in Figure 5.52 but for F120.

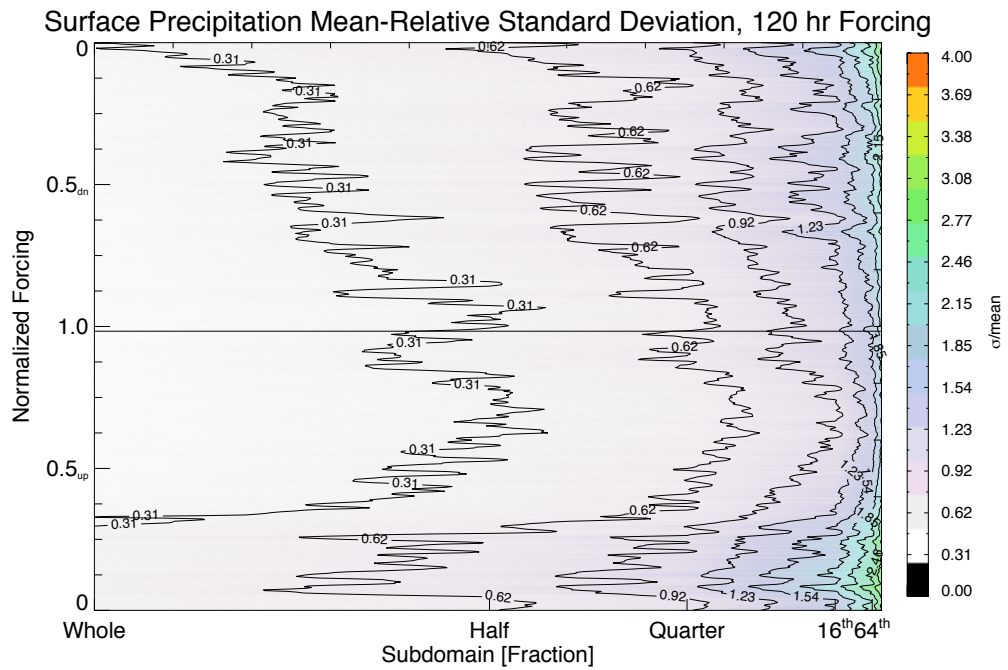


Figure 5.55. As in Figure 5.53 but for F120.

maxima have shifted relative to the normalized forcing due to the change in lag. These

figures also highlight the increase in the variability of the standard deviation and CV as period length increases. Whether this is simply an artifact of significantly longer time for which there can be extremes in a given realizations is likely but unclear.

Similar structures are found when considering cloud mass flux, cloud fraction, and non-precipitating condensate. As in the case for the period dependency analysis, those figures have been omitted, and summary plots have been used in their place. Figure 5.56 shows normalized domain area versus the maximum standard deviation. Each black curve is one periodic forcing simulation, and the green line is their average. There is no coherent pattern as to the position of the black curves relative to their forcing period length. Therefore, no distinction is made.

In terms of a functional relationship, the average curve is best approximated by an exponential decay function, such that

$$\sigma = c - b \ln(A) \quad (5.10)$$

where b and c are constants that vary depending on the variable in question, σ is the standard deviation, and A is the subdomain area.¹¹ The constant, b , controls the shape of the curve, while c most strongly controls the area at which the standard deviation becomes zero (greater c corresponds to a larger area). Conversely, this relationship can be rewritten such that the area is an exponential decay function of the standard deviation:

$$e^{\frac{c-\sigma}{b}} = A. \quad (5.11)$$

The data corresponding to the parameters of the best fit for the green (mean) curves in

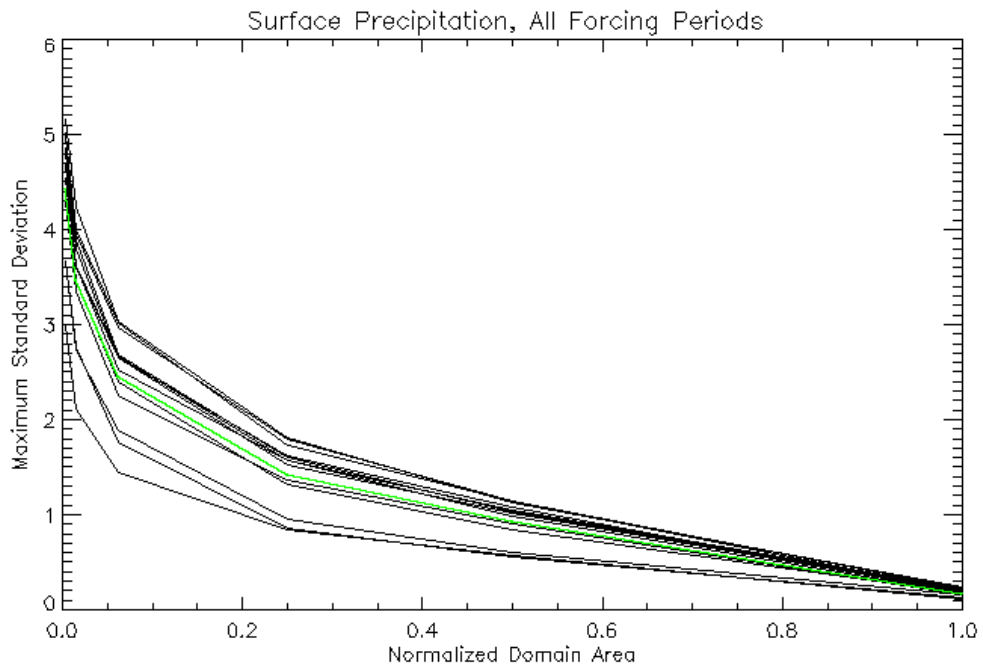
¹¹ One may expect, from prior statistical experience, that there would be a $1/\sqrt{N}$ dependence rather than the relationship shown. It should be noted that a curve of this form did not provide nearly as good of a correlation. In this case r -squared was usually greater than 0.99, whereas in the case of a curve corresponding to the $1/\sqrt{N}$ relationship, r -squared was on the order of 0.7, representing a significantly weaker correlation.

Figure 5.56 is found in Table 5.1. The high correlation coefficients indicate a very good fit to the characterization of this relationship. However, use of the standard deviations in this form does little reveal systematic variations among the different variables.

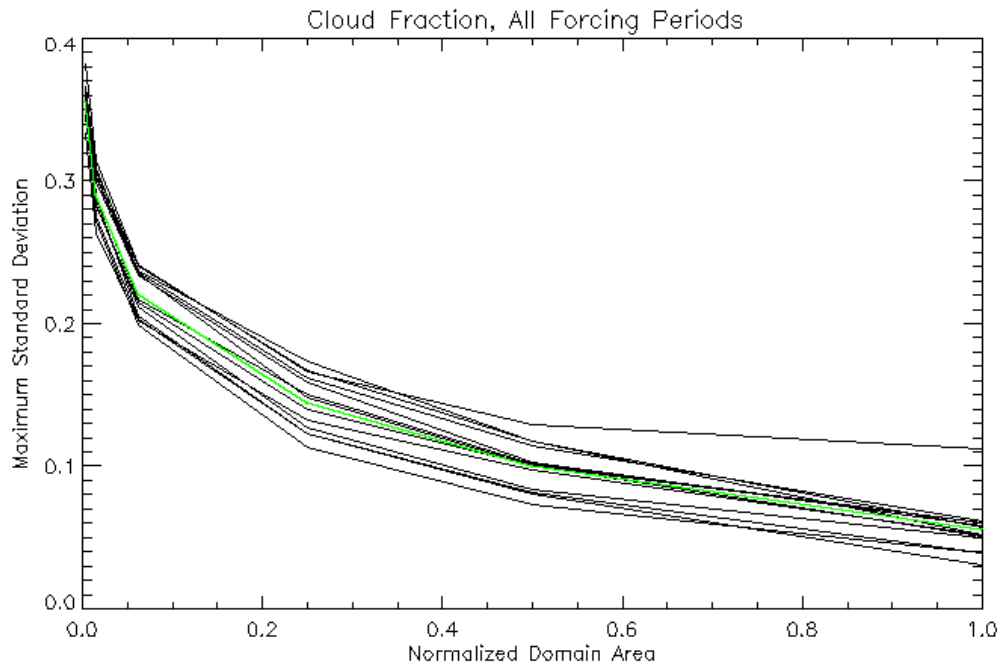
In order to adjust the values being considered so that they are comparable amongst different variables (dimensionless), the maximum standard deviations (Figure 5.56) have been transformed into their corresponding coefficients of variation (Figure 5.57). Analyzing these values in the same way as the maximum standard deviations, we see that once more the data have a logarithmic/exponential form (see equations 5.10 and 5.11). This should not surprise, since the only change has been division by a constant (the mean, in this case). Note that because of this, the correlation coefficient values (Table 5.2) are exactly the same as in the previous case. The important changes have occurred in the constants, most notably, b , which controls the shape.

The apparent pairing of values of b tend to confirm earlier suspicions that there is a clear difference in variable types, that being the “storage” variables, NPC and cloud fraction, and the “flux” variables, surface precipitation rate and the cloud mass flux (referred to before as the cloud and precipitation variables, respectively). These terms are best explained by looking at the convective process as beginning with the vertical flux of mass to form clouds, as measured by NPC and cloud fraction, where the water mass is stored until it is fluxed out of the system as precipitation. At any rate, the pairing is such that the average curve is steeper for the flux variables. Additionally, the curve for the flux variables tends to lie above that for the storage variables. This means that the flux variables are more variable, and the storage variables are less variable. This is wonderfully intuitive, since as they are defined here, the storage variables can be both added to

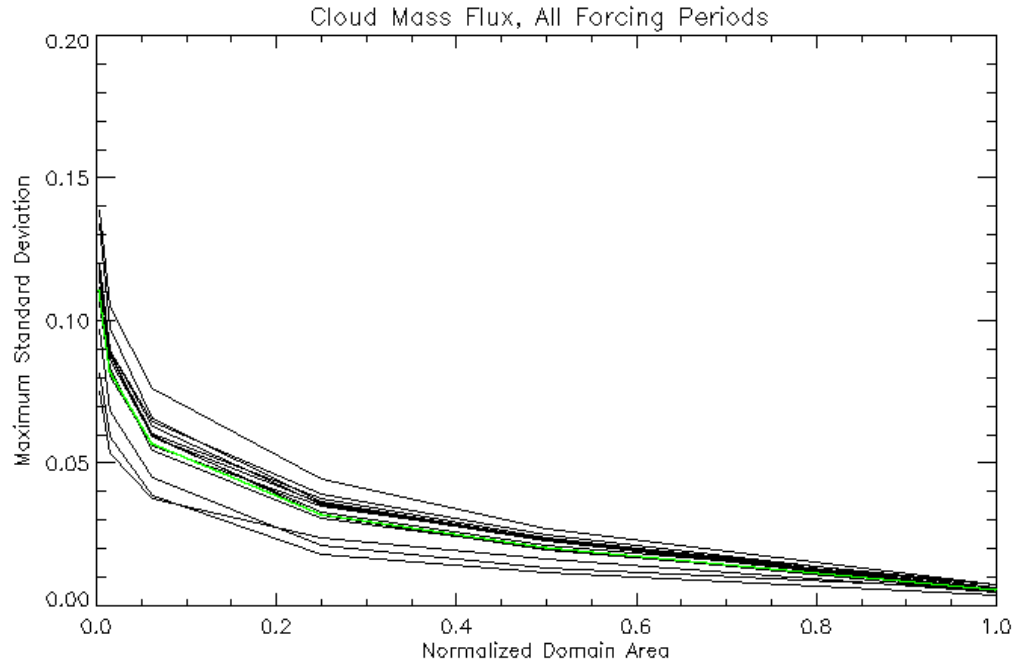
and subtracted from, while the individual flux variables only act one way. All four variables are directly related to convection but in different ways. To carry the analogy along ad nauseam, convection is a casino in Las Vegas, mass flux is the entrance, precipitation is the exit, and the cloud fraction and NPC are the gamblers.



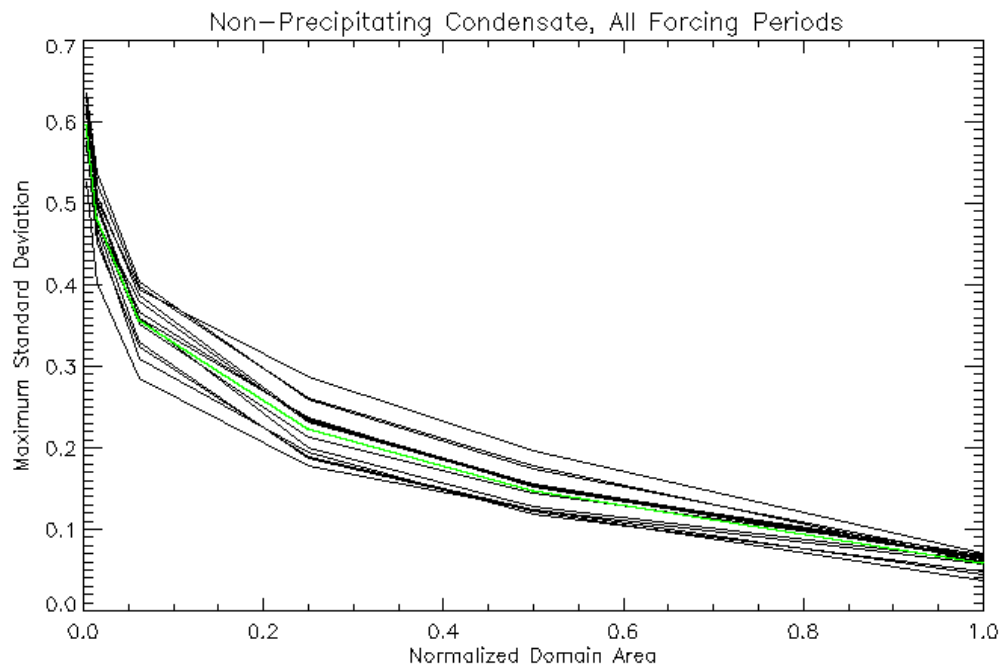
a.



b.

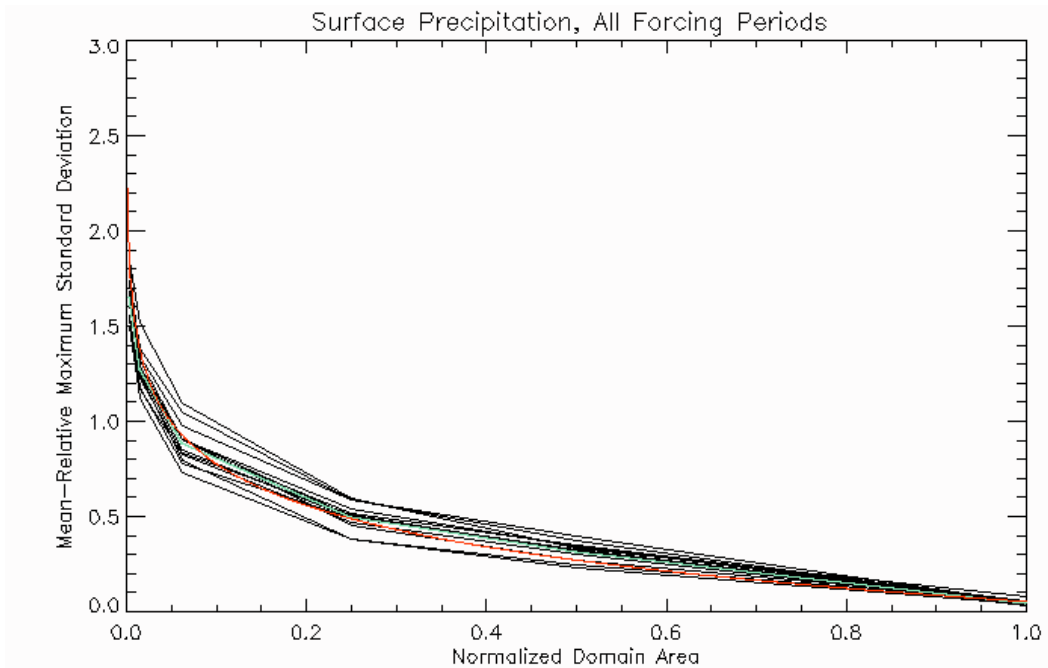


c.

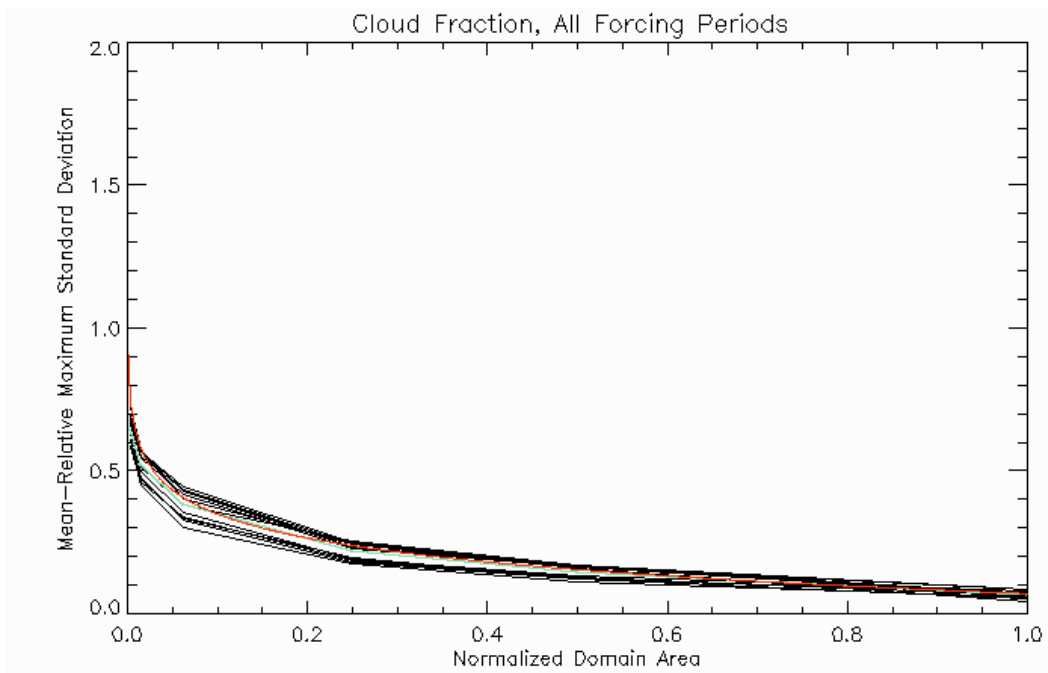


d.

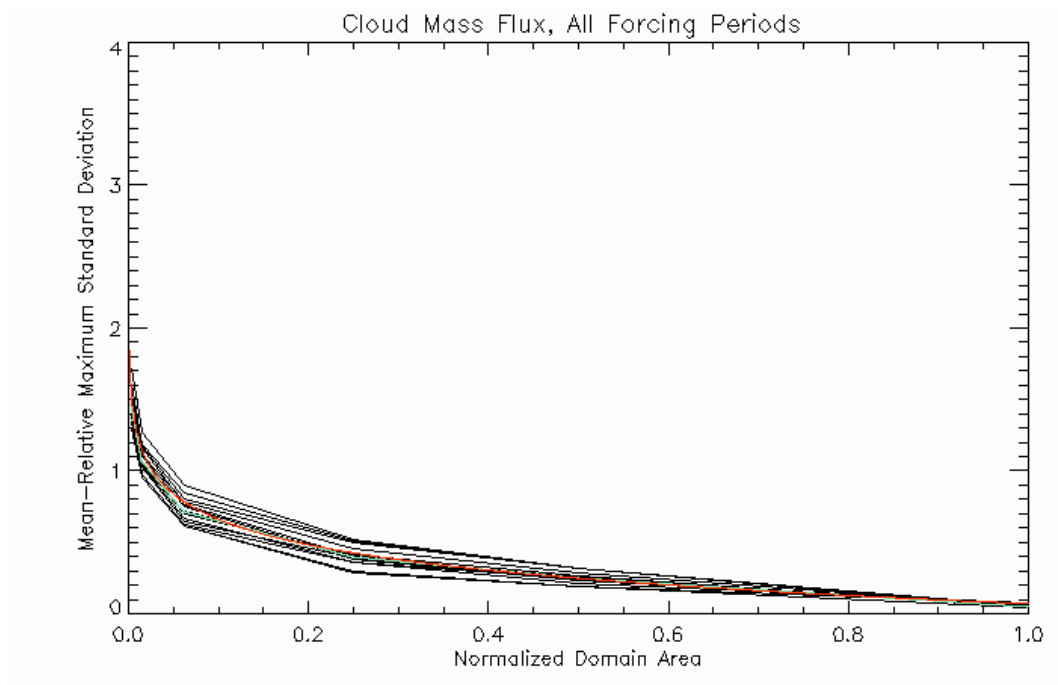
Figure 5.56. Maximum standard deviation versus normalized domain area for all periodic forcing simulations for (a.) surface precipitation rate, (b.) cloud fraction, (c.) cloud mass flux, and (d.) non-precipitating condensate. The green line is the mean of the black curves. It's “mean green”...get it?



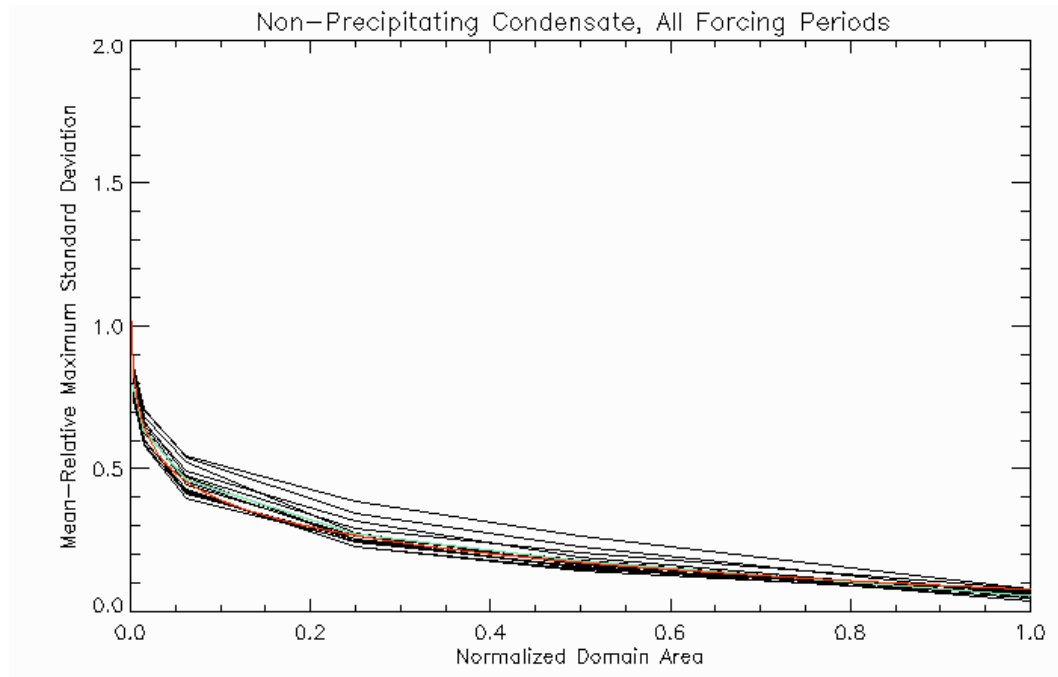
a.



b.



c.



d.

Figure 5.57. As in Figure 5.56, but for the coefficient of variation. Additionally, the red lines denotes the trend lines fit to the green curves.

Table 5.1. List of parameters b and c corresponding to the best fit curve (of the form given by equation 5.10) for the green curves of Figure 5.56 and the correlation coefficient for each best fit curve.

Variable	b	c	r^2
Surface Precipitation Rate	0.759	0.330	0.9976
Cloud Fraction	0.053	0.065	0.9974
Cloud Mass Flux	0.019	0.006	0.9988
Non-precipitating Condensate	0.097	0.076	0.9962

Table 5.2. List of parameters b and c corresponding to the best fit curve (of the form given by equation 5.10) for the green curves of Figure 5.57 and the correlation coefficient for each best fit curve.

Variable	b	c	r^2
Surface Precipitation Rate	0.283	0.091	0.9976
Cloud Fraction	0.106	0.075	0.9974
Cloud Mass Flux	0.253	0.054	0.9988
Non-precipitating Condensate	0.132	0.084	0.9962

We conclude this section by restating a few important findings. One, the variability between realizations has a small positive relationship with increasing periodic forcing length that appears to be due to an extension of the time in which convection is active. Two, the variability does, indeed, scale with the mean, but the scaling factor is not, but close to, constant. The scaling factor tends to decrease with increases in the mean. Three, the variability between realizations is logarithmically dependant upon the subdomain area.

5.2.6 Correlation Analysis

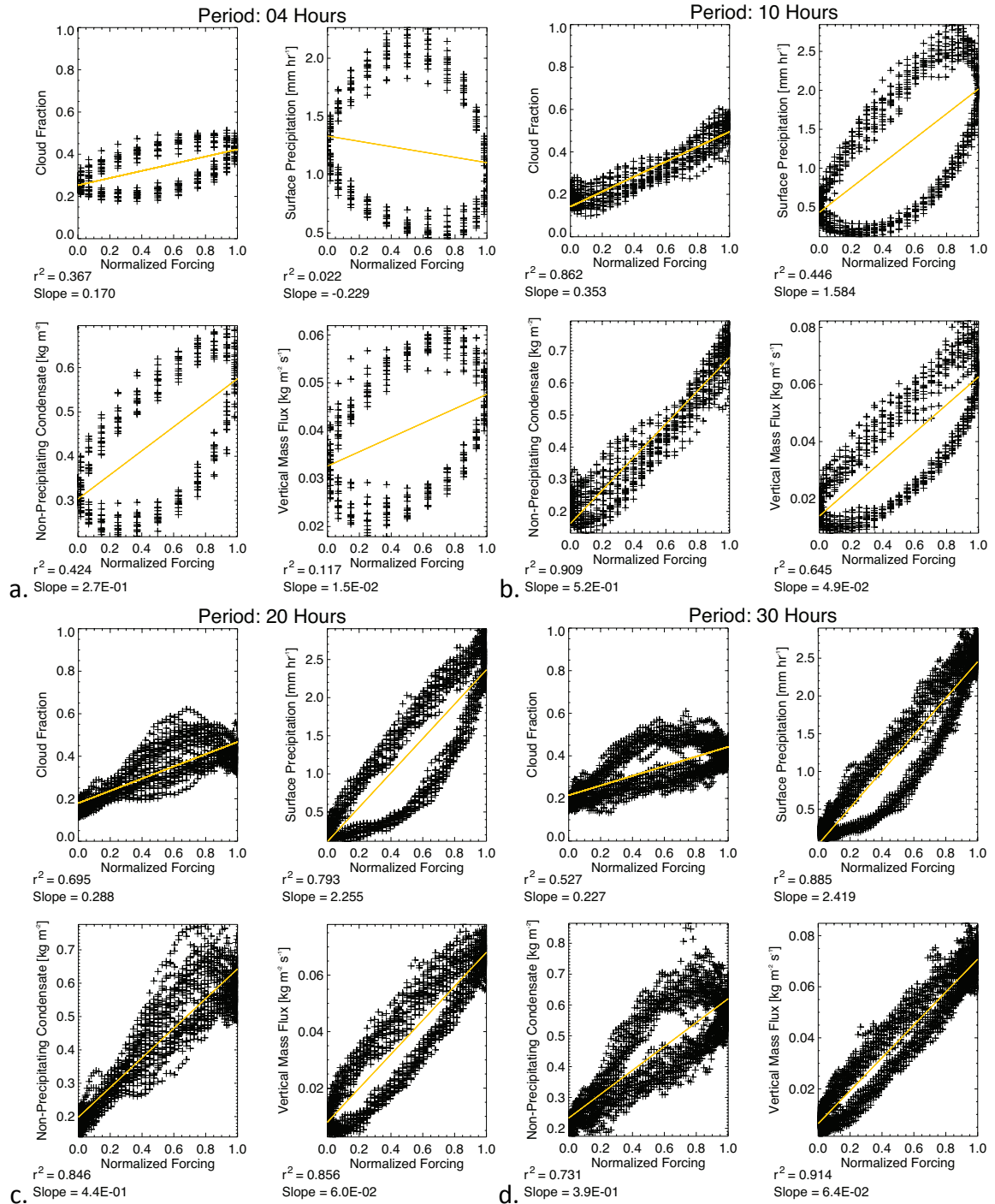
There are a number of ways in which one could determine whether the results of a

simulation tend to approximate statistical equilibrium between the large-scale and convective-scale atmospheric processes. A few of these have been presented in previous sections, and now we shall add another based on correlation analysis. In a very nearly equilibrated system, the forcing should lead the response in time with negligible lag, and in the case of a periodic forcing, the response should periodically rise and fall in accordance to the temporal structure of the forcing. For instance, if we refer once more to Figure 5.2a, which shows the mean precipitation rate from a series of constant forcing simulations, we would expect that for a periodic forcing simulation that a compilation of the data at all times in the simulation would look the same.

Testing each of the periodically forced simulations in this way will provide additional insight into the point at which statistical equilibrium is approximated in terms of the length of the period. Further, the same method can also be applied to determine the point among varying domain sizes at which statistical equilibrium is approximated. In each case, the full time series of the full domain means for cloud fraction, surface precipitation rate, non-precipitating condensate, and cloud mass flux are correlated with the the normalized periodic forcing.

The results in scatterplot form, seen in Figure 5.58 for simulations F04, F10, F20, F30, F60, and F120, take the shape of hysteresis loops. Whether the upper or lower portion of the loop is indicative of the response coincident with increasing or decreasing forcing is dependant on the period and variable in question. For instance, the lower portion of the scatterplot in Figure 5.58a (upper left panel) for cloud fraction in the F04 simulation corresponds to increasing forcing, and when the forcing period is changed to 60 hours (Figure 5.58e, upper left panel) it is the upper portion of the loop that corre-

sponds to the increasing forcing. Recall that the cloud fraction maximum leads the forcing maximum for a longer period. In determining the correct orientation of this upper/lower, increasing/decreasing distinction, please refer to the figures in Section 5.2.3.



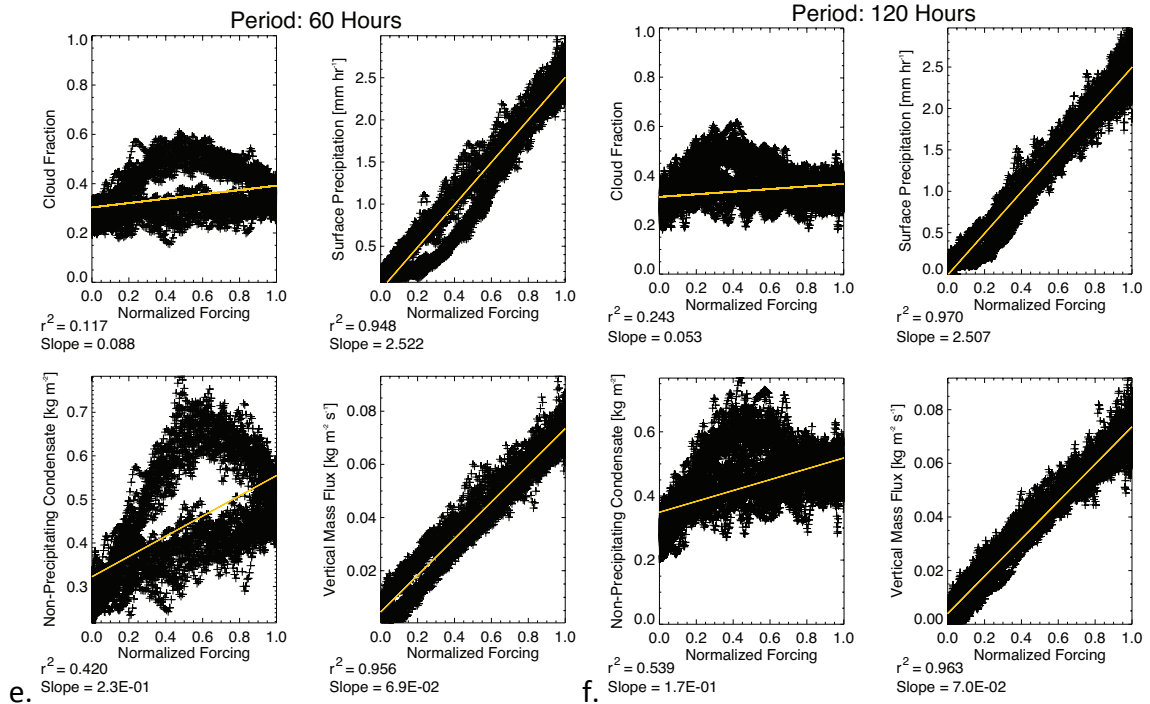


Figure 5.58. Scatterplots for the full 15 cycles of the F04 (a), F10 (b), F20 (c), F30 (d), F60 (e), and F120 (f) simulations of the full domain average values of cloud fraction (upper left), surface precipitation rate (upper right), non-precipitating condensate (lower left), and cloud mass flux (lower right) versus the normalized forcing. The golden line is the linear regression trend line. The slope of this line and the correlation coefficient (r^2) are given to the lower left of each panel.

There are a number of interesting features in Figure 5.58. One is that we are able to see this aforementioned shift between leading and lagging forcings quite clearly. Another is that we are able to get a better sense (visually) for the true range of variability of each variable, beyond that of a reported standard deviation. Bearing in mind the relationship between the normalized forcing and time it is once again evident that the high frequency variability that is seen in the longer simulations is on the order of the period of the shorter simulations. This once more demonstrates the reasons for the high frequency variability seen in the plots of means and standard deviations seen previously.

Perhaps, though, the most important feature to be gleaned from Figure 5.58 is the information surrounding the correlation and regression and the way these features change

with period. The most striking pattern is the tendency for the data points to “hug” the regression line more tightly as the period length is increased. In other words, there is a tendency for standard deviation at a particular value of the normalized forcing to decrease with increasing period. Note that this is not the same measurement as the standard deviation in the previous composite analyses as it considers the value when the forcing is *both* increasing and decreasing. This motion toward the regression line is indicative of progress toward getting the same response from a forcing regardless of whether the forcing is increasing or decreasing; it is progress toward approximate statistical equilibrium

Additionally, we see that as the period is increased, there is convergence toward a single regression slope, especially in the case of the “flux variables,” surface precipitation rate and cloud mass flux. In the case of the “storage variables,” cloud fraction and non-precipitating condensate, one may argue the case that they are converging on a slope but not in a monotonic fashion. Certainly, due to the difference in slope between the regressions for these variables in simulations F60 and F120, there is not sufficient evidence to state this convergence as fact. The pattern that is apparent is one in which the slope initially increases as the period length is increase, and then it tends to decrease toward the end of the available data.

The case for the convergence of the slopes for the flux variables is stronger, as they (generally) monotonically increase from short to long periods, with a slowing of the rate of change toward longer periods. More interesting, perhaps, are the values to which the slopes converge. Let’s focus on the case of the surface precipitation rate. Referring, once again, to Figure 5.2a, the expected slope for a simulation run at an approximation to statistical equilibrium is $\sim 2.5 \text{ mm hr}^{-1}$ per a full increase of the large-scale forcing, and

interestingly enough, that is precisely the value of the slope for simulations F60 and F120. This is supportive of the idea that while statistical equilibrium is not well approximated for quickly varying large-scale forcings, it is for slowly varying forcings.

However, there is one more element that is required to enter this idea into the realm of quasi-fact. That is the correlation. A slope closely matching that derived from the equilibrium simulations is essentially unsupportive if the correlation is not strong, as well. In the case of surface precipitation, the correlation also tends to increase with increasing period length. The correlation coefficient at F60 is 0.948, and it is 0.970 for the F120 simulation. Therefore, taking the regression slope and the correlation together, we have very strong support for the dependence of the approximation of statistical equilibrium upon the forcing period length in the case of the flux variables.

The correlation coefficients for the storage variables do not increase evenly. In fact, they are not near a maximum in either F60 or F120. This seems to be related to the shift in the forcing/response lag that moves the maximum response to a relatively earlier location. It is suspected that since it appears that the shift in the lag seems to be reducing in a relative sense with increases in the forcing period, these correlations will improve but never be very strong due the lag. It is likely, though, that a more stable slope would be encountered for simulations with more slowly varying forcings.

The other variable that needs to be checked against the correlations is the change in subdomain size. Admittedly, the results are intuitive, predictable, and not too terribly interesting, but they are shown here for completeness. We shall take as the example the cloud mass flux variable. Figure 5.59 shows the scatterplots, regression lines, and correlation coefficients for the whole, half, quarter, 16th, 64th, and 256th domain as applied to

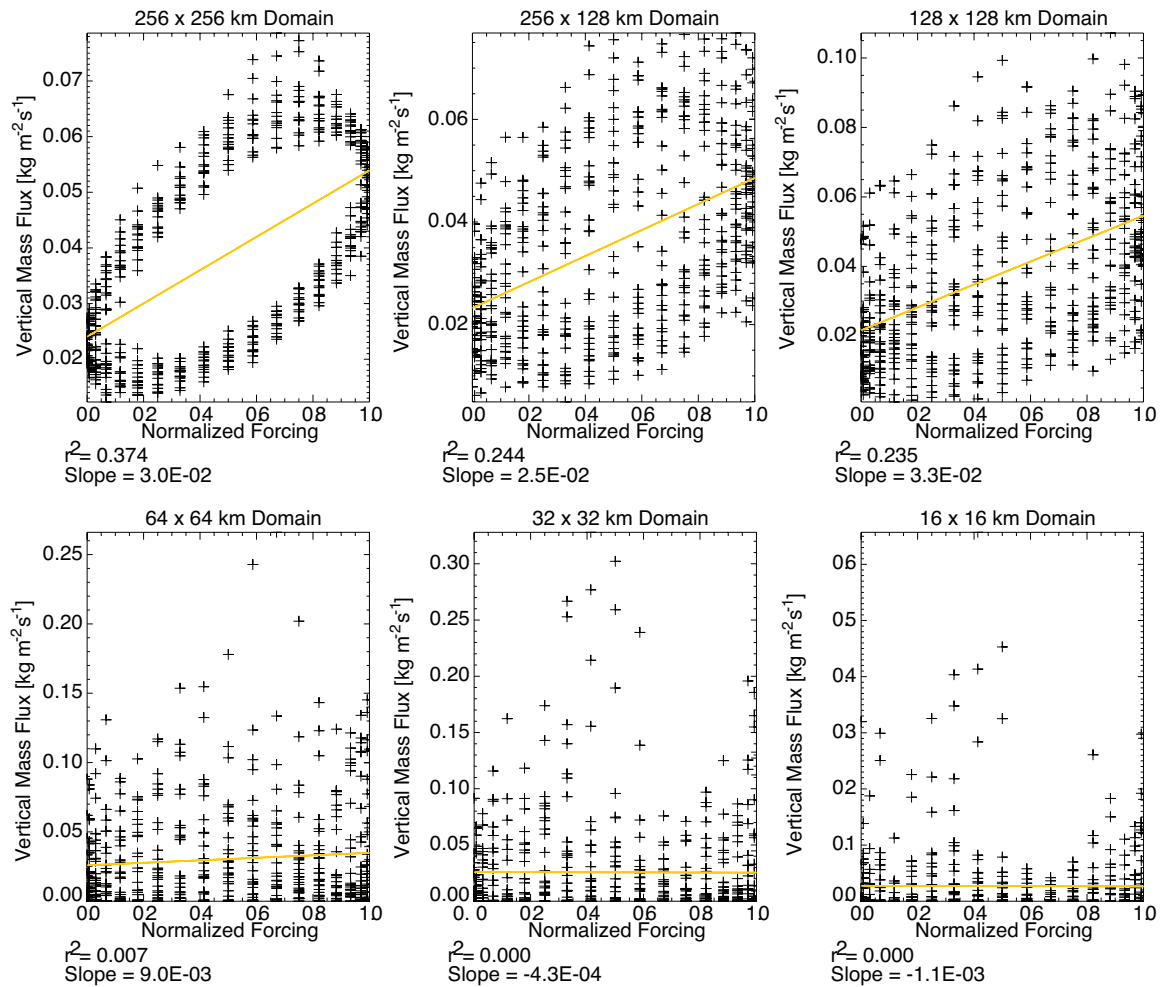


Figure 5.59. Scatterplots for the full 15 cycles of the F06 simulation of the full domain (upper left), half domain (upper center), quarter domain (upper right), 16th domain (lower left), 64th domain (lower center), and 256th domain (lower right) average values of cloud mass flux versus the normalized forcing. The golden line is the linear regression trend line. The slope of this line and the correlation coefficient (r^2) are given to the lower left of each panel.

the cloud mass flux. From these plots, we get a better understanding of the range of variability at each subdomain. Note that the ordinate axis values are variable. The correlation coefficients fall off quickly with decreasing domain size. This trend clearly shows that simulations performed at small grid spacings are not well approximated by statistical equilibrium. There is not much in the way of a trend for the regression slopes. However, one may note that there may be increase in regression slope with decreasing domain size,

but this is generally due to the introduction of very large average cloud mass flux values that are the result of averaging over such a small area and it does not hold over all averaging areas. Additionally, there are instances when the domain size is very small for which the slope becomes negative due to the sheer number of measurements that are much smaller than the maximum values for a particular subdomain.

Extending this analysis, Figures 5.60 and 5.61 show the dependence on domain size for the F20 and F60 simulations, respectively. We see much the same trend as in the F06 case, with correlation coefficients falling toward zero rather quickly. The regression slopes also lack a coherent trend associated with changes in the domain size. Comparing all three cases, however, we gain further insight into the trends that are associated with changes in the large-scale forcing period length. The ability for the data to correlate better with increasing period is visible in not only the full domain case but also for smaller averaging areas. At any rate, it is clear that this tendency for a strong correlation breaks down at domains of 16^{th} or smaller.

As a result of the correlation analyses, we have a broader understanding of the applicability of the quasi-equilibrium assumptions in terms of its dependencies on the frequency of variation of a large-scale forcing and the size of a given computational area. The idea that variability between realizations increases for smaller domains and smaller period lengths (independent of whether the forcing is increasing or decreasing) has been reinforced, and the dividing line of acceptable deviation from QE has been made more clear. It lies at the intersection of large-scale variations that are on the order of the diurnal cycle on a grid spacing scale that is between 256 km and ~ 181 km based on the above data.

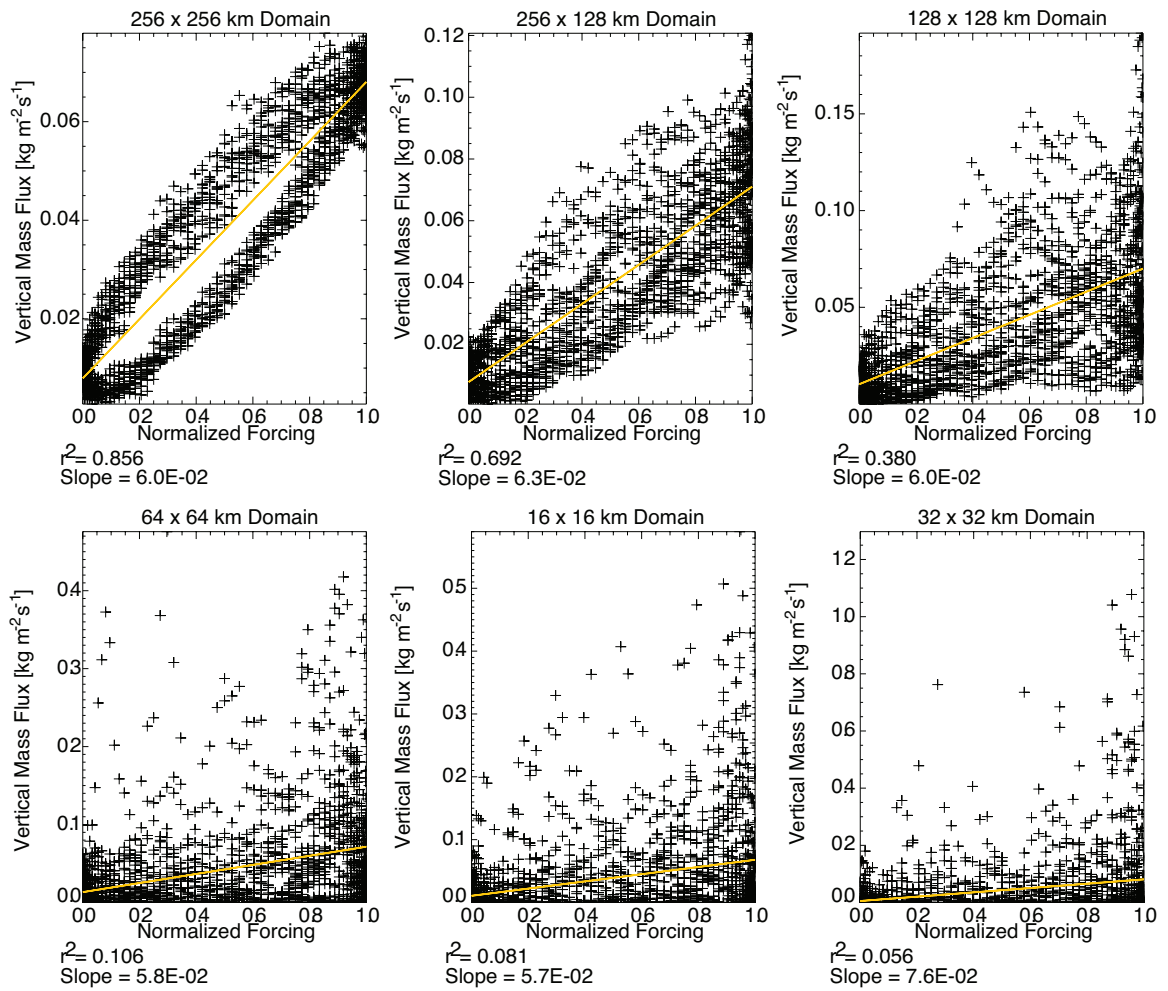


Figure 5.60. As in Figure 5.59 but for the F20 simulation.

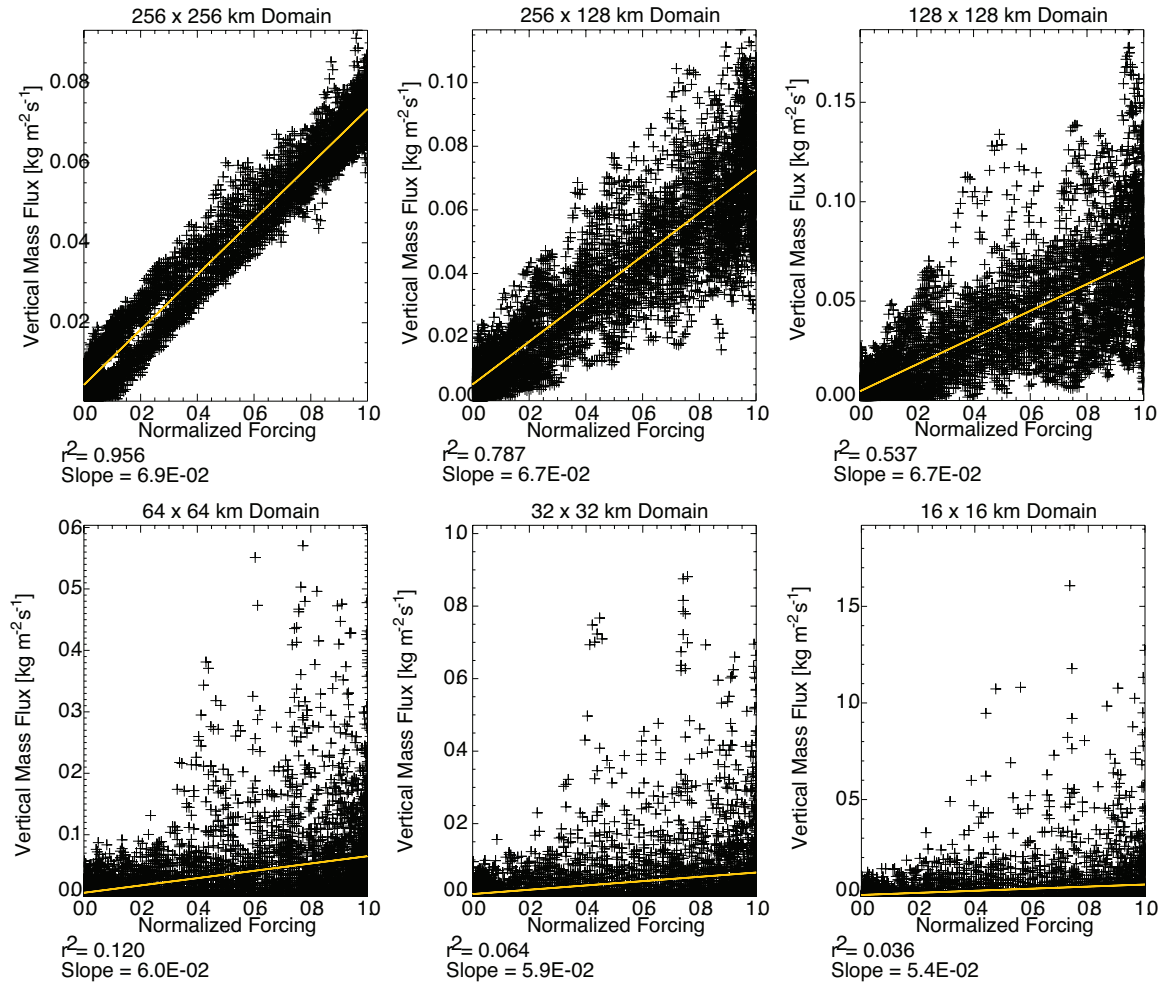


Figure 5.61. As in Figure 5.59 but for the F60 simulation.

5.2.7 *Probability Density Function Variations*

One of the main tenets of how this research might be able to aid ongoing development of stochastic convective parameterizations is by defining limits for such parameterizations. While some such limits can be gleaned from results already presented, additional and more exact limits can be defined with a basis in the probability density functions (PDFs) of some convection-related variables. For this analysis, PDFs for the domain mean column liquid water (CLW, also known as the liquid water path), non-precipitating condensate, and surface precipitation rate have been created. From these PDFs we will be able to better represent the shape of the variable distributions, which has as of yet has not been made clear. Previous discussion has focused primarily on the mean and the standard deviation but said little about the degree of skewness of the variables.

To begin, we shall examine an example distribution for the surface precipitation rate in Figure 5.62. This example has been taken from F14 and represents the frequency of occurrence (as a fractional area) of a certain bin of surface precipitation rate averaged over the full domain for the entire length of the simulation. The text on the figure that says “0 =” points to the fractional area for which precipitation is zero. There is nothing particularly special about this simulation; in fact, it has the characteristic shape that is seen in all simulations, with the only difference being the length of the positively skewed tail of the distribution. As one might expect, larger values become more prevalent for longer forcing periods. However, on plots like that in Figure 5.62, the difference is barely noticeable, visually, and therefore this is not shown. The important relationship to see here is that there is an inversely exponential relationship between areal coverage and precipitation rate. Additionally, this relationship also holds for the variables of non-

precipitating condensate and column liquid water (Figures 5.63 and 5.64, respectively), except for the fact that, on the average, NPC is never exactly zero anywhere.

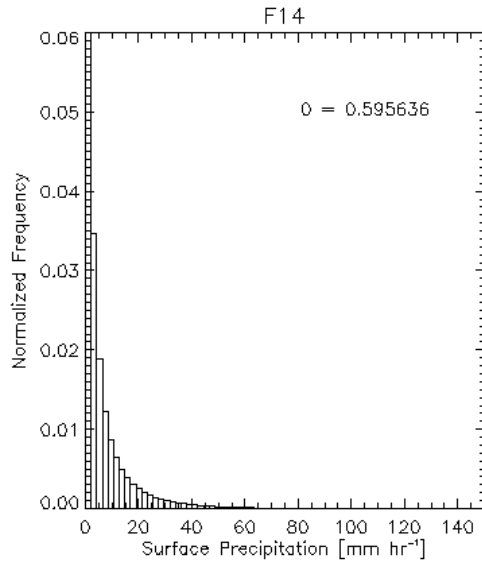


Figure 5.62. Probability density function for the surface precipitation rate calculated over the whole domain and averaged over the entire length of the F14 simulation.

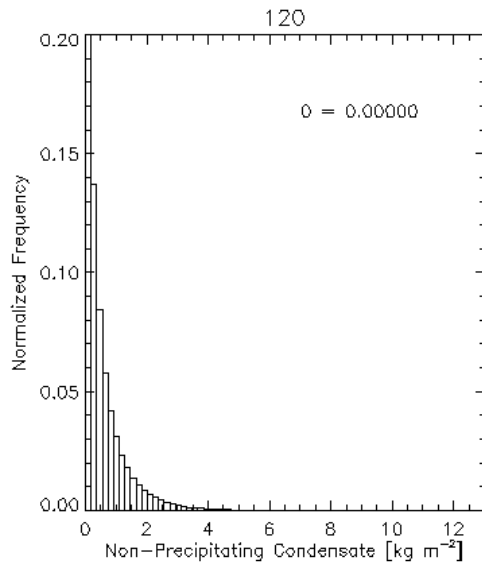


Figure 5.63. As in Figure 5.62 but for non-precipitating condensate in the F120 simulation.

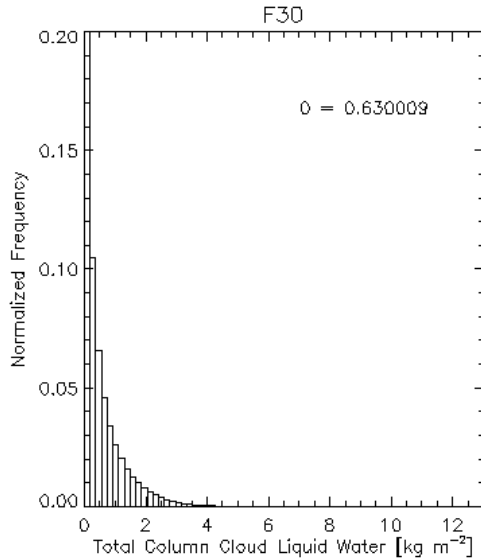


Figure 5.64. As in Figure 5.62 but for column liquid water in the F30 simulation.

As stated, these figures show the results for the average over the full length of the simulations. While this result is simple to understand, things become slightly more complicated when we begin to track the PDF as it changes through time. Figure 5.65 shows a series of PDFs for individual instances in the composite curve. This surface precipitation data are taken from the F12 simulation, and the data for other variables and simulations are very similar to what is seen in this case. The title of each plot denotes the percentage of the realization (one iteration of the large-scale forcing curve) that has passed until that point. The main feature through the cycle is the shift in the amount of rain-free area noted in the figure text. Early and late in the cycle, the forcing is small and the precipitation is relatively low (see previous sections). At this point, the vast majority of the domain (70-80%) is experiencing zero precipitation. As the forcing intensifies along with the precipitation, this precipitation free area diminishes to as low as 30%, though in most simulations it is no less than 40%.

The take-home point is that the shape of the curve really does not change through

time, but the parameters controlling it do.¹² The lengths of the tails vary, generally increasing with forcing, meaning that the mean, standard deviation, and skewness are all variable. Additionally, while the transition seen for the full domain case in Figure 5.65 is rather smooth, it can be choppier for smaller subdomains (not shown). To put it in a humorously redundant way, the variability has variability, which likely also has variability.

Even with all of this data (PDFs at each point in the composite and at all subdomains), we do not have much that can help out a stochastic parameterization. However, from this data, we can create something that will assist in reaching that goal. It can be said that any one of those average PDFs could easily be representative of a particular GCM grid cell, but the problem is choosing the correct one. From the standpoint of stochastic convective parameterizations on the large scale, there is only so much that is deterministic, and there are some more random elements for which we must account. What a GCM “knows” for “certain” is the large-scale forcing. What we seem to know now is what the range of possible responses for that large-scale forcing might be as represented by the set of 15 realizations. Now we shall try to reconcile to two, somewhat.

Based on the above calculations, we have been able to determine 15 possible distributions of various convective features. In terms of the physical distribution of these variables across a range of domain sizes, the mean, standard deviation, and skewness, among other statistics, are known. We can further create a more fundamental set of statistical distributions to describe the above statistical distributions. That is, given the set of 15 means, the mean, standard deviation, and skewness of that distribution can also be

¹² There were a couple of cases in which extreme events caused large deviations from this shape. However, they are only visible under the microscope, if you will, whereby only the smallest precipitation values ($< 0.1 \text{ mm hr}^{-1}$) were considered. Use of bins that obscure that range smooths out such variations.

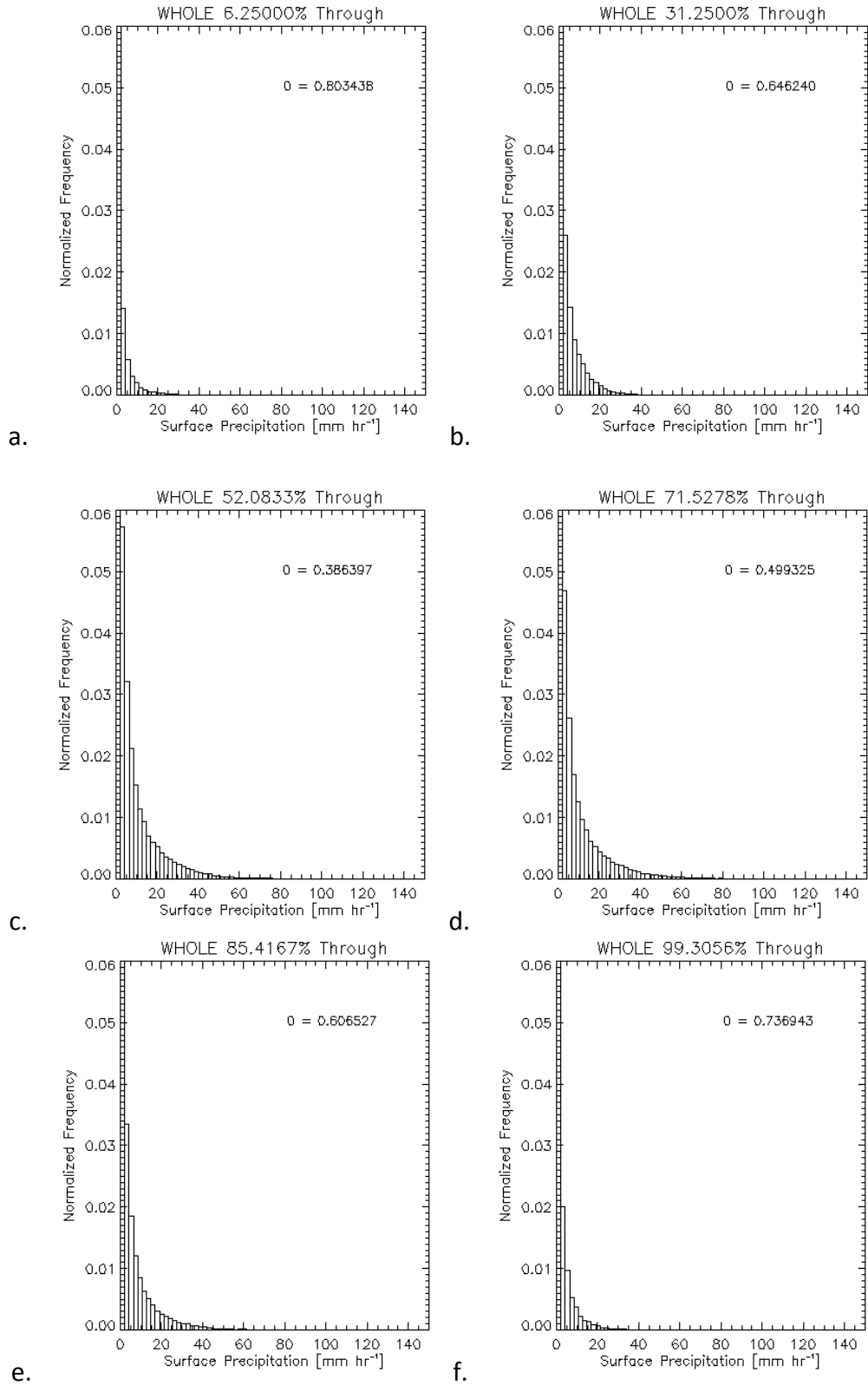


Figure 5.65. PDFs of full domain surface precipitation rate averaged over 15 realizations for noted instances in the F12 cycle.

calculated. This is quite fabulous because it is exactly what we are searching for. We need to know the probability of getting a certain set of statistical parameters for a given large-scale forcing.

While we know a few possible means, standard deviations, and skewnesses for a host of forcing and subdomain combinations, it is still not quite enough. A collection of fifteen possibilities does not seem to be the most solid foundation. However, they can be used to generalize a broader range of possibilities. For instance, since the mean and standard deviation are always positive for the chosen variables, their distribution can be approximated by a three-parameter gamma distribution (Sivapalan *et al.* 1987; Ducharne *et al.* 2000). The distribution can be calculated as:

$$PDF(x) = \frac{1}{\Gamma(\phi)\chi} \left(\frac{x - \mu}{\chi} \right)^{\phi-1} \exp\left(-\frac{x - \mu}{\chi}\right) \quad \chi, \phi > 0 \quad (5.12)$$

$$\chi = \gamma_x \sigma_x / 2 \quad (5.13)$$

$$\phi = \sigma_x^2 / \chi^2 \quad (5.14)$$

$$\mu = \bar{x} - \phi\chi \quad (5.15)$$

Here, the three parameters given by (5.12, 5.13, and 5.15) are derived from the mean (\bar{x}), standard deviation (σ_x), and skewness (γ_x) of the actual distribution of the 15 realizations. In this way, the resulting gamma distribution has the same first three moments. The benefit of this calculation is that we have essentially interpolated the statistics from the realizations into a form that is much easier to manipulate. To be clear, a sample input to this set of equations would be the mean, the standard deviation, and the skewness of 15 means associated with a 30 hour periodic forcing at a resolution comparable to half the full domain size. The result would be a distribution of means approximating the real

population of means. The same can be done with a set of standard deviations.

In the special case that a set of values is negatively skewed, a gamma distribution can be constructed with the absolute value of the skewness by utilizing symmetry about the mean (Ducharme *et al.* 2000). Other problems arise when the skewness is either zero or undefined (*e.g.* $\sigma=0$). In practice, these are artificially adjusted or thrown out. Further, an entirely different method would be required to create an analytical distribution of the skewness for sets with values both positive and negative as the gamma distribution suits monotonic datasets. However, in most cases, the GCM will most likely just require the possible mean and variance values rather than the skewness.

Included in Tables 5.3-5 are the data required to calculate the full spectrum of gamma distributions for the mean surface precipitation rate associated with the maximum composite surface precipitation rate (a specific point in the forcing cycle). The data given in Tables 5.3 and 5.4 are also presented graphically for a different perspective in Figures 5.66 and 5.67, respectively. Note that to get the complete spectrum of possible mean values based on the entirety of the simulation data, this process would need to be repeated at all points in the simulation. Currently, datasets like this only exist for the points corresponding to the maximum and minimum of the composite mean for the surface precipitation rate mean, standard deviation, and skewness. As the calculation is relatively straightforward, such data can be computed quickly if required. Additionally, storing these parameters is not at all demanding of hard drive or memory space. As such, this technique may be a powerful and efficient tool for making an informed introduction of stochastic variability in to climate and NWP models.

Much of what is shown in these tables and figures is information that can be in-

ferred from previously presented data. However, there is at least one unexpected feature that is visible when the data are presented in this way. There appears to be a discontinuity in the general pattern that has been laid out above in the case of the F24 simulation. 24 hours, of course, is the approximate duration of the diurnal cycle. However, there should be no special remnant of diurnal effects in that simulation as there is no active radiation scheme in these simulations. For some reason, there is a relative minimum in the peak composite precipitation rate and its standard deviation amongst realizations. The expected result would be a smooth transition to higher precipitation rates as the period length is increased. That pattern exists from the 2-hr forcing through the 20-hr forcing and from the 24-hr forcing through the 60-hr forcing. A secondary decline is seen going from the 60-hr to the 120-hr forcing. That decline is much less severe, but is also suspect. It is likely that this pattern is not qualitatively the same for any given variable states. There is nothing special about choosing the maximum value in the composite, especially since the maximum value does not necessarily correspond to the statistical point of maximum response as defined in Section 5.2.3; it was simply an easily obtainable example.

Table 5.3. Maximum composite values of domain mean surface precipitation rate [mm hr⁻¹] as dependant upon period length and subdomain size for use in calculating a

gamma distribution.

		Domain Size [Fraction]					
		Whole	Half	Quarter	16 th	64 th	256 th
Period of Forcing [hr]	F02	1.536	1.536	1.603	1.578	1.554	1.540
	F04	2.078	2.078	1.959	1.988	1.986	2.019
	F06	2.274	2.274	2.312	2.161	2.098	2.056
	F08	2.518	2.518	2.566	2.480	2.476	2.459
	F10	2.593	2.593	2.572	2.566	2.655	2.680
	F12	2.587	2.587	2.584	2.614	2.633	2.632
	F14	2.534	2.534	2.747	2.733	2.474	2.338
	F16	2.701	2.701	3.266	3.107	3.024	2.984
	F20	2.682	2.682	2.819	3.253	3.330	3.349
	F24	2.658	2.658	2.765	2.741	2.771	2.755
	F30	2.659	2.659	2.862	3.164	3.237	3.274
	F60	2.690	2.690	3.189	3.416	3.347	3.260
F120	2.393	2.393	2.809	2.904	3.063	3.106	

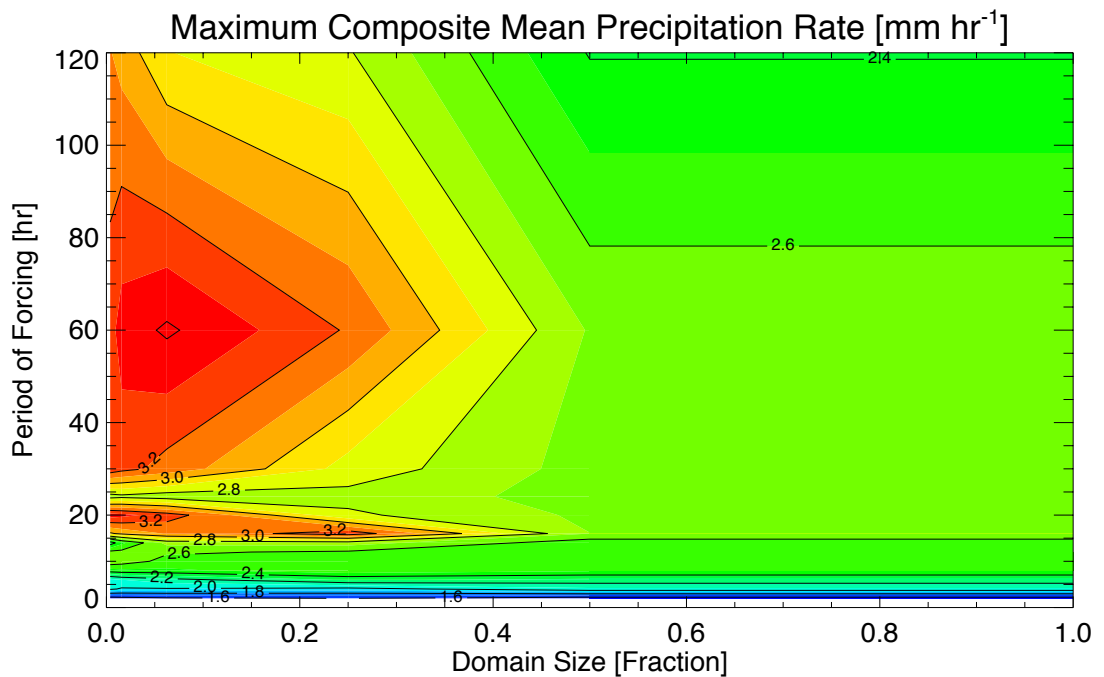


Figure 5.66. As in Table 5.3.

Table 5.4. As in Table 5.3 but for the standard deviation [mm hr⁻¹] of the means associated with the composite maximum.

		Domain Size [Fraction]					
		Whole	Half	Quarter	16 th	64 th	256 th
Period of Forcing [Fhr]	F02	0.095	0.095	0.643	0.804	0.791	0.824
	F04	0.128	0.128	0.746	0.848	0.807	0.785
	F06	0.098	0.098	0.581	0.805	0.907	0.940
	F08	0.135	0.135	0.868	1.258	1.328	1.343
	F10	0.117	0.117	1.135	1.332	1.483	1.539
	F12	0.131	0.131	0.858	1.137	1.142	1.113
	F14	0.146	0.146	1.109	1.496	1.573	1.298
	F16	0.103	0.103	1.491	1.761	1.769	1.741
	F20	0.128	0.128	1.230	1.850	1.980	2.000
	F24	0.089	0.089	1.047	1.114	1.382	1.314
	F30	0.161	0.161	1.355	1.741	1.892	1.892
	F60	0.148	0.148	1.220	1.566	1.580	1.539
F120	0.719	0.719	1.082	1.302	1.984	2.071	

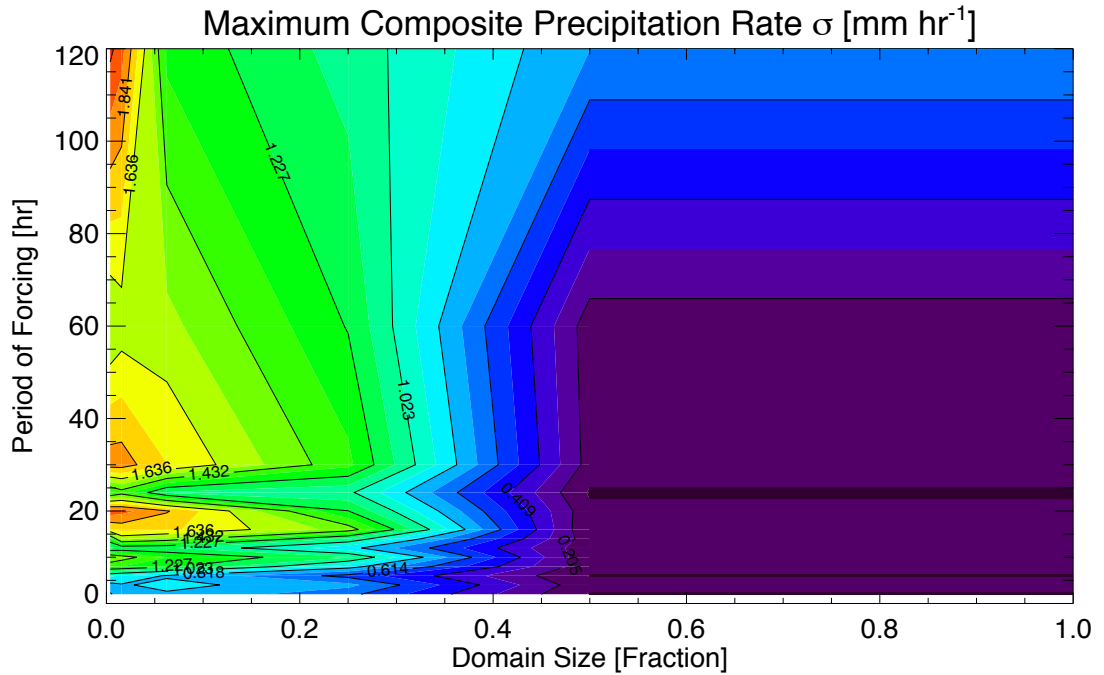


Figure 5.67. As in Table 5.4.

Table 5.5. As in Table 5.3 but for the skewness of the means associated with the composite maximum.

		Domain Size [Fraction]					
		Whole	Half	Quarter	16 th	64 th	256 th
Period of Forcing [hr]	F02	0.332	0.332	0.903	0.717	0.522	0.367
	F04	-0.233	-0.233	0.684	0.855	0.825	0.665
	F06	-0.149	-0.149	-0.538	-0.137	-0.055	-0.192
	F08	-0.328	-0.328	0.113	0.011	-0.087	-0.055
	F10	-0.046	-0.046	0.154	0.030	0.221	0.305
	F12	-0.227	-0.227	0.392	0.491	0.159	0.038
	F14	0.013	0.012	0.719	0.579	0.977	0.499
	F16	0.080	0.080	0.893	0.112	-0.075	-0.069
	F20	0.085	0.085	-0.187	0.276	0.322	0.275
	F24	0.392	0.392	0.158	0.120	-0.014	-0.009
	F30	-0.477	-0.477	-0.069	-0.216	-0.045	-0.055
	F60	0.134	0.134	0.654	0.401	0.496	0.516
F120	-2.548	-2.548	-0.842	-0.656	0.144	0.172	

5.3 More Periodic and Constant Forcing Comparisons

In addition to the comparisons made above, a couple of other areas were given attention with regard to how the periodic and constant forcings were related. First, with regard to the general atmospheric conditions, Figure 5.68 shows that in both the constant forcing simulations (a) and the periodic forcing simulations (b, c, and d) the temperature structure remains fairly constant on the average, regardless of changes in the large-scale forcing. The only thing that even slightly stands out is a slightly different vertical structure in the case of the 0.1 magnitude constant forcing simulation, which is warmer near the surface and cooler aloft. No other significant variations are noted.

The same analysis was performed in the case of relative humidity profiles. This is

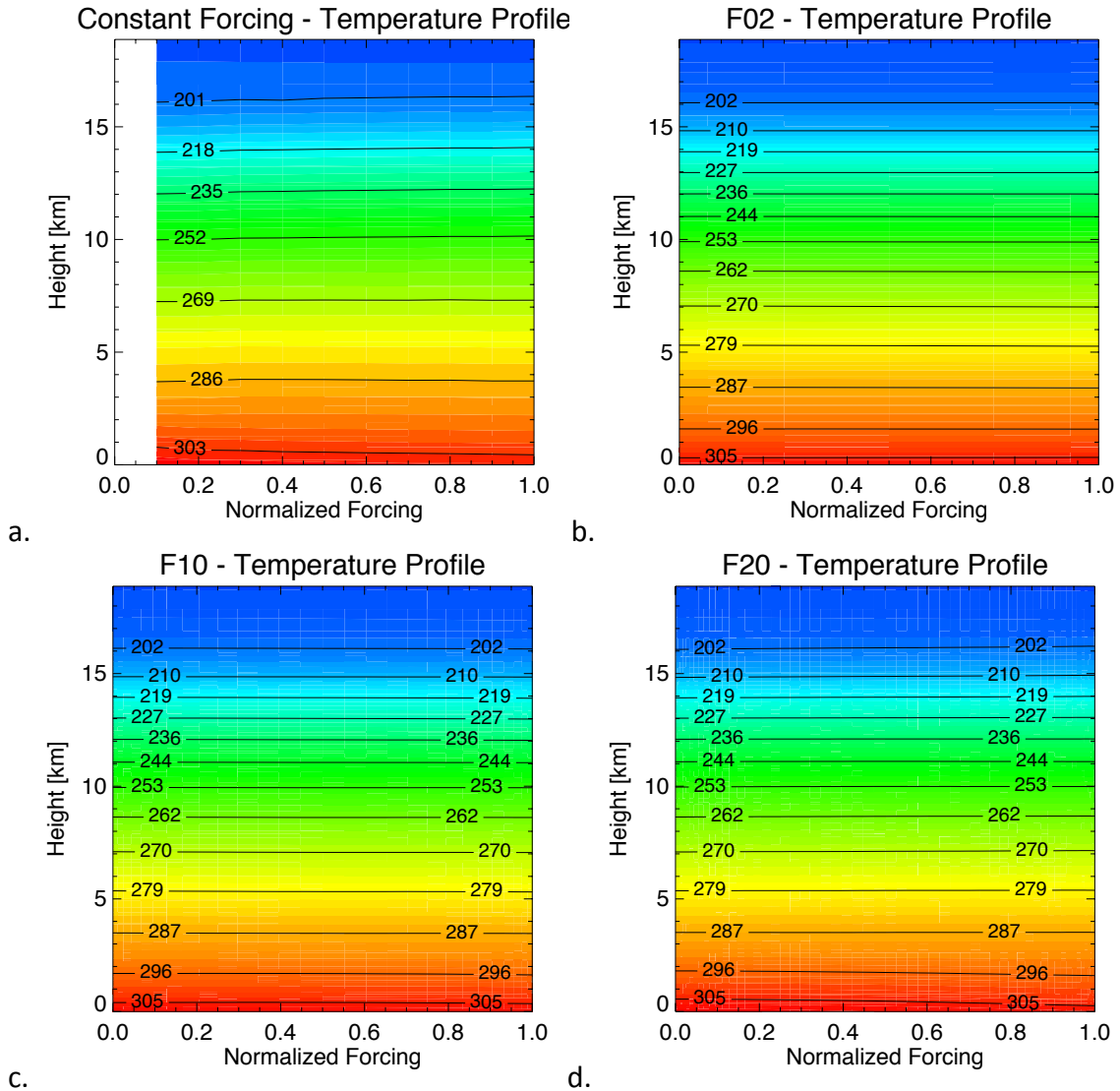


Figure 5.68. Average vertical temperature profiles [K] versus normalized large-scale forcing for (a) constant forcing simulations, (b) F02, (c) F10, and (d) F20.

shown in Figure 5.69. In this case, there is considerable variation between both the different forcing magnitudes as well as the different forcing period lengths. When the forcing is very rapid (F02), average conditions at low forcing are such that there is a reduction in relative humidity aloft moreso than when the forcing is strong. This pattern is out of sync with the results of the constant forcing simulations, which show a pattern that is progressively better reproduced as the forcing period length is increased. Constant forc-

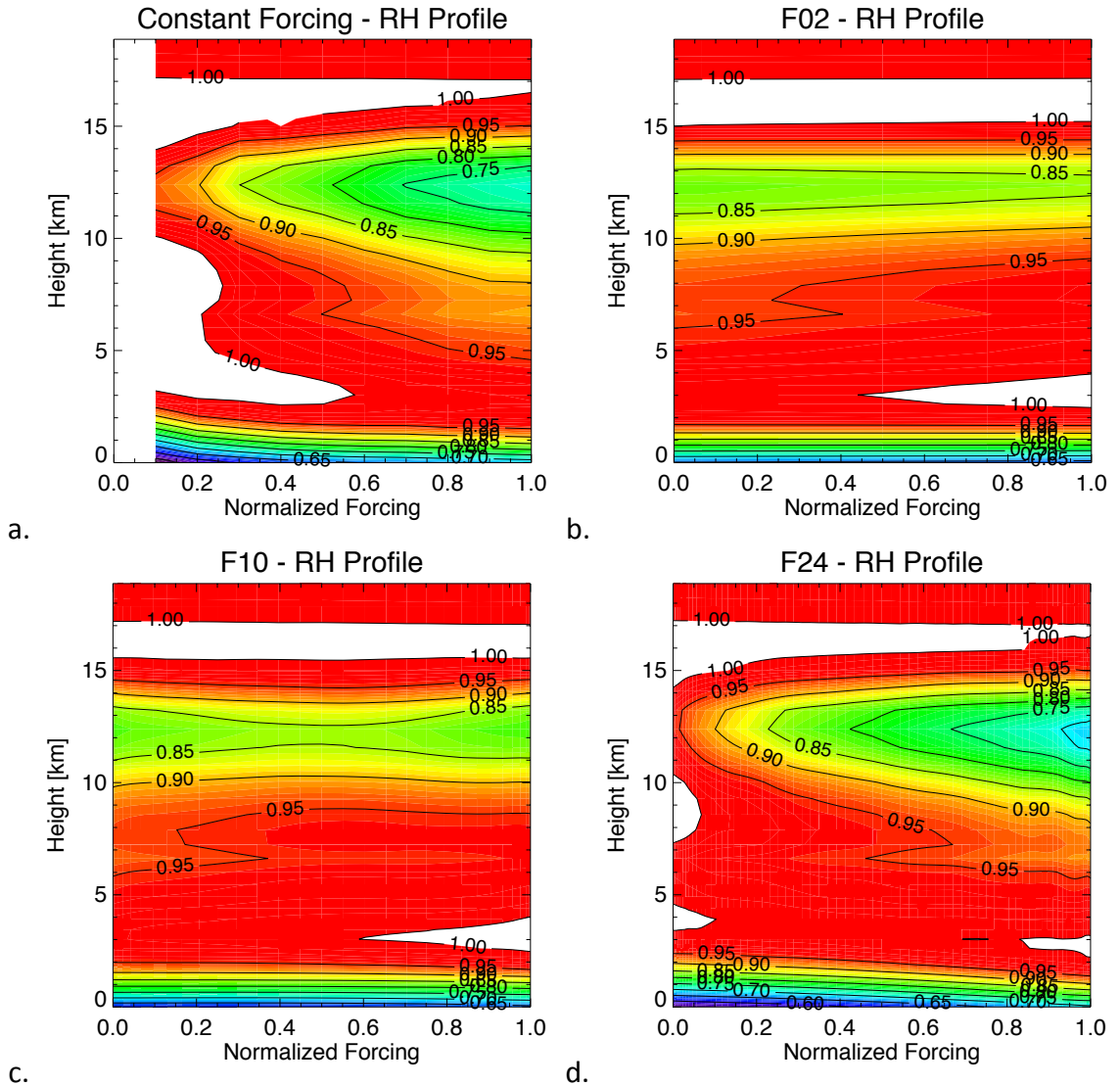


Figure 5.69. As in Figure 5.68 but for relative humidity [fraction]. Additionally, (d) is for F24 rather than F20. The white areas denote regions of supersaturation.

ing, by the way, is very similar to having a varying forcing with infinite period length. When in this state, we see that most of the column (except for very near the surface) is near saturation when the forcing is weak, and there is a dry region that is present aloft when the forcing is strong. Comparing Figure 5.69 to Figures 5.29 and 5.30, we see that the shape of the drier regions by relative humidity correspond to moist regions as defined by cloud fraction and non-precipitating condensate. Also, the white regions in the lower

levels of Figure 5.69 correspond very well with the cloud fraction maxima seen in Figure 5.29. Taking the constant forcing results (Figure 5.69a) to represent the result of a long-period simulation, we once again see the cloud cover maximum well ahead of the forcing maximum.

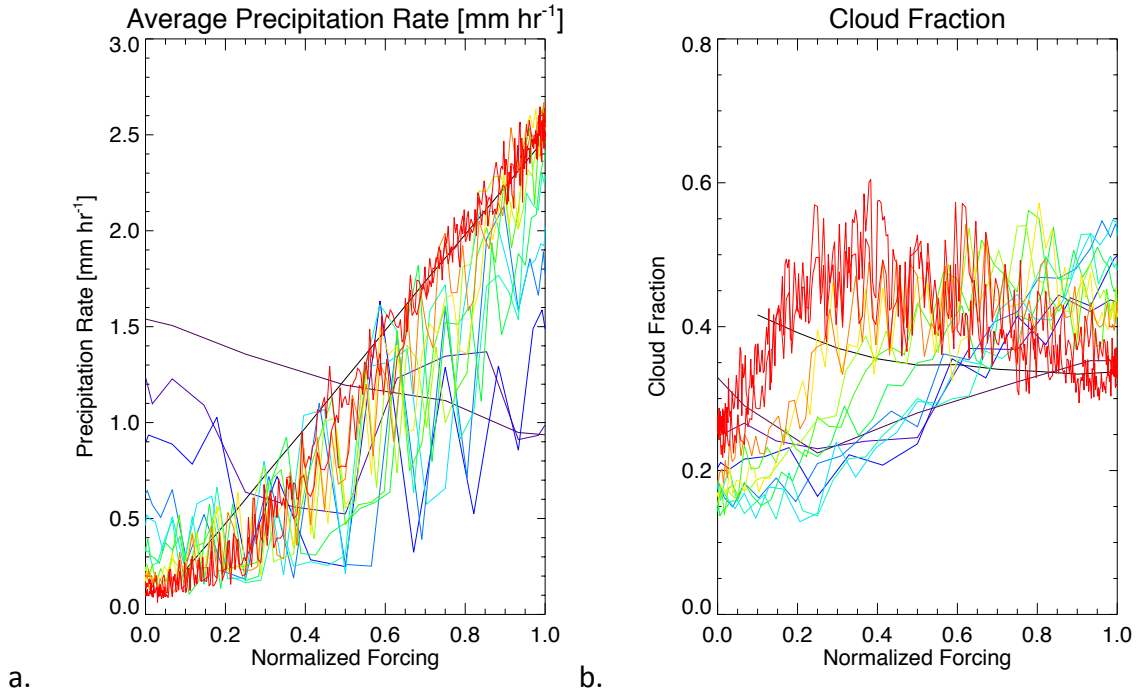


Figure 5.70. The domain averaged precipitation rate (a) and the cloud fraction (b) versus the normalized forcing for all constant and periodic forcing simulations. The black line denotes the results of the constant forcing simulations, and the colored lines represent the periodic forcing simulation results. Colors trending from blues to reds indicate longer period lengths.

More substantial comparisons were performed to determine the differences that arise due to the forcing magnitudes and their variation time scales. The results of the analysis for domain-averaged precipitation rates are shown in panel (a) of Figure 5.70. The black line, representing the results of the constant forcing simulations, is a repeat of that in panel (a) of Figure 5.2.1 with the addition of the point corresponding to zero forc-

ing/precipitation. This line is quite well behaved, showing a linear increase of precipitation rate with forcing magnitude.

The precipitation rates from the periodic forcing simulations, shown as colored lines, are not nearly so. Moving from blues to reds, the colors represent the length of the period of the forcing cycle, with red having the longest period. In these cases, the plotted values are taken from the mean values plotted in the composite plots in Section 5.2.3. Here they are shown without regard to whether the forcing is increasing or decreasing but with regard to the forcing magnitude. Different values for the same forcing are linearly averaged. The F02 simulation (deep purple line) provides a line with negative slope that is also rather well behaved, but it is unlike the constant forcing result. As the forcing period is lengthened, the result is such that there is better alignment with the constant forcing averages. One can get a better feel for the data that went into creating this plot by reviewing Section 5.2.6, specifically Figure 5.58. From this we can see that the reason for deviations from the constant forcing simulation in longer period forcing simulations, such as F120, represented by the red line, are due to the delayed response to the forcing that is brought about by the development of mesoscale organization as previously discussed. Thus, barring mesoscale organization, there is very good agreement between the constant forcing averages and the longest periodic forcing data. The mid-range forcing period lengths show a generally consistent transition from large to small deviations.

The same analysis for cloud fraction is presented in panel (b) of Figure 5.70. In this case, no cloud fraction value for zero forcing was assumed because that is entirely dependant on the initial state and also because the trend of the black curve does not do much to elucidate a solution. The results that are shown for the periodic forcing simula-

tions are rather interesting. Especially after inspection of panel (a), not to mention the most basic understanding of the development of precipitation, one would expect to see more clouds to accompany more precipitation and more large-scale forcing. This seems to be the case with most of the simulations. That is, when the forcing is zero, the cloud fraction is very near its minimum, and the cloud fraction maximum corresponds closely to the forcing maximum. However, for longer simulations (F120 in red, F60 in red-orange, F30 in orange, and to a lesser extent F24 in yellow) the cloud fraction maximum tends to be found at an intermediate forcing magnitude, mainly as a result of the cloud fraction maximum being located very early in the forcing period. This feature is similarly present in the constant forcing curve, which has its maximum at one-tenth the maximum forcing magnitude. The cloud fraction profiles shown in Figure 5.29 verify this placement relative to the forcing and indicate that these clouds are mainly present between 2 and 7 km altitude.

It is not entirely clear as to why this is the case. However, the maximum in the constant forcing simulations and the relative agreement shown by the F60 and F120 simulations seem to indicate that this is a result that's cause is a combination of the lesser magnitude forcing, as well as the increasing nature of the forcing. Investigating further, inspection of Figures 5.21 and 5.22 suggests that this is the same instance of the flux versus storage variables that was previously discussed. The argument, which can be boiled down to a kind of balance relationship between precipitation rate and cloud fraction, is supported by comparison of Figures 5.1.1 and 5.1.2. With the given forcing profile, it seems that the default state of the system is for the cloud fraction to be high with light precipitation. As that forcing's magnitude is increased, precipitation increases, thereby

the reducing cloud amount that had been built up somewhat.

It is very similar to the distinction between drizzling stratus and heavily raining cumulus. This actually appears to be the case when looking at vertical profiles of cloud fraction in CF1 and CFx (Figure 5.71). In the CF1 case, the cloud fraction is strongest nearer the surface in one thick layer, with little cloud aloft. There remains a considerable amount of cloud at low (and even lower) levels in the case of CFx, but there is a bit more aloft, especially at mid levels. This lower cloud fraction with higher elements is more indicative of cumulus than stratus.

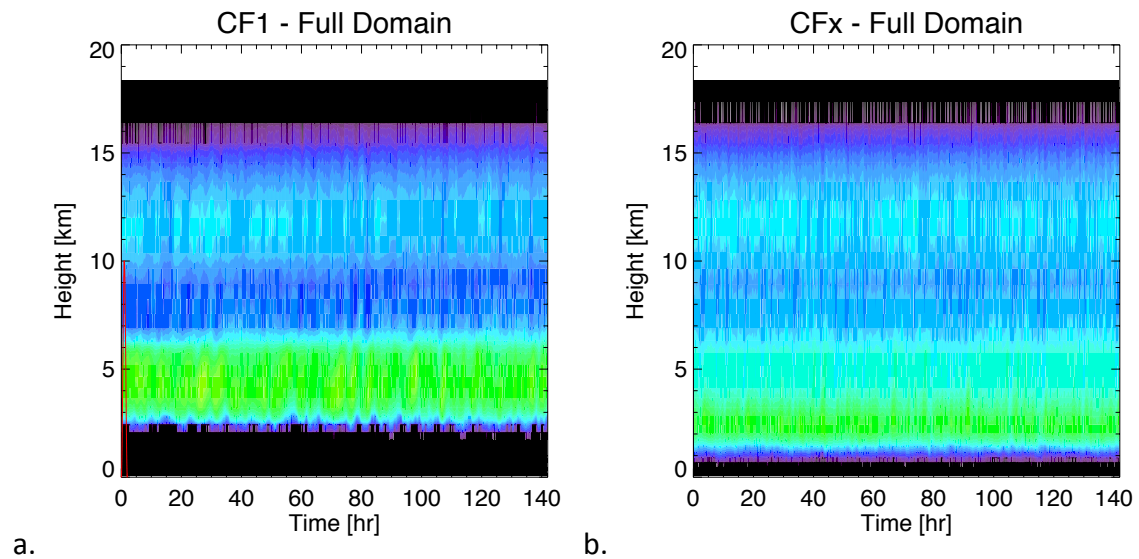


Figure 5.71. Cloud fraction vertical profiles for the CF1 (a) and CFx (b) simulations. Violets and blues are lesser, yellows and greens are greater cloud fractions.

Additionally, the concepts corresponding to the discussion around Figures 2.4 and 2.5 have some application here. Most generally, the ideas that were discussed pointed to the fact that the sufficient addition of variability to a system can cause a shift in the general mode of the system or introduce a bias. While that discussion applied to stochastic variability for use in parameterizations, Figure 5.70 looks at variability in the form of the periodic forcing in comparison to the zero variability of the constant forcing runs. Since

each of the simulations has the same amplitude, the variability with which to be concerned is the time rate of change of the forcing. Thus, shorter periods mean greater variability. That is, variability is inversely proportional to the forcing strength. When interpreted from this perspective, panel (a) of Figure 5.70 appears to show both a shift in mode, as well as a bias depending on the magnitude of the variability. When there is high frequency variability, such as in F02, F04, and to a lesser extent F06 (violet/blue curves), the form of the relationship between large-scale forcing and the precipitation rate are completely reversed from that seen in the constant forcing case.

Additionally, when the variability is much less, or when the forcing is more slowly varying, the general form of the relationship (*i.e.* the slope) is similar, but it has been shifted, or biased, toward lower precipitation values for the same forcing magnitude. Dynamically, this simply means that the more the forcing varies, the more difficult it is for strongly precipitating mesoscale convection to develop. That, in essence, is one example of a bias that results from making the large scale forcing vary, rather than stay constant. In the case of the very quickly varying forcing, a threshold has been crossed that results in a system that is unable of producing sustained mesoscale organization. The regime has shifted, all else being equal. The case for a mode shift as may be interpreted from panel (b) of Figure 5.70 is less clear, though higher variability curves do show a different relationship (slope) between cloud fraction and the forcing compared to the constant forcing simulation results. At any rate, the presence of a bias is clear.

Chapter 6 – Discussion and Conclusions

The need for cloud parameterization is not going away anytime soon since resolving individual clouds remains too computationally expensive on the large scale. QE assumptions, while essentially valid, contain a number of flaws, which derive mainly from the deterministic and diagnostic properties of QE parameterization. Variability not captured by QE can be rather successfully parameterized stochastically in a number of ways, including both methods that include or neglect prior knowledge of distributions of convective variability. This goes to support the prophetic statement made by Lorenz in 1975, “I believe that the ultimate climatic models...will be stochastic, i.e., random numbers will appear somewhere in the time derivatives” (Palmer *et al.* 2005). The variability itself has been determined to depend on a number of parameters. This presents a sizeable challenge to truly effective implementation of stochastic convective parameterizations due to the amount of information that must be conclusively determined and then applied to models.

The analysis described in this thesis has used a variety of methods to review and characterize departures from convective quasi-equilibrium. Fluctuations about the equilibrium state that are found to be present in convective simulations of a cloud-resolving model are not well represented in convective parameterizations of large-scale models, and it is now recognized that inclusion of the associated effects of nondeterministic and nondiagnostic features will prove beneficial to large-scale simulation results. It has been

the aim of this research to determine the response of the statistical characteristics of a variety of convection-related parameters to an imposed periodic large-scale forcing, thus gaining insight into the types of variations that must be considered when attempting to improve upon convective parameterizations.

While others have developed a number of approaches to stochastic parameterization (see Section 2.3) with varying levels of success, we have stepped back to the most basic analyses of what we wish to call truth in the form of cloud-resolving model simulation data to determine at the fine scale how variability is apportioned. A succinct description of what has been done might be to call this a series of case studies or even a sensitivity study with regard to the varying periodic forcing functions employed, in which the most basic and interesting scientific question has been posed, “What happens if we do this?”

In order to validate the claim that the results that are produced by the VVM are actually close to truth, the model was subjected to an intercomparison test, which was designed to compare the results of CRM simulations from a number of models under the same forcing and other conditions (see Chapter 3). While only a selection of model results are currently available, analysis of the results that could be procured suggested that the VVM produces acceptable representations of actual events. Concerns remain regarding a number of features of the VVM’s performance in the intercomparison study, especially with regard to the lack of high frequency temporal variability that was present in most other models and observations. The effect that this may have on the analysis presented in this thesis is not well understood, but that uncertainty implies the need for similar types of analyses to be performed using at least one model that has demonstrated the

high frequency temporal variability that is absent in the VVM data. Because of this, it does not appear to be an ideal model for testing under the prescribed circumstances. However, overall performance was in good agreement with a selection of observed variables and the other models participating in the intercomparison. The degree to which these data are correlated defend the use of the VVM in characterizing the statistical properties of convection under a variety of conditions and permits the simulation results to be considered as nearly empirical, high-resolution data.

Use of the model for characterizing convective properties was accomplished by subjecting the model to a series of tests that varied the rate at which a periodic large-scale forcing oscillated in time. As a control, the model was also subjected to a series of constant forcing simulations for a variety of large-scale forcing magnitudes, which provided a cloud-resolving model representation of statistical equilibrium. There it was shown that the coefficient of variation is not independent of forcing magnitude, particularly those that are very small or very large. This result flies in the face of conventional wisdom, which dictates that variability should scale with the mean. As a consequence, parameterizations that use such an assumption fail to correctly represent variability brought on by nondeterminism (as represented by fluctuations of a response to a constant forcing). This is particularly important because not only must a parameterization include representation of the fact that the convective elements within a large grid cell are not always the same for a giving forcing, but it must also include a representation of the fact that the relationship of the nondeterministic variability is not a simple function of the mean response to the forcing. Such seemingly minor variations are expected to bias aspects of GCM simulations in ways that can alter the representation of statistical (periodic) features. These

types of ideas are well suited for implementation into a parameterization based on a stochastic precept.

While the equilibrium simulation results are alone useful, we find that there are additional layers of complexity to the way in which convection varies in response to a forcing if the forcing has a variable component. With the application of a periodic forcing at varying period lengths and consideration of the simulation results on a series of subdomain sizes, it was shown that there is a considerable range of responses to a given large-scale forcing that are dependent upon the rate of change in the forcing and in the size of the averaging domain.

Specifically, the analyses show that the more slowly a forcing varies, the more it is well approximated by an equilibrium assumption. It was even shown that the introduction of variability can shift convection into different modes or bias it to be less than its expected statistical equilibrium values (see Section 5.3). While it was seen for a number of variables that variability increased with forcing period length, a clear functional relationship was not able to be defined, due mainly to inconsistent variations between simulations of more rapidly oscillating forcings. The point at which the transition between being an acceptable approximation of equilibrium or not occurs is approximately located where the timescale of the variation of the large-scale forcing is greater than 30 hours. With this periodicity, values measuring convective response in simulations with varying forcing very closely match those found in simulations with constant forcing, and the time lag between the forcing and the response is below 5% of the length of the forcing period. While convective response values are comparatively close for shorter periods (as short as 8-10 hours for some variables) the time lag is so great that it should not be considered

equilibrium. Adding to the complexity were the confirmed nondiagnostic effects of lagged responses to forcings that arise due to a number of factors, not the least of which is the presence of mesoscale activity, which has the ability to independently sustain and propagate convection. This was clearly manifested in simulated differences in convective activity that were dependent upon whether the large-scale forcing was increasing or decreasing and also the rate at which it was doing so.

Further, nondeterministic variability for a given situation is much greater at smaller domain sizes; this is the problem of insufficient sample size, which is one that grows in importance as grid spacing in GCMs approaches the lower tens of kilometers. This relationship was determined to be best described by a logarithmic function of the domain area. The definition of where to draw the line between equilibrium and non-equilibrium and determinism and non-determinism based on this criterion is somewhat subjective, especially in terms of the given weather regime as determined by the vertical wind shear. Based on the statistics for the weather regime presented in this thesis, the best recommendation is that the line should be drawn such that the considered area (grid box area) is no smaller than about half the domain size used in this thesis. This is equivalent to about 33,000 km² or grid spacing slightly larger than 180 km (approximately T80 spectral resolution). It is at this point that the coefficient of variation is larger than about one half. This means that the standard deviation is half of the mean. This seems to be a fitting definition of not exactly being deterministic. Just to put out the numbers, when the standard deviation is the same magnitude of the mean, if that is where one may choose to draw the line, the computational domain is between a quarter and one 16th of the full do-

main that was used. This is somewhere in the vicinity of a 100 km grid spacing (approximately T125 spectral resolution).

The simulations showed considerable agreement with previous work (*e.g.* X92), but due to differences in experiment design and a lack of additional work for comparison, there is little to say with regard to how these results compare to those obtained previously. For that reason alone, this type of analysis should be repeated with additional models for verification of the presented results. The additional call for such a comparison as a byproduct of the results of the intercomparison study makes for a very strong case for the need for more data. Current intentions are to proceed with this action using SAM (see Chapter 3), which showed considerably more temporal variability in the intercomparison simulation and is a documented and readily available model.

Cumulatively, the results of the performed experiment highlight both the complexity underlying the development of, and the need for, stochastic convective parameterization. Classical assumptions about quasi-equilibrium are never exact and break down altogether when the time scale for changes in the resolved-scale weather is near or less than the convective adjustment time. This is a problem that is made more severe in newer high-resolution models (*e.g.* Arribas 2004; Bechtold *et al.* 2008) just because shorter time scales are inherent in convective systems with smaller spatial scales. The basics of a statistical approach for the development of a stochastic parameterization as outlined at the end of Section 5.27, which are based on the results of the statistical analyses, are a likely path for future work, following a necessary complementary analysis using another CRM. Such an approach seems promising in that it captures the effect of statistical variations in a diagnostic manner given a relatively wide variety of predictors. Previ-

ous studies have shown that there is promise in stochastic parameterizations when it comes to improvement of GCM simulations (See Chapter 1), and it is likely that this approach will have a similar effect.

Appendix 1 – TWP-ICE Simulation Data List

3-DIMENSIONAL, 3-HOURLY	PROFILES, 10-MINUTE	SCALARS, 10-MINUTE
<i>Air temperature</i>	<i>Mean air pressure</i>	<i>Mean liquid water path</i>
<i>Zonal wind speed</i>	<i>Mean air temperature</i>	+ Max.
<i>Meridional wind speed</i>	<i>Reference air density</i>	+ where surface precipitation rate < 0.02 mm h ⁻¹
<i>Vertical wind speed</i>	<i>Mean zonal wind speed</i>	+ Max.
<i>Water vapor mixing ratio</i>	<i>Mean meridional wind speed</i>	+ at 4-km res.
<i>Cloud water mixing ratio</i>	<i>Min. vertical wind speed</i>	+ at 25-km res.
<i>Rain water mixing ratio</i>	+ Max.	+ at 55-km res.
<i>Ice (all forms) mixing ratio</i>	<i>Mean relative humidity</i>	<i>Mean ice water path</i>
<i>Relative Humidity</i>	+ Min.	+ Max.
	+ Max.	+ where surface precipitation rate < 0.02 mm h ⁻¹
	+ Min. at 55-km res.	+ Max.
	+ Max. at 55-km res.	+ at 4-km res.
	<i>Mean water vapor mix. rat.</i>	+ at 20-km res.
	+ Min.	+ at 55-km res.
	+ Max.	<i>Mean surface precipitation rate</i>
	+ Min. at 55-km res.	+ Max.
	+ Max. at 55-km res.	+ at 55-km res.
	<i>Mean cloud water mix. rat.</i>	<i>Mean precipitation rate at 2.5 km elevation</i>
	+ Max.	..+ Max. at 2.5-km res.
	+ where surface precipitation rate < 0.02 mm h ⁻¹	<i>Fractional area where precipitation at 2.5-km elevation and res. > 0.02 mm h⁻¹</i>
	+ Max.	..+ > 00.20 mm h ⁻¹
	+ Max. at 55-km res.	..+ > 02.00 mm h ⁻¹
	<i>Mean rain water mix. rat.</i>	..+ > 20.00 mm h ⁻¹
	+ Max.	<i>Mean cloud base height</i>
	+ Max. at 55-km res.	+ Min.
	<i>Mean ice mix. rat.</i>	+ Max
	+ Max.	+ at 4-km res.
	+ where surface precipitation rate < 0.02 mm h ⁻¹	+ at 55-km res.
	+ Max	<i>Mean cloud top height</i>

	+ Max. at 20-km res.	+ Min.
	+ Max. at 55-km res.	+ Max
	Cloud fraction	+ at 4-km res.
	+ vertical wind $> 0 \text{ m s}^{-1}$	+ at 55-km res.
	+ buoyant	Fractional area covered by cloudy columns
	+ vertical wind $> 5 \text{ m s}^{-1}$	Mean shortwave downwelling flux at TOA
	Mass flux averaged over cloudy grid cells with vertical wind $> 0 \text{ m s}^{-1}$	Mean shortwave upwelling flux at TOA
	+ buoyant	+ Min. at 4-km res.
	Mass flux averaged over cloudy grid cells with vertical wind $> 5 \text{ m s}^{-1}$	+ Max. at 4-km res.
	Mean boundary layer tracer mixing ratio	Mean longwave upwelling flux at TOA
	+ Min.	+ Min. at 4-km res.
	+ Max.	+ Max. at 4-km res.
	Mean lower-troposphere tracer mixing ratio	Mean latent heat flux at surface (excluding precipitation)
	+ Min.	+ Min.
	+ Max.	+ Max.
	Mean mid-troposphere tracer mixing ratio	Mean sensible heat flux at surface
	+ Min.	+ Min.
	+ Max.	+ Max.
	Mean upper-troposphere tracer mixing ratio	
	+ Min.	
	+ Max.	
	Mean shortwave downwelling radiative flux	
	+ Min.	
	+ at 55-km resolution	
	+ Max.	
	+ at 55-km resolution	
	+ where surface precipitation rate $< 0.02 \text{ mm h}^{-1}$	
	+ Min.	
	+ Max	
	Mean shortwave upwelling radiative flux	
	+ Min.	
	+ at 55-km resolution	

	+ Max.	
	+ at 55-km resolution	
	+ where surface precipitation rate < 0.02 mm h ⁻¹	
	+ Min.	
	+ Max	
	Mean longwave downwelling radiative flux	
	+ Min.	
	+ at 55-km resolution	
	+ Max.	
	+ at 55-km resolution	
	+ where surface precipitation rate < 0.02 mm h ⁻¹	
	+ Min.	
	+ Max	
	Mean longwave upwelling radiative flux	
	+ Min.	
	+ at 55-km resolution	
	+ Max.	
	+ at 55-km resolution	
	+ where surface precipitation rate < 0.02 mm h ⁻¹	
	+ Min.	
	+ Max	
	Mean shortwave broadband heating rate	
	+ Min.	
	+ Max.	
	+ where surface precipitation rate < 0.02 mm h ⁻¹	
	+ Min.	
	+ Max.	
	Mean longwave broadband heating rate	
	+ Min.	
	+ Max.	
	+ where surface precipitation rate < 0.02 mm h ⁻¹	
	+ Min.	
	+ Max.	
	Mean latent heating rate	
	Mean water vapor tendency	
	Mean large-scale water vapor horizontal flux conver-	

	<i>gence</i>	
	<i>Mean large-scale water vapor vertical flux convergence</i>	
	<i>Mean water vapor resolved and subgrid-scale vertical flux convergence</i>	
	<i>Mean water vapor tendency from exchange with hydrometeors</i>	
	<i>Mean water vapor tendency from nudging</i>	
	<i>Mean hydrometeor tendency</i>	
	<i>Mean large-scale hydrometeor vertical flux convergence</i>	
	<i>Mean hydrometeor resolved and subgrid-scale vertical flux convergence</i>	
	<i>Mean sedimentation flux convergence of hydrometeors</i>	
	<i>Mean potential temperature tendency</i>	
	<i>Mean large-scale potential temperature horizontal flux convergence</i>	
	<i>Mean large-scale potential temperature vertical flux convergence</i>	
	<i>Mean potential temperature resolved and subgrid-scale vertical flux convergence</i>	
	<i>Mean potential temperature tendency from microphysics</i>	
	<i>Mean potential temperature tendency from radiative heating</i>	
	<i>Mean potential temperature tendency from nudging</i>	

Reference List

- Abdullaev, S.M., A.A.Zhel'nin, and O. Yu. Lenskaya, 2009: Life cycle of mesoscale convective systems. *Russian Meteorol. and Hydrol.*, **34**, 285-292.
- Arakawa, A., 2004: The cumulus parameterization problem: past, present, and future. *J. Climate*, **14**, 2493-2525.
- , A. and W.H. Schubert, 1974: Interaction of a cumulus cloud ensemble with the large-scale environment, Part I. *J. Atmos. Sci.*, **31**, 674-701.
- Arribas, A., 2004: Results of an initial stochastic physics scheme for the Met Office Unified Model. *Forecasting Research Tech. Rpt. No. 452*.
- Ball, M.A., and R.S. Plant, 2008: Comparison of stochastic parameterization approaches in a single column model. *Phil. Trans. R. Soc. A*, **366**, 2605-2623.
- Bechtold, P., M. Köhler, T. Jung, F. Doblas-Reyes, M. Leutbecher, M. J. Rodwell, F. Vitart, G. Balsamo, 2008: Advances in simulating atmospheric variability with the ECMWF model: from synoptic to decadal time-scales. *Quart. J. Roy. Meteor. Soc.*, **134**, 1337-1351, also available as ECMWF Tech. Memo, 556.
- Berloff, P. S., 2005: Random-forcing model of the mesoscale oceanic eddies. *J. Fluid Mech.* **529**, 71-95.
- Bright, D.R. and S.L. Mullen, 2002: Short-range ensemble forecasts of precipitation during the Southwest monsoon. *Wea. Forecasting*, **17**, 1080-1100.
- Buizza, R., M. Miller, and T.N. Palmer, 1999: Stochastic representation of model uncertainties in the ECMWF ensemble prediction system. *Quart. J. Roy. Meteor. Soc.*, **125**, 2887-2908.
- Byun, Y.-H. & Hong, S.-Y., 2007: Improvements in the subgrid-scale representation of moist convection in a cumulus parameterisation scheme: the single-column test and its impact on seasonal prediction. *Mon. Weather Rev.*, **135**, 2135-2154.
- Craig, G.C., and B.G. Cohen, 2006: Fluctuations in an equilibrium convective ensemble. Part I: Theoretical formulation. *J. Atmos. Sci.*, **63**, 1996-2004.
- Cohen, B.G., and G.C. Craig, 2006: Fluctuations in an equilibrium convective ensemble. Part II: Numerical experiments. *J. Atmos. Sci.*, **63**, 2005-2014.

- Corti S., F. Molteni, T.N. Palmer, 1999: Signature of recent climate change in frequencies of natural atmospheric circulation regimes, *Nature*, **398**, 799–802.
- Ducharne, A., R. D. Koster, M. J. Suarez, M. Stieglitz, and P. Kumar, 2000: A catchment-based approach to modeling land surface processes in a general circulation model. 2. Parameter estimation and model demonstration. *J. Geo. Res.*, **105**, 24,823–24,838.
- Fidlind, A., A. Ackerman, J. Petch, P. Field, A. Hill, G. McFarquhar, S. Xie, M. Zhang, T. Jones *et al.*, 2010: TWP-ICE CRM intercomparison study. Manuscript in progress.
- , ----, ----, ----, J.-P. Chaboreau, J. Fan, T. Jones, H. Morrison, S. Park, X. Wu, and J.-I. Yano, 2009: “ARM/GCSS/SPARC TWP-ICE CRM Study.” Graphical presentation. Fall 2009 ARM Meeting. Cloud Modeling Working Group. Boulder, CO. September 29. http://science.arm.gov/wg/cpm/scm/pass/2009_fallMeeting/index.html
- Hasselmann, K., 1976: Stochastic climate models. Part I. Theory. *Tellus*, **28**, 473–485.
- Horinouchi, T., S. Pawson, K. Shibata, U. Langematz, E. Manzini, M. A. Giorgetta, F. Sassi, R. J. Wilson, K. Hamilton, J. de Grandpré, and A. A. Scaife, 2003: Tropical cumulus convection and upward-propagating waves in middle-atmospheric GCMs. *J. Atmos. Sci.*, **60**, 2765–2782.
- Houze, R.A., 1997: Stratiform precipitation in regions of convection. *Bull. Amer. Meteor. Soc.*, **78**, 2179–95.
- Jung, J.-H., and A. Arakawa, 2008: A three-dimensional anelastic model based on the vorticity equation. *Mon. Wea. Rev.*, **136**, 276–294.
- Jung, T., 2005: Systematic errors of the atmospheric circulation in the ECMWF forecasting system. *Q. J. R. Meteorol. Soc.*, **131**, 1045–1073.
- Kain, J.S., 2004: The Kain-Fritsch convective parameterization: An update. *J. Appl. Meteor.*, **43**, 170–181.
- Katzfey, J.J., and B.F. Ryan, 2000: Midlatitude frontal clouds: GCM-scale modeling implications. *J. Climate*, **13**, 2729–2745.
- Khairoutdinov, M. F. and D. A. Randall, 2003: Cloud resolving modeling of the arm summer 1997 iop: Model formulation, results, uncertainties, and sensitivities. *J. Atmos. Sci.*, **60**, 607–625.
- Krueger, S.K., 1998: Numerical simulation of tropical cumulus clouds and their interaction with the subcloud layer. *J. Atmos. Sci.*, **45**, 2221–2250.
- Lin, J.W.-B., and J.D. Neelin, 2002: Considerations for stochastic convective parameterization. *J. Atmos. Sci.*, **59**, 949–975.

- Lord, S.J. and A. Arakawa, 1980: Interaction of a cumulus cloud ensemble with the large-scale environment, Part II. *J. Atmos. Sci.*, **37**, 2677-2692.
- Lorenz, E.N., 1963: Deterministic nonperiodic flow. *J. Atmos. Sci.*, **20**, 130-141.
- May, P. T., J. H. Mather, G. Vaughan, and C. Jakob, 2008: Characterizing oceanic convective cloud systems—The Tropical Warm Pool International Cloud Experiment, *Bull. Am. Meteorol. Soc.*, **154**, 153-155.
- Molteni F, and S. Tibaldi, 1990: Regimes in the wintertime circulation over the northern extra-tropics. II. Consequences for dynamical predictability, *Q. J. R. Meteorol. Soc.*, **116** 1263-1288.
- Neelin, J.D., O. Peters, J.W.-B. Lin, K. Hales, and C.E. Holloway, 2008: Rethinking convective quasi-equilibrium: observational constraints for stochastic convective schemes in climate models. *Quart. J. Roy. Meteor. Soc.*, submitted.
- Nicolis, C., 2004: Dynamics of model error: the role of unresolved scales revisited. *J. Atmos. Sci.* **61**, 1740–1753.
- Ormsby, J.F.A., 1961: Design of numerical filters with application to missile data processing. *J. Assoc. Comput. Mach.*, **8**, 440-466.
- Palmer, T.N., and P.D. Williams, 2008: Introduction. Stochastic physics and climate modelling. *Phil. Trans. R. Soc. A*, **366**, 2421-2427.
- , G.J. Shutts, R. Hagerdorn, F.J. Doblas-Reyes, T. Jung, and M. Leutbecher, 2005: Representing model uncertainty in weather and climate prediction. *Annu. Rev. Earth Planet Sci.*, **33**, 163-193.
- , 2001: A nonlinear dynamical perspective on model error: a proposal for non-local stochastic-dynamic parameterization in weather and climate prediction models. *Q.J.R. Meteorol. Soc.* **127**, 279–304.
- , 1997: On parametrizing scales that are only somewhat smaller than the smallest resolved scales with application to convection and orography. In *Proc. ECMWF Workshop on New Insights and Approaches to Convective Parametrization, Reading, UK, 4–7 November 1996*.
- Petch, J.C., P.N. Blossey, and C. S. Bretherton, 2008: Differences in the lower troposphere in two- and three-dimensional cloud-resolving model simulations of deep convection. *Q.J.R. Meteorol. Soc.*, **134**, 1941-1946.
- Piani, C., Norton, W. A. & Stainforth, D. A., 2004: Equatorial stratospheric response to variations in deterministic and stochastic gravity wave parameterizations. *J. Geophys. Res.* **109**, D14 101.

- Plant, R.S., and G.C. Craig, 2008: A stochastic parameterization for deep convection based on equilibrium statistics. *J. Atmos. Sci.*, **65**, 87-105.
- Randall, D.A., and C. Konor, 2008: Simulation of global cloudiness. *J. Physics: Conf. Ser.*, **125**, doi:10.1088/1742-6596/125/1/012021.
- , P. Ding, and D.-M. Pan, 1997a: The Arakawa-Schubert Parameterization. In *The Physics and Parameterization of Moist Atmospheric Convection* (ed. R.K. Smith), pp. 281-296, Kluwer Academic Publishers: The Netherlands.
- , P. Ding, and D.-M. Pan, 1997b: Quasi-equilibrium. In *The Physics and Parameterization of Moist Atmospheric Convection* (ed. R.K. Smith), pp. 359-385, Kluwer Academic Publishers: The Netherlands.
- , Q. Hu, K.-M. Xu, and S.K. Krueger, 1994: Radiative-convective disequilibrium. *Atmos. Res.*, **31**, 315-327.
- Ricciardulli, L. & Garcia, R. R., 2000: The excitation of equatorial waves by deep convection in the NCAR Community Climate Model (CCM3). *J. Atmos. Sci.*, **57**, 3461–3487.
- Roy, S.B. 2009: A quest for the mesoscale gap. *Geophysical Research Abstracts*, **11**, EGU2009-10067. EGU General Assembly 2009.
- Sardeshmukh, P., Penland, C. & Newman, M., 2001: Rossby waves in a stochastically fluctuating medium. In *Stochastic climate models* (ed. P. Imkeller & J.-S. von Storch), pp. 369–384. Basel: Birkhäuser.
- Scott, R. B., 2003: Predictability of SST in an idealized, one-dimensional, coupled atmosphere-ocean climate model with stochastic forcing and advection. *J. Clim.* **16**, 323–335.
- Shutts, G.J., T. Allen, and J. Berner, 2008: Stochastic parameterization of multiscale processes using a dual-grid approach. *Phil. Trans. R. Soc. A*, **366**, 2623-2639.
- , and T.N. Palmer, 2007: Convective forcing fluctuations in a cloud-resolving model: Relevance to the stochastic parameterization problem. *J. Climate*, **20**, 187-202.
- , and ----, 2004: The use of high resolution numerical simulations of tropical circulation to calibrate stochastic physics schemes. In *Proc. ECMWF/CLIVAR workshop on simulation and prediction of intra-seasonal variability with emphasis on the MJO, 3–6 November 2003*, pp. 83–102.
- Sivapalan, M., K. Beven, and E. F. Wood, 1987: On hydrologic similarity, 2, A scaled model of storm runoff production, *Water Resour. Res.*, **23**, 2266-2278.

- Song, Y., C.K. Wikle, C.J. Anderson, and S.A. Lack, 2007: Bayesian estimation of stochastic parameterizations in a numerical weather forecasting model. *Mon. Wea. Rev.*, **135**, 4045-4059.
- Sui, C.-H., and M. Yanai, 1986: Cumulus ensemble effects on the large-scale vorticity and momentum fields of GATE. Part I: Observational evidence. *J. Atmos. Sci.*, **43**, 1618-1642.
- Teixeira, J., and C.A. Reynolds, 2008: Stochastic nature of physical parameterizations in ensemble prediction: A stochastic convection approach. *Mon. Wea. Rev.*, **136**, 483-496.
- Tompkins, A. M., and J. Berner, 2008: A stochastic convective approach to account for model uncertainty due to unresolved humidity variability. *J. Geophys. Res.*, **113**, D18101
- van der Hoven, I. 1957: Power spectrum of the horizontal wind speed spectrum in the frequency range from 0.0007 to 900 cycles per hour. *J. Atmos. Sci.*, **14**, 160-164.
- Vaughan, G., Schiller, C., MacKenzie, A. R., Bower, K., Peter, T., Schlager, H., Harris, N. R. P., and May, P. T.: Studies in a natural laboratory, High-altitude aircraft measurements around deep tropical convection, *Bull. Amer. Meteor. Soc.*, **89**, 647-662, 2008.
- Wilks, D.S., 2008: Effects of stochastic parameterization on conceptual climate models. *Phil. Trans. R. Soc. A*, **366**, 2475-2488.
- Williams, P.D., 2005: Modelling climate change: the role of unresolved processes. *Phil. Trans. R. Soc. A*, **363**, 2931-2946.
- Xie, S., T. Hume, C. Jakob, S. A. Klein, R. McCoy, and M. Zhang 2009: Observed large-scale structures and diabatic heating and drying profiles during TWP-ICE, *submitted to Journal of Climate*.
- Xu, K.-M., 1994: A statistical analysis of the dependency of closure assumptions in cumulus parameterizations on the horizontal resolution. *J. Atmos. Sci.*, **51**, 3674-3691.
- , and D.A. Randall, 1998: Influence of large-scale advective cooling and moistening effects on the quasi-equilibrium behavior of explicitly simulated cumulus ensembles. *J. Atmos. Sci.*, **55**, 896-909.
- , and A. Arakawa, 1992: Semiprognostic tests of the Arakawa-Schubert parameterization using simulated data. *J. Atmos. Sci.*, **49**, 2421-2436.
- , ----, and S.K. Krueger, 1992: The macroscopic behavior of cumulus ensembles simulated by a cumulus ensemble model. *J. Atmos. Sci.*, **49**, 2402-2420.

- Yanai, M., S. Esbensen, and J.-H. Chu, 1972: Determination of bulk properties of tropical cloud clusters from large-scale heat and moisture budgets. *J. Atmos. Sci.*, **30**, 611-627.
- Zavala-Garay, J., Moore, A. M. & Perez, C. L., 2003: The response of a coupled model of ENSO to observed estimates of stochastic forcing. *J. Clim.* **16**, 2827–2842.
- Zeng X., Tao W.K., Zhang M., Peters-Lidard C., Lang S., Simpson J., Kumar S., Xie S., Eastman J.L., Shie C.L., Geiger J.V., 2007: Evaluating clouds in long-term cloud-resolving model simulations with observational data. *J. Atmos. Sci.* **64**, 4153–4177.